Natural and Modified Active Sites in [FeFe] Hydrogenases in the Crosshairs of Biophysical Methods

Inaugural-Dissertation

zur Erlangung des Doktorgrades
der Mathematisch-Naturwissenschaftlichen Fakultät
der Heinrich-Heine-Universität Düsseldorf

vorgelegt von

Constanze Sommer
aus Langen

Düsseldorf, Februar 2018

aus dem Max-Planck Institut für Chemische Energiekonversion
in Mülheim an der Ruhr
und der Heinrich-Heine-Universität Düsseldorf

Gedruckt mit der Genehmigung der
Mathematisch-Naturwissenschaftlichen Fakultät der
Heinrich-Heine-Universität Düsseldorf

Berichterstatter:

1. Prof. Dr. Wolfgang Lubitz

2. Prof. Dr. Henrike Heise

Tag der mündlichen Prüfung: 03.05.2018

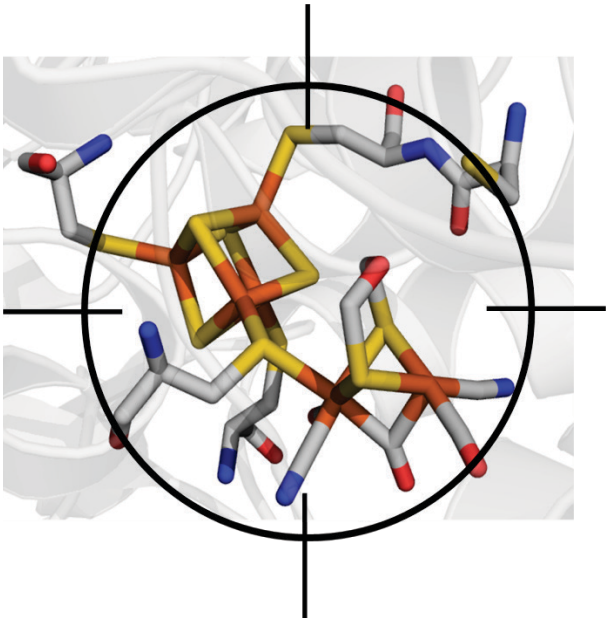

Table of Contents

A. List of Abbreviations

Abbreviation	Description
A	Hyperfine coupling constant
CpI	[FeFe] Hydrogenase from *Clostridium pasteurianum*
HydA1	[FeFe] Hydrogenase from *Chlamydomonas reinhardtii*
CA	Cyclic chronoamperometry
CV	Cyclic voltammetry
CW	Continuous wave
DdH	[FeFe] Hydrogenase from *Desulfovibrio desulfuricans*
DET	Direct electron transfer
DFT	Density function theory
E. coli	*Escherichia coli*
EPR	Electron paramagnetic resonance
FID	Free-induction decay
FTIR	Fourier-transform infrared
HABA	2-(4-Hydroxyphenylazo)-benzoic acid
HIPIP	High potential iron-sulfur proteins
IPTG	Isopropyl β-D-1-thiogalacto-pyranoside
J	Heisenberg exchange coupling constant
$\mathbf{k_B}$	Boltzmann constant
MO	Molecular orbital
NMR	Nuclear magnetic resonance
PCET	Proton coupled electron transfer
PFE	Protein film electrochemistry
PGE	Pyrolytic graphite edge
QM/MM	Quantum mechanics/molecular mechanics
RF	Radiofrequency
ROS	Reactive oxygen species
SAM	S-adenosylmethionine
$\mathbf{T_1}$	Longitudinal (spin-lattice) relaxation time
$\mathbf{T_2}$	Spin-spin relaxation time
TIM	Triose phosphate isomerase
ZFS	Zero field splitting

Abbreviation	Description
[2M]-XXX	Formula representing the free precursor complexes where M can be Fe or Ru
-ADT	aza-propane-dithiolate ligand
-PDT	propane-dithiolate ligand
-ODT	oxa- propane-dithiolate ligand
-ADSe	aza-propane-diselenate ligand
-PDSe	propane-diselenate ligand

B. Declaration

Ich versichere an Eides Statt, dass die Dissertation von mir selbstständig und ohne unzulässige fremde Hilfe unter Beachtung der "Grundsätze zur Sicherung guter wissenschaftlicher Praxis an der Heinrich-Heine Universität Düsseldorf" erstellt worden ist. Alle verwendeten Quellen sind angegeben. Teile der Dissertation sind bereits publiziert (siehe „List of Publications".

I assure you on oath that this dissertation has been written independently and without any unauthorized foreign assistance. The principles of "Grundsätze zur Sicherung guter wissenschaftlicher Praxis an der Heinrich-Heine Universität Düsseldorf" were followed. All sources and references that I used are given. Parts of the thesis are already published (see "List of Publications").

_____

Constanze Sommer

C. List of Publications

This thesis includes the following publications, which are given in section 4. Paper I, II and III are already published. Paper IV, V and VI are submitted or under revision (as at Feb 2018). All publications are based on joint work with colleagues and/or other scientific groups. My contributions and the contributions of others are indicated. To give a full overview over the work done, publications that are not included in the thesis are given at the end of the list.

I Proton Coupled Electronic Rearrangement within the H-Cluster as an Essential Step in the Catalytic Cycle of [FeFe] Hydrogenases

C. Sommer, A. Adamska-Venkatesh, K. Pawlak, J.A. Birrell, O. Rüdiger, E.J. Reijerse, W. Lubitz, J Am Chem Soc. **2017**, *139*, 1440-3.

II Chalcogenide substitution in the [2Fe] cluster of [FeFe]-hydrogenases conserves high enzymatic activity

L. Kertess, F. Wittkamp, C. Sommer, J. Esselborn, O. Rüdiger, E.J. Reijerse, E. Hofmann, W. Lubitz, M. Winkler, T. Happe, U.-P. Apfel, Dalton Trans. **2017**, *46*, 16947-58.

III ^{1}H NMR Spectroscopy of [FeFe] Hydrogenase: Insight into the Electronic Structure of the Active Site

S. Rumpel, E. Ravera, C. Sommer, E.J. Reijerse, C. Farès, C. Luchinat, W. Lubitz, J Am Chem Soc. **2017**, *140*, 131-34.

IV Spectroscopic Investigations of a semi-synthetic [FeFe] hydrogenase with propane di-selenol as bridging ligand in the binuclear subsite

C. Sommer, S. Rumpel, S. Roy, C. Farès, V. Artero, M. Fontecave, E. Reijerse, W. Lubitz

Submitted; Journal of Biological and Inorganic Chemistry on 02.02.2018

Published 07.04.2018, DOI: 10.1007/s00775-018-1558-4

V Direct Detection of the Terminal Hydride Intermediate in [FeFe] Hydrogenase by NMR Spectroscopy

S. Rumpel, C. Sommer, E. Reijerse, C. Farès, W. Lubitz

Revised; Journal of the American Chemical Society; Published 09.03.2018, DOI: 10.1021/jacs.8b00459

VI The [RuRu] analogue of [FeFe] hydrogenase traps the key metal bound hydride intermediate in the enzymes catalytic cycle

C. Sommer, C. Richers, W. Lubitz, E. Reijerse, T. Rauchfuss

Submitted, Angewandte Chemie International Edition on 13.02.2018

Published 26.03.2018, DOI: 10.1002/anie.201801914

Publications not considered for this thesis

- **Following [FeFe] Hydrogenase Active Site Intermediates by Time-Resolved Mid-IR Spectroscopy**

M. Mirmohades, A. Adamska-Venkatesh, C. Sommer, E. Reijerse, R. Lomoth, W. Lubitz, L. Hammarström, J. Phys. Chem. Lett. **2016**, *7*, 3290-93

- **Unique Spectroscopic Properties of the H-Cluster in a Putative Sensory [FeFe] Hydrogenase**

N. Chongdar, J.A. Birrell, K. Pawlak, C. Sommer, E.J. Reijerse, O. Rüdiger, W. Lubitz, H. Ogata, J. Am. Chem. Soc. **2018**, *140*, 1057-68

- **Reaction Coordinate Leading to H_2 Production in [FeFe]-Hydrogenase Identified by Nuclear Resonance Vibrational Spectroscopy and Density Functional Theory**

V. Pelmenschikov, J.A. Birrell, C.C. Pham, N. Mishra, H. Wang, C. Sommer, E. Reijerse, C.P. Richers, K. Tamasaku, Y. Yoda, T.B. Rauchfuss, W. Lubitz, S.P. Kramer, J. Am. Chem. Soc. **2017**, 139, 46, 16894-16902

- **Engineering a microbial [FeFe]-hydrogenase: towards an algal-like enzyme with oxygen resistance**

G. Caserta, C. Papini, A. Adamska-Venkatesh, L. Pecqueur, C. Sommer, E. Reijerse, W. Lubitz, C. Gauquelin, I. Maynial-Salles, D. Pramanik, V. Artero, M. Atta, M. del Barrio, B. Faivre, V. Fourmond, C. Léger, M. Fontecave

Under revision, Journal of the American Chemical Society

D. Abstract

In this work spectroscopic and electrochemical investigations on [FeFe] hydrogenases are presented leading to an improved understanding of the catalytic cycle and giving insight into the electronic structure of the H-cluster, a complex 6Fe6S cluster in the active site of the enzyme. Overexpression in *E. coli* and artificial maturation of [FeFe] hydrogenases with the natural or modified precursor complexes are discussed in detail.

The redox states of the H-cluster in the catalytic cycle are analyzed with pH dependent FTIR-spectroelectrochemistry revealing a proton coupled electronic rearrangement during the stepwise reduction of the H-cluster. This rearrangement is presumed to ensure a smooth energy surface over the catalysis pathway. The [FeFe] hydrogenase HydA1 is studied for the first time using paramagnetic ^{1}H NMR spectroscopy. This technique allows measuring at physiological temperatures and direct detection of protons. Despite the large size of HydA1 (48 kDa) high resolution NMR spectra can be obtained. The $[4Fe\text{-}4S]_H$ $[2Fe]_H$ active site, is studied in the three states (H_{ox}, H_{ox}-CO, H_{hyd}). The chemical shifts and temperature dependencies of the β-CH_2 proton signals are interpreted based on an exchange coupling model and known magnetic coupling constants. Furthermore, sulfur to selenium (S-to-Se) exchange in the active site was studied with an aza-propane- or a propane-bridging ligand. Hydrogenases maturated with the aza-propane-diselenate bridging ligand show full activity. This is the first modification without any activity loss but with reduced stability under laboratory conditions. HydA1 with a propane-diselenate bridge is more stable and allows detailed spectroscopic analysis of the S-to-Se exchange. Selenium affects the ligand vibrations, changes the electronic structure and reduces the spin density on the bridging ligand in the active site.

Finally, the artificial maturation process has been expanded to the first non-iron hydrogenase with a $[2Ru]_H$ site that stabilizes the key terminal hydride intermediate.

E. Zusammenfassung

In dieser Arbeit werden [FeFe] Hydrogenasen spektroskopisch und elektrochemisch untersucht, wodurch ein besseres Verständnis des Katalysezykluses und Einblicke in die elektronische Struktur des H-Clusters gewonnen werden. Die Probenherstellung, einschließlich der Überexpression in *E. coli* und der künstlichen Reifung der [FeFe] Hydrogenasen mit dem natürlichen oder modifizierten Vorläuferkomplexen werden diskutiert. Die Redoxzustände des H-Clusters im Katalysezyklus werden mit einer pH-abhängigen FTIR-Spektroelektrochemie analysiert, wobei bei der schrittweisen Reduktion des H-Clusters eine protonengekoppelte elektronische Umlagerung beobachtet wird. Durch diese Umlagerung wird vermutlich eine erhöhte Übergangsenergie im Zyklus vermieden.

Die [FeFe] Hydrogenase HydA1 wird erstmals mittels paramagnetischer ^{1}H NMR Spektroskopie untersucht. Diese Technik ermöglicht Messungen bei physiologischen Temperaturen und die direkte Detektion von Protonen. Trotz einer Größe von 48 kDa können hochaufgelöste NMR-Spektren von HydA1 in drei Zuständen (H_{ox}, H_{ox}-CO, H_{hyd}) gemessen werden, die Einblicke in die elektronische Struktur ermöglichen.

Desweiteren wird der Schwefel gegen Selen Austausch (S-zu-Se) im aktiven Zentrum mit einem Aza-propan- oder einem Propan-Brückenliganden untersucht. Hydrogenasen mit Aza-propan-diselenat-Brückenligand zeigen volle katalytische Aktivität; dies ist die erste Modifikation ohne Aktivitätsverlust, allerdings bildet sich schnell der CO inhibierte Zustand unter Laborbedingungen. Eine detaillierte Analyse des S-zu-Se Austauschs ist mit Propan-diselenat-Brücke möglich. Selen beeinflusst die Ligandenvibrationen, verändert die elektronische Struktur und reduziert die Spindichte am verbrückenden Liganden im aktiven Zentrum. Abschließend wird der Prozess der künstlichen Reifung auf Nicht-Eisen Hydrogenasen erweitert. [RuRu] Hydrogenasen stabilisieren das terminale Hydrid-Intermediat.

1. INTRODUCTION

1.1 Power generation industry: Hydrogen as (great) white hope

Hydrogen is the first element in the periodic table and represents about 66 % of the total mass of the entire cosmos.[1] Under standard conditions it forms molecular hydrogen, H_2, with a heating value of 120 $MJ \cdot kg^{-1}$ (≈three times higher than gasoline) which underlines the potential of hydrogen as a future energy carrier.[2] The combustion of hydrogen with oxygen leads only to environmental friendly water. Unfortunately, most hydrogen on earth is already bound in water. Therefore, industrial production methods for molecular hydrogen were developed. About 80 % of the world wide hydrogen production is based on crude oil and petroleum gas, 16 % on coal and only 4 % on water electrolysis.[1] Most of these processes need expensive metal catalysts like platinum and rhodium, produce CO/CO_2 as side product(s), and are highly endothermic. The alkaline water electrolysis is the only clean way of producing hydrogen but requires electricity and is only of commercial interest if the used electricity is cheap. From an environmental point of view, electrolysis is only useful if the electricity can be produced from renewable sources so as to limit global warming. From a sociopolitical perspective all changes in power supply need to provide sufficient secure and affordable energy (energy consumption is rising constantly).

Steam-reforming is the major source of hydrogen nowadays but it requires desulfurized educts (mainly petroleum gas), a Ni catalyst and temperatures above 973 K with 40 bar pressure and results only in a carbon monoxide / hydrogen gas mixture. Thermal cracking of crude oil is also a catalytic endothermic process which is used to produce low-boiling hydrocarbons and has hydrogen as a side product. A potentially mobile process of hydrogen production without catalyst is the exothermic reaction of heavy fuel oil with oxygen and water vapor, which might be of interest in fuel cells powering automobiles. It requires a two-step process in which coal reacts with water vapor at temperatures above 973 K to carbon

monoxide and hydrogen and in a consecutive catalytic reaction with water vapor (known as water gas shift reaction) to produce carbon dioxide and a second equivalent of hydrogen.[1]

In 2016 Germany produced 648.4 TWh electricity and 29 % were derived from various renewable sources.[3] The announced aim from the German government in 2013 coalition agreement is 40-45 % in 2025 and 55-60 % in 2035.[4] But also with a sufficient amount of environmental friendly electricity, technical problems related to the use of hydrogen have to be solved for example transportation/liquefying and safety.

In terms of clean hydrogen production, learning from nature can play a key role.[5] Earth's early hydrogen dominated atmosphere resulted in the evolution of a family of highly efficient enzymes that can catalyze the splitting of molecular hydrogen into protons and electron and *vice versa*.[6] These so called hydrogenases are in interplay with electron and proton generating enzymes/pathways like the photosynthetic apparatus[7] and use abundant metals (iron and nickel) for the active site where the conversion takes place.

1.2 [FeFe] Hydrogenases: Enzymes with a special active site

[FeFe] Hydrogenases belong to the family of hydrogenases which is divided into three phylogenetically unrelated classes based on the metals used in the active site. Besides [FeFe] hydrogenases there are [NiFe]- and [Fe]-only hydrogenases.[6b] Recently a new classification within the three classes based on sequence, binding motifs, genetic organization and biochemical properties was presented.[8] By this approach, [NiFe] hydrogenases, which are the most widespread, expand over four groups with 22 subgroups, although they only occur in one domain of life, the prokaryotes. For [Fe]-only hydrogenases, which only occur in methanogenic archaea and catalyze the hydrogenation of methenyltetrahydromethanopterin, only one small group was found.[8] [FeFe] Hydrogenases, which are expressed in pro- as well as eukaryotes, are subdivided into three groups (A-C) according to their genetic organization with six different types (A1-A4, B and C). Group A consists of fermentative and bifurcating

hydrogenases, which are then further classified into prototypical (A1), glutamate synthase linked (A2), bifurcating (A3) and formate dehydrogenase linked (A4) [FeFe] hydrogenases. Except for group A2, structural and/or biochemical information on all A-groups is known where group A1 is best characterized. Group B and C are uncharacterized. Members of group C constitute putative sensory hydrogenases that induce a signal cascade as response of sensing hydrogen.[9]

[FeFe] Hydrogenases have the highest conversion rates for the H^+/H_2 couple (equation 1.1) at physiological conditions with low over potentials.[6b, 10] The heterolytic reaction pathway has been proven by H/D exchange experiments in the late 1970s.[11]

$$2\,H^+ + 2\,e^- \rightleftharpoons H^+ + H^- \rightleftharpoons H_2 \qquad (1.1)$$

The reaction takes place at the buried active site of [FeFe] hydrogenases, the so called H-cluster. It consists of a $[4Fe\text{-}4S]_H$ cluster which is linked via a cysteine to a $[2Fe]_H$ subsite that carries a unique propane-dithiolate ligand with an amine function in the bridge head. Most [FeFe] hydrogenases have one or more accessory clusters (referred to as “F-cluster”) next to the $[4Fe\text{-}4S]_H$ cluster in the active site. The F-cluster are in electron transfer distance to each other (≈8-12 Å) and form an electron relay between the active site and the protein surface where redox partners take over or deliver the needed electrons (see fig. 1A).

Four highly conserved amino acids form a proton transfer pathway (PTP).[12] It consists of a glutamate, serine, a second glutamate one water molecule and one cysteine close to the amino bridgehead group (C169 in HydA1) that finally transfers the proton to the reaction site. The molecular hydrogen is efficiently released via a hydrophobic gas channel[13] extending from the active site to the protein surface enabling fast turnover rates and preventing product inhibition.

Each iron in the $[2Fe]_H$ subsite has two terminal ligands (CN^- and CO) and share one bridging μCO in most of the redox states. The iron directly connected to the $[4Fe\text{-}4S]_H$ cluster is named Fe_p (proximal) and the other Fe_d (distal). Both irons are in low spin configuration due to the strong field/ σ-donating ligands. The distal iron is usually five coordinated and thus has a free binding site (see arrow in fig. 1B) where catalysis as well as inhibition can take place. The two irons are bridged by an aza-propane-dithiolate (ADT= $-\mu(CH_2S)_2NH$) moiety being essential for the catalytic reactivity (see chapter 1.2.2).

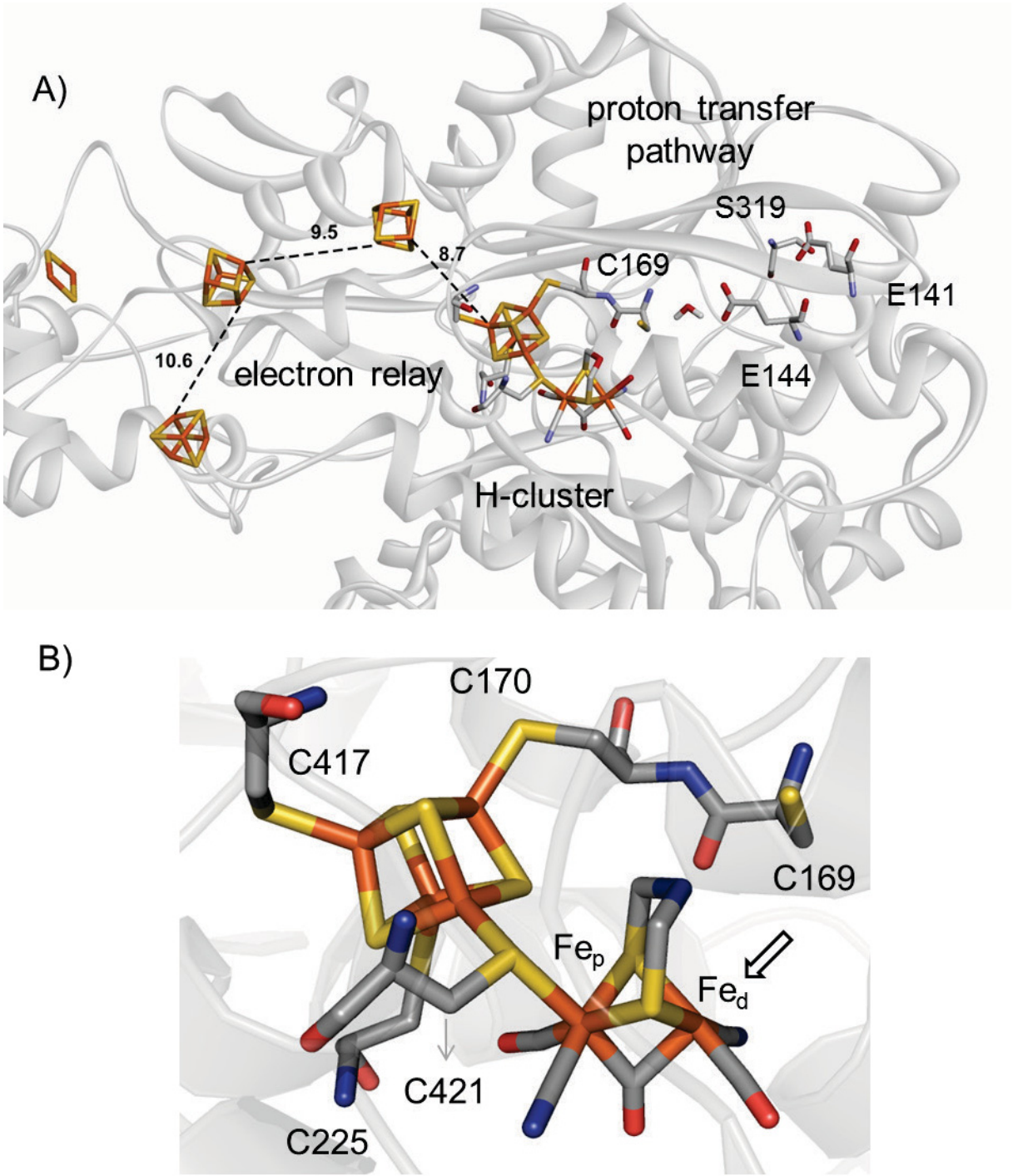

Figure 1 A) Overview of the electron relay and proton transfer pathway (PTP) in [FeFe] hydrogenases and B) close up of the active site of [FeFe] hydrogenases. A) Shows all prosthetic groups of the [FeFe] hydrogenase from *Clostridium pasteurianum* building the electron relay and the amino acids (E141, C169, E144, S319, all numberings are based on Q9FYU1 for *Chlamydomonas reinhardtii*) and water molecule forming the PTP. b) The four cysteines coordinating the $[4Fe\text{-}4S]_H$ sub-cluster (C170, C225, C417, C421) and C169 as essential proton shuttle are indicated as sticks. The arrow points at the open coordination site at the distal iron (Fe_d). PDB entry 3C8Y was used but in B) the bound ligand at Fe_d was removed and the bridgehead atom changed to nitrogen. Color coding: iron: orange, sulfur: yellow, carbon: grey, oxygen: blue, nitrogen: red.

1.2.1 Maturation of [FeFe] hydrogenase

In vivo the assembly of the H-cluster is a process which is still under investigation. It is known since 2004[14] that three FeS containing maturases HydG, HydE and HydF are needed. The maturation machinery is highly specific and encoding genes are only found in host organisms with hydrogenases. HydG and HydE are radical S-adenosylmethionin (SAM) enzymes and preassemble parts of the H-cluster. They harbor one [4Fe-4S] cluster at the N-terminus which is coordinated by three cysteines and has a free binding site for SAM (bound over carboxylate and amine group).[15] C-terminal HydG binds a second, for its function essential, [4Fe-4S] cluster. The two cubane clusters in HydG are located at the end of a triose phosphate isomerase (TIM) barrel through which the two sites seem to be connected via a tunnel.[16] In HydE an additional [2Fe-2S] exists that can be removed without losing activity in cell lysate assays.[17] It is assumed that HydE is involved in building and transferring the precursor for the ADT bridge. Here the natural substrate as well as the chemical mechanism are under debate. Much more is known about the functionality of HydG. HydG produces a $Fe(CO)_2(CN)$ synthon by Cα-Cβ splitting of L-tyrosine resulting in dihydroglycine and *p*-cresol.[18] This synthon additionally binds a cysteine[19] that might be the source of the ADT bridge since it was shown that HydG can activate the apo-hydrogenase to a certain extent without the other maturases.[20]

The third maturation factor is the GTPase HydF. The maturase HydF is the scaffold for the active site precursor and it was shown spectroscopically that the $[2Fe]_H$ sub-site can be fully assembled on HydF.[21] The GTPase activity of HydF is presumably important for the interaction with HydG and HydE but is not needed for the final transfer of the precursor to the hydrogenase.[21b, 22] Co-expression with HydG/E showed that prior to the interaction with HydG/E HydF is a dimer[23] and the iron atom of the [4Fe-4S] cluster are coordinated by three cysteines and one more labile glutamate which is exchangeable.[21b, 24] If HydF binds in its

functional form an additional [2Fe-2S] cluster is under debate and might be dependent on the host organism.[23-24]

To produce high yields of hydrogenase, overexpression in *Escherichia coli* (*E. coli*) was established.[25] Since *E. coli* has no hydrogenases in its genome, no maturases are encoded either. Overexpression of a hydrogenase gene leads to a so called apo-form of the protein that only harbors the $[4Fe\text{-}4S]_H$ cluster[26] and shows for some hydrogenases a cationic cavity[27] ending at the active site. In X-ray crystallographic structures of holoenzymes with the assembled $[2Fe]_H$ subsite this cavity is missing. In *E. coli* [4Fe-4S] clusters are assembled post-translationally by the iron sulfur cluster (ISC) system. The corresponding operon has upstream the genes for the auto-regulating [2Fe-2S] containing repressor iscR.[28] To enhance the incorporation of the $[4Fe\text{-}4S]_H$ cluster in apo-hydrogenases and other heterologously expressed FeS proteins, the repressor gene was knocked out leading to *E. coli* ΔiscR BL21 (DE3) strain.[29] In 2009 it was shown that the $[4Fe\text{-}4S]_H$ cluster in the apo-hydrogenase is essential for the maturation process.[30] With the genetically modified strain and coexpression of the maturases the hydrogenase activity improved up to 35 times. Higher yields were achieved by adding iron and sulfur sources to the pH regulated growth medium.[31]

Artificial maturation of [FeFe] hydrogenases was reported in 2013.[32] Herein the purified apo-hydrogenase is maturated with synthesized, artificial active site precursor [2Fe]-ADT ($[Fe_2(\mu\text{-}(CH_2S)_2NH)(CO)_4(CN)_2]^{2-}$). After incubating the apo-hydrogenase with [2Fe]-ADT full activity is observed. Formally, the precursor has to substitute one CO ligand by a cysteine that then coordinates one iron of the cubane cluster. By forming additionally one bridging μCO ligand, an open coordination site at the distal iron is generated that, depending on the organism, can be inhibited by CO after maturation. Despite the molecular restraints, artificial maturation results in active [FeFe] hydrogenases that cannot be distinguished from extracted hydrogenase of the host organism.[32b]

It is likely that the native $[2Fe]_H$ precursor is similar or even identical to the synthesized mimic since binding the synthesized precursor to HydF with subsequent maturation also results in a fully active hydrogenase.[24] This is the only example known in which the active site can be chemically synthesized and incorporated into the protein matrix. Maturation conditions are rather simple: Anaerobic atmosphere, room temperature, moderate excess of precursor (≈2-5x) in aqueous buffer and reaction times, depending on the hydrogenase type, from several minutes up to ≈50 hours.[33]

1.2.2 Active site redox properties and the catalytic cycle

In [FeFe] hydrogenases the $[4Fe\text{-}4S]_H$ and the $[2Fe]_H$ subsite are redox active. The cubane cluster can be oxidized (2+) or reduced (+) whereas the $[2Fe]_H$ can be reduced $[Fe_p(I)\ Fe_d(I)]$, mixed valence $[Fe_p(I)\ Fe_d(II)]$ or oxidized $[Fe_p(II)\ Fe_d(II)]$. Additionally, the bridging CO ligand can become terminal at Fe_d if $[2Fe]_H$ is reduced. The open coordination site at Fe_d can be occupied by H_2, H^-, CO or O_2. Not all of these possible combinations are detected as states in [FeFe] hydrogenase but the variability at so many sites within the H-cluster explains the complexity of the analysis.

In the [FeFe] hydrogenase family there are some differences which are based on slight changes in the protein surrounding and the presence of F-clusters. The hydrogenase from *Desulfovibrio desulfuricans Dd*H is the only one that can be purified aerobically resulting in a "over-oxidized" state with a proposed configuration $[4Fe\text{-}4S]_H^{2+}$ $[Fe_p(II)\ Fe_d(II)]$. The first one electron reduction leads to the so-called H_{trans} state where the reduction equivalent is centered at the cubane cluster. The H_{trans} state is isoelectronic to the H_{ox} state with a $[4Fe\text{-}4S]_H^{2+}$ $[Fe_p(I)\ Fe_d(II)]$ active site.[34]

A further extreme is the hydrogenase from the green algae *Chlamydomonas reinhardtii*, HydA1. It contains no accessory clusters and can be stabilized in the "super-reduced", named H_{sred} state which is characterized by a $[4Fe\text{-}4S]^+$ $[Fe_p(I)\ Fe_d(I)]$ configuration.[35] The bridging

μCO ligand that is present in the H_{ox} state becomes terminal at $Fe_{d.}$ This super reduced state is not stable in other hydrogenases because the cubane cluster is readily reoxidized by the F-clusters. By protein film electrochemistry it was shown that at the potential at which the H_{sred} state is populated, the catalytic current (indicative for hydrogen production) is high.[36] This is illustrative for a direct involvement in the catalytic cycle of the H_{sred} state.

The active H_{ox} state is observed in all [FeFe] hydrogenases and is often referred to as the starting/ end point of catalysis. For hydrogen conversion two protons and two electrons are required which, somehow, have to be stored at or near the H-cluster. The electrons reach the active site via the F-clusters or directly at the $[4Fe\text{-}4S]_H$ subcluster. It is generally assumed that the protons are entering the active site through the well-conserved proton transport pathway (PTP).[12] Cys169 (numbering according to Q9FYU1, *C. reinhardtii,* see fig. 1A) could pass the protons to the amine function of the ADT ligand that acts as proton shuttle[37] toward the open coordination site at the distal iron of the $[2Fe]_H$ subsite.

Starting from the H_{ox} state a combined, not well understood, proton coupled electron transfer step (see fig. 2, grey box) leads to the H_{red} state, which has a $[4Fe\text{-}4S]_H^{2+}$ $[Fe_p(I)\ Fe_d(I)]$ active site in which the bridging μCO becomes semi-bridging or terminal (see fig. 2, dotted line in H_{red} state). The question whether proton and electron transport are coupled events and if additional protonation sites in the surrounding of the H-cluster may affect its redox properties are under debate and will be explored for the native system and artificially modified enzymes within this thesis.

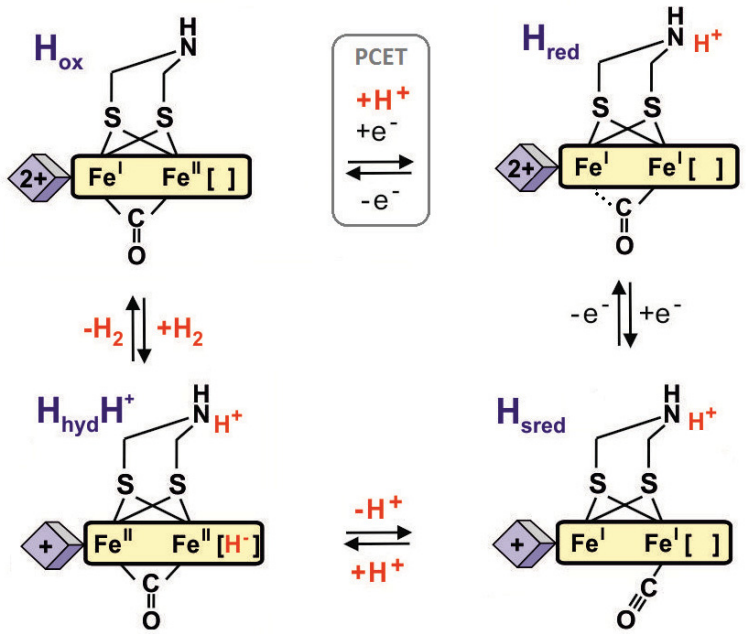

Figure 2 Proposed active cycle of [FeFe] hydrogenases. The $[4Fe\text{-}4S]_H$ cluster is represented by a purple cube and the $[2Fe]_H$ site, consisting of Fe_p and Fe_d, are shown as a yellow rectangle. The CO and CN^- ligands, except of μCO, are omitted for clarity.

A second electron reduces the $[2Fe]_H$ subsite forming H_{sred} $[4Fe\text{-}4S]_H^+$ $[Fe_p(I)\ Fe_d(I)]$ with a terminal CO and a protonated amine group.[38] As a next step, it is assumed that the proton of the amine group exchanges to the $[2Fe]_H$ subsite and binds as a hydride to the open coordination site (squared brackets in fig. 2) at Fe_d. The proton transfer from the bridgehead group to the hydride was found to be energetically favored.[39] At the same time, another proton is delivered to the ADT bridgehead from the PTP. The group of King *et. al*. used the HydA1 C169S mutant to block the proton transport to the active site thereby stabilizing the H_{hyd} state under reducing conditions. It was assigned as a putative doubly reduced state with a configuration of $[4Fe\text{-}4S]_H^+$ $[Fe(II)\ Fe(II)(H^-)]$ with a bridging μCO.[38] The hydride then recombines with another proton provided by the amine and is released as molecular hydrogen. After releasing molecular hydrogen the H-cluster is again in the H_{ox} state ready for another turnover.

The spectroscopic patterns in EPR and FTIR that are obtained from the H-cluster in the different [FeFe] hydrogenases are very similar for the different redox states signifying the

highly conserved binding motif for the H-cluster.[40] By site directed mutagenesis it was shown that the amino acids surrounding the H-cluster are important structural factors tuning the catalytic behavior of the active center.[41] Side groups of the amino acids are involved in hydrogen bonding to CN^- ligands as well as the bridgehead amino group and show electrostatic interactions with the bridging μCO.[40, 42] The protein matrix is therefore an important part of the later results that are detected spectroscopically.

In figure 3 theoretically possible active states (without CO- and O_2-inhibiton) are shown in a schematic way, focusing on the $[4Fe\text{-}4S]_H$ cluster and the $[2Fe]_H$ subsite. Up to six different singly reduced configurations are conceivable depending on the protonation level of the H-cluster. In figure 3 it is assumed that protonation of Fe_d (hydride formation) is only possible if $[2Fe]_H$ is reduced to [Fe(I) Fe(I)] (oblique arrows).

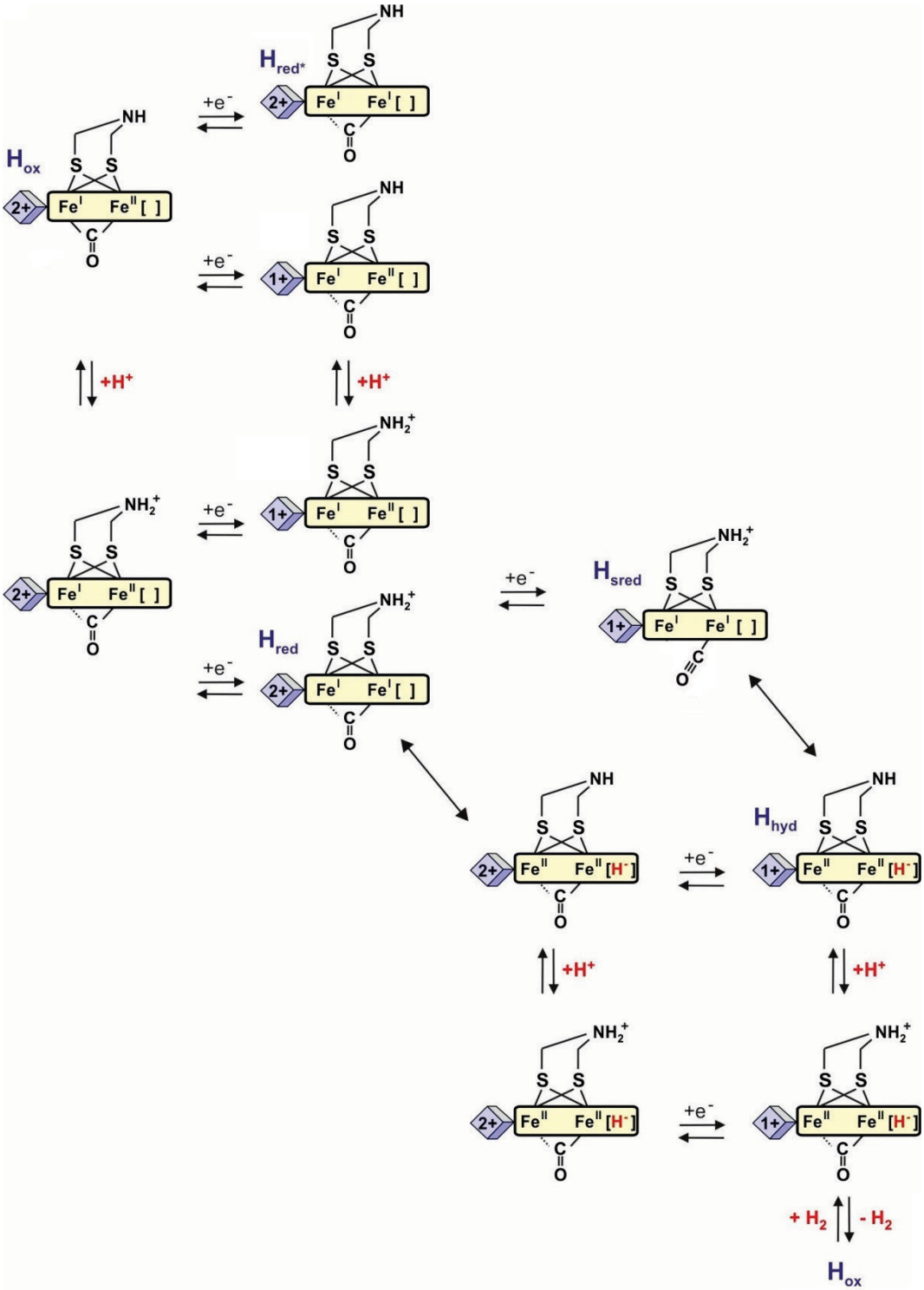

Figure 3 Scheme of theoretically possible active states in [FeFe] hydrogenases. The scheme shows electron transfers horizontally and proton transfers vertically. The H_{ox} state is used as starting (upper left corner) and end point (bottom right). Named states (H_{ox}, H_{red*}, H_{red}, H_{sred} and H_{hyd}) are known from literature and are partly characterized.

The H_{hyd} state was recently spectroscopically detected in [FeFe] hydrogenases by Reijerse *et al.*[43] and Winkler *et al.*.[44] It was stabilized by inhibiting the PTP (site directed

mutagenesis/ non-natural precursor see chapter 1.2.3) or by shifting the equilibria between the active states through increased substrate and/ or product concentrations making use of the principle of Le Chatelier. By H/D exchange both groups proved that [FeFe] hydrogenases use a terminal hydride species and not a bridging hydride which is thermodynamically more stable but kinetically inaccessible.[39, 45] This proof is possible using FTIR since the metal hydride is positioned *trans* to the bridging CO ligand to which it is vibrationally coupled. The metal deuteride vibration is, however, not coupled to the μCO stretch. Therefore, H/D exchange can be detected through a frequency shift of the μCO vibration.[46]

The catalytic cycle can be reversibly inhibited by an external carbon monoxide ligand bound to Fe_d. CO-Inhibition occurs preferentially at high potentials. The formed H_{ox}-CO state is isoelectronic to the H_{ox} state, $[4Fe\text{-}4S]_H^{2+}$ $[Fe_p(I)\ Fe_d(II)]$, and can be reduced to the H_{red}-CO state ($[4Fe\text{-}4S]_H^{+}$ $[Fe_p(I)\ Fe_d(II)]$) at low potentials.[35, 47] The H_{ox} and H_{ox}-CO state are paramagnetic due the coupling of the formally diamagnetic $[4Fe\text{-}4S]_H$ cluster with the $[2Fe]_H$ subsite with a S=1/2 spin state. In EPR spectroscopy they show very different g-values. Furthermore, in the H_{ox} state the spin density is more evenly distributed over the $[2Fe]_H$ site[48] while in the H_{ox}-CO state the spin density is shifted in the direction of the cubane cluster leading to about five times higher spin density at Fe_p compared to Fe_d.[48] An opposite potential behavior is shown by the reversible inhibition with formaldehyde, that preferentially inhibits at low potentials.[49] Furthermore, already small traces of molecular oxygen inhibit or even destroy the active site of hydrogenases. How these inhibitions occur in detail is further discussed in chapter 2.6.3.

1.2.3 Engineering the active site properties

Based on the artificial maturation procedure it became possible to manipulate structural elements of the H-cluster and gain information about the structure-function relationship. The natural [2Fe]-ADT ($[Fe_2(ADT)(CO)_4(CN)_2]^{2-}$, ADT= aza-propane-dithiolate, -$\mu(CH_2S)_2NH$)

precursor was modified at several positions (see fig. 4) and could still be incorporated into the protein matrix of HydA1 from *Chlamydomonas reinhardtii*. In the first study of non-natural precursors the –NH bridgehead group was changed to $–CH_2$, resulting in a bridging ligand called PDT (propane-dithiolate, $-\mu(CH_2S)_2CH_2$), and –O thus named ODT (oxa-propane-dithiolate, $-\mu(CH_2S)_2O$).[32a] All modified complexes were incorporated by the hydrogenase and will be named hereafter HydA1-XDT, X depending on the used precursor.

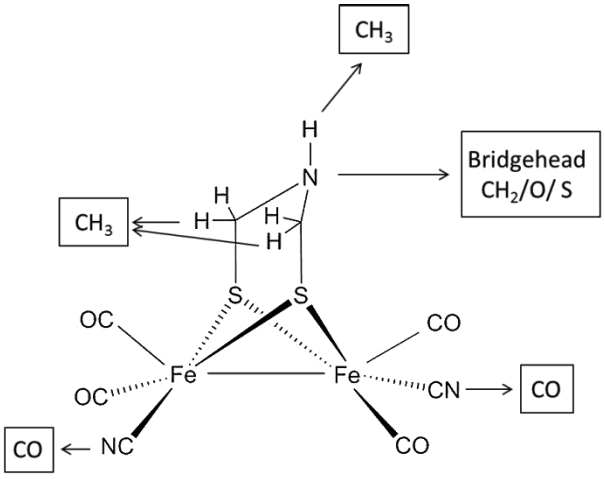

Figure 4 [2Fe]-ADT precursor complex with spectroscopically studied modifications. Most modifications were introduced in the part bridging of the two iron site.

In FTIR spectroscopy the obtained vibrational patterns are similar except the one from the ODT variant. HydA1-ODT shows vibrations which are significantly shifted to higher wavenumbers suggesting a [Fe_p(II) Fe_d(II)] configuration with an additional bound ligand in *trans* position to the bridging CO ligand (similar to *Desulfovibrio desulfuricans*[50] and *Desulfovibrio vulgaris*[51]). Recently this additional ligand was spectroscopically assigned as a hydride.[43-44] The variant with a PDT bridge was found to be a good electronic model of the H-cluster, simplifying the redox properties to an oxidized and a reduced state similar to the ones of the wild-type active site.[35]

Thereafter in an additional study of HydA1 the bridgehead group of the used complexes was also substituted with $–NCH_3$, -S and ones more with $–CH_2$.[52] Interestingly residual activities

were observed for $–CH_2$ and $–NCH_3$ bridgeheads. These might be explained by the strong reducing conditions in the solution assay to determine the hydrogen production exploiting additional moieties acting as base at or near the $[2Fe]_H$ subsite, for example the thiol groups of the bridge. Exchange of the bridging propane groups with $-CH(CH_3)$ resulted in a totally inactive enzyme.

Furthermore one CN^- ligand was replaced by a CO ligand resulting in an activity loss of approximately 50 %.[52] This illustrates the flexibility of the first coordination sphere of the H-cluster. These experiments, however, also show that the H-cluster ligands and its protein surrounding are finely tuned for maximum activity. Additionally the $[2Fe]_H$ precursor can be isotope labeled during synthesis. This opens a spectroscopic toolbox which can help to assign FTIR and NMR signals, disentangle coupled vibrations, and determine magnetic coupling constants in EPR.[53]

When [FeFe] hydrogenase are overexpressed in *E. coli* the $[4Fe\text{-}4S]_H$ cluster is built by housekeeping enzymes (ISC system, iron sulfur cluster system). However, established procedures (see chapter 2.2)[54] allow to extract and reconstitute [4Fe-4S] clusters and introduce isotope labels[55] (e.g. ^{57}Fe) or Se instead of S. Changing only the $[4Fe\text{-}4S]_H$ cluster to a $[4Fe\text{-}4Se]_H$ cluster results for the maturated HydA1 in a fully active enzyme with similar FTIR properties.[54d]

Further, site directed mutagenesis was used to exchange single amino acids in the protein matrix to influence the proton transfer pathway and the electron relay. The highly conserved amino acids of the PTP cannot be manipulated without losing its functionality.[12] The electron pathway with its [4Fe-4S] clusters in electron transfer distance[56] were also analyzed. A recent study shows the influence of cysteines around the $[4Fe\text{-}4S]_H$ cluster highlighting that one cysteine (located over the bridge, C170) is essential for the formation of a $[4Fe\text{-}4S]_H$ cluster.[41] The hydrophobic gas channel(s)[57] provided by the protein matrix[58] are necessary

for high activity and stability. It is assumed that oxygen uses the same hydrophobic channel to inhibit the active site. O_2 sensitivity is the main drawback of [FeFe] hydrogenase preventing biotechnological applications. To genetically improve O_2 tolerance, first and second generation mutants are tested for hydrogen productivity[59] under aerobic conditions. So far an oxygen tolerance up to 14 times higher than the wild-type could be achieved.[60]

1.3 Aim of the work

The artificial maturation of [FeFe] hydrogenases introduced in 2013 opened a new research field for inorganic chemist as well as biochemists to study the structure-function relationship of the $[2Fe]_H$ subcluster of the enzyme's active site.[61] The main aim of my work was to explore these new experimental capabilities in studying the [FeFe] hydrogenase HydA1 from *Chlamydomonas reinhardtii*. For this endeavor, the yield of the HydA1 apo-hydrogenase had to be improved. The first step was the codon-optimization of the *HydA1* gene for overexpression in *E. coli* as executed in the thesis of Judith Siebel.[62] The improvement of the protein yield due to experimental conditions during the expression is part of my thesis. A high protein yield enables studies requiring large amounts of enzyme and will expand the range of applied biophysical methods in [FeFe] hydrogenase research.

The finding that maturation of apo-HydA1 with the synthetic native [2Fe]-ADT cofactor yields an enzyme indistinguishable from the isolated enzyme[32b] of the native green algae allows studying the mechanism of the catalytic cycle in detail. At the beginning of my work the proposed catalytic cycle was based on the observation of three redox states H_{ox}, H_{red}, and H_{sred}[35, 63] and theoretical considerations as well as DFT calculations. The required protonation steps in the catalytic mechanism were under debate and will be addressed in my thesis.

In combination with site-directed mutagenesis, artificial maturation allows engineering the [FeFe] hydrogenase active site and its first ligand sphere. With these modifications the aim is to overcome the drawbacks of oxygen sensitivity and, possibly, improve the catalytic activity. The gained knowledge can be transferred to molecular catalyst that can be used in technical applications. One extensive study focused on variants of the $[2Fe]_H$ subcluster bridging dithiol ligand was published in 2015.[52] In my thesis, I extend these studies to chalcogenide and metal exchange in the active site. Different $[2Fe]_H$ variants stabilize different states of the H-

cluster and enable the detailed investigation of charge and electron spin distribution in these states.

2. EXPERIMENTAL METHODS

2.1 Heterologous overexpression of [FeFe] hydrogenase HydA1 from *Chlamydomonas reinhardtii* in *Escherichia coli* and *in vitro* artificial maturation

Heterologous overexpression in *Escherichia coli* (*E. coli*) is widely used in biotechnology to produce a desired protein in high yields. Thereby the *E. coli* cells are transformed with an expression plasmid containing the genetic information of the target protein. Common methods to transform bacteria with plasmids are the calcium chloride heat-shock or electroporation. The plasmid contains usually an oriC (origin of replication), a sequence for antibiotic resistance, a promotor with the downstream cloned cDNA of the target protein and a gene regulation system. Insertion of DNA in the expression plasmid takes place in the so called multiple cloning site and is performed with restriction enzymes.

For overexpression of the [FeFe] hydrogenase HydA1 from *Chlamydomonas reinhardtii* a pET21b plasmid with ampicillin resistance, T7 promotor, *lac* repressor and restriction sites for XhoI and NheI was used. The pET 21b *CrHydA1* expression plasmid with codon-optimized gene sequence and N-terminal fused strep-II affinity tag and *tobacco edge virus* (TEV) cleaving site was set up by Judith Siebel.[62] To optimize the yield of the $[4Fe\text{-}4S]_H$ cluster in the enzyme (apo-HydA1), the repressor of the bacterial FeS cluster machinery (ΔiscR) was deleted in the employed *E. coli* strain.

Transformation of calcium chloride competent ΔiscR *E. coli* cells was performed with the heat shock method and the genetically altered bacteria selected by ampicillin resistance on agar plates. *E. coli* bacteria grow easily in so called full media which provide all necessary supplements. Modified ΔiscR *E. coli* cells were grown in liquid LB-medium (lysogeny broth) in an aeriated flask till an "optical density" of the cell culture of $OD_{600\,nm}$=0.65 was reached. Before the suspension was gased with argon to remove oxygen, the pH was adjusted to 7.4. Due to the higher cell density and the pH adjustment the yield could be increased to an

average of 120 mg/l.[64] Isopropyl β-D-1-thiogalactopyranoside (IPTG) was added to the bacteria suspension to induce the protein expression of apo-HydA1.

To purify apo-HydA1 after sonication from the lysate (mobile phase), affinity chromatography was used. It is based on the affinity of a small, specific sequence, a tag, fused to the target protein that binds to a stationary phase while other proteins in the mobile phase can be washed out. In the further process a second small molecule with an even higher affinity displaces the target protein with the fused tag. The resin can be recycled. For apo-HydA1 the affinity of the fused N-terminal strep-II tag to a streptactin resin (stationary phase) was used. Elution of the tagged target protein occurs with desthiobiotin. The tag was removed by proteolysis resulting in apo-HydA1 with a high degree of purity which was directly used for artificial maturation or stored at -80 °C. *In vitro* artificial maturation was performed with diluted apo-HydA1 and an excess (2-5 times) of synthesized precursor. After incubation at room temperature the non-bound precursor was removed and the obtained maturated protein could be analyzed.

2.2 Reconstitution of Fe/S cluster

Iron sulfur clusters are found in numerous proteins of bacterial or eukaryotic origin. They play a role in metabolic and regulatory processes and are used for electron transfer. By EPR and chemical analysis first evidence for these metal-containing cofactors was found in the early 1960s.[65] Soon thereafter the first reactivated Fe/S clusters were built with a [2Fe-2S] protein chemical reconstitution process.[54a] The first sulfur to selenium exchange was performed in a [2Fe-2S] protein in which sulfur was replaced by Se^{80}.[66] Over the years many unfolding processes were established starting from a mercurial procedure[54a] over the use of trichloric acid[66] to urea[54d] and chaotropic salts like guanidine hydrochloride.[67] The refolding process always includes the addition of a reducing agent and an excess of the

desired ions. In most studies sulfur is replaced but the substitution of iron by gallium for example is also possible.[68]

2.3 Activity assays for hydrogen conversion

Since hydrogenase catalyzes hydrogen production as well as hydrogen consumption, two activity rates can be determined (see fig. 5). Molecular hydrogen can easily be detected via gaschromatography. By using a column specific and volume dependent internal standard value the amount of hydrogen produced by the hydrogenase can be quantified. To follow hydrogen consumption it is best to quantify the generated electrons. The electrons reduce colorless methyl viologen (MV) to the blue MV radical. The increase of the MV radical concentration in the assay solution can be followed at 578 nm with UV/Vis spectroscopy.

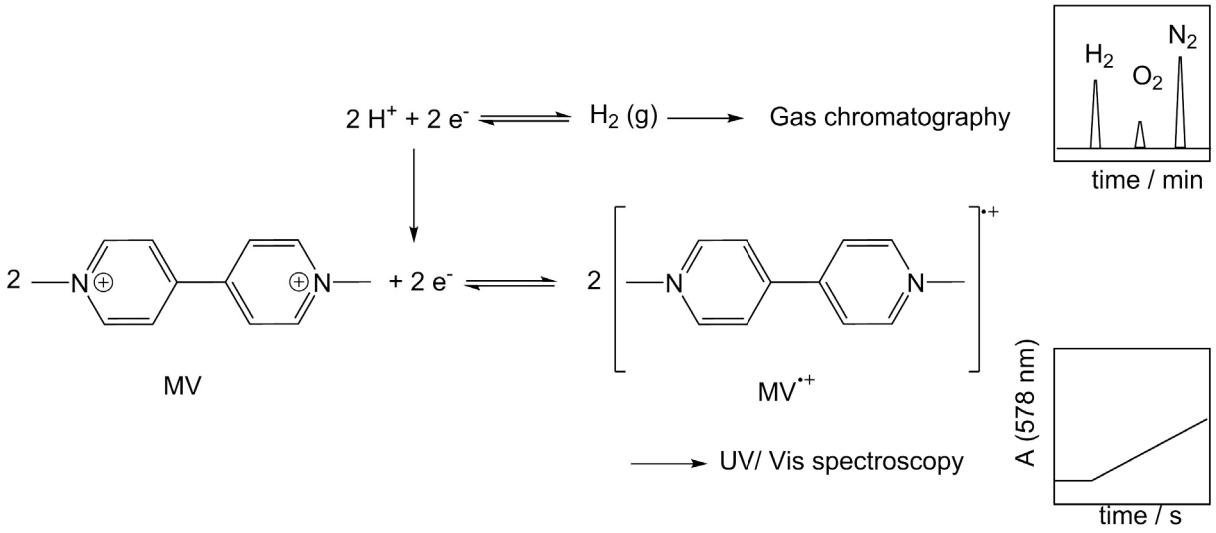

Figure 5 Overview of used activity assays to determine hydrogen production and consumption of hydrogenases. Produced molecular hydrogen can directly be detected, for hydrogen consumption methyl viologen is used as electron acceptor and spectroscopic probe.

2.4 Infrared Spectroscopy of proteins

2.4.1 Basic principles and measurement techniques

Energetically a molecule has rotational, vibrational and electronic transitions. Based on the used electromagnetic irradiation ($h \cdot \nu$) these transitions are stimulated when the energy matches the energy difference ΔE of the excited state E'' and the ground state E'.[69]

$$\Delta E = h \cdot \nu = E'' - E' \tag{2.1}$$

where h is the Planck constant and ν the frequency

Infrared light contains photons of the energy matching the energy difference of the ground to the first excited vibrational state. The observed intensity of the vibration is proportional to the square of the change in transition dipole moment. There are two types of vibrational modes, stretching and bending vibrations (see fig. 6). Stretching vibrations are characterized by a changing bond length during the symmetric or asymmetric vibration and are typically strong for CO ligands. Bending vibrations are subdivided into four types having in common a change in the bond angle during the vibration.

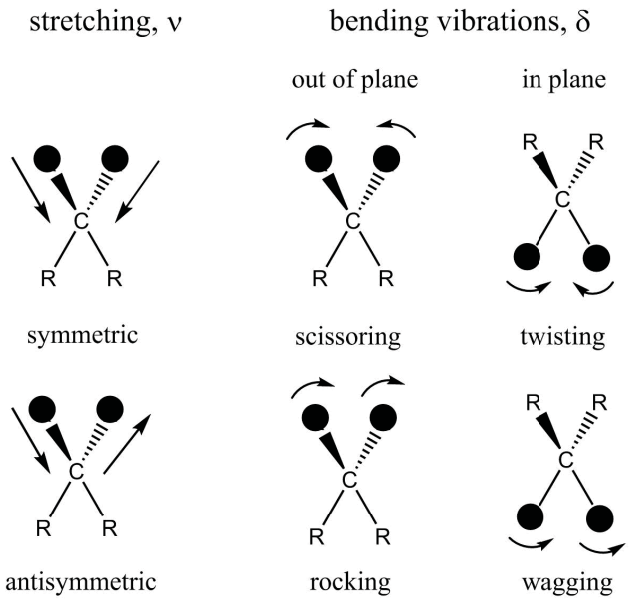

Figure 6 Schematic presentation of stretching and bending vibrations. The vibrations refer to the atoms schematically shown as black balls.

According to the harmonic oscillator with its equidistant energy levels the approximate frequency ν of a vibration is based on the reduced mass μ (including m1 and m2 of the two atoms forming a bond, see equation 2.2) and the binding constant k, reflecting the bond type and the bond strength.

$$\nu = \frac{1}{2\pi}\sqrt{\frac{k}{\mu}} \qquad \text{with } \mu = \frac{m1 \cdot m2}{m1+m2} \tag{2.2}$$

With the Morse potential in the anharmonic oscillator the distance of the two vibrating atoms are taken into account (repulsion and dissociation), resulting in a reduction in energy level spacing towards higher energy levels.

The frequency of a vibration is sensitive to the environment. It can be influenced by inductive, mesomeric and redox effects that change the charge distribution. Further, the frequency can be coupled to other vibrations whereby information about molecular geometry becomes available giving insight in the three dimensional structure. The intensity of a vibrational signal correlates with the change in transition dipole moment which is reflected by the polarity of the bond. The third parameter of an observed band is the line width which is determined by conformational freedom. Heterogeneous line broadening is a consequence of translation motion. Thus changing the environment shifts the observed vibrational peaks and influences the peak width. All mentioned general influences on a vibration can be applied to [FeFe] hydrogenase research as is discussed in chapter 2.4.3.

The infrared spectral region is divided into near infrared (0.78 μm - 2.5 μm), mid infrared (2.5 μm - 50 μm) and the far infrared (50 μm - 1000 μm). Thus FTIR spectroscopy covers the energy range between UV/Vis spectroscopy and microwave techniques. Instead of the frequency ν the wavenumber $\tilde{\nu}$ in inverse centimeters is used on the x-axis. The wavenumber represents the number of waves per unit length. Typically, mid infrared irradiation is used since the energy difference of most transitions from the ground state to the first excited state

are covered in the wavenumber range from 4000-200 cm^{-1}. All used units can be interconverted by

$$\tilde{\upsilon} = \frac{\upsilon}{c} = \frac{1}{\lambda} \tag{2.3}$$

where $\tilde{\upsilon}$ is the wavenumber, ν the frequency, c the speed of light in vacuum and λ the wavelength.

Most laboratories use modern infrared spectrometers with an interferometer like the Michelson interferometer[70] instead of dispersive infrared spectrometers with double monochromator technique. The main advantage of the interferometer are the fast data collection and the high light intensity that reaches the detector being essential for a good signal to noise ratio.[71] Typically protein solutions are measured in the transition mode. For transmission FTIR the sample is sandwiched between two IR transparent windows. An alternative is the measurement with an attenuated total reflection (ATR) cell (see fig. 7). In an ATR cell the protein solution is placed on an internal reflection element (IRE e.g. diamond, silicon, Ge or ZnSe) with an index of refraction n1 much larger than that of the protein solution (n2).[71-72]

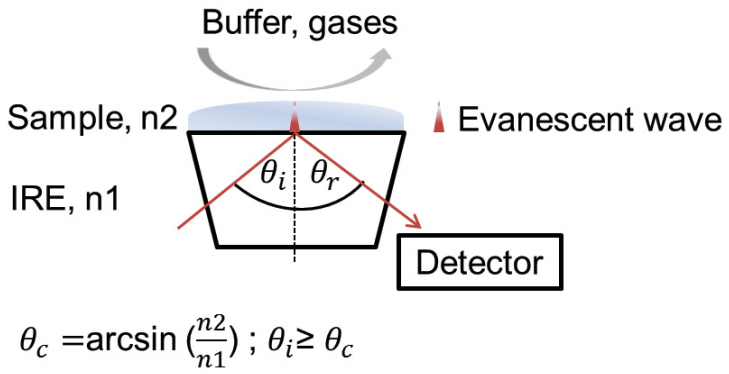

Figure 7 Schematic illustration of the total reflection at the interface of an internal reflection element (IRE) and a liquid sample in an ATR cell.

The light beam is coupled into the IRE with an angle of incidence θ_i greater than the critical angle θ_c and hence totally reflected at the IRE-protein interface. Usually, several reflections

occur in an ATR cell before the beam is focused on the detector. At each reflection at the interface a standing wave penetrates into the protein sample (0.5 - 2 µm) and is partially absorbed.[72] The penetration depth of this so called evanescent wave depends on the wavelength, the ratio of reflection indices between IRE and sample, and on the angle of incidence, θ_i. The advantage of an ATR set up is the fast sample mounting and easy access to the protein surface facilitating buffer and gas exchange. For [FeFe] hydrogenases inhibition experiments with CO or O_2 or buffer exchanges to study the pH dependent formation of redox states can be performed easily with an ATR set up. The disadvantage is the problematic preparation of a stable film[71] and the risk to dry out and thereby irreversible damage the protein sample. To alleviate both problems, a permeable membrane can be placed above the protein film.

2.4.2 Infrared spectroscopy of protein samples

Structure determination, as it is/ was done with small organic molecules, is not possible for biomolecules because of their size and the arising overlapping vibrations.[71] FTIR spectroscopy can be used for secondary structure analysis as well as for investigations of a catalytic reaction mechanism[73] in which amino acid side chains undergo a change (e.g. protonation, phosphorylation). Due to the repeated protein backbone (see fig. 8), characteristic vibrations give insight into the secondary structure and provide information concerning the protein folding/ unfolding.[71] The protein backbone has five different vibrations from which the Amide I and Amide II vibrations are predominantely used for structural studies. The Amide I (≈ 1650 cm^{-1}) band is dominated by the νCO vibration with minor contributions of the out of phase νCN, in plane δNH and the CCN deformation vibration. The amount of contribution depends thereby on the backbone structure.[74] The Amide II (≈ 1550 cm^{-1}) band is composed of phase combination of the in plane δNH and νCN vibration. Additionally the δCO in plane bend and the CC and NC stretching vibrations

contribute to Amide II. Deuteration of the protein backbone for example leads to a decoupling of the δNH and the νCN vibrations resulting in a red shift of the δNH bend down to 1490-1460 cm^{-1}.[71]

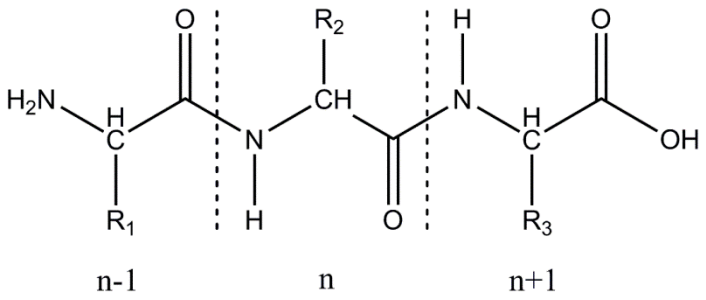

Figure 8 Tripeptide representing the protein back bone of a biological sample. The peptide is shown from N- to C-terminus without specified amino acid side chains R_x. The numbering of n-1, n and n+1 is used to show connectivity.

In enzyme catalyzed reactions amino acid side chains often take part in the reaction. With an additionally IR active cofactor the structure-function relationship and the molecular mechanism active site can be studied as it is possible with the ligands of the H-cluster in [FeFe] hydrogenases (see next chapter). The usually buried position of a cofactor in a protein backbone depends the narrow line width of cofactor related vibrations what distinguishes them from the broad amide vibrations. To study the mechanism of reactions, time-resolved and difference measurements[73], site-directed mutagenesis[75], isotope labelling[76] and kinetic enrichment of intermediates are often used methods that can be combined with density function theory (DFT) calculations.[77]

2.4.3 Fourier-Transform Infrared Spectroscopy in [FeFe] hydrogenase research

[FeFe] Hydrogenases can be studied with FTIR spectroscopy because in their unique H-cluster the CO and CN^- ligands can be used as IR active probes (see fig. 10). The CO and CN^- ligand vibrations in a maturated [FeFe] hydrogenase do not overlap with the protein backbone vibrations. Their vibrations are directly influenced by the environment e.g. by hydrogen bonding of the CN^- ligand to surrounding amino acid residues. Furthermore the

vibrations are sensitive to the redox state of the $[2Fe]_H$ subsite as well as of the $[4Fe\text{-}4S]_H$ cluster since the two sites are coupled. This sensitivity is based on the binding situation and the nature of the ligands. The observed shift size after a redox event depends on the structural change that occurs and the distance of the ligand to the site of reaction.

Each vibration is characterized by its position, intensity and line width. Typically carbonyl vibrations are measured in the range of 2120 - 1850 cm^{-1} and CN^- vibrations between 2200 - 2050 cm^{-1}.[69, 78] CO and CN^- ligands are strong π-acceptors meaning they accept electrons from the d-orbitals of the irons so that both irons are stabilized in low spin configuration. For both ligands the wavenumbers decrease when more electron density is transferred from the iron d-orbitals in the antibonding π*-orbital weakening the internal ligand bond strength.[78] Carbonyl ligands are even stronger π-acceptors than the cyanides what results in stronger vibrational shifts for the CO ligands compared to the vibrational shift of the CN^- ligands in all observed transitions. The bridging CO ligand in [FeFe] hydrogenases is vibrating at lower frequencies than the CO in terminal position since it has more orbital overlap with both irons. Additionally the geometry of the cluster decides about the coupling of vibrations. For [FeFe] hydrogenases it was shown that in the hydride state the bridging CO ligand in *trans* position is coupled to the Fe-H vibration resulting in a shift for the bridging CO vibration.[44]

The formation of each redox state can be followed by monitoring a so called marker band that should be free of any overlapping vibrations. In case of the shown H_{ox} state of HydA1-ADT the intensity of the vibration of the terminal bound CO at 1939 cm^{-1} (see fig. 9) can be easily monitored e.g. over time or against an inhibitor concentration. The intensities of the CO and CN^- vibrational bands depend on the polarity of the bonds. The more polar a bond is the higher is the intensity of the corresponding vibration.[71] The electronegativity of N is smaller

than the one of O, leading to a more polarized bond in the CO ligand and consequently in more intense bands for the CO ligands (see fig. 9).

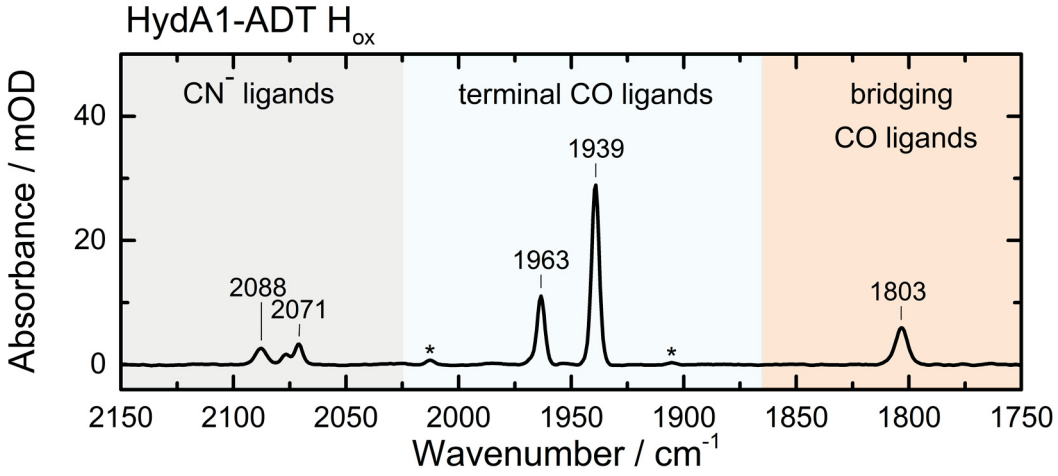

Figure 9 FTIR spectrum of HydA1-ADT in the H_{ox} state with colored regions for the typical observed vibrations. Small contributions marked with an asterisk belong to other redox states. Spectrum was taken at 288 K with a spectral resolution of 2 cm^{-1}.

Since the artificial maturation process requires inorganic precursor complexes their structure as well as the maturation process over time can be analyzed with FTIR spectroscopy at ambient temperatures. The dissolved precursor complexes of the type $[Fe_2(XDT)(CO)_4(CN)_2]^{2-}$ are free in their translational motion what is reflected by broad vibrations in the FTIR spectrum. The wavenumber of the CO and CN^- bands of the precursors are solvent dependent since the ligands are undergo interactions with the solvent molecules. After incorporation into an apo-hydrogenase the rigidity of the protein backbone and the formed polar interactions restrict the possible conformations of the ligands yielding in narrow bands.

2.5 Magnetic Resonance Techniques

2.5.1 Physical concept of magnetic resonance

Most elementary particles possess a spin angular momentum $\hbar\vec{S}$, and consequently a magnetic moment $\vec{\mu}$. Here, $\vec{S}$ is a dimensionless vector with a magnitude quantized with the same unit as $\hbar$. For every particle the relationship between angular and magnetic moment can be described as

$$\vec{\mu} = \gamma \cdot \hbar\vec{S} \text{ with } \hbar = \frac{h}{2\pi} \tag{2.4}$$

where γ represents the gyromagnetic ratio for the respective particle and h is the Planck constant. The intrinsic angular momenta of particles are referred to as spins. For an electron $\gamma_e = g_e \frac{e}{2m_e}$ where g_e is the electron g-factor (2.0023 for a free electron), e is the elementary charge, and m_e is the electron mass. For a proton the gyromagnetic ratio is $\gamma_p = g_p \cdot \frac{e}{2 \cdot m_p}$. with g_p as the proton's g-factor and m_p the mass of the proton.

The spin angular momentum $\hbar\vec{S}$ is a quantum mechanical observable and is described by: S(S+1) and m_I or m_S, where S is the spin quantum number and m_I or m_S are the spin angular momenta along the z-axis. For protons and electrons I=1/2 and S=1/2 respectively. The spin angular momenta m_I and m_S can range from +I to –I or analogue from +S to –S in/with an integer interval. A S=½ particle will therefore have two allowed spin states (m_I or m_S +1/2 or -1/2). S=1 particles have three allowed spin states (m_I =1, 0. -1) etc.

In a magnetic field $\overrightarrow{B_0}$ the magnetic moment $\vec{\mu}$ of the particle will align preferentially along the magnetic field. Figure 11 shows the Zeeman energy splitting of electron (S=1/2) and proton (I=1/2) spins in a magnetic field with the two possible energy levels. Since the gyromagnetic ratio of the electron spin in negative due to its negative charge, the spin

moments of electron and protons (see fig. 11, blue arrows) are aligned opposite in the magnetic field. Their magnetic moments are equally aligned.

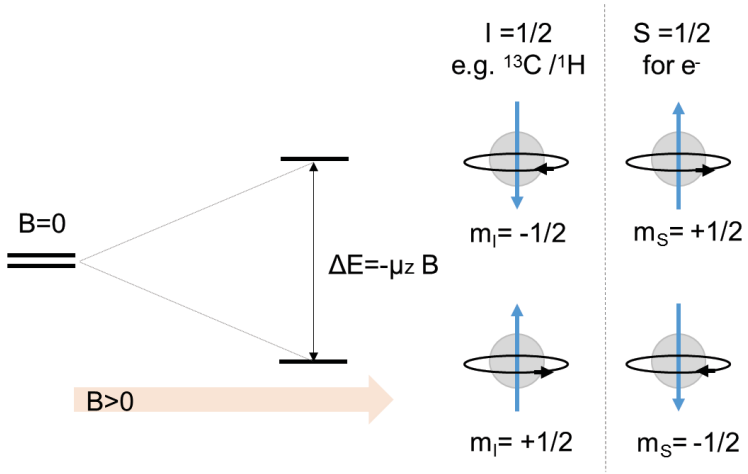

Figure 10 Zeeman splitting for a spin I=1/2 and a S=1/2 particle in an applied magnetic field with the two states $m_I = \pm 1/2$ and $m_S = \pm 1/2$, respectively.

Since the proton mass is three orders of magnitude larger than that of an electron, its gyromagnetic ratio and magnetic energy splitting is three orders of magnitude smaller, this explains the different magnetic fields used in the two techniques.

Since the particle can only have distinct spin states, the magnetic energy is also quantized. By choosing the axis system such that $\overrightarrow{B_0}$ is aligned along the z-axis, the energies for each level can by conveniently determined:

$$E = -\mu_z \cdot \overrightarrow{B_0} \tag{2.5}$$

$$\text{for protons with } \mu_Z = g_p \cdot \mu_p \cdot m_I \; ; \;\; \mu_p = \frac{e \cdot \hbar}{2 \cdot m_p}$$

$$\text{for electrons with } \mu_Z = g_e \cdot -\mu_B \cdot m_S \; ; \; \mu_B = \frac{e \cdot \hbar}{2 \cdot m_e}$$

The magnetic moment is herein expressed as product of the corresponding g-factor g_e/g_p and the magneton μ_B/μ_p for electrons or protons respectively. The energy difference between the magnetic levels is, therefore:

$$\Delta E = g_e \cdot \mu_B \cdot B = h \cdot \nu \tag{2.6}$$

$$\Delta E = g_p \cdot \mu_p \cdot B = h \cdot \nu \tag{2.7}$$

Magnetic resonance occurs when the energy (frequency) of the externally applied electromagnetic radiation (typically in the MHz to GHz range) matches the energy difference ΔE of the magnetic spin levels of the particle.

The sensitivity of magnetic resonance techniques is given by the net absorption of energy. The absorption is directly proportional to the spin population difference of excited spins (N_+) to spins in the ground state (N_-) which is defined by the Boltzmann distribution. In general, the sensitivity of the magnetic resonance experiment can be enhanced by going to higher field and frequencies.

$$\frac{N_+}{N_-} = \exp\left(\frac{-\Delta E}{k_B \cdot T}\right) \tag{2.8}$$

where k_B is the Boltzmann constant and T the absolute temperature.

In a sample the unpaired electrons, protons and other nuclei do not only “experience” the external magnetic field but also internal magnetic fields generated by other magnetic moments, and electrons in the molecule. These internal fields can be very large for paramagnetic systems due to the strong magnetic interactions of unpaired electrons within a molecule, especially in metal complexes. For nuclei, the magnetic coupling interactions within a molecule are much smaller (in the range of ppm). Therefore, the resonance conditions of ESR and NMR are expressed using slightly different notations:

$$\Delta E_{ESR} = h \cdot \nu = g \cdot \mu_B \cdot B_0 \tag{2.9}$$

$$\Delta E_{NMR} = h \cdot \nu = (1 - \sigma) \cdot g_N \cdot \mu_N \cdot B_0 = (1 - \sigma) \cdot \gamma_N \cdot \hbar \cdot B_0 \tag{2.10}$$

Where σ represents the experimental shielding constant (ppm range) and g_N, μ_N, γ_N, are tabulated constants (nuclear g-factor, nuclear magneton, gyromagnetic ratio) for the corresponding nucleus.

2.5.2 Nuclear Magnetic Resonance

In NMR spectroscopy equations are usually expressed by the gyromagnetic ratio instead of the nuclear magneton.[79] The energy for a given orientation is expressed with the Lamor frequency ν_L which depends on the gyromagnetic ratio.

$$E_{m_I} = -m_I \cdot h \cdot \nu_L \quad ; \nu_L = \frac{\gamma_N \cdot B_0}{2\pi} \tag{2.11}$$

In an experiment the Lamor frequency depends on the local magnetic field B_{loc} the nucleus experiences. Since each dipole in the sample interacts with the magnetic field, the local field differs for each nucleus. The influence of the dipoles is given in σ the so called shielding constant.[79]

$$\nu_L = \frac{\gamma_N \cdot B_{loc}}{2\pi} = (1-\sigma) \cdot \frac{\gamma_N \cdot B_0}{2\pi} \tag{2.12}$$

Since it is difficult to determine the NMR magnetic field at the sample position with sufficient accuracy, the shielding constant σ is determined relative to an agreed reference compound such as tetramethylsilane (TMS=$Si(CH_3)_4$). The usually reported chemical shift δ is thus independent of the used magnetic field. Multiplication by 10^6 leads to the typical chemical shift x-axes in ppm (parts per million). Since the protons in TMS are very strongly shielded almost all other compounds have weaker shielding and show their resonance at higher frequency or lower field.[79] The NMR spectrum is plotted from low field to high field (assuming constant RF frequency). The chemical shift δ, therefore runs from positive (low field) to negative (high field) with $\delta(TMS) = 0$.

In modern NMR spectroscopy, experiments are performed using radiofrequencies (RF) pulses in a stationary magnetic field. Pulse techniques lead to a better signal-to-noise ratio and entail versatility.[79] Magnetic dipole moments pre-align in an outer magnetic what results in a net magnetization $\vec{M}$ (see fig 11A). The RF pulses are used to induce transitions between the magnetic spin levels and create coherences in the magnetic moments of the individual spins resulting in a detectable coherent response after the single pulse or pulse sequence. These experiments can be conveniently described in the classical model of a rotating magnet in a magnetic field. The spinning magnetic moment will tend to describe a precession movement around the magnetic field vector. This movement is described by the Bloch equation[80]:

$$\frac{d\vec{M}}{dt} = \gamma_N \cdot \vec{M} \times \overrightarrow{B_0} \tag{2.13}$$

where the magnetization $\vec{M}$ represents the sum of all magnetic moments. The precession frequency or angular frequency in rad/s is given by $\omega = \gamma_N \cdot B$ which corresponds to the energy difference between the magnetic spin levels.

To describe the effect of RF pulses it is most convenient to introduce a rotating frame of axis (x′, y′, z) that rotates with the Lamor frequency ν_L.of the spin particle. Thereby the effect of the external magnetic field has been cancelled and the magnetization is stationary. Then the Bloch equation (in the rotation frame) becomes:

$$\frac{d\vec{M}}{dt} = \gamma_N \cdot \overrightarrow{M} \times \vec{B}_1 \tag{2.15}$$

Now, the magnetization starts precessing around the $\vec{B}_1$axis (e.g. the x′-axis) and moves away from the z-axis. In figure 11B a 90° RF pulse is shown that transfers the magnetization $\vec{M}$ in the x′y′ plane. The occurring B_1 field during the pulsed irradiation is indicated (see fig. 11, pale green arrow).

The spin will dephase leading to a free induction decay with a rate constant T_2' (spin-spin or transverse relaxation time). Eventually, also the magnetization in the z-direction will be restored, again in an exponential process with a characteristic time T_1 (i.e. the spin-lattice or longitudinal relaxation time). The evolution of the magnetization signal in the x′y′ plane can be recorded in the NMR probe-head as free induction decay (FID).

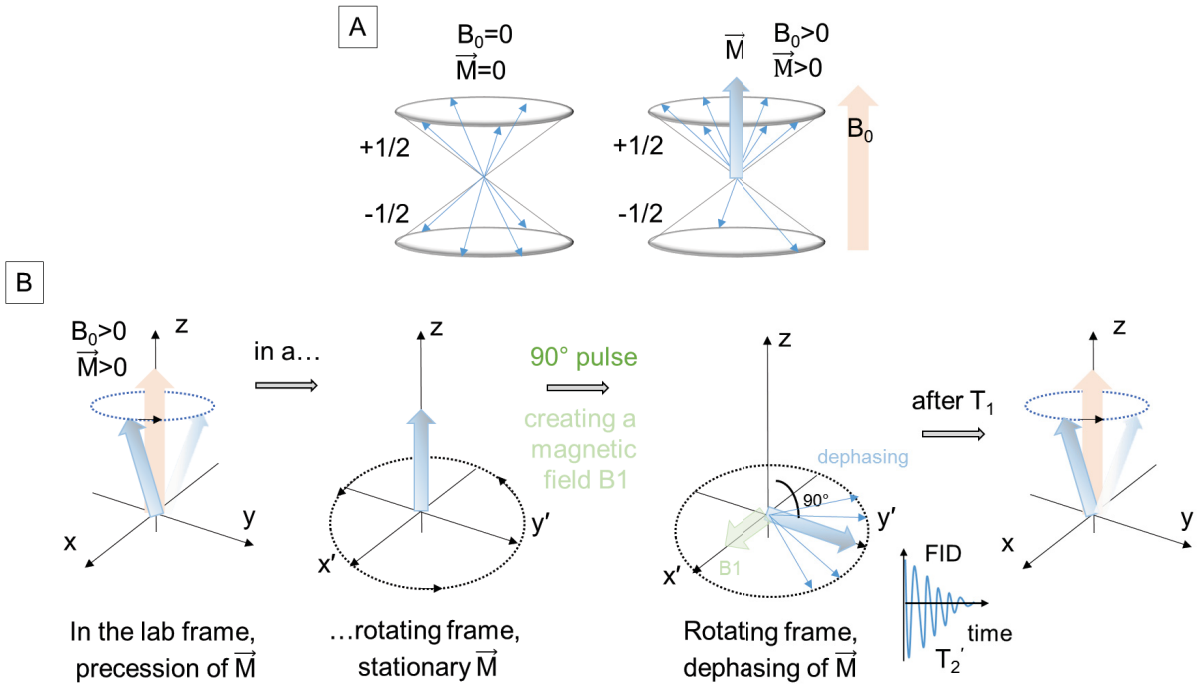

Figure 11 Relative populations of the spin in a system and the effect of a 90° RF pulse. A) Shows the spin population with and without an applied magnetic field B_0 (orange). In a magnetic field the spins align predominantly with the magnetic field, resulting in a magnetization $\vec{M}$ (blue), B) represents the displacement of $\vec{M}$ by a 90° RF pulse and its evolution over time.

Fourier transformation of the FID results in the NMR spectrum. The total transversal relaxation rate T_2 is determined by T_2' and T_1 and can be used to calculate the line broadening of a signal (under non saturating conditions, ($\frac{1}{T_2} = \frac{1}{T_1} + \frac{1}{T_{2'}}$).)

2.5.3 Paramagnetic ^{1}H NMR spectroscopy

^{1}H NMR can also be applied in the structure determination of paramagnetic metalloproteins and has been intensely used in the study of iron-sulfur proteins.[81] At first sight, the loss of

information due to the interaction of the unpaired electron spin with the nuclear spin can be considered as disadvantage.[82] But the introduced paramagnetic restraints can also be used as an advantage to gain insight into the electronic structure of these systems. Temperature dependencies in combination with further NMR techniques allow sequence specific assignments around the metal sites and the determination of the metals oxidation state.[83] In general, large chemical shifts for proton resonances in metalloproteins are observed. The observed chemical shift (δ^{obs}) consists of several components. The diamagnetic part of the chemical shift (δ^{dia}) is the shift that an analogous but diamagnetic compound would undergo. The paramagnetic part of the chemical shift, the hyperfine shift, is split into the pseudo-contact shift (δ^{PC}) and the contact shift (δ^{C}). To separate the contribution of the pseudo-contact shift and the contact shift is not trivial.[84]

$$\delta^{obs} = \delta^{dia} + \delta^{PC} + \delta^{C} \tag{2.16}$$

The pseudo-contact shift originates from the dipolar coupling between the nuclear magnetic moment and that of the unpaired electron and has a distance dependence of r^{-3}. It only occurs if the magnetic susceptibility χ is anisotropic (see fig. 12) and can be described by equation 2.17.[82]

$$\delta^{PC} = \frac{1}{12 \cdot \pi \cdot r_i^{-3}} \left\{ \Delta\chi_{ax} \cdot (3\, cos^2\, \theta - 1) + \frac{3}{2}\, \Delta\chi_{rh}\ \ sin^2\, \theta \cos 2\phi \right\} \tag{2.17}$$

with r_i is the distance of the resonating nucleus to the metal, $\Delta\chi_{ax}$ and $\Delta\chi_{rh}$ the axial and rhombic components of the magnetic susceptibility tensor, θ the angle between nucleus-metal vector and the z-axis of the χ tensor and ϕ the angle of the x axis of the χ tensor and the projection of the nucleus-metal vector in the xy plane.[85]

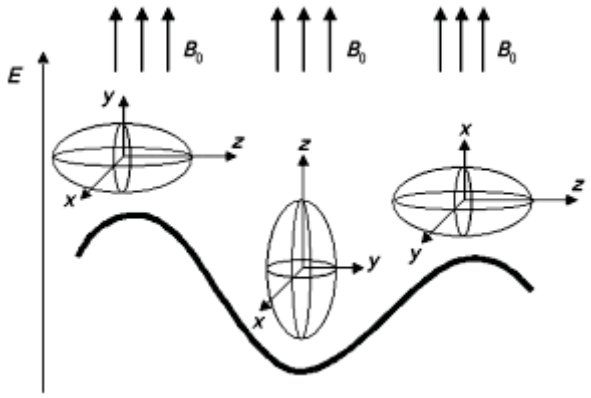

Figure 12 Representation of a magnetically anisotropic characteristic and its orientation dependent energy in an outer magnetic field B_0. Figure taken with permission from [86].

The information gained from the pseudo-contact shift alone is not sufficient for structure determination, it can be used as an additional set of constraints in combination with dihedral angles (see next section) and the nuclear Overhauser effect (showing connectivities among nuclei).[82]

The second component of the hyperfine shift is the contact shift δ^C. The contact shift is caused by an additional magnetic field generated at the site of the nucleus which decreases fast with increasing number of bonds between the metal and the nucleus under investigation. This additional magnetic field is based on the fast motion of electrons in molecular orbitals (MO) that causes an average induced electron magnetic moment at the nucleus. The electron magnetic moment depends on the spin density at the nucleus which can be positive or negative according to spin polarization of the core electrons induced by the unpaired electron(s).[87] Thus the contact shift is indicative for the spin density at the nucleus.

In some systems the contact shift can be parametrized using the dihedral angle between two planes spanned by the metal (M), a donor atom (D) and the resonating nucleus (H) (see fig. 13B). Often the contact contribution is only considered for directly bound protons or protons in close proximity or rather those that experience the contact shift through H-bonding or angle dependent orbital overlap from donor atoms bound to the metal center.[82]

Dihedral angle dependence of β-CH_2 protons from cysteine-coordinated [4Fe-4S] cluster

In proteins containing [4Fe-4S] cluster(s), which are coordinated by cysteines, β-CH_2 protons and α-CH protons of the cysteine residues undergo large chemical shifts. It was found that these shifts are dominated by the contact contribution[88] although three σ-bonds are between the protons and the iron ion. The dihedral angle θ between the Fe-S-C and the S-C-H-plane (see fig. 13A) dictates the orbital overlap between the p_z-orbital of sulfur and the 1s orbital of the proton. Thus electron delocalization occurs.[87]

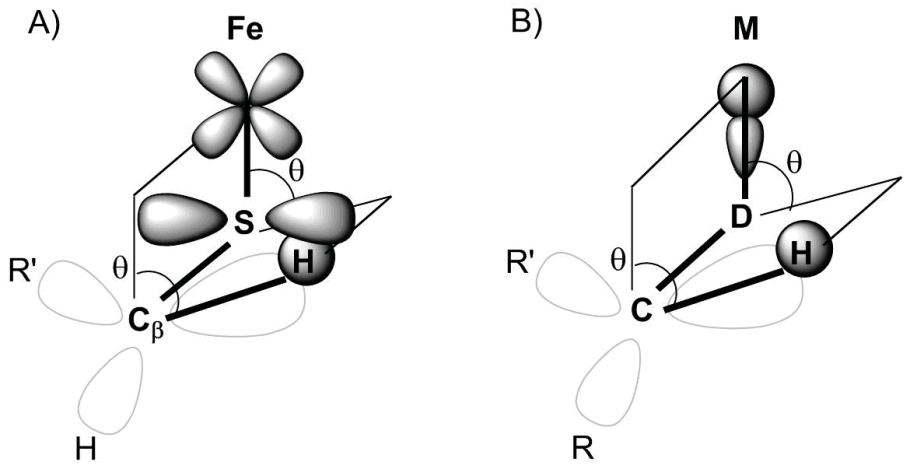

Figure 13 Illustration of the dihedral angle θ in two different systems A) in a metal complex consisting of a metal **M** with a donor **D** bound to a sp^3 carbon with two moieties R and R' B) binding situation for one cysteine in a [4Fe-4S] cluster. In both systems two planes, spanned up by the atoms along the bold bonds, define θ. Grey shaded orbitals take part in the delocalization mechanism (see text).

The size of the contact shifts depend on the unpaired spin density in the p_z-orbitals of the sulfurs and the orbital overlap which is determined by the dihedral angel θ. A parametric equation links the contact shift δ^C with the dihedral angel θ.[88] For systems with a donor that has a p_z-orbital orthogonal to the metal-donor σ-bond, as sulfur in cysteine-coordinated [4Fe-4S] clusters (compare fig. 13A), the equation

$$\delta^C = a \cdot sin^2\theta + b \cdot \cos\theta + c \qquad (2.18)$$

is obtained. It includes a, b and c as numerical coefficients that have been determined as a=10.3, b=-2.2 and c=3.9 for cysteine-coordinated [4Fe-4S] cluster.[88] For other systems for example an octahedral Ni(II) complex with an amine moiety[89] the contact shift dependence on the dihedral angle can be described by the general Karplus relationship[90] ($\delta = a' \cdot cos^2\theta + b' \cdot \cos\theta + c'$) in which the coefficients b′ and c′ can often be neglected.[88] The equations differ because of the location of the spin density in the two systems. The amine is lacking a donating p_π-orbital and the spin density is located in the Ni-N bond so that the 1s orbital of the amine protons experience most spin density at 0 and 180° (see fig. 13B).

Cysteine coordinated [4Fe-4S] cluster in ^{1}H NMR studies

In general, there are three oxidation states of [4Fe-4S] cluster formed by formally:

a) 3 Fe(III) and 1 Fe(II) resulting in: $[4Fe\text{-}4S]^{3+}$
b) 2 Fe(III) and 2 Fe(II) resulting in: $[4Fe\text{-}4S]^{2+}$
c) 1 Fe(III) and 3 Fe(II) resulting in: $[4Fe\text{-}4S]^{+}$

$[4Fe\text{-}4S]^{3+/2+}$ are the oxidation states found in high potential iron-sulfur proteins (HIPIPs) whereas $[4Fe\text{-}4S]^{2+/+}$ clusters are the oxidized and reduced state in bacterial ferredoxins. The β-CH_2 protons of coordinated cysteines have larger hyperfine shifts than the α-CH protons since the β-CH_2 protons are three bonds away from the iron compared to the distance of five bonds for the α-CH protons. The hyperfine shifts found in a [4Fe-4S] cluster are dominated by the contact shift so that the pseudo-contact contribution can be neglected. The contact shift arises from unpaired electron density at the nucleus through electron delocalization.

The typical temperature dependences of the hyperfine shifted signals in [4Fe-4S] cluster are based on the spin magnetization and a shift in Boltzmann distribution from the allowed magnetic spin levels of the unpaired electron. Temperature dependences are classified according to the Curie law which says that the absolute value of the spin magnetization

decreases with increasing temperature resulting in a smaller chemical shift. The opposite behavior is named anti-Curie. The term pseudo-Curie addresses in general anti-Curie behavior but takes the sign into account (see fig. 15, region III).[91] Protons that belong to the same cysteine should show the same temperature dependence of their chemical shift.

In polymetallic systems the induced magnetic moment per metal ion has to be considered. Magnetic coupling within the cluster occurs when the metal ions' electronic spin magnetic moments interact. Interaction of spin S_1 and spin S_2 lead a to linear combination of the spin functions of each metal ion resulting in quantized new spin levels with S′ varying from S_1+S_2 to $\left|S_1-S_2\right|$.[87] In general the separation of the S′ levels increases with the amount of coupled metals in the system. The Heisenberg Hamiltonian (here for a dimer) includes the spin operators of the metal ions and a constant J.

$$\mathcal{H} = J\,\boldsymbol{S_1}\,\boldsymbol{S_2} \tag{2.19}$$

If J is negative, as in most systems, the coupling is antiferromagnetic, meaning that the spins orient in opposite directions. If J is positive the magnetic coupling is ferromagnetic and the spins would co-align with each other.

In [4Fe-4S] cluster all irons are tetragonally coordinated and, in combination with sulfur as a weak ligand, all irons are in the high spin configuration. The irons within a cluster can be grouped in pairs (see fig. 14) that behave like the large spin S_1 and the smaller spin S_2 and show a combined spin of S_A (larger spin) and S_B (smaller spin).[81] The pairs are antiferromagnetically coupled with a large Heisenberg exchange interaction constant J.[92] In figure 14 the larger spin S_A is aligned along the magnetic field so that a nearby nucleus (e.g. ^{1}H) experiences higher spin density which results in a downfield shift. The complementary is true for a nucleus influenced by S_B that is aligned opposite B_0, seeing a negative spin density shifting the nearby nucleus upfield.

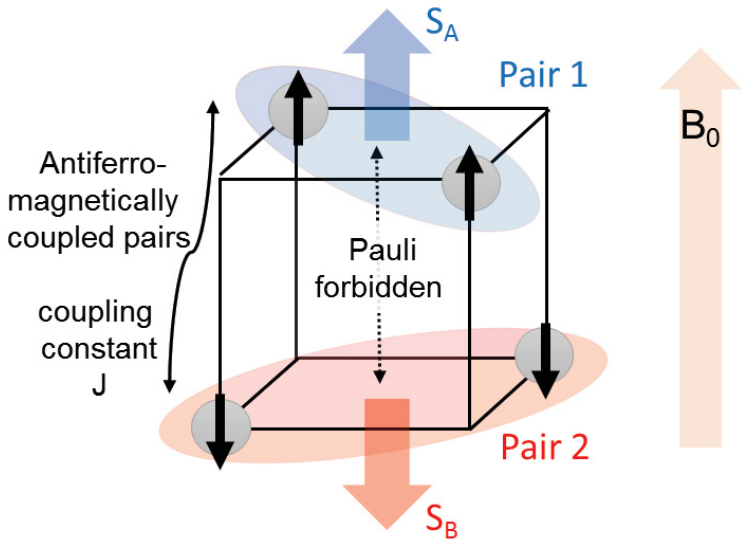

Figure 14 Schematic representation of the four irons in a [4Fe-4S] cluster forming two antiferromagnetically coupled pairs. The spin of the blue pair 1 is aligned along the applied magnetic field B, the spin of pair 2 is forced in the opposite direction.

With an often used magnetic coupling model[91, 93] it is possible to relate the temperature dependence of the cysteines protons to their hyperfine shift. Within the model three temperature regions (I, II, II in fig. 15) have to be distinguished based on the exchange coupling constant J in relation to the energy given be k_BT.

If $k_BT > J$, as in region I, then the spins S_A and S_B are uncoupled and align both parallel with the magnetic field. Consequently all nuclei experience positive spin density resulting in downfield shifts. For protons experiencing S_A the shift is Curie and for the protons related to S_B it is pseudo Curie.

In temperature region II the energies form k_BT and J are in the same range. This results in downfield shifts with Curie dependence for protons belonging to S_A and anti-Curie dependence for protons of the cysteines belonging to pair 2 with S_B. For an antiferromagnetic system with a large coupling constant J ($J \gg k_BT$), S_A will fully aligned along the applied magnetic field B_0 whereas S_B is forced (by antiferromagnetic coupling) to align in the opposite direction. The generated magnetic field of S_A will increase the field that is

experienced by the nucleus. The magnetic field induced by S_B will be of opposite sign and results in an upfield shift for the related protons.[81]

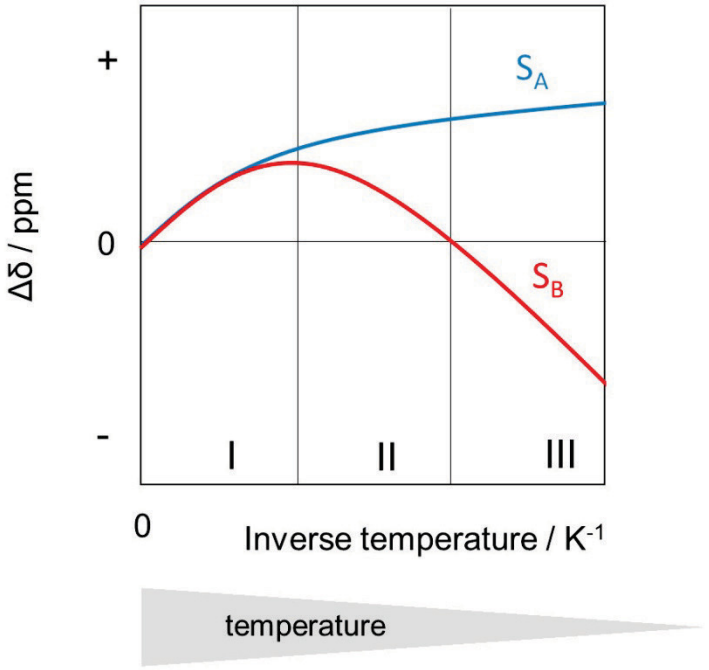

Figure 15 Schematic representation of the predicted temperature dependence of the hyperfine shifts from nuclei sensing antiferromagnetically coupled spins S_A and S_B.

2.5.3.1 The active site of [FeFe] hydrogenases and the isolated $[4Fe\text{-}4S]_H$ cluster state

The redox state of the $[4Fe\text{-}4S]_H$ cluster in [FeFe] hydrogenases changes within the catalytic cycle between 1+ and 2+. ^1H paramagnetic NMR spectroscopy is applied to the cubane cluster in an apo-hydrogenase as well as the complete H-cluster in journal article III, IV and V.

The oxidized cubane cluster with a charge of 2+ contains formally 2 Fe(II) and 2 Fe(III). Due to the high spin, Fe(II) has a spin of S= 2 whereas Fe(III) has a spin of S= 5/2. One iron each form together a valence delocalized pair[93b] (see table 1) with a combined spin of S_A/S_B= 9/2. The two 9/2 spins are antiferromagnetically coupled, usually with a large J to a diamagnetic ground state with a total spin of S_{total}= 0. In other FeS proteins of the bacterial ferredoxin type

all shifted β-CH_2 protons of coordinated cysteines exhibit increased shifts with increasing temperature what is described as anti-Curie temperature dependence (AC).[94],[95]

The by one electron reduced $[4Fe\text{-}4S]^+$ is formally composed of 3 Fe(II) and one Fe(III) with a total spin S= 1/2. Experimentally it was found,[96] that the electron is delocalized on one mixed pair of Fe(II) Fe(III) with S_A= 9/2, so that the second pair harbors Fe(II) Fe(II) with a S_B= 4 (see table 1).

In the literature there are studies about $[4Fe\text{-}4S]^{2+}$ clusters that are coupled to an additional metal site M. This is the case in the oxidized sulfite reductase from *E. coli*[97] with M being Fe^{3+} and for the carbon monoxide dehydrogenase (CODH) with M= Ni^+. For both systems the covalent link between M and the $[4Fe\text{-}4S]^{2+}$ cluster was found to form an exchange pathway with a coupling constant j between the two sites. By the exchange interaction an excited state is mixed into the S_{total}= 0 ground state of the oxidized cubane. The larger j is, the larger is the energy difference between the excited and the ground state.[93b]

Table 1: Chemical and physical properties of $[4Fe\text{-}4S]^{+/2+}$. The cluster is composed of two antiferromagnetically coupled iron pairs and based on the spin of each pair, S_A and S_B, the predicted temperature dependence of protons from the coordinating cysteines are given. S_{total} gives the spin state of the complete cluster in the ground state.

State	Pair 1	S	S_A	Pair 2	S	S_B	S_{total}
Oxidized	Fe(II)	2	9/2	Fe(II)	2	9/2	0
$[4Fe\text{-}4S]^{2+}$	Fe(III)	5/2		Fe(III)	5/2		
Reduced	Fe(II)	2	9/2	Fe(II)	2	4	1/2
$[4Fe\text{-}4S]^+$	Fe(III)	5/2		Fe(II)	2		

2.5.4 Electron Paramagnetic Resonance

In EPR spectroscopy the magnetic spin transitions of systems with one or more unpaired electrons are stimulated. In biological samples paramagnetism arises from unpaired electron e.g. from intermediates/radicals in enzymatically catalyzed reactions of transition metals in prosthetic groups of a protein, like the $[4Fe\text{-}4S]_H$ cluster and the $[2Fe]_H$ subsite in [FeFe]

hydrogenases. EPR spectroscopy is applied to [FeFe] hydrogenases in journal article IV and VI.

A paramagnetic system can be investigated for its electronic structure by observing the interactions of the magnetic moments of the unpaired electron with each other, with nuclear spins, with the magnetic moment of their orbitals and the static magnetic field B. Since the orbitals containing the unpaired electron(s) are usually quite close in energy to higher unoccupied orbitals, multiple interactions may occur. Therefore, the description of the magnetic spin energies becomes very complicated and these interactions are parameterized in an effective spin Hamiltonian containing only spin operators.

$$\mathcal{H}_S = \overbrace{\vec{B}\cdot\bar{\bar{g}}\cdot\vec{S}}^{\text{Electron Zeeman}} + \underbrace{\vec{S}\cdot\bar{\bar{D}}\cdot\vec{S}}_{\text{Zero Field}} + \overbrace{\vec{S}\cdot\bar{\bar{A}}\cdot\vec{I}}^{\text{Hyperfine Interaction}} + \underbrace{\vec{I}\cdot\bar{\bar{P}}\cdot\vec{I}}_{\text{Nuclear Quadrupol}} - \overbrace{\gamma\hbar\vec{B}\cdot\vec{I}}^{\text{Nuclear Zeeman}} \tag{2.20}$$

The first and last terms describe the interaction of the electron and nuclear spin with the static magnetic field $\vec{B}$, the so called Zeeman interaction. The g-tensor $\bar{\bar{g}}$ is represented by a 3x3 matrix containing the anisotropic components (g_x, g_y, and g_z) of the electron Zeeman interaction. The g-tensor parameterizes the effect of spin-orbit couplings. The nuclear Zeeman interaction is assumed to be isotropic.

The frozen solution EPR spectrum allows to extract the principal values of the g-tensor (see fig. 16). In case $g_x = g_y = g_z$ only one resonance line is observed and the Zeeman interaction is called “isotropic”. If only one g-value deviates from the other two (representing the unique axis), the Zeeman interaction is called “axial”. If all three principle values differ, the interaction is “rhombic”.

The second term in equation 2.20, referred to as zero field splitting contribution, describes electron spin – electron spin interaction and thus only occurs when there is more than one

unpaired electron (see next chapter). In that case, the total electron spin is larger than S= 1/2 (e.g. S=1, 3/2, etc). The zero field tensor $\overline{\overline{D}}$ describes the interactions between the unpaired electrons and contains contributions from spin orbit and dipolar interactions. The third term describes the interaction between the unpaired electron and the nuclear spin(s), the so called hyperfine interaction with the hyperfine tensor $\overline{\overline{A}}$.

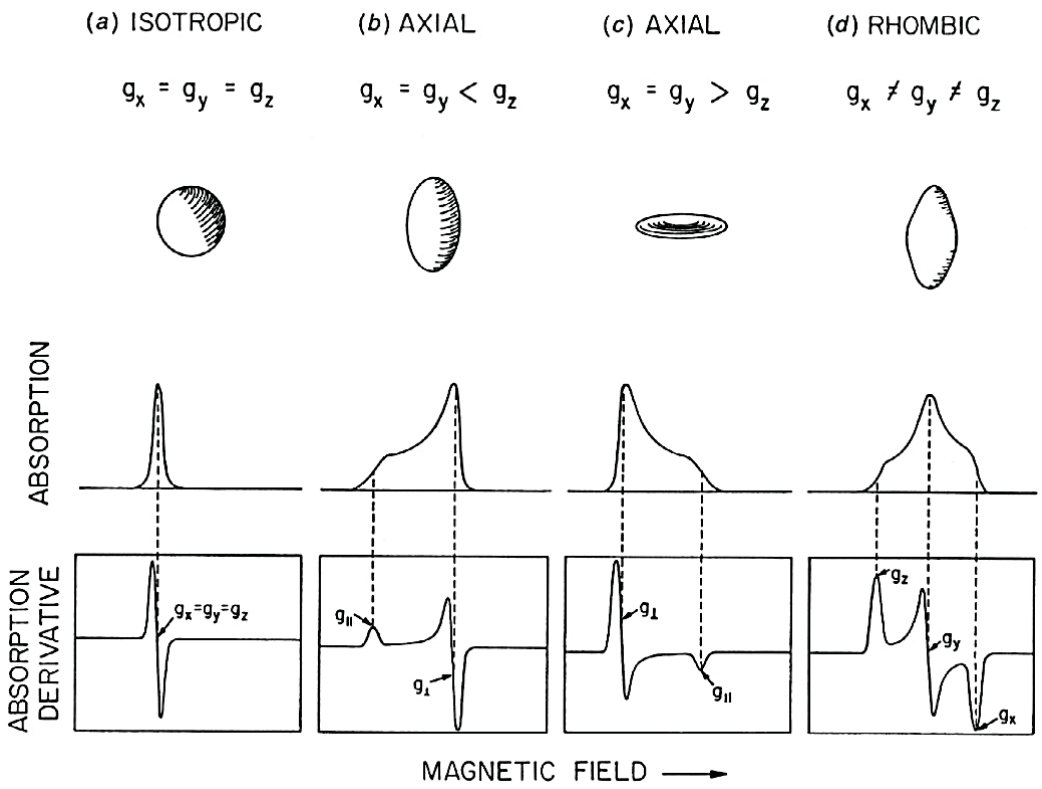

Figure 16 Possible line shapes of a spin S= 1/2 system in EPR spectroscopy. Depending on the relations of the principal values of the g-tensor to each other the corresponding signals are isotropic, axial or rhombic (taken from [98] with permission).

The forth term describes the interaction between the quadrupole moment of the nucleus and the electric field gradient around the nucleus. It is only present with quadrupole nuclei (I> 1/2). Within this thesis only the Zeeman interactions and zero field splitting contribution are of greater interest.

An EPR spectrum can be recorded in continuous wave (CW) or pulsed mode. In the continuous wave mode the frequency is kept constant while the magnetic field is varied. Due

to field modulation, which increases the resolution and sensitivity, the observed spectrum is the first derivative of the absorption spectrum (see fig. 16). The linewidth in a CW EPR spectrum is usually too broad to resolve the smaller interactions. Similar to NMR spectroscopy microwaves can be applied in pulse sequences addressing certain interactions. These techniques are summarized under the term pulse EPR.

Systems with multiple unpaired electrons: High Spin Systems

In EPR spectroscopy systems with S= 1/2 and systems with higher spin S≥ 1 show a different behavior due to the interaction of the unpaired electrons that is independent of the external magnetic field. In FeS cluster proteins the unpaired electrons on the Fe sites can couple to higher spin states. A high spin system is part of journal article IV.

Usually, the zero field splitting in these systems is dominating the Zeeman interaction which is often isotropic. In this case the spin Hamiltonian simplifies to:

$$\mathcal{H}_S = g\mu_B B_0 + \vec{S} \cdot \overline{\overline{D}} \cdot \vec{S} \qquad (2.21)$$

Since the zero field tensor $\overline{\overline{D}}$ is traceless, i.e. the sum of the principal components ($D_x + D_y + D_z$) is zero. By diagonalization of the zero field tensor the two independent parameters D and E are obtained, which derive from the principal values.[99]

$$D = \frac{3}{2} D_z \; ; \quad E = \frac{1}{2}\left(D_x - D_y\right) \qquad (2.22\text{ a-b})$$

The ratio of E/D is defined as rhombicity η and ranges between $0 \leq \eta \leq \frac{1}{3}$.

For half integer spins (S= 3/2, 5/2, etc) the energy levels are grouped into pairs that are degenerate without an applied magnetic field B_0. They are called Kramer doublets and have the opposite values of m_s ($m_S = \pm 1/2, \pm 3/2, \pm 5/2$). As long as the zero field interaction is dominating the Zeeman interaction only transitions between the Kramers doublets are observed. The effective g-values for these transitions are independent of the magnitude of D.

Only the rhombicity parameter η affects the resonance positions[99] and helps to understand the temperature dependence of high spin systems. Rhombograms for every half integer spin give the dependence of the g-values to the rhombicity.[100]

2.6 Electrochemistry of biological samples

2.6.1 Basic principles of protein film electrochemistry

Electrochemical investigations can provide a variety of information about enzymes activity, mechanism and other properties.[101] Protein film electrochemistry (PFE) is a technique used to study the behavior of a redox active enzyme (with electron flow) adsorbed on the electrode surface in response to an applied potential (see fig. 17). The monitored current i depends on the amount of transferred electrons n, the Faraday constant F, the rate of the reaction k_{cat}, the electroactive surface coverage Γ and the area A of the electrode surface.[101]

[FeFe] hydrogenases have been studied by PFE allowing kinetic and mechanistic investigations of theses enzymes. For [FeFe] hydrogenases the monitored current i reflects the activity, and allows kinetic and mechanistic studies. One common problem using PFE with hydrogenases is that the determination of the electroactive coverage Γ is difficult. Thus direct calculations of e.g. the turn over frequencies (TOF) is not possible.[6b]

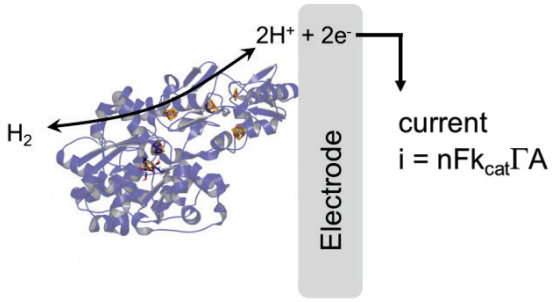

Figure 17 Schematic representation of a [FeFe] hydrogenase adsorbed on an electrode.

To perform an electrochemical experiment, a potentiostat and a cell with three electrodes are usually needed. Each of these electrodes has a specific task; the working electrode (WE) is where the reaction under investigation takes place and the resulting current flows through the counter electrode (CE), while the reference electrode (RE) is used to relate the measured/applied potential to a standardized system like the standard hydrogen electrode (SHE). Basically two main electrochemical techniques have to be distinguished, namely,

cyclic voltammetry (CV) and chronoamperometry (CA). During a CV, the potential between the WE and the RE is modulated while the current is measured between the WE and the CE. This set up is necessary to avoid a net current flowing through the RE that could change its potential and might damage it.[102]

In a CV experiment, the potential is swept linearly back and forth between two values while the current response from the enzyme is recorded. CV experiments provide valuable data about the behavior of hydrogenases at different potentials and the preferred redox direction (redox bias). Different [FeFe] hydrogenases show very different behaviors especially at high potentials (see fig. 18). In general, hydrogenases produce hydrogen at low potential (light grey area) till the $H_2/ 2H^+$ formal redox potential is reached, then the hydrogen is split into protons and electrons at higher potentials (dark grey area). In the case of [FeFe] hydrogenase HydA1, as the potential is increased, the H_2 oxidation current starts to drop around 0 V. This means that the hydrogenase is getting inactivated. As the potential is swept back to lower potentials, HydA1 becomes active again – this phenomenon is called reversible high-potential inactivation. It is characterized by the switch potential E_{Switch}, which is determined from the first derivative of the reductive sweep[103] (in the high potential region, see fig. 18). Furthermore, the optimal activity conditions for parameters like pH, substrate concentrations etc. can be tested easily with CV. In a chronoamperometry (CA) experiment, the current response is monitored over time at a fixed potential usually followed by a perturbation e.g. a potential step or the addition of a substrate or inhibitor. A change in the current for a [FeFe] hydrogenase at a fixed potential is equal to a change in the catalytic rate.[104]

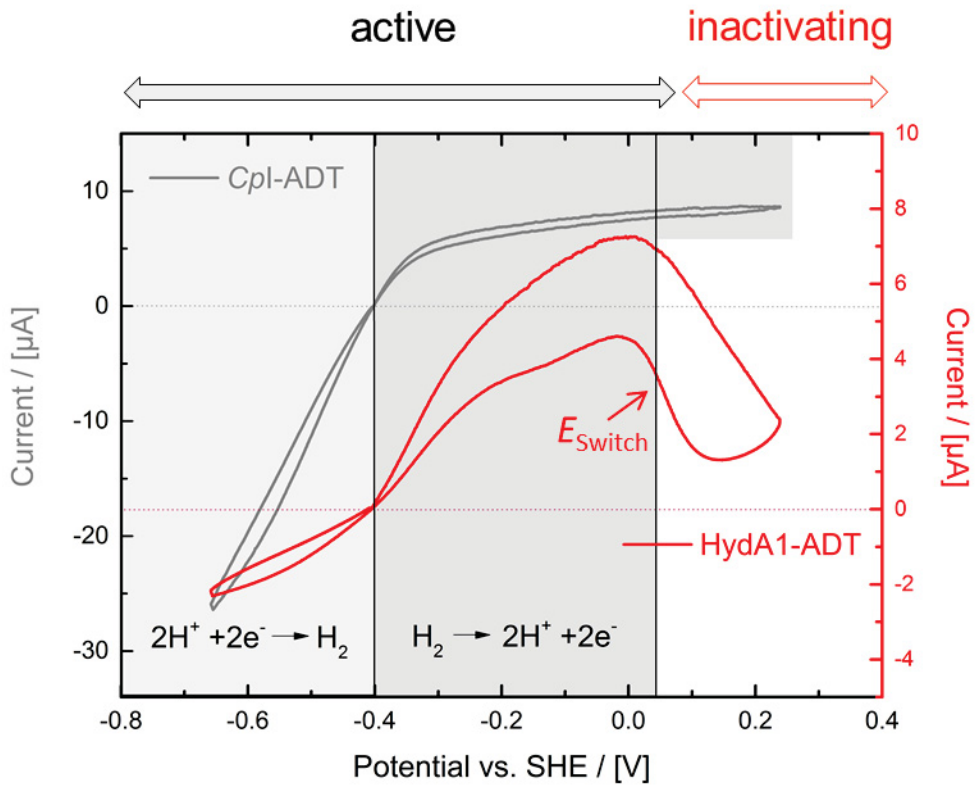

Figure 18 CVs of the two [FeFe] hydrogenases *Cp*I-ADT and HydA1-ADT. In the light and dark grey regions the hydrogenases are active. HydA1-ADT becomes inactivated at high potentials. Both CVs are measured under 100% H_2 with a rotating disk electrode (2000 rpm) at 298 K and a scan rate of 0.02 V/s.

The working electrode material plays a key role in the protein film electrochemistry since the formation of a stable protein film is crucial for interfacial direct electron transfer with the electrode. One very common WE for PFE is the pyrolytic graphite edge (PGE) electrode. Polishing a PGE before use leads to a rough and hydrophilic surface containing different acidic oxides that can increase the electrostatic interactions with the enzyme.[105] Due to its chemical heterogeneity, many enzymes can be adsorbed on a PGE electrode and the stability of each particular enzyme can be optimized by adjusting the pH, the ionic strength of the used electrolyte or by introducing a co-adsorbate.[104]

In general, the adsorbed protein film stability is based on the protein-electrode as well as the protein-protein interactions within the film. Between the electrode and the protein surface only non-covalent forces (electrostatic, hydrophobic) occur. Interclusteral interactions are avoided due to the insulating polypeptide chains surrounding the active sites. Lowered

temperatures can be used in long term experiments to increase the film stability; however, the catalytic current will decrease accordingly. In order to increase the long term stability, the enzyme can be covalently attached to a functionalized electrode surface through the exposed cysteine or lysine residues on the protein surface.[106]

Enzymes show on one hand general disadvantages for being studied by direct electron transfer. They are large in size compared to a molecular catalyst and need a big electrode surface area. On the covered electrode the active site density of a protein film is small; nevertheless, a film in the range of pico-mole of enzyme on an electrode is sufficient to establish an electrochemical experiment.[101] On the other hand, they reduce the required over potential for a reaction, show full reversibility on the electrode and are able to produce high catalytic currents (depends on the studied enzyme).[107] Interclusteral interactions are avoided due to the insulating polypeptide chains surrounding the active sites.

2.6.2 Electrochemical investigations on [FeFe] hydrogenase

[FeFe] hydrogenases are suitable enzymes to be studied by PFE due to their high catalytic rates. The F-cluster containing hydrogenase from *Desulfovibrio desulfuricans* was one of the first [FeFe] hydrogenases studied with PFE on a PGE electrode.[108] In this study, the authors analyzed the reversible inactivation at high potentials which protects the hydrogenase against oxygen damage and inhibition by adding carbon monoxide.

Studies with oxygen and carbon monoxide [13a, 101, 109] were performed with hydrogenases from different hosts. CO gas and molecular oxygen are the most intense studied inhibitors. Generally, [FeFe] hydrogenases are irreversibly damaged by oxygen with some minor exceptions.[109b] However, it remains under debate where exactly and how the oxygen damages the active site. Since the CO inhibited hydrogenases are protected from oxygen damage and it is known that CO binds to the Fe_d,[50] it was suggested that oxygen attacks the same binding site or proximal to it. In a combined electrochemical and EXAFS study on

HydA1 from *Chlamydomonas reinhardtii* it was shown that the $[4Fe\text{-}4S]_H$ cluster instead of the $[2Fe]_H$ site was affected by oxygen.[109a] Based on both findings two hypothesis are conceivable in which the oxygen binds initially to Fe_d and the cubane cluster is damaged consecutively. In the first hypothesis oxygen becomes partially reduced and reactive oxygen species (ROS) are formed which then attack the $[4Fe\text{-}4S]_H$ cluster. In the second hypothesis the bound oxygen becomes a superoxide and the cubane cluster is damaged by long-ranged through bond electron transfer.[6b]

Carbon monoxide shows a high affinity to the oxidized state of the [FeFe] hydrogenases.[13a] This affinity decreases when the potential is lowered.[110] CO-inhibition of a hydrogenase in the oxidized state results in the H_{ox}-CO state which can be transformed back to a fully functionalized hydrogenase. Adding CO to the hydrogenase at low potentials (H_{red} state) damages the enzyme partly whereas at very negative potentials (H_{sred} state) the CO affinity is too low to induce any damage.[110] Compared to CO, formaldehyde shows the almost complementary affinity behavior. It binds with high affinity at low potentials and is a stronger inhibitor than CO.[49, 111]

2.6.3 Nernst equation and FTIR-spectroelectrochemistry

Potentiometric titrations under equilibrium condition can be used to determine the ratio between an oxidized species O and a reduced species R in a reaction solution close to the electrode surface. Mathematically the dependence of the potential E on the ratio of concentrations is described with the Nernst equation (2.29) which is based on the Gibbs free energy ΔG (2.28). The Nernst equation is valid for reversible systems with fast kinetics.

$$\Delta G = \Delta G^0 + R \cdot T \cdot ln\frac{[O]}{[R]},\ with\ \Delta G = -n \cdot F \cdot E\ \ and\ \Delta G^0 = -n \cdot F \cdot E^0 \qquad (2.28)$$

$$\Rightarrow E = E^0 + R \cdot T \cdot ln\frac{[O]}{[R]} \qquad (2.29)$$

Where $\Delta G^0$is the the Gibbs free energy at standard conditions, R the gas constant, T the absolute temperature, n the amount of transferred electron, F the Faraday constant and E^0 the potential at standard conditions. The Nernst equation can be applied to follow the potential dependent evolution of CO marker bands of [FeFe] hydrogenases monitored with FTIR Spectroscopy.[63, 112]

For the FTIR-spectroelectrochemistry measurement, a three-electrode-containing measuring cell with two CaF_2 windows is used.[6b] The heart of the measuring cell is a semitransparent gold mesh, the WE, on which the sample is loaded. The second window and two rubber rings which are pressed together in the final step of assembly are sealing the measuring compartment (see fig. 19). A thin platinum layer is used as a counter electrode and an Ag/AgCl electrode in a 1 M KCl solution is used as a reference. The total sample volume that is titrated is approx. 50 µL. KCl is used as an electrolyte within the sample buffer and redox mediators can be added to obtain faster equilibration times. The sample is titrated by applying different potentials in a stepwise manner, with sufficient equilibration time before the FTIR measurement is started.

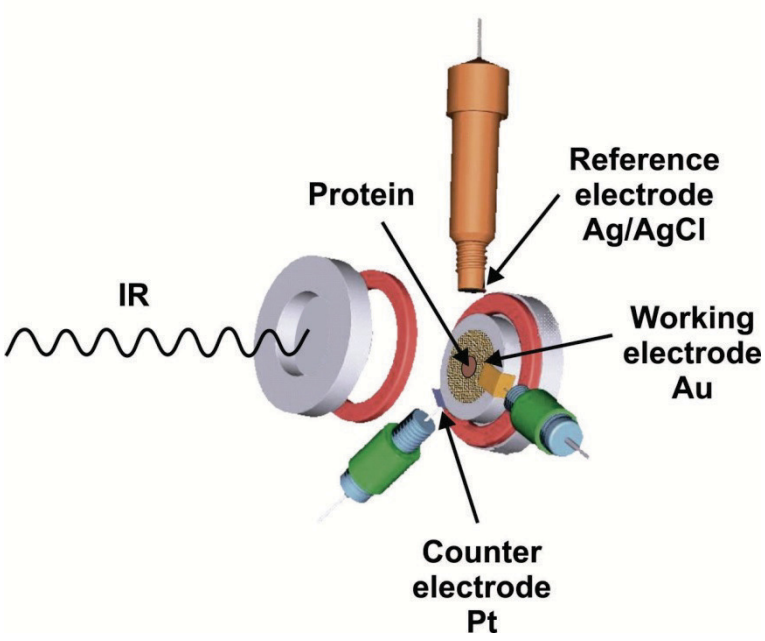

Figure 19 Schematic, exploded close-up of the FTIR-spectroelectrochemical cell used for potential titration. Adapted with permission from Lubitz W, Ogata H, Rüdiger O, Reijerse E. Hydrogenases. *ChemRev* 2014, 114: 4081-4148. Copyright 2014 American Chemical Society.

To determine the concentration ratio of two redox states, the specific CO marker bands (see chapter 2.4.3) are followed in their intensities and evaluated using the Nernst equation (eq. 2.29). Since [FeFe] hydrogenases show two one electron reduction steps, three states (H_{ox}→ H_{red}→ H_{sred}) have to be fitted. For the fitting, the general assumption that the populations of all states together equal one ([ox]+[red]+[sred]=1) is combined with the two Nernst equations belonging to the midpoint potentials $E_{(ox/red)}$ and $E_{(red/sred)}$.[36] At low pH values, the model has to be expanded to six states, because the protonated version of each state must be taken into account.

3. SUMMARY OF JOURNAL ARTICLES

3.1 Paper I: Proton Coupled Electronic Rearrangement within the H-Cluster as an Essential Step in the Catalytic Cycle of [FeFe] Hydrogenases

At the start of this study, the nature of the singly reduced species H_{red} (assumed to be in a $[4Fe\text{-}4S]^{2+}[Fe_p(I)\ Fe_d(I)]$ configuration) in the catalytic mechanism (see chapter 1.2.2) was not fully understood. While in the bacterial [FeFe] hydrogenase (*Dd*HydAB, *Cp*I) the H_{red} state does not show a bridging CO ligand, in HydA1 (from *Chlamydomonas reinhardtii*) this ligand is retained during reduction from H_{ox} to H_{red}. It was anticipated that this discrepancy could be related to protonation, which is an essential step in the catalytic cycle (see fig. 2). We therefore studied the pH dependence of the H_{ox} to H_{red} transition in HydA1 using FTIR monitored spectro-electrochemistry with five suited redox mediators at five different pH values ranging from pH 5 to 10. These resolved the redox and protonation events in the catalytic cycle and lead to the conclusion that the H_{red} state consists of two electronically different configurations (see fig. 20) with a protonation event pK_a of about 7.2, which is very close to the pH optimum of the catalytic activity. The unprotonated reduced state is referred as H_{red} state and the protonated reduced state as $H_{red}H^+$ state. The protonation of the NH group causes an electron rearrangement of the H-Cluster resulting in an electron transfer (ET) from the cubane cluster to the $[2Fe]_H$ site (see fig. 20) so that in the $H_{red}H^+$ state a configuration $[4Fe\text{-}4S]_H^{2+}\ [Fe_p(I)\ Fe_d(I)]$ with a protonated bridgehead group and two terminal bound CO ligands at the Fe_d is found.

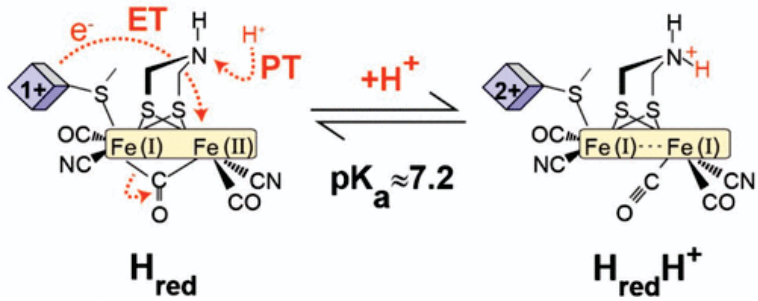

Figure 20 Schematic representation of the electronic rearrangement and the protonation step from the new H_{red} state to the $H_{red}H^+$ state.

Since the $H_{red}H^+$ state is only dominant at low pH, we assume that the electronic rearrangement is triggered by the protonation. The rearrangement can be seen as a charge neutralization effect. The spectroelectrochemistry also resolved the second reduction event leading to $H_{sred}H^+$ ("superreduced" state) featuring a $[4Fe\text{-}4S]_H^+$ cluster.

Table 3.1 FTIR ligand vibrations in the H_{red} and $H_{red}H^+$ state.

state	FTIR ligand vibrations / cm^{-1}			
	CN^-	CO	CO	μCO
H_{red}	2083/2067	1962	1933	1791
$H_{red}H^+$	2071/2032	1968	1914	1891

The individual selected marker bands of each of the four redox states (H_{ox}, H_{red}, $H_{red}H^+$, $H_{sred}H^+$) observed, e.g. 1933 cm^{-1} for H_{red} were plotted against the applied potential. Based on the model in figure 21 and by taking E_2 and E_3 as "overdetermined" the six state model simplifies to a chain of equilibria: $H_{ox}H^+ \rightleftharpoons H_{ox} \rightleftharpoons H_{red} \rightleftharpoons H_{red}H^+ \rightleftharpoons H_{sred}H^+ \rightleftharpoons H_{sred}$.

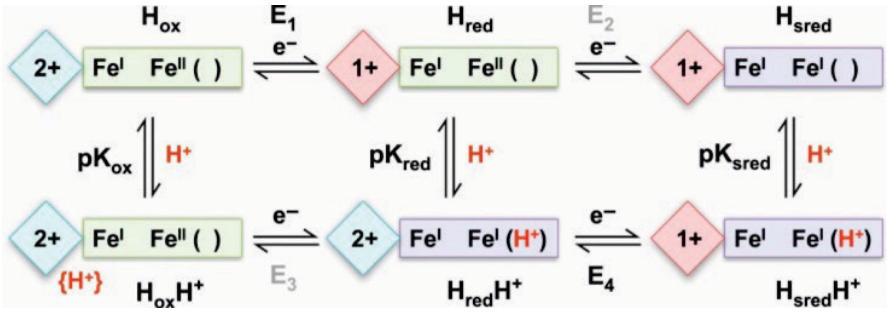

Figure 21 Equilibrium model with six states. It shows horizontally electron transfers with corresponding midpoint potentials E_1 to E_4 and vertically (de-) protonation events with pK_a values.

Based on this model the data obtained by FTIR-spectroelectrochemistry could be fitted to obtain the midpoint potentials. The equilibria are pH and potential dependent. By the fitting the midpoint potential of H_{ox}/H_{red} transition was found to be -375±10 mV and for the $H_{red}H^+/H_{sred}H^+$ transition -418±10 mV vs. SHE. Thus both redox events occur close to the H^+/H_2 potential (-400 mV assuming 1 bar H_2) what provides a smooth energy landscape throughout the catalytic cycle enabling the fast turnover rate that is observed for [FeFe] hydrogenases.

3.2 Paper II: Chalcogenide substitution in the [2Fe] cluster of [FeFe]-hydrogenases conserves high enzymatic activity

Modifications in the active site of [FeFe] hydrogenases are used to explain structure-function relationship and to design hydrogenases with higher activity.

In this work the synthesis of the selenium instead of sulfur containing precursor complex of the active site is presented. The $[Fe_2(\mu(SeCH_2)_2NH)(CO)_4(CN)_2]^{2-}$ precursor abbreviated in analogy to the „native“ precursor [2Fe]-ADSe. For the synthesis of the hexacarbonyl precursor a benzyl carbamat (Cbz) protection group was needed that could be removed later on. The deprotected selenium containing hexacarbonyl precursor was studied with cyclic voltammetry (CV) revealing a fully reversible redox chemistry with the same overpotential for H_2 formation but with an increased catalytic current compared to the sulfur containing hexacarbonyl precursor. Starting from this compound, the dicyanide containing [2Fe]-ADSe could be generated for the first time.

The [2Fe]-ADSe precursor complex was used in artificial maturation for the [FeFe] hydrogenases *Cp*I from *Clostridium pasteurianum* and HydA1 from *Chlamydomonas reinhardtii*, resulting in modified enzymes showing full activity in solution assays as compared to the native systems. The modification of sulfur to selenium in the two iron site is the first that does not lead to an activity loss (compare chapter 1.2.3). The presence of the two seleniums was confirmed by X-ray structure analysis. The anomalous electron density of Se was observed and a X-ray absorption scan over the theoretical K-edge of selenium resulted in a peak with only minor deviation to the theoretical value of 12,666 eV.

FTIR analysis proved the incorporation of the [2Fe]-ADSe into the protein matrix by significantly smaller line width due to the rigidity of the protein matrix compared to the [2Fe]-ADSe complex in solution (see chapter 2.4.3). The maturated enzymes are instable and show the tendency to rest in the H_{ox}-CO state. All ligand vibrations in *Cp*I-ADSe compared to

*Cp*I-ADT are red shift by 4 to 11 cm^{-1}. These red shifts are attributed to the increased electron density at the iron atoms which leads to stronger π-backbonding to the CO and CN^- ligands. A less pronounced red shift is observed for the CN^- ligands since they are less good π-acceptor than the CO ligands.

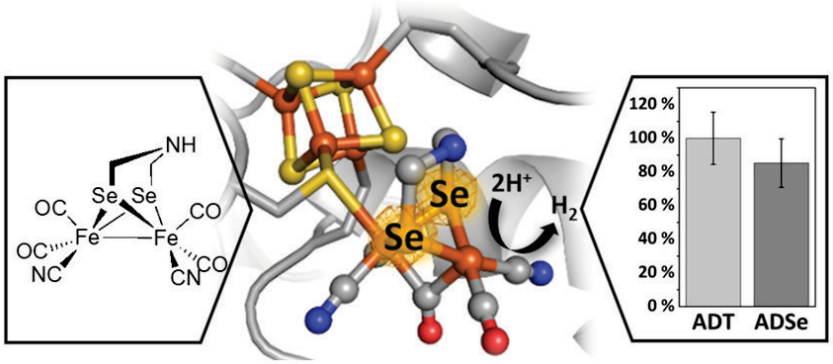

Figure 22 Cover art showing the synthesized selenium containing precursor on the left, the X-ray structure with anomalous electron density from selenium in the middle and the compared activity with the native system (ADT) measured on solution in the right.

With CV it could be shown that *Cp*I-ADSe is biased towards hydrogen production. Unfortunately the maturated enzyme cannot be thawed without losing activity. The degradation induced by oxygen is one major issue in biotechnological applications of [FeFe] hydrogenase. To analyze if the selenium containing active site in *Cp*I is more resistant to oxygen than the native *Cp*I, chronoamperometry (CA) at -39 mV vs. SHE with oxygen perturbation (see chapter 2.6.3) was performed. Already with the first addition of 13.4 µmol/L O_2, *Cp*I-ADSe loses about 75 % of its initial activity whereas the native enzyme loses only 25 %. Interestingly the protein film is more stable with *Cp*I-ADSe, as well as HydA1-ADSe compared to the corresponding native enzymes.

Within this publication it was shown that modifications within the two iron site do not unavoidably result in a loss of enzyme activity. The sulfur to selenium exchange was introduced as a promising modification in the two iron site for further [FeFe] hydrogenase studies.

3.3 Paper III: ^{1}H NMR Spectroscopy of [FeFe] Hydrogenases: Insight into the Electronic Structure of the Active Site

The [FeFe] hydrogenase HydA1 from *Chlamydomonas reinhardtii* in the apo- and the native form was studied with ^{1}H NMR spectroscopy at room temperature. For the first time hyperfine shifted proton signals originating from the iron coordinating cysteines and protons of the bridging ligand in the $[2Fe]_H$ site were detected for this class of enzymes. ^{1}H paramagnetic NMR spectroscopy is difficult to apply to HydA1 because of the large protein size. Additionally high concentrations (>1.2 mM) are necessary with samples volumes of about 400 µL. Improved yields in the overexpression (see chapter 2.1) as well as the finding of the artificial maturation are the basis for this publication. It opens a new field in [FeFe] hydrogenase research that will allow sequence specific assignments in the future.

The apo-hydrogenase, only containing the $[4Fe\text{-}4S]_H$ cluster, was studied in the oxidized and the reduced state revealing a bacterial ferredoxin-like behavior. Hyperfine shifted proton resonances with anti-Curie temperature dependence are detected in the otherwise diamagnetic oxidized state ($[4Fe\text{-}4S]^{2+}$ cluster) because low-lying higher spin states that are populated at room temperature. In the reduced state the proton signals show the typical line broadening arising from the interaction with the paramagnetic total spin state of S= 1/2. Two of the observed peaks show Curie and two anti-Curie temperature dependence.

Apo-HydA1 was artificially maturated with $[Fe_2(ADT)(CO)_4(CN)_2]^{2-}$. The analysis became more complex with the complete H-cluster that is a six iron containing system of the form $[4Fe\text{-}4S]_H$-$[Fe_p(I/II)\ (Fe_d(I/II)]$ in which the cubane is bridged by a cysteine residue to the two iron active site. Over this bridging cysteine the two sites are coupled what is characterized by the coupling constant j. Furthermore the stability of the redox state under investigation becomes more challenging. In this publication the H_{ox} and H_{ox}-CO state are studied. Both have an oxidized $[4Fe\text{-}4S]_H^{2+}$ cluster which features the two valence delocalized iron pairs $[2Fe]_A$ and $[2Fe]_B$ with S_A= 9/2 and S_B= 9/2 being antiferromagnetically coupled with a large

J_{Cube} to a diamagnetic S= 0 ground state. In both states the two iron site has a total spin of S_H= 1/2. (see fig. 23a). The coupling constant j between the cubane and the two iron site is, in general, much smaller than J_{Cube}. Nevertheless, the intercluster exchange coupling j induces spin mixing in the $[4Fe\text{-}4S]_H$ subcluster leading to substantial effective spin density at the formally diamagnetic cubane cluster and a reduced spin density at the $[2Fe]_H$ site.

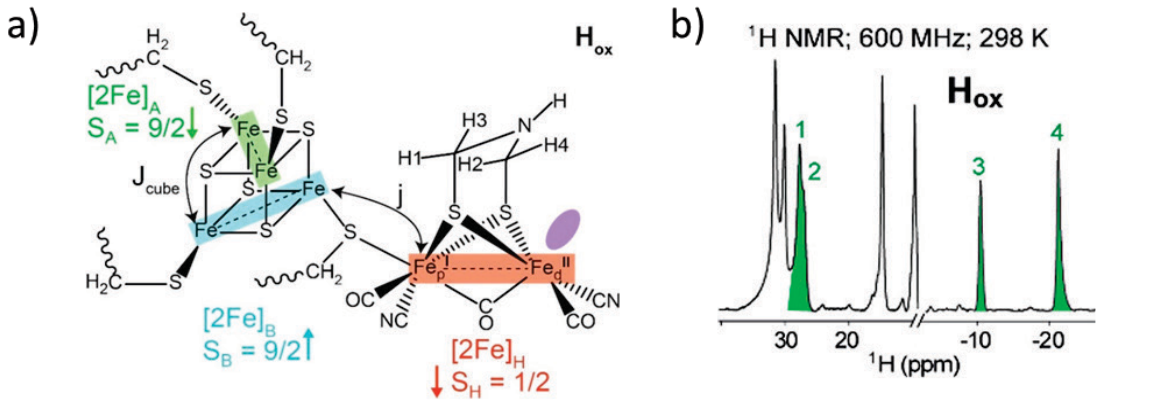

Figure 23 Schematic model of the H-cluster with β-CH_2 protons and protons of the ligand bridge in the H_{ox} state and the corresponding ^{1}H NMR spectrum. In a) the spins state of the two iron pairs and the two iron site with their orientations are indicated. In b) only the region containing the protons of the ligand bridge of the two iron site are shown and highlighted in green.

To unambiguously assign the protons of the ADT ligand bridge, deuterated ADT was used and 1D NOE spectra of HydA1-PDT (using a different precursor complex with -CH_2 instead of –NH bridgehead) in the H_{ox} state were recorded. Both lead to the assignment of the equatorial protons being the upfield shifted protons 3+4 and the axial protons, which are located close(er) to Fe_p, being the downfield shifted signals 1+2 (see fig. 23b).

In the H_{ox} state the chemical shifts of the β-CH_2 protons from the cubane cluster are larger than those recorded for the single $[4Fe\text{-}4S]_H^{2+}$ cluster which visualizes the intercluster exchange coupling j. In addition, two β-CH_2 resonances show a Curie temperature dependence (instead of four times anti-Curie as with the $[4Fe\text{-}4S]_H^{2+}$ cluster).

In the H_{ox}-CO state j is four times larger than in the H_{ox} state[48] leading to a higher effective spin density in the $[4Fe\text{-}4S]_H$ subcluster. The protons 1+2, pointing towards the $[4Fe\text{-}4S]_H$ cluster, show more pronounced downfield shifts, while the chemical shifts of the protons 3+4 become less negative.

This work shows the first ^1H NMR experiments at room temperature on a [FeFe] hydrogenase. The properties of the active site were explored and provide a solid basis for further investigations of other catalytic states using mutants or other variants. Especially the assignment of the proton signals 1-4 gives the possibility to study the spin density at four positions within the two iron site.

3.4 Paper IV: Spectroscopic Investigations of a Semi-Synthetic [FeFe] Hydrogenase with Propane-di-selenol as Bridging Ligand in the Bi-nuclear Subsite

Encouraged by the results of publication II, we established a system with more stable redox states to study the effect of the chalcogenic exchange spectroscopically. Additionally, the S-to-Se substitution is performed in the $[4Fe\text{-}4S]_H$ cluster via reconstitution of the apo-hydrogenase. A systematic knowledge about structural and electronic changes within the H-cluster upon substitutions is necessary to design improved hydrogenases and catalysts.

The iron precursor complex with propane-dithiolate bridge, [2Fe]-PDT ($[Fe_2(\mu(CH_2\mathbf{S})_2(CO)_4(CN)_2]^{2-}$) can be incorporated into HydA1 from *Chlamydomonas reinhardtii* and is known for its two stable redox states H_{ox} and H_{red}.[35] Therefore we decided to establish the synthesis of the selenium exchanged precursor which is named [2Fe]-PDSe (propane-diselenate). HydA1 could be maturated with [2Fe]-PDSe so that we could study the exact S-to-Se effect in terms of charge (FTIR, FTIR-spectroelectrochemistry) and spin density distribution (EPR, ^{1}H NMR) in the H-cluster. Furthermore the $[4Fe\text{-}4Se]_H$ apo-HydA1 was studied with EPR and ^{1}H NMR in comparison to the natural $[4Fe\text{-}4S]_H$ apo-enzym.

For the selenium containing enzyme HydA1-PDSe, the FTIR vibrations in the two redox states are red shifted by about -8 cm^{-1} compared to HydA1-PDT due to the lower electronegativity of Se. In the reductive titration a slightly more negative midpoint potential for the H_{ox}/H_{red} transition was found, reflecting a higher electron density in HydA1-PDSe compared to HydA1-PDT. In HydA1-PDSe an additional state was observed which is identified as the oxidized CO inhibited state and shows a rhombic EPR spectrum (see fig. 24). The much larger spin orbit contribution of Se shifts the signal to higher g-values compared to the native system since HydA1-PDT lacks this state.

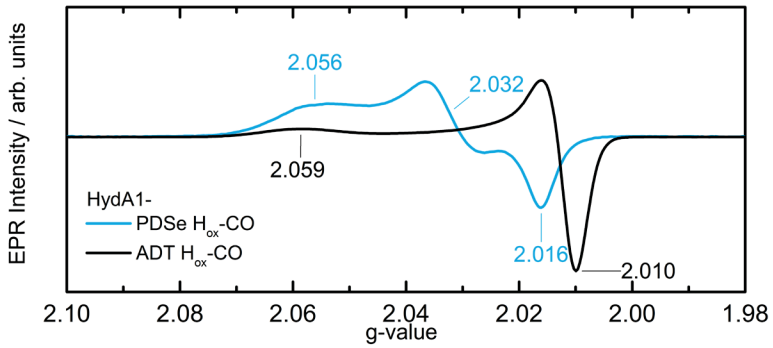

Figure 24 Superimposed CW EPR spectra of HydA1-ADT H_{ox}-CO and HydA1-PDSe H_{ox}-CO. The HydA1-PDSe sample in the H_{ox}-CO state shows a rhombic signal unlike the known axial signal of HydA1-ADT H_{ox}-CO. Spectra are taken at 20 K.

The ^{1}H NMR spectrum of HydA1-PDSe in comparison to HydA1-PDT shows a reduced spin density for the resonating protons related to the $[4Fe\text{-}4S]_H$ and for the ones in the ligand bridge. The reconstitution of the apo-hydrogenase with a $[4Fe\text{-}4Se]_H$ cluster was confirmed and studied by ^{1}H NMR spectroscopy. The oxidized cubane (two Fe(II)Fe(III) pairs, antiferromagnetically coupled) has formally a S= 0 ground state. The contact shifted β-CH_2 protons of the cysteines coordinating the $[4Fe\text{-}4Se]_H$ show larger downfield shifts than in the $[4Fe\text{-}4S]_H$ analogue. The S-to-Se substitution in the cubane cluster apparently reduces the antiferromagnetic coupling between the iron pairs somewhat bringing the excited states closer leading to stronger magnetic interactions. The resonances of the reduced $[4Fe\text{-}4Se]_H$ cluster are broadened beyond detection alluding to a higher spin state.

With CW EPR spectroscopy S= 7/2 and S= 3/2 spin states were observed. From the temperature dependence a zero field splitting constant of D= -1.07 cm^{-1} was estimated. In the literature it is assumed that the occurrence of high spin components of the Se substituted cubane cluster is related to its coordination environment which is modulating the intra-cluster exchange coupling(s) since modifications in the environment lead to a spin cross over.[113] This cross over is observed for $[4Fe\text{-}4Se]_H$ HydA1-PDT and –ADT.

3.5 Paper V: Direct Detection of the Terminal Hydride Intermediate in [FeFe] Hydrogenase by NMR Spectroscopy

Hydrogen production catalyzed by [FeFe] hydrogenases involves an intermediate state in which a proton and an electron are stored as a hydride bound to the Fe_d of the active site. So far this terminal iron bound hydride state could only be inferred from redox coupled changes in the FTIR spectra of the H-cluster at ambient temperatures. More recently, the Fe-H bending mode could also be detected using Nuclear Resonance Vibrational Spectroscopy but only at low temperature in frozen solution. Here, we present the first successful detection of the hydride ^{1}H NMR resonance of the key intermediate of an [FeFe] hydrogenase in solution at room temperature.

^{1}H NMR spectroscopy is applied to a mutant of HydA1 from *Chlamydomonas reinhardtii* C169A, which is easily trapped in the hydride state due the interrupted proton transfer pathway to the active site. This mutant was maturated with $[Fe_2(ADT)(CO)_4(CN)_2]^{2-}$ and with a deuterated bridging ADT ligand (^{2}H-adt) (see fig. 25). FTIR spectra confirmed that in aqueous solution the hydride state is formed. In the samples of the non-labeled bridge the buffer exchange to 100 % D_2O revealed that signal **g** at -1.9 ppm and signal **j** at -9.6 ppm are solvent exchangeable. By comparison of HydA-C169A-^{2}H-adt to the unlabeled sample, the axial and equatorial protons of the bridging ligand could be identified. Signal **g** most likely arises from the bridgehead amine group, and not as it could be possible from an amino acid residue nearby, since in the H_{ox}-CO inhibited sample a buffer exchange to D_2O does not lead to a signal loss of **g**.

Signal **j** is assigned with high confidence to the terminal bound hydride .due to its pronounced upfield shift that is even strong than in model complexes.

The larger shift could be related to the protein surrounding which is missing in the analogous model compounds. We suggest that the second coordination sphere has not only a stabilizing

effect on the H-cluster but also an activating effect by increasing the negative spin density of the terminal hydride rendering it more reactive towards protons when compared to the reported biomimetic complexes.

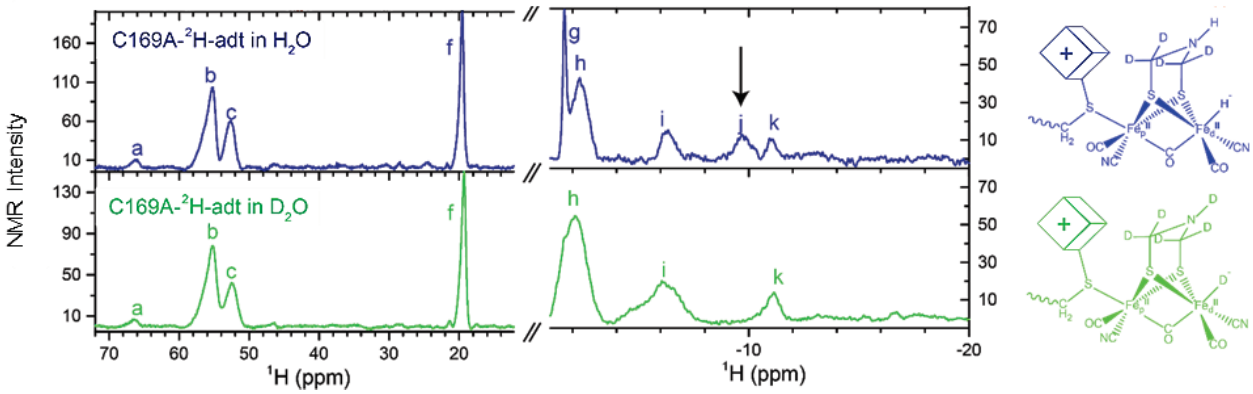

Figure 25 Down- and upfield region of the ^{1}H 1D NMR spectra (600 MHz, 298 K) of HydA1-C169A maturated with $[Fe_2(^{2}H\text{-adt})(CO)_4(CN)_2]^{2-}$ in H_2O (blue) and 100 % D_2O (green). Sample concentrations are between 1.2−1.4 mM.

3.6 Paper VI: The [RuRu] analogue of [FeFe] hydrogenase traps the key metal bound hydride intermediate in the enzyme's catalytic cycle

Many different semi-synthetic [FeFe] hydrogenases have been studied with the help of artificial maturation in recent years (see chapter 1.2.3). All of the used modified precursors were based on the binuclear iron core and modifications were only introduced to the bridging ligand and the CO and CN^- ligands or as shown in the journal articles II and IV, sulfur was exchanged to selenium. In this work, it is shown for the first time that both irons in the binuclear subcluster can be substituted with ruthenium. Two precursor complexes were used in the maturation experiments: $[Ru_2(XDT)(CO)_4(CN)_2]^{2-}$ where XDT represents ADT or PDT. Both complexes were predissolved in DMSO and incubated with apo-HydA1 from *Chlamydomonas reinhardtii* (in aqueous buffer). The maturation process could be followed using FTIR and indicated that the [2Ru] analogues were successfully incorporated forming a [RuRu] hydrogenase. The obtained [RuRu] hydrogenases show that the irons play no decisive role in the incorporation during artificial maturation (see chapter 1.2.1). This is not true for the catalytic activity, since both hydrogenase variants are inactive.

The dominant species for both ADT and PDT based subclusters is the one in which a terminal hydride is bound to the open coordination site, i.e. the key intermediate in the catalytic cycle. It is known that the precursors $[Ru_2(XDT)(CO)_4(CN)_2]^{2-}$ are rapidly protonated in aqueous solution forming a bridging hydride as apparent from the characteristic blue shifts of the CO and CN^- stretches in FTIR. To verify if a [2Ru] subcluster with bridging hydride could also be accommodated in the protein, we incubated apo-HydA1 with both precursors $[(\mu H)Ru_2(XDT)(CO)_4(CN)_2]^-$ (pre-dissolved in H_2O). Interestingly, the same terminal hydride state is formed as was observed in the experiments with unprotonated precursors (pre-dissolved in DMSO). This shows that the protein surrounding in HydA1 enforces the formation of the catalytically competent terminal hydride and prevents "rotation" to the thermodynamically more stable bridging hydride. By H/D exchange it could be shown

through monitoring the frequency of the μCO stretch that in both variants a terminal hydride is bound to the distal ruthenium. This vibration is coupled to that of the metal hydride but not in the corresponding metal deuteride. Therefore, H/D exchange of the hydride has a profound effect on the μCO stretch (blue shift of +10 cm^{-1}) while leaving all other CN^- and CO vibrations unaffected. The μCO shift upon D_2O buffer exchange was only observed for the ADT containing $[2Ru]_H$ subcluster and not for the PDT variant. H/D exchange for the PDT containing $[2Ru]_H$ subcluster could, however, be accomplished by maturating apo-HydA1 in D_2O under D_2 atmosphere. This finding shows that the terminal hydride in [FeFe] hydrogenase is only accessible through the NH amine function in the ADT bridge. Indeed, the HydA1-$[2Ru]_H$-ADT variant shows, apart from the hydride state, an additional species (see fig. 26) that was assigned to a state which lacks the terminal hydride but is probably protonated in the ADT bridge. This protonated reduced species could be in rapid exchange with the terminal hydride and might connect this species to the proton transport pathway of the protein.

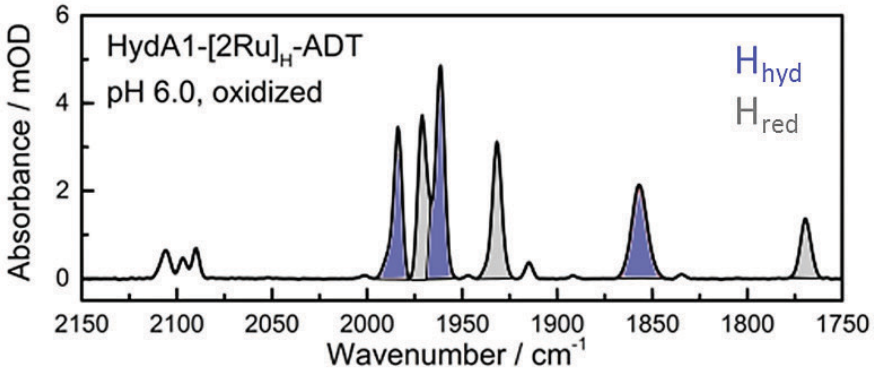

Figure 26 FTIR spectrum of HydA1-$[2Ru]_H$-ADT at pH 6.0 under oxidizing conditions. Purple colored peaks arise from the CO ligands in the hydride state H_{hyd}, grey deposited peaks belong to the CO ligands in the reduced state H_{red}. The spectrum is recorded at 298 K with a resolution of 2 cm^{-1}.

4. JOURNAL ARTICLES

4.1 Paper I

Proton Coupled Electronic Rearrangement within the H-Cluster as an Essential Step in the Catalytic Cycle of [FeFe] Hydrogenases

C. Sommer, A. Adamska-Venkatesh, K. Pawlak, J.A. Birrell, O. Rüdiger, E.J. Reijerse, and W. Lubitz

J. Am. Chem. Soc., 2017, 139, 1440–1443

DOI: 10.1021/jacs.6b12636

Journal: Journal of the American Chemical Society

Author: First Author

Contribution: 60 %

- I prepared all biological samples

- I measured the activity a different pH values

- I tested the used mediators in cyclovoltammetry in the used pH range

- I measured and processed all FTIR-spectroelectrochemistry experiments

- I was involved in interpreting the data and in writing the manuscript

K. Pawlak, J.A. Birrell and E. Reijerse did the data fitting; O. Rüdiger measured the ATR experiments. All others discussed the results and were involved in writing the manuscript.

JACS
JOURNAL OF THE AMERICAN CHEMICAL SOCIETY
Communication
pubs.acs.org/JACS

Proton Coupled Electronic Rearrangement within the H-Cluster as an Essential Step in the Catalytic Cycle of [FeFe] Hydrogenases

Constanze Sommer, Agnieszka Adamska-Venkatesh, Krzysztof Pawlak, James A. Birrell, Olaf Rüdiger, Edward J. Reijerse,* and Wolfgang Lubitz*

Max-Planck-Institut für Chemische Energiekonversion, Stiftstrasse 34-36, 45470 Mülheim/Ruhr, Germany

Supporting Information

ABSTRACT: The active site of [FeFe] hydrogenases, the H-cluster, consists of a [4Fe−4S] cluster connected via a bridging cysteine to a [2Fe] complex carrying CO and CN^- ligands as well as a bridging aza-dithiolate ligand (ADT) of which the amine moiety serves as a proton shuttle between the protein and the H-cluster. During the catalytic cycle, the two subclusters change oxidation states: $[4Fe{-}4S]_H^{2+} \Leftrightarrow [4Fe{-}4S]_H^{+}$ and $[Fe(I)Fe(II)]_H \Leftrightarrow [Fe(I)\text{-}Fe(I)]_H$ thereby enabling the storage of the two electrons needed for the catalyzed reaction $2H^+ + 2e^- \rightleftarrows H_2$. Using FTIR spectro-electrochemistry on the [FeFe] hydrogenase from *Chlamydomonas reinhardtii* (*Cr*HydA1) at different pH values, we resolve the redox and protonation events in the catalytic cycle and determine their intrinsic thermodynamic parameters. We show that the singly reduced state H_{red} of the H-cluster actually consists of two species: $H_{red} = [4Fe{-}4S]_H^{+} - [Fe(I)Fe(II)]_H$ and $H_{red}H^+ = [4Fe{-}4S]_H^{2+} - [Fe(I)Fe(I)]_H$ (H^+) related by proton coupled electronic rearrangement. The two redox events in the catalytic cycle occur on the $[4Fe{-}4S]_H$ subcluster at similar midpoint-potentials (−375 vs −418 mV); the protonation event ($H_{red}/H_{red}H^+$) has a $pK_a \approx 7.2$.

Hydrogenases catalyze the conversion of protons and electrons into molecular hydrogen (H_2) using the abundant metals Ni and/or Fe in their active site.[1] [FeFe] hydrogenases are particularly active in both hydrogen production (up to 8700/s) and oxidation (up to 150 000/s).[2,3] The active site of these enzymes, the "H-cluster", is composed of a "classical" cubane [4Fe−4S] cluster and a unique [2Fe] cluster coordinated by three CO and two CN^- ligands as well as an aza-dithiolate (ADT) ligand bridging the two iron atoms. The two subclusters are connected through a bridging cysteine side group coordinating $[4Fe{-}4S]_H$. The iron of the $[2Fe]_H$ subsite distal to $[4Fe{-}4S]_H$, Fe_d, is five-coordinate in most redox states and has an open coordination site where substrates (H_2 and protons) as well as inhibitors (e.g., CO) can bind (Figure 1). The amino headgroup of the ADT ligand is assumed to serve as a Brønsted base that shuttles protons between the open coordination site and the proton channel of the enzyme.[1] Three well characterized redox states of the H-cluster are postulated to play a role in the catalytic cycle:[4] $H_{ox} \rightleftarrows H_{red} \rightleftarrows H_{sred}$. Although H_{ox} and H_{red} are observed both in bacteria and algae,[5] H_{sred} is best characterized in algae.[4] The oxidized state H_{ox} is characterized by a mixed valence binuclear subsite: Fe(I)Fe(II) and an oxidized cubane subcluster $[4Fe{-}4S]_H^{2+}$.[6]

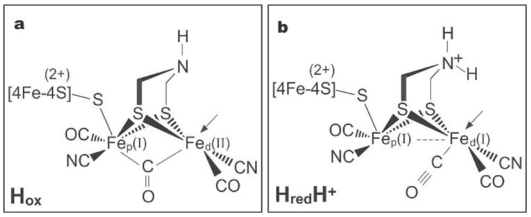

Figure 1. Structure of the H-cluster in the H_{ox} and the protonated reduced state $H_{red}H^+$.[7,8] The arrow indicates the open coordination site where hydrogen, CO and oxygen species can bind.

The reduced state H_{red} features a homovalent $[2Fe]_H$ subsite, Fe(I)Fe(I),[6] whereas a second reduction leads to the "superreduced" state H_{sred} in which the cubane subcluster is also reduced $[4Fe{-}4S]_H^{+}$.[4] In addition, the H_{ox} and H_{red} states can also bind an extrinsic CO ligand leading to the inhibited states H_{ox}−CO and H_{red}−CO.[9] Under strongly reducing conditions as well as in a mutant in which the proton transfer pathway has been blocked, the enzyme shows an FTIR signature assigned to a putative hydride state featuring an oxidized $[2Fe]_H$ core, Fe(II)Fe(II), and a terminal hydride bound to Fe_d.[10] The ordering of protonation and redox steps in the catalytic mechanism has been frequently discussed but remains largely speculative.[4,11] By studying the [FeFe] hydrogenase from *Chlamydomonas reinhardtii* (*Cr*HydA1) using pH dependent FTIR spectro-electrochemistry, we were able to resolve the redox and protonation events in the catalytic cycle. We show that the active reduced state H_{red} occurs in both protonated and unprotonated states, each with a different electronic configuration. Our spectro-electrochemical titrations allow the extraction of the intrinsic redox potentials (assuming Nernst-like behavior) as well as the pK_a for the $H_{red}/H_{red}H^+$ protonation event. These new data strongly support an "internal" PCET step connecting H_{red} and $H_{red}H^+$ and add new essential details to our understanding of the catalytic cycle.

Samples of *Cr*HydA1 were prepared[12] at pH 6.0, 7.0, 8.0, 9.0, and 10.0 showing pH dependent hydrogen production up to 600/s (700 μmol H_2/(min·mg) (see Figures S1−2). These samples were characterized using FTIR spectro-electrochemical experiments in the range −650 to −200 mV vs standard hydrogen electrode (SHE) at 288 K. Figure 2A shows FTIR

Received: December 8, 2016
Published: January 11, 2017

DOI: 10.1021/jacs.6b12636
J. Am. Chem. Soc. 2017, 139, 1440−1443

spectra at pH values and potentials highlighting the different species occurring during the electrochemical titrations.

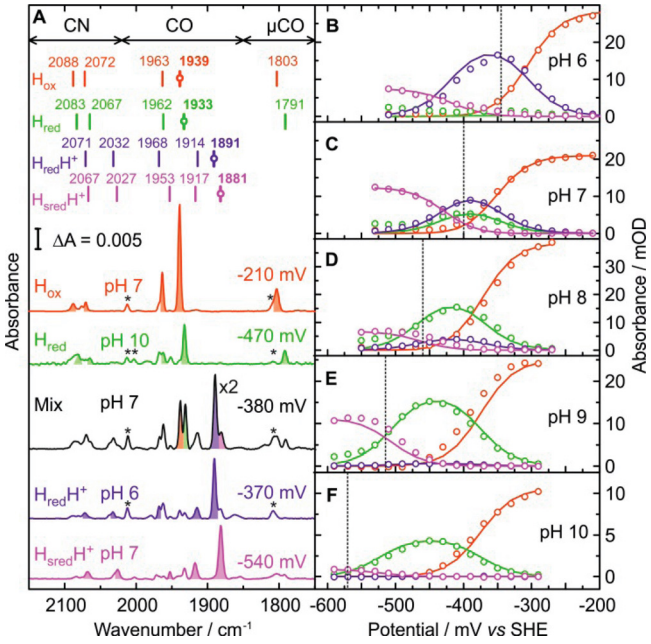

Figure 2. (A) Selected FTIR spectra recorded at optimal pH and potential, T = 288 K. (B–F). FTIR spectro-electrochemical data obtained for reductive titrations for the observed states H_{ox} (1939 cm^{-1}), H_{red} (1933 cm^{-1}), $H_{red}H^+$ (1891 cm^{-1}), $H_{sred}H^+$ (1881 cm^{-1}) at different pH. The characteristic band frequencies for each state are indicated above the spectra. The asterisks indicate the most prominent band positions of the $H_{ox/red}$–CO state that is present in small amounts in most preparations (see Figure S3–4). The dotted black lines represent the equilibrium H^+/H_2 potentials at 1 bar (100%) H_2 at each pH value (see Figure S5). The solid lines (same color code as in panel A) represent a least-squares fit to the model depicted in Figure 3. The optimized fit parameters are $pK_{ox} < 5$, $pK_{red} = 7.2 \pm 0.2$, $pK_{sred} = 9.1 \pm 0.4$, $E_1 = -375 \pm 10$ mV, $E_4 = -418 \pm 10$ mV. $E_2(H_{red}/H_{sred}) = -527 \pm 10$ mV and $E_3(H_{ox}H^+/H_{red}H^+) > -250$ mV.

It turned out that the bands at 1891 and 1933 cm^{-1}, previously assigned to the active reduced state H_{red} in *Cr*HydA1,[13] actually belong to two separate reduced states one of which (H_{red} identified by the 1933 cm^{-1} band) is dominating at pH 10 whereas the other (identified by the 1891 cm^{-1} band) reaches its maximum amplitude near pH 6. At neutral pH, both bands are visible and show identical behavior as a function of the electrochemical potential (see Figure 2C,D) which is the reason that these were originally assigned to one species.[4,9,13] We assume that the newly identified H_{red} state is protonated and refer to it as $H_{red}H^+$.

It now becomes apparent that the H_{red} state observed at pH 10 and identified by the CO stretches 1962, 1933, 1791 cm^{-1} shows great similarity with the reduced state previously observed in *Cr*HydA1-PDT,[9] i.e., a variant of *Cr*HydA1 in which the ADT ligand has been replaced with propanedithiolate (PDT) containing a methylene group instead of the amine moiety. *Cr*HydA1-PDT shows only two redox states: H_{ox}(PDT) which is almost identical in electronic structure and FTIR spectrum to the native H_{ox}(ADT) state and H_{red}(PDT) which corresponds to the native H_{red}(ADT) state identified in the current study. It can be argued that both H_{red}(PDT) and H_{red}(ADT) are characterized by a $[4Fe–4S]^+_H$ – [Fe(I)Fe(II)] configuration due to the very small red shift (3–7 cm^{-1}) of the CO bands with respect to H_{ox}(PDT/ADT), which suggests the reduction event cannot take place at the binuclear subsite.[9] In contrast, the *Cr*HydA1 $H_{red}H^+$ state observed at pH 6 is identified by the characteristic bands 1968, 1914, 1891 cm^{-1} associated with the H_{red} state previously observed for the [FeFe]-hydrogenase from *Desulfovibrio desulfuricans* (*Dd*HydAB).[14] The redox states of the H-cluster in *Dd*HydAB have been originally analyzed by Mössbauer spectroscopy[6] indicating a homovalent $[2Fe]_H$ configuration in H_{red} and an oxidized $[4Fe–4S]^{2+}_H$ subcluster. The loss of the bridging CO band in FTIR as well as the large red shift of most of the CO stretches indicates that the $[2Fe]_H$ subsite has been reduced to a homovalent [Fe(I)Fe(I)] configuration.[15,16] The transition from H_{red} to $H_{red}H^+$, therefore, involves electron transfer from the $[4Fe–4S]_H$ subcluster to the $[2Fe]_H$ subsite. Since the $H_{red}H^+$ state is only dominant at low pH, it is justified to assume that this internal electron transfer is coupled to a protonation step, presumably at the ADT ligand. This process is not a "classical" PCET reaction[17] because the electron transfer occurs within the H-cluster as an electronic rearrangement. An early DFT study by Yu et al. of the FTIR signatures of the various H-cluster states in different organisms had already pointed out that the H_{red} state reported in *Cr*HydA1 could actually consist of two species, possibly related to an electron transfer step between the two subclusters.[18] This suggestion has been validated experimentally in our current study. Furthermore, a recent low temperature Resonance Raman study on *Cr*HydA1 reported that the protonated H_{red} state can be transiently photoexcited to the unprotonated form (referred to as Hred').[19]

Proton coupled electronic rearrangement from H_{red} to $H_{red}H^+$ prepares the H-cluster for a second reduction. This reduction again takes place at the $[4Fe–4S]_H$ subcluster affording the superreduced state that we assume to be protonated at neutral pH (i.e., $H_{sred}H^+$). Taking into account two reduction steps and one protonation event we arrive at the six-state scheme of equilibria[17] (Figure 3) characterized by

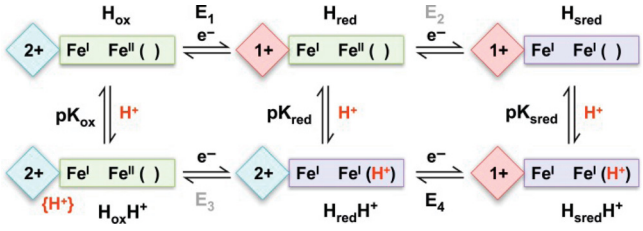

Figure 3. Equilibrium model used to analyze the pH dependent FTIR spectro-electrochemical data of *Cr*HydA1. Parameters E_2 and E_3 are taken as "overdetermined" and are calculated from the other equilibrium constants (see text and SI). The protonation of the different states is indicated by "(H^+)". For $H_{red}H^+$ and $H_{sred}H^+$, we assume that the ADT bridge is protonated.

midpoint potentials E_1...E_4 and pK_a values: pK_{ox}, pK_{red}, and pK_{sred}. Because the equilibria are interdependent not all parameters can be chosen freely. If we choose E_2 and E_3 as "overdetermined", the set of equilibria simplifies to a linear chain: $H_{ox}H^+ \rightleftarrows H_{ox} \rightleftarrows H_{red} \rightleftarrows H_{red}H^+ \rightleftarrows H_{sred}H^+ \rightleftarrows H_{sred}$ and E_2 and E_3 can be calculated from the other parameters:

$$E_3 = E_1 - \ln(10)(pK_{ox} - pK_{red})(RT)/F \quad (1)$$

DOI: 10.1021/jacs.6b12636
J. Am. Chem. Soc. 2017, 139, 1440–1443

$$E_2 = E_4 - \ln(10)(pK_{sred} - pK_{red})(RT)/F \quad (2)$$

where F is Faraday's constant, R is the gas constant, and T is the experimental temperature in Kelvin.

As explained in the SI, the calculations of the state fractions for this model, given the individual equilibrium constants, is straightforward. The equilibria between the various species are pH and potential dependent (Figure 2B–F). The FTIR spectra, however, only allow four species to be distinguished: H_{ox}, H_{red}, $H_{red}H^+$, and $H_{sred}H^+$. Protonation of the H_{ox} and H_{sred} states might induce slight changes in the electronic structure of the H-cluster leading to a blue shift (≈10 cm^{-1}) of the CO bands similar to what was reported for the putative hydride state.[10] The absence of additional $H_{ox}H^+$ and H_{sred} species in our FTIR spectra recorded in the range of pH 6.0–10.0 would suggest that pK_{ox} < 6 and pK_{sred} > 10. However, the separate observation of protonated and unprotonated species is not relevant for full modeling of the experimental data with the six-state scheme (Figure 3).[20] Catalytic H_2 production at negative potentials may cause deviations from the equilibrium scheme suggested in Figure 3. As addressed in the SI, this deviation will in particular affect the extracted potential associated with the H_{sred} state (E_4).

The fits to the equilibrium scheme are presented in Figure 2B–F with solid curves. It turns out that the midpoint potential for the H_{ox}/H_{red} transition is quite close to that of the $H_{red}H^+/H_{sred}H^+$ transition (i.e., E_1 = −375 ± 10 mV and E_4 = −418 ± 20 mV). This is not surprising because both transitions involve the same reduction event of the $[4Fe–4S]_H$ subcluster. Due to the deviation from equilibrium at low potentials (see SI), the fitted $|E_4|$ value will be overestimated and the difference between E_1 and E_4 becomes even smaller.

The pH dependence of the H_{ox}/H_{red} and H_{red}/H_{sred} transitions is mainly determined by the $H_{red}/H_{red}H^+$ protonation event modeled with a pK_{red} = 7.2 ± 0.2. Due to the limited available pH range (6.0–10.0), the pK_{ox} parameter could adopt a range of values (pK_{ox} = 1.0–5.0).

The spectro-electrochemical experiments in Figure 2B–F can also be fitted individually for every pH to the three-state model previously used to extract the midpoint potentials $E(H_{ox}/H_{red})$ and $E(H_{red}/H_{sred})$, where H_{red} represents the sum of both reduced states[9,13,14] The individual fits are presented in figure S6 (SI) and the extracted potentials are summarized in Figure 4 (inset and data points). The pH dependence of the three-state midpoint potentials $E(H_{ox}/H_{red})$ and $E(H_{red}/H_{sred})$ can be calculated from the six-state parameters (pK_{ox}, pK_{red}, pK_{sred}, E_1…E_4) combined with the pH value.[20]

$$E(H_{ox}/H_{red}) = E_1 - \frac{RT}{F}\ln\left\{\frac{1 + 10^{(pKox-pH)}}{1 + 10^{(pKred-pH)}}\right\} \quad (3)$$

$$E(H_{red}/H_{sred}) = E_2 - \frac{RT}{F}\ln\left\{\frac{1 + 10^{(pKred-pH)}}{1 + 10^{(pKsred-pH)}}\right\} \quad (4)$$

Figure 4 shows that for extreme pH values the midpoint potentials reach plateau values at the "intrinsic" midpoint potentials E_1, E_2, E_3, and E_4. Because the value for E_3 is dependent on pK_{ox}, which is poorly defined, this plateau value is also inaccurate as demonstrated by the multiple curves calculated for different pK_{ox} all fitting the data satisfactorily (inset and data points). Figure 4 shows that the difference between $E(H_{ox}/H_{red})$ and $E(H_{red}/H_{sred})$ is smallest when the pH is close to the pK_{red} value (7.2). This may explain why for

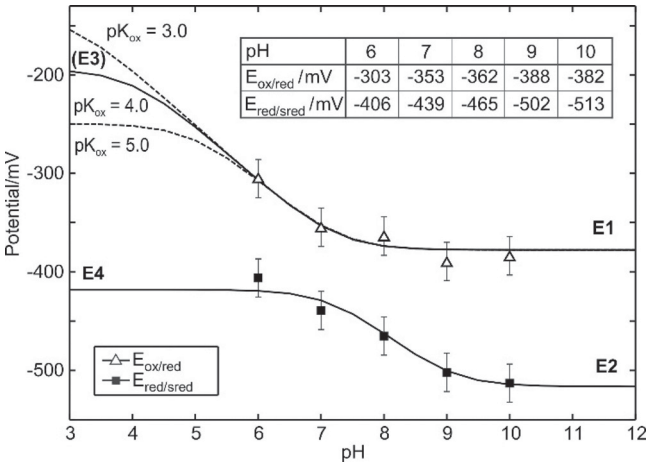

pH	6	7	8	9	10
$E_{ox/red}$ /mV	-303	-353	-362	-388	-382
$E_{red/sred}$ /mV	-406	-439	-465	-502	-513

Figure 4. Experimental pH dependence of the three-state $E_{ox/red}$ and $E_{red/sred}$ midpoint potentials as determined by the fits in Figure S6 (symbols and inset table) as compared to the pH dependence based on the six-state model (Figure 3) and eqs 1–4. For pK_{ox}, only the upper limit (<5.0) can be given. Fit parameters: pK_{red} = 7.2 ± 0.2, pK_{sred} = 9.0 ± 0.2, E_1 = −377 ± 10 mV, E_4 = −417 ± 10 mV. E_2 = −520 mV (using eq 2). Using eq 1, we arrive at the plateau values for E_3 depending on the value of pK_{ox}.

*Cr*HydA1 the two midpoint potentials (at pH 8.0) are closer together (−362 and −465 mV) than for the [FeFe] hydrogenase of *D. desulfuricans* (−395 vs −540 mV).[14] Because at pH 8.0 the H-cluster of *Dd*HydAB almost exclusively shows the $H_{red}H^+$ species, its pK_{red} parameter must be substantially larger than 8.0.

The current FTIR spectro-electrochemical study on *Cr*HydA1 suggest that the first steps in the catalytic (proton reduction) cycle are characterized by a sequential "ECE" mechanism linking $H_{ox} + e^- \rightarrow H_{red} + H^+ \rightarrow H_{red}H^+ + e^- \rightarrow H_{sred}H^+$. However, kinetics under turnover may follow a different EC order at extreme pH values or potentials. The ECE mechanism is appealing because both redox events occur at a potential close to the equilibrium H^+/H_2 potential at pH 7 (≈ −400 mV assuming 1 bar H_2), and the proton transfer between the two H_{red} states has a pK_a of ≈7. This would provide a smooth energy landscape throughout the catalytic cycle, which is required for efficient reversible catalysis. The hydrogen exposure experiment described in the SI (Figure S5) confirmed that the enzyme is in equilibrium with both the H^+/H_2 couple and the electrode/mediators system at the corresponding potentials. As can be seen in Figure 2B–F, the potential at which the catalytically competent H_{sred} state starts to be populated is always close to the hydrogen potential with the best match at pH 7. This correlates nicely with the pH dependent activity of the enzyme (Figure S1).

Protonation of H_{red} triggers electronic rearrangement to form $H_{red}H^+$, probably through a charge neutralization effect. Such an event involving the $[4Fe–4S]_H$ subcluster has been previously described in a DFT study on the possible hydride states in the catalytic mechanism[21] as well as in a study on inorganic mimics of the H-cluster.[15] The current study provides the first experimental support of this mechanism. The updated working model of the catalytic cycle[4] is presented in Scheme 1.

We speculate that a similar internal PCET step is involved in the stabilization of the putative terminal hydride in the catalytic cycle upon binding of H_2 to H_{ox}. In such a scenario, H_2 is heterolytically split, the proton is captured in the ADT bridge

DOI: 10.1021/jacs.6b12636
J. Am. Chem. Soc. 2017, 139, 1440–1443

Scheme 1. Proposed Catalytic Cycle Including Proton Coupled Electronic Rearrangement between H_{red} and $H_{red}H^{+}$[a]

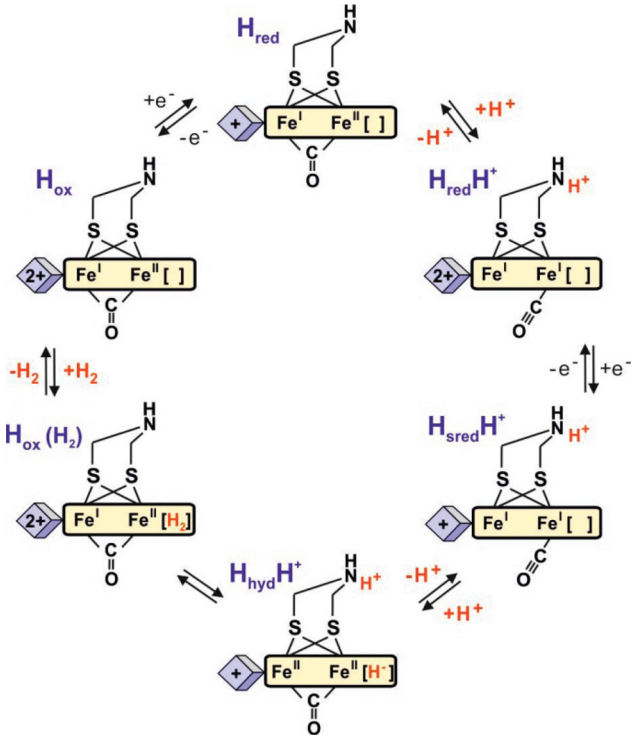

[a]A similar internal step is assumed upon H_2 formation/splitting between $H_{hyd}H^{+}$ and $H_{ox}(H_2)$.

while the hydride is stabilized on the distal iron of the $[2Fe]_H$ subsite in concert with electron transfer from $[2Fe]_H$ to $[4Fe–4S]_H$ (see Scheme 1 and Figure S7). Taking into account the highly conserved structure of the H-cluster in both bacterial and eukaryotic [FeFe] hydrogenases,[22] it is likely that the proton coupled electronic rearrangement described here is valid for all [FeFe] hydrogenases.

■ ASSOCIATED CONTENT

Supporting Information

The Supporting Information is available free of charge via the Internet at The Supporting Information is available free of charge on the ACS Publications website at DOI: 10.1021/jacs.6b12636.

Material and Methods; pH dependent enzyme activity; mediators used; FTIR bands overview; electrochemical titrations under equilibrium conditions; H_2 exposure experiment in ATR cell; treatment of a multiple-state chain of equilibria; three-state model; PCET as initial/final step in H_2 oxidation/production (PDF)

■ AUTHOR INFORMATION

Corresponding Authors

*Edward.Reijerse@cec.mpg.de
*Wolfgang.Lubitz@cec.mpg.de

ORCID

Wolfgang Lubitz: 0000-0001-7059-5327

Notes

The authors declare no competing financial interest.

■ ACKNOWLEDGMENTS

The authors thank Mr. Alaa Alsheikh Oughli for the synthesis of the −523 mV mediator (see SI). The Max Planck Society is gratefully acknowledged for financial support.

■ REFERENCES

(1) Lubitz, W.; Ogata, H.; Ruediger, O.; Reijerse, E. *Chem. Rev.* **2014**, *114*, 4081.
(2) Glick, B. R.; Martin, W. G.; Martin, S. M. *Can. J. Microbiol.* **1980**, *26*, 1214.
(3) Hatchikian, E. C.; Magro, V.; Forget, N.; Nicolet, Y.; Fontecilla-Camps, J. C. *J. Bacteriol.* **1999**, *181*, 2947.
(4) Adamska, A.; Silakov, A.; Lambertz, C.; Ruediger, O.; Happe, T.; Reijerse, E.; Lubitz, W. *Angew. Chem., Int. Ed.* **2012**, *51*, 11458.
(5) Adams, M. W. W. *Biochim. Biophys. Acta, Bioenerg.* **1990**, *1020*, 115.
(6) Pereira, A. S.; Tavares, P.; Moura, I.; Moura, J. J. G.; Huynh, B. H. *J. Am. Chem. Soc.* **2001**, *123*, 2771.
(7) Nicolet, Y.; de Lacey, A. L.; Vernede, X.; Fernandez, V. M.; Hatchikian, E. C.; Fontecilla-Camps, J. C. *J. Am. Chem. Soc.* **2001**, *123*, 1596.
(8) Nicolet, Y.; Lemon, B. J.; Fontecilla-Camps, J. C.; Peters, J. W. *Trends Biochem. Sci.* **2000**, *25*, 138.
(9) Adamska-Venkatesh, A.; Krawietz, D.; Siebel, J.; Weber, K.; Happe, T.; Reijerse, E.; Lubitz, W. *J. Am. Chem. Soc.* **2014**, *136*, 11339.
(10) Mulder, D. W.; Ratzloff, M. W.; Bruschi, M.; Greco, C.; Koonce, E.; Peters, J. W.; King, P. W. *J. Am. Chem. Soc.* **2014**, *136*, 15394.
(11) Greco, C.; Bruschi, M.; Fantucci, P.; Ryde, U.; De Gioia, L. *ChemPhysChem* **2011**, *12*, 3376.
(12) Esselborn, J.; Lambertz, C.; Adamska-Venkatesh, A.; Simmons, T.; Berggren, G.; Noth, J.; Siebel, J.; Hemschemeier, A.; Artero, V.; Reijerse, E.; Fontecave, M.; Lubitz, W.; Happe, T. *Nat. Chem. Biol.* **2013**, *9*, 607.
(13) Silakov, A.; Kamp, C.; Reijerse, E.; Happe, T.; Lubitz, W. *Biochemistry* **2009**, *48*, 7780.
(14) Roseboom, W.; De Lacey, A. L.; Fernandez, V. M.; Hatchikian, E. C.; Albracht, S. P. J. *J. Biol. Inorg. Chem.* **2006**, *11*, 102.
(15) Olsen, M. T.; Rauchfuss, T. B.; Wilson, S. R. *J. Am. Chem. Soc.* **2010**, *132*, 17733.
(16) Huynh, M. T.; Wang, W. G.; Rauchfuss, T. B.; Hammes-Schiffer, S. *Inorg. Chem.* **2014**, *53*, 10301.
(17) Dempsey, J. L.; Winkler, J. R.; Gray, H. B. *Chem. Rev.* **2010**, *110*, 7024.
(18) Yu, L.; Greco, C.; Bruschi, M.; Ryde, U.; De Gioia, L.; Reiher, M. *Inorg. Chem.* **2011**, *50*, 3888.
(19) Katz, S.; Noth, J.; Horch, M.; Shafaat, H. S.; Happe, T.; Hildebrandt, P.; Zebger, I. *Chem. Sci.* **2016**, *7*, 6746.
(20) Zu, Y. B.; Couture, M. M. J.; Kolling, D. R. J.; Crofts, A. R.; Eltis, L. D.; Fee, J. A.; Hirst, J. *Biochemistry* **2003**, *42*, 12400.
(21) Bruschi, M.; Greco, C.; Kaukonen, M.; Fantucci, P.; Ryde, U.; De Gioia, L. *Angew. Chem., Int. Ed.* **2009**, *48*, 3503.
(22) Vignais, P. M.; Billoud, B. *Chem. Rev.* **2007**, *107*, 4206.

DOI: 10.1021/jacs.6b12636
J. Am. Chem. Soc. 2017, 139, 1440–1443

SUPPORTING INFORMATION

Proton Coupled Electronic Rearrangement within the H-Cluster as an Essential Step in the Catalytic Cycle of [FeFe] Hydrogenases

Constanze Sommer, Agnieszka Adamska-Venkatesh, Krzysztof Pawlak, James A. Birrell, Olaf Rüdiger, Edward J. Reijerse, Wolfgang Lubitz

Materials and Methods

*Cr*HydA1 protein expression and maturation as well as FTIR spectro-electrochemical experiments followed previously published protocols and procedures.[1,2,3] In expression as well as maturation no sodium dithionite was used and the maturation was performed with a threefold excess of ADT in 0.1 M Tris/HCl buffer, 0.15 M NaCl pH 8.0. The spectro-electrochemistry experiments (reductive titrations) were performed using potassium phosphate buffer at pH 6 and 7, and Tris/HCl at pH 8, Glycin/MES/HEPES at pH 9 and 10. Furthermore, five redox mediators (each 0.5 mM) were used during the electrochemical titrations (see below). This reduced the stabilization time between different potentials to 15 minutes. All experiments were conducted at 15 ^{o}C with a continuously (dry N_2) purged sample chamber accommodating the FTIR spectro-electrochemical cell. Data processing was performed using home written scripts in the Matlab® programming environment. A general approach was used, described below, which allowed modeling of an arbitrary linear chain of equilibria. To fit the pH dependent midpoint potentials (figure S3) a local minimizer was used with a three-state model. To treat the complete set of experiments (figure 2 B-F), global minimization (using a grid search) was applied. The FTIR extinction coefficients of the marker bands assigned to the individual species (H_{ox}, H_{red}, $H_{red}H^+$, and $H_{sred}H^+$) are unknown. Therefore, the amplitudes of the marker bands were rescaled to the experimental data for each pH during the fit procedure.

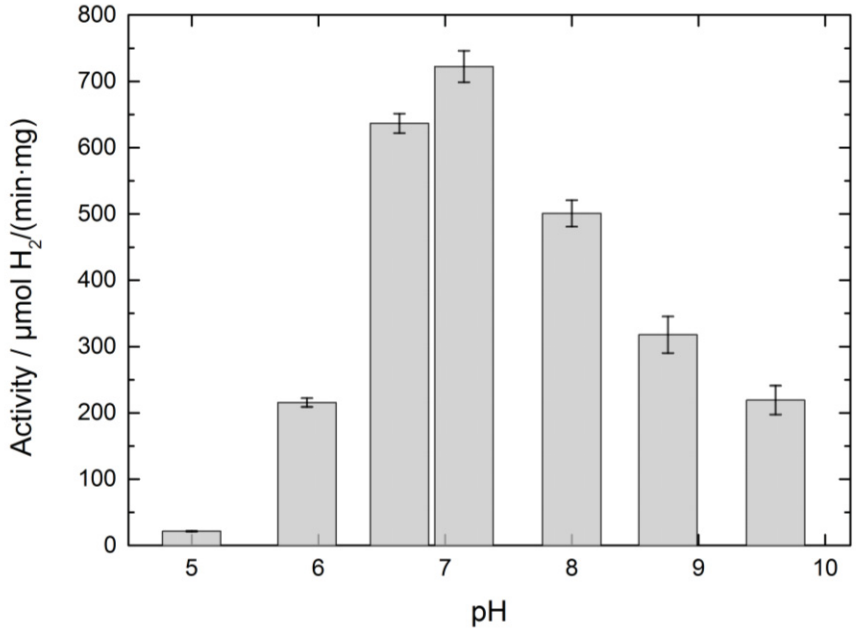

Figure S1. H_2 production activity of *Cr*HydA1 as a function of pH based on the activity assay used in reference[4] but with a buffer concentration of 200 mM. Each value was measured in triplicate. Experimental details: 10 mM methyl viologen, 100 mM NaDT, 100 ng protein, 5 min degassing under argon at RT; 20 min incubation at 37°C. 300 µL head space volume from a sealed 2 ml Eppendorf tube was measured on a GC column: RT-MSieve 5A, Carrier: argon.

Mediators used in the FTIR spectro-electrochemical experiments

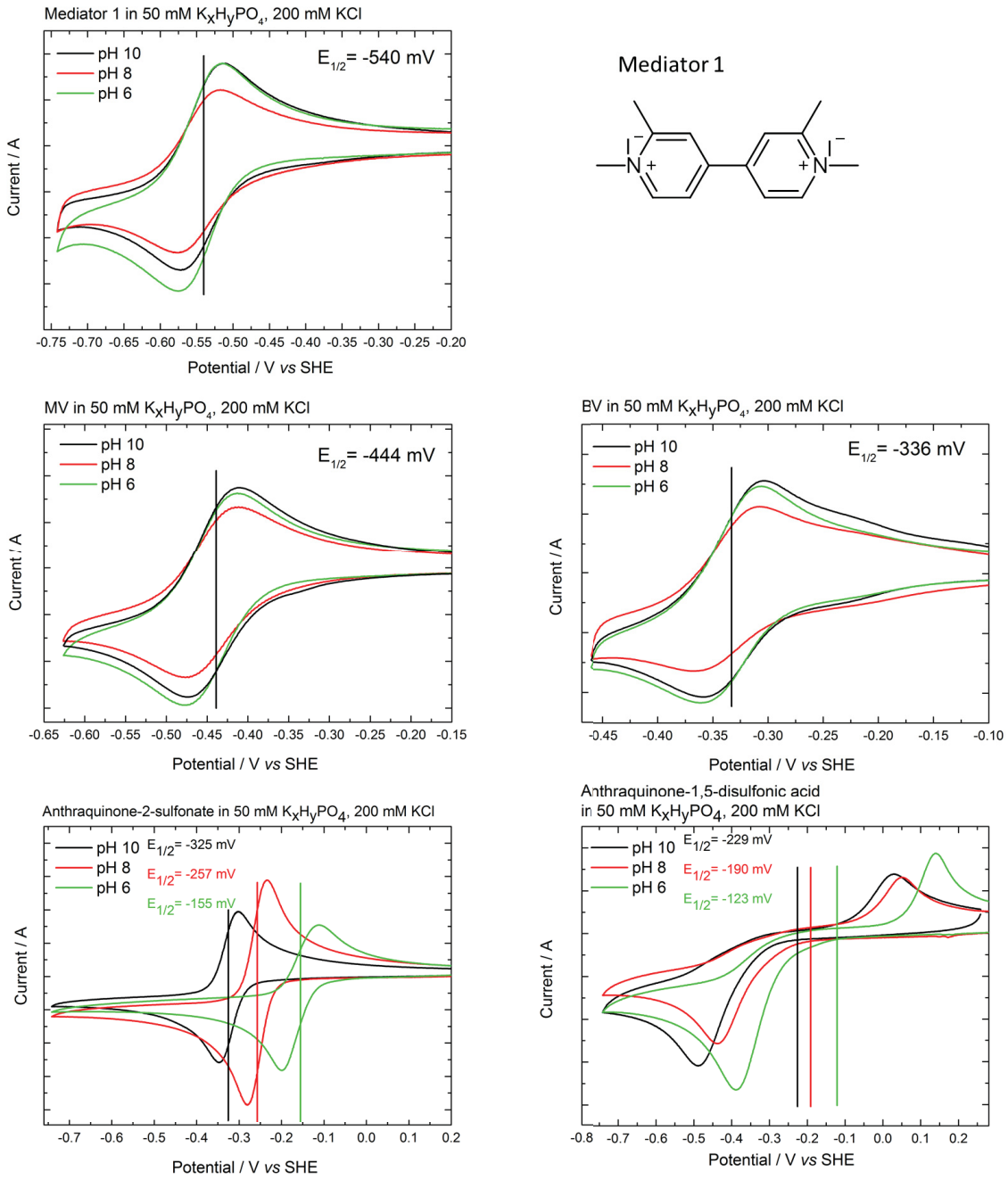

Figure S2. Cyclic voltammograms of the mediators used (0.5 mM 0.02 V/s, 25°C) in phosphate buffer at pH 6, 8, and 10 indicating that these are stable and reversible. Mediator 1, methyl viologen (MV) and benzyl viologen (BV) show no pH dependence whereas the redox potential of the quinone based mediators increase with decreasing pH.

1) 1,1’,2,2’-Tetramethyl-[4,4’-bipyridine]-1,1’-diium iodide ($E_{1/2}$= -540 mV vs. SHE)

2) Methyl viologen, MV ($E_{1/2}$= -449 mV vs. SHE) [5,6]

3) Benzyl viologen, BV ($E_{1/2}$= -358 mV vs. SHE) [5,6]

4) Sodium anthraquinone-2-sulfonate ($E_{1/2}$= -277 mV vs. SHE, pH 8) [5,6]

5) Anthraquinone-1,5-disulfonic acid ($E_{1/2}$= -234 mV vs. SHE, pH 8) [5,6]

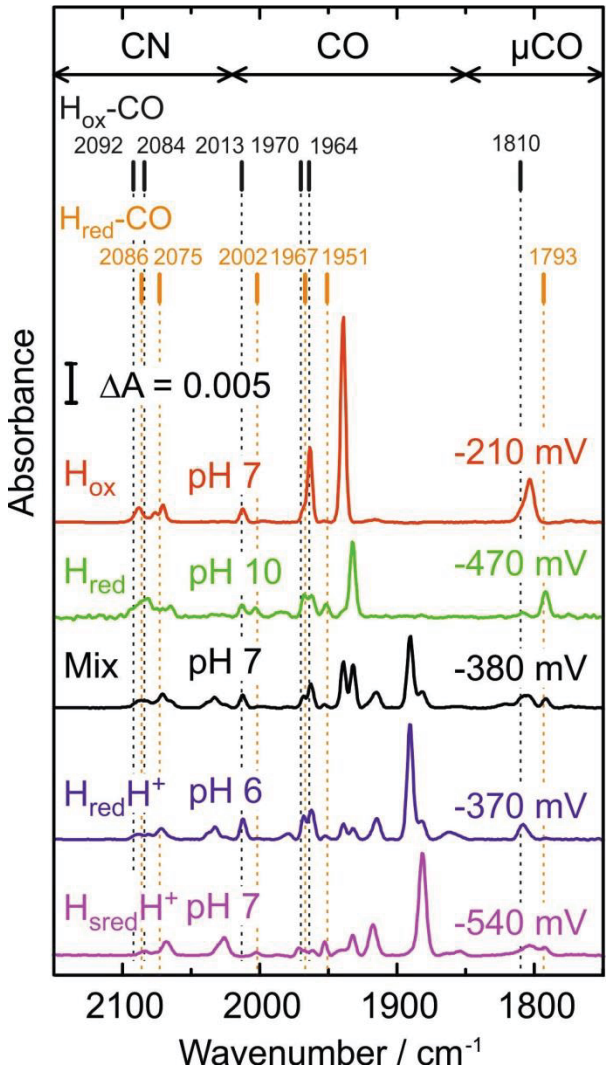

Figure S3. FTIR spectra of figure 2 (main text) overlaid with the band positions of the H_{ox}-CO and H_{red}-CO species that are present in most preparations in variable concentrations. The bands at 2002 and 2013 cm^{-1} do not overlap with features of the other H-cluster states and can be used to estimate the contribution of the inhibited states. The bands in the range 1950-1970 cm^{-1} and 1790-1810 cm^{-1} show serious overlap with those of the H-cluster states followed in the electrochemical experiments (figure 2). Therefore the marker bands of H_{ox}, H_{red}, $H_{red}H^+$, and $H_{sred}H^+$ are chosen outside these regions.

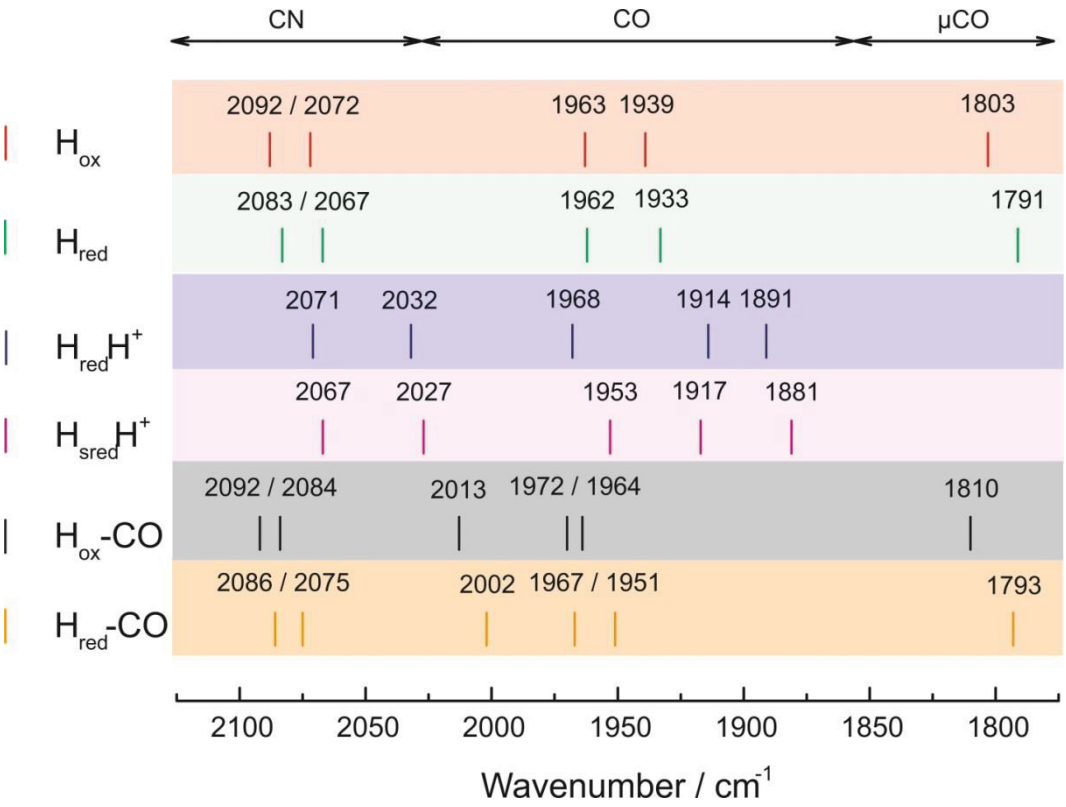

Figure S4. Band positions of all states observed during the spectro-electrochemical experiments (including CO inhibited states). The band colors of H_{ox}, H_{red}, $H_{red}H^+$, and $H_{sred}H^+$ are corresponding to those in figure 2 (main text).

Electrochemical titrations under equilibrium conditions

The FTIR spectro-electrochemical cell is a further improvement of the one described previously.[1,7] The cell is designed to be gas-tight. At low potentials, proton reduction by the hydrogenase will produce H_2, which will accumulate until the H_2/H^+ couple is in equilibrium with the electrode potential. It should be noted that, although the enzyme is highly active in both H_2 oxidation and H^+ reduction (maximum turnover rates up to 600 s^{-1}), the actual activity in the spectro-electrochemical cell is limited by the diffusion of the mediators (see figure S2) between enzyme and electrode. Typical electrochemical reaction rates are estimated to be in the range 1-10 $hour^{-1}$ which is consistent with the 15 minutes equilibration time required to obtain stable states in the cell.

We verified that the H_2/H^+ potential generated in the spectro-electrochemical cell matches the electrode potential by observing the formation of the reduced species under H_2 (10% and 100%) at pH 10 and pH 7 in a gas-tight ATR cell (figure S5). These conditions correspond to redox potentials of -570/-540 mV (pH 10) and -400/-370 mV (pH 7). Here, the ratios between the H_{red}, $H_{red}H^+$ and H_{sred} states agree with the ratios observed during the spectro-electrochemical titrations in Figure 2. Indeed, during the FTIR spectro-electrochemical titrations no catalytic currents were observed after 15 minutes equilibration time. This implies that our spectro-electrochemical cell can maintain an H_2/H^+ potential to at least 1 bar of H_2. At lower potentials (left of the black dotted lines in figure 2B-F), deviation from equilibrium may occur, which might be the reason for not fully reaching the zero level at the time of FTIR measurement. Nevertheless, the experimental titration curves in figure 2B-F show Nernst-like behavior even down to very low potential. We can, therefore, still estimate the midpoint potentials and pKa values associated with the H_{sred} states.

If deviations at low potential occur then this could be due to H_2 leaking out of the spectro-electrochemical cell under high pressure. Assuming that pressures significantly above 1 bar cannot be maintained in the cell, at electrode potentials below the H^+/H_2 couple (1 bar H_2) the bulk electrochemical potential will be affected by competition between the electrode and the H^+/H_2 potential (see figure 2). This would lead to an estimation of the bulk electrochemical potential more negative than the actual value. Therefore, the $H_{red}H^+/H_{sred}$ redox midpoint potential (E_4) would be also estimated at a value lower than its true value. Consequently, our estimated value of E_4 should be regarded as a lower limit. This conclusion is consistent with the idea that reduction of $[4Fe\text{-}4S]_H$ in both the H_{ox} and $H_{red}H^+$ states occurs with essentially the same redox potential which shows the importance of protonating H_{red} (see main text).

An alternative mechanism requiring two successive redox steps or two successive protonation steps should only be possible at very low redox potentials or very low pH values, respectively. This is because the energy required to place two extra negative or positive charges (electrons or protons) on the H-cluster is too high when not coupled to transfer steps of the opposite charge.

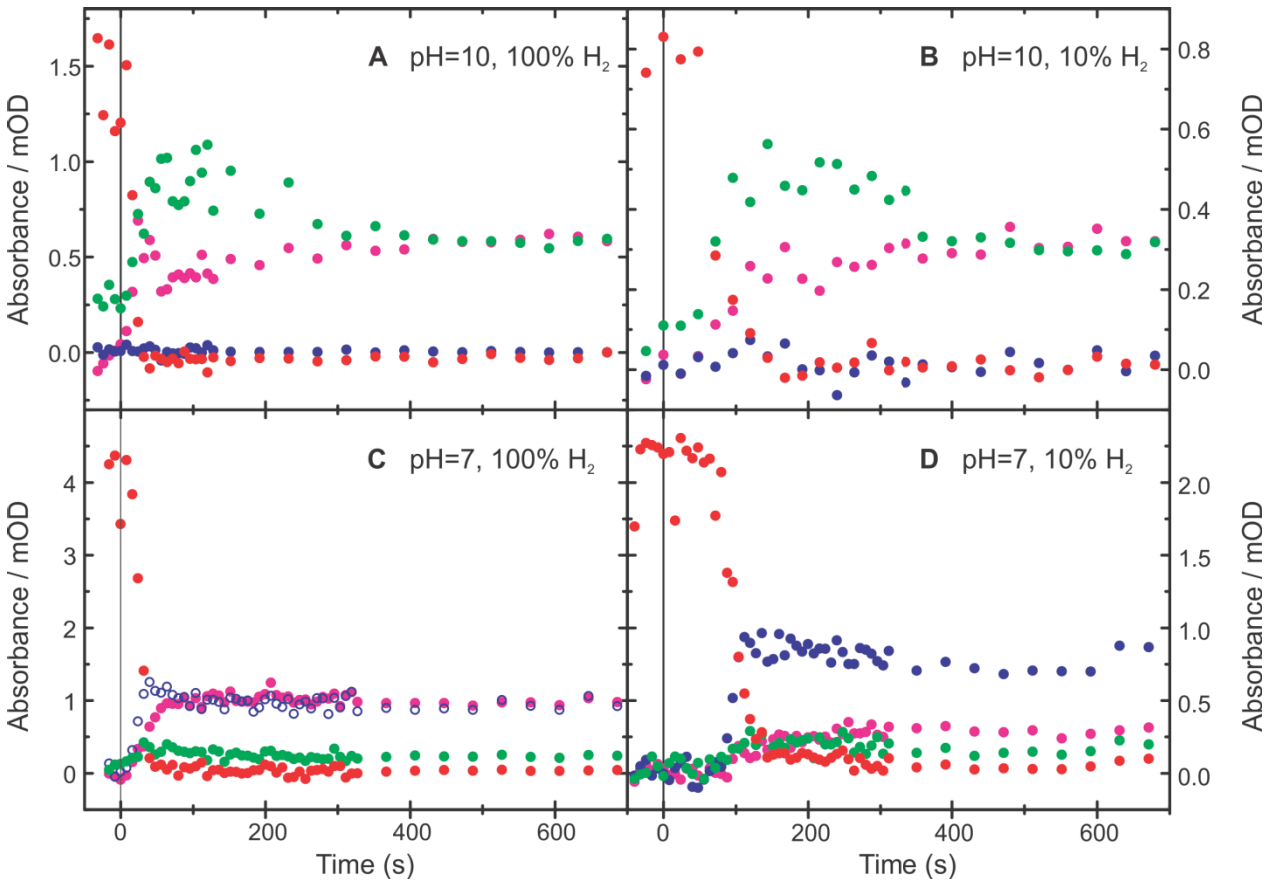

Figure S5. Time dependence of H-cluster states in *Cr*HydA1 after H_2 exposure starting from H_{ox} as observed by FTIR (minimum recording time 10s). At pH 10, after equilibration H_{red} and $H_{sred}H^+$ form the main contributions for both 100% and 10% H_2 exposure. These conditions correspond to -570 and -540 mV H^+/H_2 potential. As seen in figure 2F at these potentials H_{red} and $H_{sred}H^+$ have similar concentrations. In contrast, at pH 7 the ratio of $H_{red}H^+$ to $H_{sred}H^+$ increases when going from 100% to 10% H_2 exposure. These conditions correspond to -400 and -370 mV H^+/H_2 potential, respectively. The same trend is observed in Figure 2C at the corresponding potentials.

Treatment of a multiple-state chain of equilibria

We assume that the different H-cluster states and their dependence on each other can be described as a linear (unbranched) chain of equilibria: $X_1 \rightleftarrows X_2 \rightleftarrows X_3 \rightleftarrows \dots \rightleftarrows X_n$, Where X_i represents the fraction of state "i" and $\sum_i^n X_i = 1$. The equilibrium constants are given as $K_{i,j} = X_i/X_j$. The equilibrium constants between the H-cluster states i = 1 to 6 ($H_{ox}H^+$, H_{ox}, H_{red}, $H_{red}H^+$, $H_{sred}H^+$, H_{sred}) are dependent on pH and electrochemical potential and are given as:

$$K_{1,2} = \frac{X(H_{ox}H^+)}{X(H_{ox})} = 10^{(pKox-pH)}\ ,\ K_{3,4} = \frac{X(H_{red})}{X(H_{red}H^+)} = 10^{(pH-pKred)},\ K_{5,6} = \frac{X(H_{sred}H^+)}{X(H_{sred})} = 10^{(pKsred-pH)}$$

and

$$K_{2,3} = \frac{X(H_{ox})}{X(H_{red})} = e^{((E-E1)F/RT)},\ K_{4,5} = \frac{X(H_{red}H^+)}{X(H_{sred}H^+)} = e^{((E-E4)F/RT)}$$

where E is the electrochemical potential, F is Faraday's constant (F = 96485,34 C mol^{-1}), R is the gas constant (R = 8,31447 C V mol^{-1} K^{-1}), and T is the experimental temperature in Kelvin.

For given equilibrium constants, $K_{i,i+1}$, the state fractions are completely determined and can be calculated as:

$$X_1 = \left\{1 + \sum_{i=1}^{n-1}\prod_{k=1}^{i} K_{i,i+1}^{-1}\right\}^{-1}$$

$$X_{1+l} = X_1 \prod_{i=1}^{n-1} K_{i,i+1}^{-1}$$

Note that $K_{i,i+1} = \frac{X_i}{X_{i+1}}$

Three-state model versus Six-state Model

The pH dependent electrochemical titrations as presented in figure 2b (main text) can also be analyzed within the standard three-state model $H_{ox}\rightleftarrows H_{red}\rightleftarrows H_{sred}$ that has been used previously.[1,7,8] In this case, the protonated and unprotonated species of the six state model are not distinguished and represented as $[H_{ox}+H_{ox}H^+] \rightleftarrows [H_{red}+H_{red}H^+] \rightleftarrows [H_{sred}+H_{sred}H^+]$. The protonation equilibrium constants can be derived from the pH dependence of the midpoint potentials $E_{ox/red}$ and $E_{red/sred}$ according to eq. 3 and 4 (main text). Figure S6 shows the individual fits at the different pH values. The amplitudes of H_{red} and $H_{red}H^+$ (see figure 2 main text) were added to represent H_{red} in the three-state model. During this procedure, the model curves were rescaled to the experimental data. The extracted midpoint-potentials are collected in figure 4 (inset) of the main text.

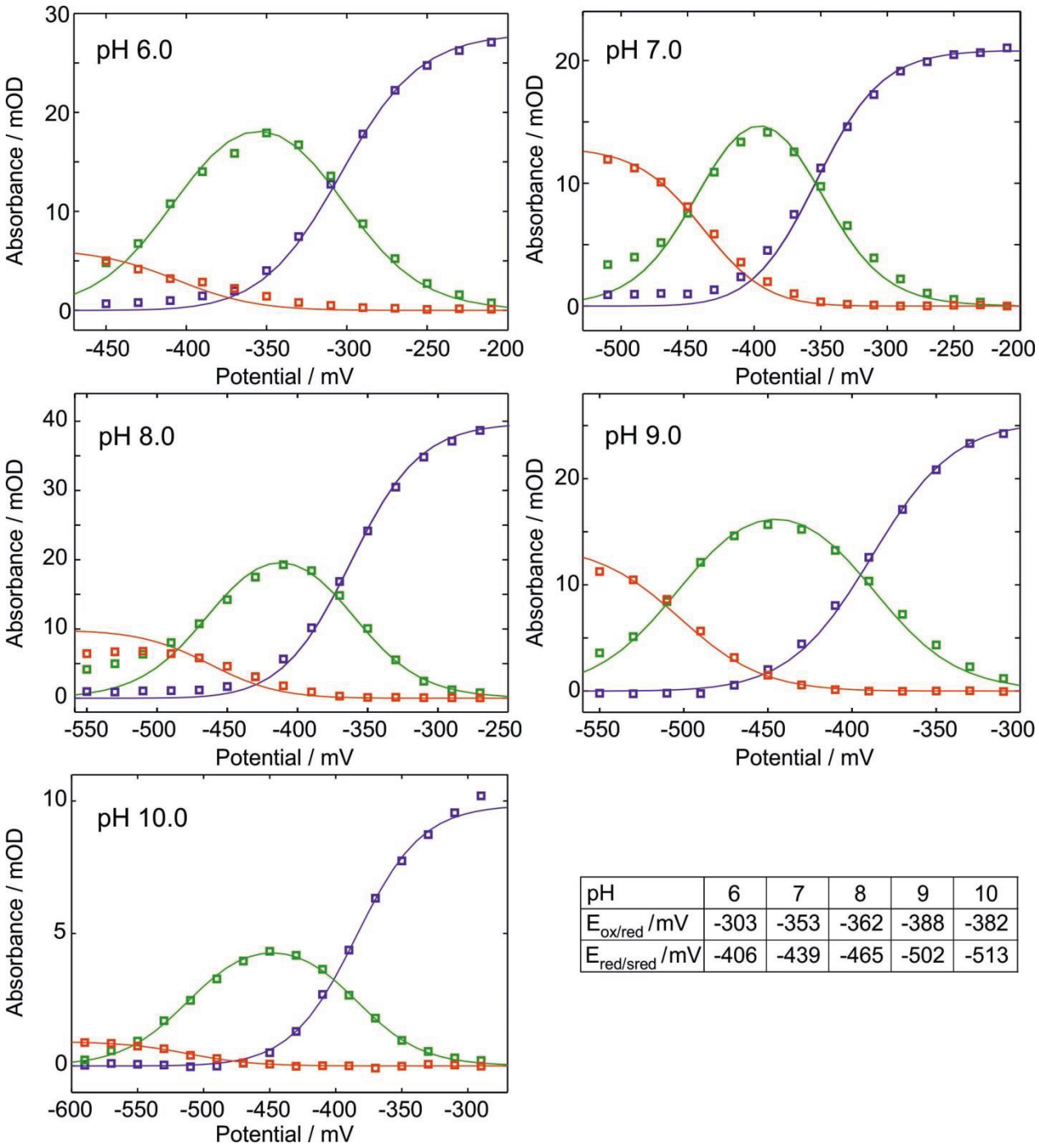

pH	6	7	8	9	10
$E_{ox/red}$ /mV	-303	-353	-362	-388	-382
$E_{red/sred}$ /mV	-406	-439	-465	-502	-513

Figure S6. Fit of experimental data (squares) to the three-state model $H_{ox} \rightleftarrows H_{red} \rightleftarrows H_{sred}$ (see inset of figure 4 in main text). Color code: H_{ox}=blue; H_{red}=green; H_{sred}=red. All curves were scaled to the data; $H_{red} = H_{red} + H_{red}H^+$ (see figure 2 main text). The fitted midpoint potentials $E_{ox/red}$ and $E_{red/sred}$ for every pH are collected in figure 4 (inset).

PCET as initial/final step in H_2 oxidation/production

A very recent paper by Mulder et al.[9] suggested that the putative hydride H_{hyd} state is unprotonated. In this case H_{hyd} would be related to $H_{sred}H^+$ by proton transfer from the ADT ammonium to the distal iron. Subsequent protonation of H_{hyd} would then induce electron transfer from $[4Fe\text{-}4S]_H$ to $[2Fe]_H$ similar to the transition from H_{red} to $H_{red}H^+$. Figure S7 summarizes all conceivable scenarios for the catalytic cycle, including internal PCET steps.

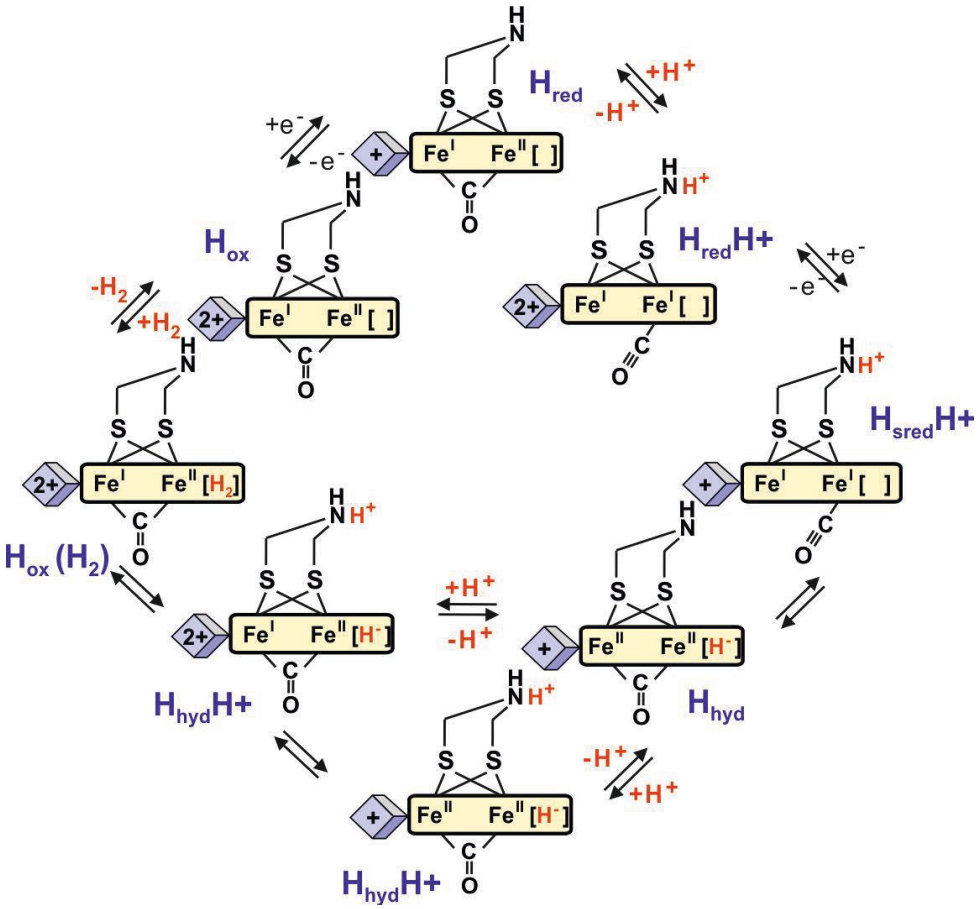

Figure S7. Working model for the catalytic cycle of [FeFe] hydrogenases including all conceivable short lived intermediates $H_{hyd}H^+$, $H_{ox}(H_2)$ that are not (yet) experimentally verified. Note that both the transition from H_{red} to $H_{red}H^+$ and the transition from H_{hyd} to $H_{hyd}H^+$ may be accompanied with internal electron rearrangement (PCET) involving electron transfer from $[4Fe\text{-}4S]_H$ to $[2Fe]_H$.

References

(1)Adamska-Venkatesh, A.; Krawietz, D.; Siebel, J.; Weber, K.; Happe, T.; Reijerse, E.; Lubitz, W. *J. Am. Chem. Soc.* **2014**, *136*, 11339.
(2)Berggren, G.; Adamska, A.; Lambertz, C.; Simmons, T.; Esselborn, J.; Atta, M.; Gambarelli, S.; Mouesca, J.; Reijerse, E.; Lubitz, W.; Happe, T.; Artero, V.; Fontecave, M. *Nature* **2013**, *499*, 66.
(3)Esselborn, J.; Lambertz, C.; Adamska-Venkatesh, A.; Simmons, T.; Berggren, G.; Nothl, J.; Siebel, J.; Hemschemeier, A.; Artero, V.; Reijerse, E.; Fontecave, M.; Lubitz, W.; Happe, T. *Nat. Chem. Biol.* **2013**, *9*, 607.
(4)Siebel, J. F.; Adamska-Venkatesh, A.; Weber, K.; Rumpel, S.; Reijerse, E.; Lubitz, W. *Biochemistry* **2015**, *54*, 1474.
(5)DeLacey, A. L.; Stadler, C.; Fernandez, V. M.; Hatchikian, E. C.; Fan, H. J.; Li, S. H.; Hall, M. B. *J. Biol. Inorg. Chem.* **2002**, *7*, 318.
(6)Birrell, J. A.; Wrede, K.; Pawlak, K.; Rodriguez-Maciá, P.; Rüdiger, O.; Reijerse, E. J.; Lubitz, W. *Isr. J. Chem.* **2016**, *56*, 852.
(7)Silakov, A.; Kamp, C.; Reijerse, E.; Happe, T.; Lubitz, W. *Biochemistry* **2009**, *48*, 7780.
(8)Roseboom, W.; De Lacey, A. L.; Fernandez, V. M.; Hatchikian, E. C.; Albracht, S. P. J. *J. Biol. Inorg. Chem.* **2006**, *11*, 102.
(9)Mulder, D. W.; Guo, Y.; Ratzloff, M. W.; King, P. W. *J. Am. Chem. Soc.* **2016**, 10.1021/jacs.6b11409.

4.2 Paper II

Chalcogenide substitution in the [2Fe] cluster of [FeFe]-hydrogenases conserves high enzymatic activity

L. Kertess, F. Wittkamp, C. Sommer, J. Esselborn, O. Rüdiger, E. J. Reijerse, E. Hofmann, W. Lubitz, M. Winkler, T. Happe and U.-P. Apfel

Reproduced with author permission; *Dalton Trans.* 2017, 46, 1647-16958.

DOI: 10.1039/c7dt03785f.

Journal name: Dalton Transaction

Author: Equal contribution of L. Kertess, F. Wittkamp and C. Sommer

Contribution: – 20 %

– I performed and analyzed all FTIR data on the maturated enzymes

– I performed the protein films and analyzed the data of the CV and CA experiments with the maturated enzymes

- I was involved in writing the manuscript

F. Wittkamp synthesized the selenium containing precursor and measured CVs of it in solution. L. Kertess made the biological samples, measured the activities, crystalized and measured the samples and modeled the x-ray structure together with J. Esselborn and E. Hofmann. All others discussed the results and were involved in writing the manuscript.

Dalton Transactions

PAPER

View Article Online
View Journal

Cite this: DOI: 10.1039/c7dt03785f

Chalcogenide substitution in the [2Fe] cluster of [FeFe]-hydrogenases conserves high enzymatic activity†

L. Kertess, ‡[a] F. Wittkamp,‡[b] C. Sommer,‡[c] J. Esselborn, [a] O. Rüdiger, [c] E. J. Reijerse,[c] E. Hofmann, [d] W. Lubitz, [c] M. Winkler,[a] T. Happe *[a] and U.-P. Apfel *[b]

[FeFe]-Hydrogenases efficiently catalyze the uptake and evolution of H_2 due to the presence of an inorganic [6Fe–6S]-cofactor (H-cluster). This cofactor is comprised of a [4Fe–4S] cluster coupled to a unique [2Fe] cluster where the catalytic turnover of H_2/H^+ takes place. We herein report on the synthesis of a selenium substituted [2Fe] cluster $[Fe_2\{\mu(SeCH_2)_2NH\}(CO)_4(CN)_2]^{2-}$ (ADSe) and its successful *in vitro* integration into the native protein scaffold of [FeFe]-hydrogenases HydA1 from *Chlamydomonas reinhardtii* and CpI from *Clostridium pasteurianum* yielding fully active enzymes (HydA1-ADSe and CpI-ADSe). FT-IR spectroscopy and X-ray structure analysis confirmed the presence of structurally intact ADSe at the active site. Electrochemical assays reveal that the selenium containing enzymes are more biased towards hydrogen production than their native counterparts. In contrast to previous chalcogenide exchange studies, the S to Se exchange herein is not based on a simple reconstitution approach using ionic cluster constituents but on the *in vitro* maturation with a pre-synthesized selenium-containing [2Fe] mimic. The combination of biological and chemical methods allowed for the creation of a novel [FeFe]-hydrogenase with a [2Fe2Se]-active site which confers individual catalytic features.

Received 9th October 2017,
Accepted 16th November 2017

DOI: 10.1039/c7dt03785f

rsc.li/dalton

Introduction

[FeFe]-Hydrogenases are able to reversibly catalyze the evolution and uptake of hydrogen, with the former favored.[1] This reaction is facilitated by a unique inorganic cofactor (H-cluster) within the enzyme's active site. In its native form, the H-cluster consists of a [4Fe–4S] cluster coupled to a [2Fe] moiety which carries three carbonyl (CO), two cyanide (CN^-) ligands as well as an unprecedented ADT group (ADT = $-SCH_2(NH)CH_2S-$) that bridges both iron centers. The simplest [FeFe]-hydrogenase, HydA1 from *Chlamydomonas reinhardtii*, carries only the H-cluster while the bacterial [FeFe]-hydrogenase CpI from *Clostridium pasteurianum* harbors four accessory [Fe–S] clusters. While natural selenium containing [FeFe]-hydrogenases are unknown, selenium plays a key role for the characteristics of [NiFeSe]-hydrogenases as it is responsible for their decreased oxygen sensitivity and their bias towards hydrogen production.[1,2] We previously demonstrated that inactive apo [FeFe]-hydrogenase which solely contains the [4Fe-4S] cluster moiety can be maturated *in vitro* by adding a synthetic [2Fe] mimic thereby forming a native-like active holoenzyme in a self-assembly step.[3] Following this method, numerous derivatives of [2Fe] mimics altered at the bridgehead atom of the dithiolate ligand (*e.g.* NH (ADT) to S (SDT), O (ODT), or CH_2 (PDT)) as well as their monocyanide [2Fe] analogs and a mononuclear iron complex were incorporated into the active site pockets of HydA1 and CpI.[3,4] While in most cases the defined orientation of the [2Fe] cluster was unaltered compared to wild type enzyme, the catalytic turnover rate was unanimously reduced to only a fraction of the wild

[a]*Ruhr-Universität Bochum, Lehrstuhl für Biochemie der Pflanzen, AG Photobiotechnologie, Universitätsstraße 150, 44801 Bochum, Germany. E-mail: Thomas.Happe@rub.de*
[b]*Ruhr-Universität Bochum, Anorganische Chemie I/Bioanorganische Chemie, Universitätsstraße 150, 44801 Bochum, Germany. E-mail: Ulf.Apfel@rub.de*
[c]*Max-Planck-Institut für Chemische Energiekonversion, Stiftstraße 34-36, 45470 Mülheim an der Ruhr, Germany*
[d]*Ruhr-Universität Bochum, Lehrstuhl für Biophysik, AG Röntgenstrukturanalyse an Proteinen, Universitätsstraße 150, 44801 Bochum, Germany*
†Electronic supplementary information (ESI) available: Additional catalytic activity, spectroscopy, structural and electrochemistry data. CCDC 1570441 and 1570440. For ESI and crystallographic data in CIF or other electronic format see DOI: 10.1039/c7dt03785f
‡These authors contributed equally.

type activity. Notably, although inactive in the enzymatic environment, the synthetic [2Fe] mimics comprising altered bridgehead atoms (NH to CR_2, NR, O, S, Se, or SiR_2) allow for an electrocatalytic generation of hydrogen by different mechanistic pathways at increased overpotentials.[5–10] Such altered mechanisms are, however, not feasible to realize within the enzymatic cofactor binding site due to structural deviations of the mimics which are incompatible with the native protein environment, including a perfectly directed proton transfer pathway *via* the secondary amine of the ADT ligand towards the distal iron (Fe_d), the site of catalytic turnover.[11–18] Based on activity assays, FT-IR spectroscopy and X-ray crystallographic data, we recently demonstrated that manipulation of the neighboring [4Fe–4S] cluster by a sulfur to selenium exchange does not notably affect the structural and catalytic features of the H-cluster.[19] These data and the respective selenium containing mimics reported by Weigand[6,7] and Song,[20] prompted us to survey the consequences of sulfur to selenium exchange in the [2Fe] site, the actual subsite of catalytic turnover. The incorporation of selenium into the synthetic mimic frameworks led to an enhancement of the catalytic activity towards H_2 development due to an increase of the electron density on iron and a faster electron transfer rate.[6,8,21] These beneficial properties, however, come at the price of a diminished ability to adopt the catalytically crucial rotated state that opens the coordination site at the Fe_d.[22]

In continuation of our previous attempts to manipulate the [FeFe]-hydrogenase, we aimed to combine the previous chemical[6,7] and biological[3] approaches by incorporating *in vitro* a synthetic selenium containing [2Fe] mimic that bears the important secondary amine bridge into apoHydA1 and apoCpI. The unprecedented semi-artificial selenium containing [FeFe]-hydrogenases were characterized by X-ray structure analysis, FT-IR spectroscopy and electrochemistry. Compared to their native forms, the selenium containing [FeFe]-hydrogenases exhibited a stronger bias towards hydrogen production in electrochemical investigations.

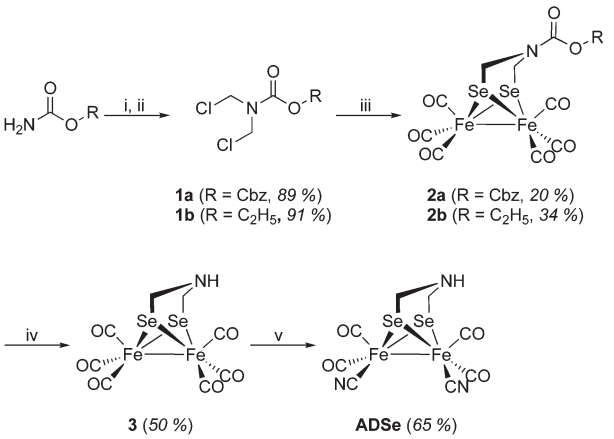

Scheme 1 Synthetic route to ADSe. (i) $(CH_2O)_x$, KOH, 120 °C, (ii) $SOCl_2$, (iii) $Fe_2Se_2(CO)_6$, $LiEtBH_3$, 25 °C, THF, (iv) BF_3, Me_2S, 25 °C, CH_2Cl_2, (v) $Et_4N^+CN^-$, CH_3CN, 0 °C.

Results

Synthesis

We initially attempted the synthesis of $[Fe_2\{\mu(SeCH_2)_2NH\}(CO)_4(CN)_2]^{2-}$ (in the following ADSe) from $Fe_2(\mu\text{-}Se)_2(CO)_6$ according to the method described for its sulfur-counterpart $[Fe_2\{\mu(SCH_2)_2NH\}(CO)_4(CN)_2]^{2-}$ (in the following ADT).[23,24] However, this pathway proved to be ineligible and did not yield any desired product. We thus aimed at an alternative approach towards ADSe by utilizing *tert*-butyl dimethyl silyl[25] or carbamate[20] (ethyl-, benzyl-) protected amines for the coupling with $Fe_2(\mu Se)_2(CO)_6$. While the silyl-route allowed for the formation of $[Fe_2\{\mu(SeCH_2)_2NH\}(CO)_6]$ (**3**) in low-yield (16%), the carbamate-route proved to be more suitable due to the higher stability of the intermediates and thus, easier synthetic handling. Although the synthesis of $[Fe_2\{\mu\text{-}(SeCH_2)_2N(Cbz)\}(CO)_6]$ was previously reported,[20] the synthesis of $(ClCH_2)_2NC(O)OR$ (R = ethyl-, benzyl-) was not described. We found that such compounds are accessible by reaction of a carbamate, KOH and paraformaldehyde in neat thionyl chloride. $(ClCH_2)_2NC(O)OCH_2Ph$ or $(ClCH_2)_2NC(O)OEt$ can be obtained in 89% and 91% yield, respectively. Subsequent, reaction of **1a** or **1b** (Scheme 1) with $[Fe_2\mu Se_2(CO)_6]^{2-}$, generated from $Fe_2\mu Se_2(CO)_6$ and $LiEt_3BH$, affords the desired hexacarbonyl complexes **2a** (20%) and **2b** (34%) in moderate yields as red crystalline materials (Scheme 1, Fig. S6 and Table S3†). While we were not able to remove the protection group from complex **2b**, complex **3** can be obtained by treatment of complex **2a** with BF_3 and Me_2S.[26] The reaction progress herein was monitored by IR following the carbamate band at 1709 cm^{-1}. Owing to the high air-sensitivity of complex **3**, it is inevitable to work under perfect anaerobic conditions during the reaction and work up.

Complex **3** shows a characteristic ^{77}Se NMR signal at 784 ppm and CO stretching frequencies at 2062, 2021 and 1981 cm^{-1}. Likewise, the Mössbauer isomer shift (0.07 mm s^{-1}) and quadrupole splitting (0.65 mm s^{-1}) confirms the formation of an all-Fe^I complex with an antiferromagnetic coupling between both iron centers. Reaction of **3** with two equivalents of tetraethylammonium cyanide afforded ADSe as a dark red solid in 65% yield. The presence of the CN^--ligands was unequivocally shown by the new set of signals in the IR spectrum at 2022, 1991, 1940 and 2075 cm^{-1}. Notably, the ^{77}Se NMR spectrum remains unaltered by the incorporation of the two additional CN^- groups.

Maturation and catalytic activity

ADSe was dissolved in 0.1 M K_2HPO_4/KH_2PO_4 buffer (pH 6.8) under anaerobic conditions and immediately used for *in vitro* maturation of the [FeFe]-hydrogenases apoHydA1 and apoCpI.

We subsequently tested the enzymatic activity of the semi-artificial hydrogenase variants as a first measure for a successful and functional incorporation of ADSe into, HydA1 and CpI. In our standard solution based assay, using sodium dithionite (NaDT) as the electron donor and methyl viologen

(MV) as electron mediator, CpI-ADSe and HydA1-ADSe revealed rates for hydrogen evolution right after *in vitro* maturation in the same range (about 70 to 130%) as observed for the respective native proteins (Fig. 1).

However, storage under anaerobic conditions at −80 °C leads to a decrease of activity to about 60% for CpI-ADSe and HydA1-ADSe, while we routinely observe no such effect in case of the native proteins (Fig. S1†). Furthermore the hydrogen uptake was determined for all variants in a solution assay. This is based on the spectrophotometrically detection of the MV reduction by the hydrogenases and therefore its colorimetric change from clear to dark purple once reduced. Analyzing the ratio of the hydrogen uptake to hydrogen evolution rates revealed a bias of the ADSe variants towards hydrogen evolution (Table S2†) since their uptake/evolution ratios appeared 3.5 to 4 times lower than for the ADT counterparts (CpI-ADSe 5.0×10^{-2}; CpI-ADT 17.6×10^{-2}; HydA1-ADSe 9.5×10^{-2}; HydA1-ADT 38.6×10^{-2}).

Electronic states

The successful incorporation of ADSe into CpI was further confirmed by FT-IR spectroscopy (Fig. 2 and S3†). While free ADSe showed several broad bands centered at 2077, 2038, 2003 and 1943 cm^{-1} in 0.1 M K_2HPO_4/KH_2PO_4 buffer (pH 6.8) (Fig. 2 and S4†), the ADSe-maturated CpI reveals CN^- vibrations at 2086 and 2072 cm^{-1} and CO-stretching frequencies at 2006, 1964 and 1802 cm^{-1} with considerable line narrowing. Notably, in comparison to CpI-ADT, the maturated CpI-ADSe shows a much larger amount of a CO-inhibited state with main νCO bands at 2006, ≈1965 and 1802 cm^{-1}. This state is characterized by a terminal CO binding to Fe_d leading to a reversible inhibition of catalytic turnover. The bands at 1942 and 1922 cm^{-1} are likely to originate from the catalytically relevant oxidized and reduced states. Homogeneous enzyme CO-inhibited samples were obtained in a CO atmosphere. In the CO treated samples the CO– and CN^--ligand bands are red shifted by 4 to 9 cm^{-1} as compared to the native enzyme. Two CO vibrations are very similar in energy in both species and are overlapping leading to one broad signal at ≈1973/≈1965 cm^{-1} (Fig. S5†).[27] Further sample treatments did not allow for a selective conversion of the CO-inhibited sample to any other redox state.

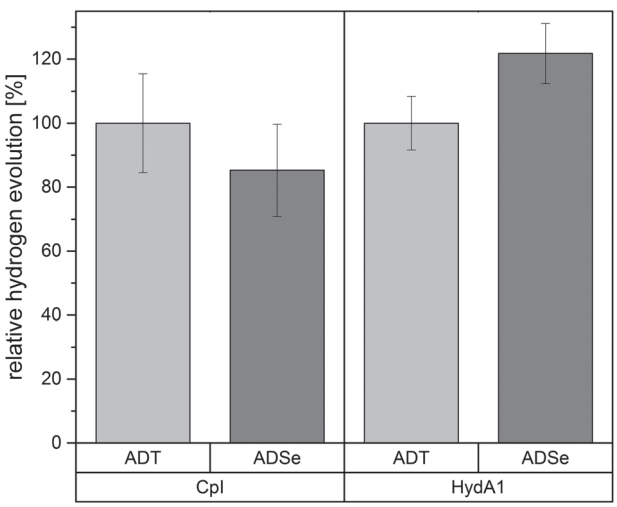

Fig. 1 Hydrogen evolution activity of CpIA1-ADSe and HydA1-ADSe relative to wild-type HydA1-ADT and CpI-ADT activity. Activity tests for methyl viologen dependent H_2 production were carried out in 100 mM K_2HPO_4/KH_2PO_4 buffer (pH 6.8), 10 mM methyl viologen and 100 mM sodium dithionite. Representative data of HydA1-ADSe and CpI-ADSe from two independent preparations. Measurements were performed in triplicates two times. Error bars indicate standard deviations. Absolute values are presented in Table S1.†

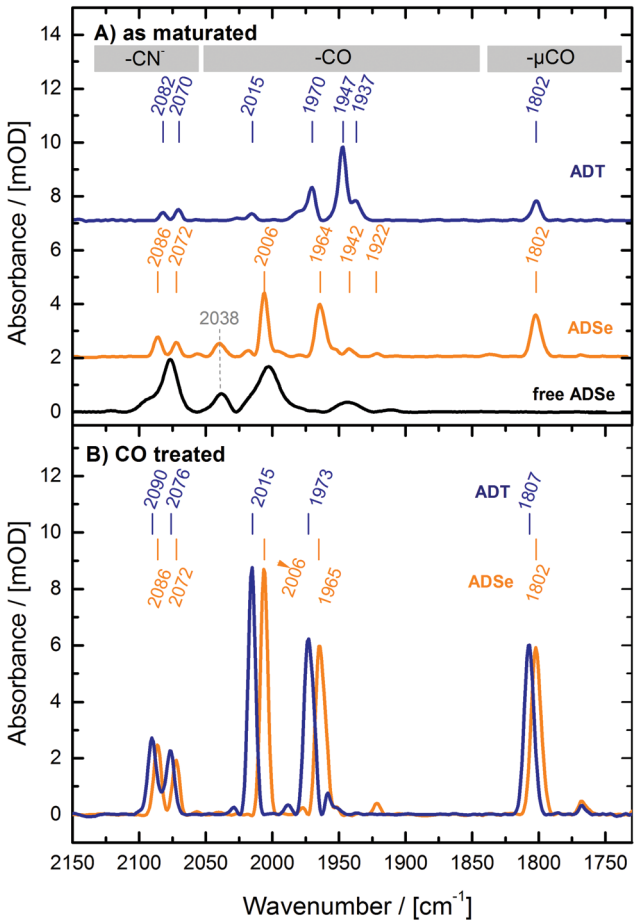

Fig. 2 FT-IR spectra of CpI-ADT (blue) and CpI-ADSe (orange) at 15 °C. (A) Samples measured directly after maturation (once thawed) showing the instability of CpI-ADSe as indicated by a much higher amount of the CO-inhibited state and (B) CO treated samples (350 μM) which demonstrate a redshift for all ligand vibrations in CpI-ADSe. Spectra in (A) are taken in an ATR cell, 500 scans; spectra in (B) are recorded in transmission with 1000 scans. The signal at 2038 cm^{-1} corresponds well to a similar peak in the spectrum of the free ADSe in aqueous solution depicted as black trace in (A).

Protein structure

Under crystallization conditions recently described for CpI maturated with other [2Fe] mimics,[28] CpI-ADSe readily crystallized under strictly anaerobic conditions leading to rod shaped brown crystals. The crystal structure (PDB: 5OEF) was deter-

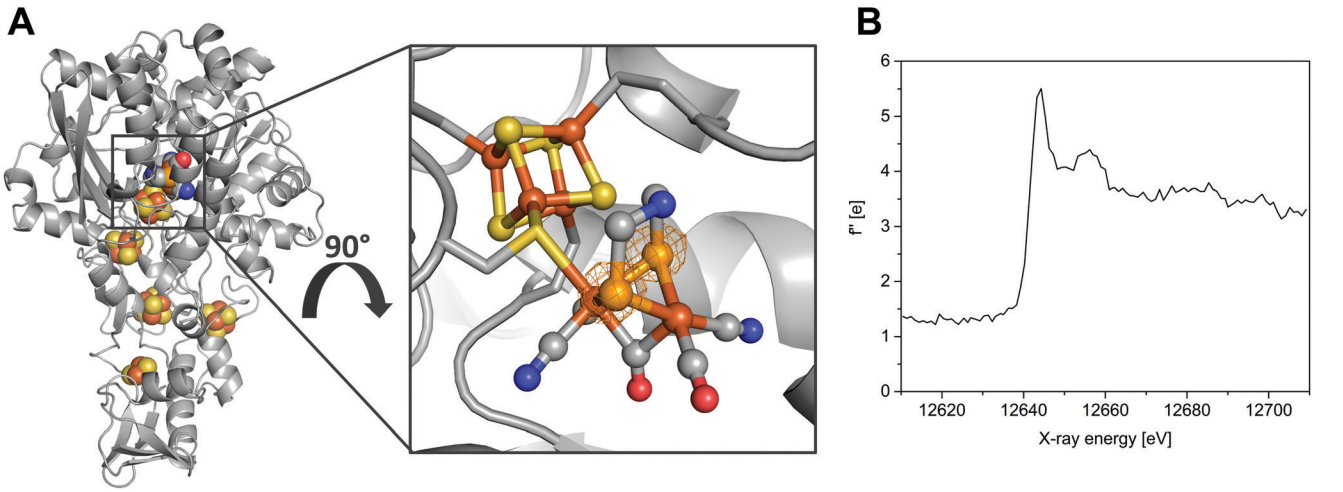

Fig. 3 Crystal structure of CpI-ADSe (PDB: 5OEF; 2.05 Å) and X-ray absorption edge scan of the CpI-ADSe crystal. (A) A cartoon model of the CpI-ADSe structure and a detailed view of the [2Fe] cluster is shown (magnification). The Se anomalous electron density is presented as an orange mesh contoured at 6 σ (protein backbone, grey; Fe, brown; Se, ochre; S, yellow; C, grey, N, blue and O, red). (B) X-ray fluorescence of the CpI-ADSe crystal while scanning over different excitation energies around the theoretical K-edge of X-ray absorption for Se at 12 666 eV. Peak of f'' is at 12 644 eV.

mined at 2.05 Å resolution (Fig. 3 and Table S5†) and clearly confirms the successful incorporation of ADSe into the active site of CpI. The refinement of ADSe within the protein environment was based on an adapted model applied for the [2Fe] mimics.[28] The overall occupancy of the intact ADSe appeared to be about 65% based on electron density. The reduced occupancy suggests a (partial) degradation of ADSe within the active site after the *in vitro* maturation process during the one-week growth of suitable crystals. Nonetheless, the strong anomalous scattering of Se at 12 644 eV allows for its unambiguous localization within the [2Fe] cluster, clearly visible in the anomalous difference Fourier map (Fig. 3A). Furthermore, the presence of Se in the crystals was confirmed by measurements of the X-ray fluorescence spectrum and fluorescence-detected X-ray absorption around the Se-edge (Fig. 3B and S7†).

Overall, the S to Se exchange within the bridge did not cause structural changes on the surrounding protein pocket (Fig. S9†). While the obtained resolution of 2.05 Å allows to confirm the successful incorporation of ADSe into CpI with a wild-type like structure and ligand arrangement, details of geometry and atomic distances within the cluster itself cannot be elucidated.

Electrochemistry and oxygen tolerance

We subsequently performed cyclic voltammetry (CV) measurements for **3** and its sulfur containing counterpart [Fe_2{μ$(SCH_2)_2NH$}$(CO)_6$] (Fig. 4). Both compounds show a cathodic signal at about −1.2 V *vs.* SHE representing a two-electron transfer step ($Fe^IFe^I \rightarrow Fe^0Fe^0$) as described previously.[29] However, while the reduction of the ADT-mimic is quasi-reversible, the reduction of compound **3** is fully irreversible under the same experimental conditions (Fig. 4, inset). Upon addition of ten equivalents of acetic acid, both compounds

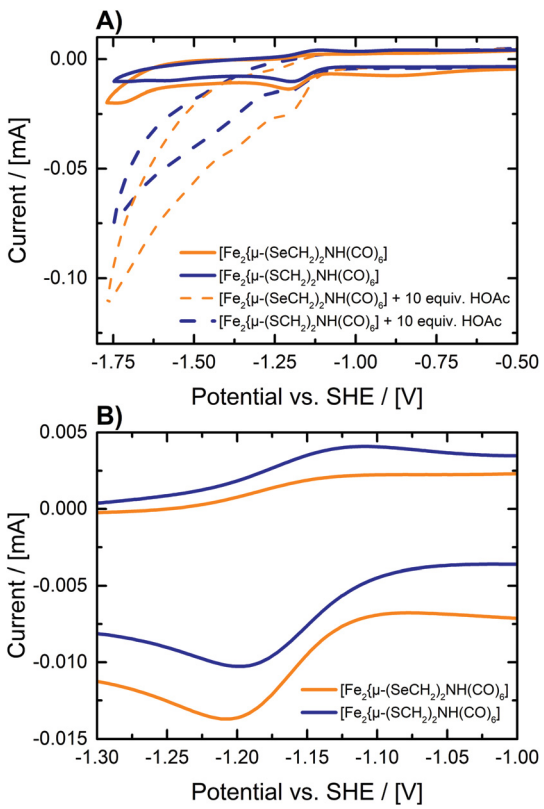

Fig. 4 (A) Cyclic voltammograms of [Fe_2{μ$(SeCH_2)_2NH$}$(CO)_6$] (**3**) (orange) and [Fe_2{μ$(SCH_2)_2NH$}$(CO)_6$] (blue) *vs.* SHE without background correction. (B) Magnification of the $Fe^IFe^I \rightarrow Fe^0Fe^0$ transition. The compounds were measured as 0.5 mM solutions in dry acetonitrile at 100 mV s^{-1} with 0.05 M $TBAPF_6$ as electrolyte with a stationary glassy carbon electrode.

display a similar trend. For both, a catalytic current is visible following the reduction to the Fe^0Fe^0 level. Although the overpotential for H_2 formation is the same in both cases, the catalytic efficiency displayed by the current is altered. Notably, the current for the selenium containing mimic **3** is increased compared to its sulfur-containing $[Fe_2\{\mu(SCH_2)_2NH\}(CO)_6]$ counterpart.

Therefore, we performed the electrochemical characterization of HydA1-ADSe and CpI-ADSe in comparison to the ADT counterparts. Both enzymes were adsorbed on a pyrolytic graphite edge (PGE) electrode and tested *via* protein film electrochemistry. The ADSe variants yielded overall lower currents than the ADT equivalents which is most likely due to the inevitable freezing and storage of the sample prior to the measurements. Therefore, a decrease in absolute HydA1-ADSe activities was observed under electrochemical conditions similar to the samples analyzed in solution assays after prolonged storage. Eventually the CO inhibition of the enzyme which is obvious according to FTIR spectroscopy (Fig. 2) blocks the enzymatic site of a fraction of the sample but upon CO release under catalytic conditions displays full activity.[30]

The cyclic voltammograms in each panel of Fig. 5 are normalized to the highest hydrogen oxidation current (see asterisk) to highlight differences in proton reduction (see Fig. S10† for raw data). It is known that CpI is biased towards proton reduction while HydA1 at similar overpotential oxidizes H_2 more rapidly at neutral pH.[31–33] The CV for CpI-ADSe shows a slightly lower catalytic current on the return scan compared to CpI-ADT, indicative of lower stability for the Se variant (see Fig. 5). The high potential inactivation commonly described for these enzymes[34] is less pronounced for the HydA1-ADSe and the corresponding switch potential[35] is shifted by ≈20 mV to lower potential compared to HydA1-ADT. For both species, the enzymes maturated with ADSe show (based on 5 measurements) an average increase in the proton reduction ratio to 126 ± 8% for CpI and to 279 ± 49% for HydA1 compared to corresponding values for enzymes maturated with ADT. To obtain these numbers the CVs were scaled at the highest oxidation rates (see asterisks Fig. 5) and the occurring normalized current for proton reduction of the ADT maturated samples was set to 100%. This data confirms the trend towards hydrogen production of the ADSe variants already observed in the solution assays.

Furthermore, to investigate possible effects of sulfur to selenium exchanges within the [2Fe] cluster, on the inherent oxygen sensitivity of [FeFe]-hydrogenases, solution based assays (Fig. S2†) and chronoamperometric oxygen tolerance tests with oxygen-saturated buffer were performed at −39 mV *vs.* SHE (Fig. 6). The chronoamperometric measurements in the absence of O_2 revealed a lower stability for the CpI-ADSe hydrogenase. To evaluate the O_2 effect on the activity, the current was normalized to the value just before O_2 addition. Adding two subsequent 50 μL amounts (grey arrows) of O_2 saturated buffer (66.5 nmol O_2) to CpI-ADSe adsorbed on the electrode results in a fast decrease of the catalytic current which is much more pronounced compared to what is observed for CpI-ADT, 70% and 25% decay, respectively. These results clearly show an increased O_2 sensitivity for the CpI-ADSe compared to the CpI-ADT, while CpI-ADSe still appears to be more stable towards oxygen than HydA1-ADSe (Fig. S11†).

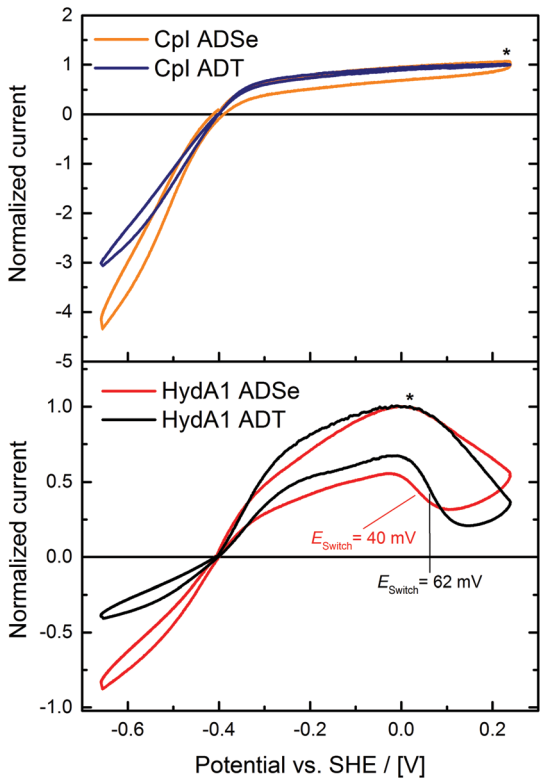

Fig. 5 Normalized and scaled cyclic voltammograms at pH 7.0 of CpI and HydA1 each maturated with either ADSe or ADT. Measurements are carried out at 25 °C, 100% H_2 with 20 mV s^{-1} scan rate, electrode rotation of 2000 rpm.

Discussion

The first studies on *in vitro* sulfide to selenide exchange in iron sulfur clusters started about 50 years ago by modification of [2Fe–2S] clusters into [2Fe–2Se] clusters within putidaredoxin,[36] adrenodoxin[37] and ferredoxin.[38] This work was expanded to [4Fe–4S] clusters contained in proteins likewise involved in the electron transport such as clostridial ferredoxins[38] and the nitrogenase Fe protein.[39] Only a handful of such sulfide to selenide exchanges within [4Fe–4S] clusters of enzymatic relevance were reported, such as aconitase[40] and biotin-synthase.[41] In the former, an increase in enzymatic activity was observed and in the later, the formation of a selenium-containing product (selenobiotin) could be detected. In all reported cases the sulfide to selenide exchange is based on a two-step *in vitro* procedure. Therein, the native iron sulfur cluster is first removed leading to an apo-protein. Subsequently, the simple addition of iron and selenide to the apo-protein forms an iron-selenide cluster. This approach was used in a previous study of

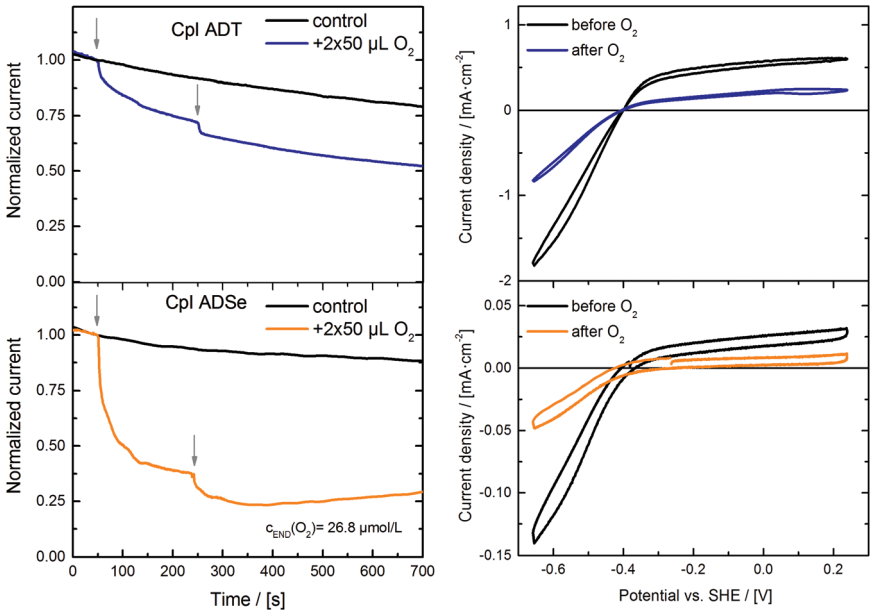

Fig. 6 Chronoamperometry (CA) for the evaluation of oxygen sensitivity on CpI-ADSe and CpI-ADT. Currents normalized to the value just before the first O_2 addition. Each arrow indicates the addition of 50 µL O_2 saturated buffer to a total volume of 5 mL, respectively. The CVs represent experiments on the protein films before and after addition of oxygen. CA was recorded at −39 mV *vs.* SHE at 25 °C, 100% H_2, pH 7.0 and an electrode rotation of 2000 rpm. Individual protein films were used for the oxygen exposed and control experiments.

our group, where we transformed the [4Fe–4S] moiety of the H-cluster into a [4Fe–4Se] cluster in which full hydrogen evolution activity was maintained.[19]

In contrast to preceding studies involving the electron pathway iron sulfur clusters, we present herein the *in vitro* incorporation of a selenium containing [2Fe] cluster active site mimic (ADSe). The presence of selenium in this unique [2Fe] cluster resulted in an active enzyme with a bias towards hydrogen evolution as observed in electrochemical experiments. This is in strong contrast to recent findings from all other types of synthetic [2Fe] mimics, including the most prominent representatives PDT, ODT and SDT. Despite all of these being electrochemically active, none of them afforded a catalytic active enzyme version due to the lack of an amine bridge head that serves as proton-acceptor and shuttle.[3,42] While numerous synthetic [2Fe] analogs are described in the literature, the ADSe cofactor mimic containing the amine bridge head with selenium instead of sulfur at the bridging positions has never been reported before. Several groups have independently suggested various approaches towards ADT, an analogous pathway was found unsuitable for the synthesis of ADSe and required the elaborate use of protection groups (*e.g.* Cbz, silyl groups) in $RN(CH_2Cl)_2$ frameworks.[20] While silyl-protecting groups were found suitable, the synthetic lability directed our attention towards Cbz protecting groups, which are significantly more stable and suitable for the coupling of the dichlorides and $[Fe_2\mu Se_2(CO)_6]^{2-}$ and afforded the desired compound $[Fe_2\{\mu(SeCH_2)_2NH\}(CO)_6]$ (**3**) in reasonable yields. Reaction of **3** with two equivalents of tetraethylammonium cyanide affords ADSe in sufficient quantities for the downstream *in vitro* maturation of apoHydA1 and apoCpI. Contrary to ADT, the selenium-derivative decomposes readily under non-anaerobic conditions. While intrinsically instable, in this work a reproducible procedure for the synthesis of ADSe was established.

The incorporation of ADSe into the protein binding pocket of CpI and HydA1 requires the synthetic mimic to pass through the maturation channel, bind to the bridging cysteine, release one of the CO-ligands and adopt the "rotated conformation" leading to an open coordination site at the Fe_d.[1] All of these steps were expected to be potentially influenced by the sulfur to selenium exchange. Notably, compared to its lighter homolog sulfur, selenium comprises an increased van-der-Waals-radius, less electronegativity and more than twice of the atomic weight. These differences result in a slightly altered cluster geometry by means of an increased Fe–Fe distance. Compared to $[Fe_2\{\mu(SCH_2)_2NPh\}(CO)_6]$ (Fe–Fe: 2.50 Å)[23] the Fe–Fe distance of **2a** increases about 0.04 Å. While the larger Fe–Fe distance was reported to influence the adjustment of the rotated state in [2Fe–2Se] mimics by making it energetically disfavored,[6,7,22,43] it may also affect the general catalytic activity and cluster stability due to the lower bond strength. This hypothesis is even more supported by the finding that while direct protonation of sulfur-based hexacarbonyl di-iron cluster mimics was never observed in the presence of HBF_4, selenium incorporation was reported to lead to a significant increase of electron density on iron and allowed for formation of a bridging hydride.[44] Since native-like catalytic activities in solution were obtained for CpI-ADSe and HydA1-ADSe, the maturation process appears to not have severely been affected by the different size, charge and weight of the ADSe compared

to the native ADT. However, we noted a decreased shelf-life stability of the ADSe variants, an effect generally observed for selenium substituted iron sulfur clusters.[38]

Interestingly, the catalytic activities recorded in electrochemical studies of both, the synthetic mimic **3** alone as well as CpI-ADSe and HydA1-ADSe were remarkably biased towards hydrogen evolution. This was further confirmed by in solution assays of CpI-ADSe and HydA1-ADSe determining the hydrogen uptake to hydrogen evolution ratio. As the presence of selenium enriches the electron density at the Fe–Fe core, a bias to hydrogen production could be anticipated. Electrochemical studies on sulfur to selenium exchanged in [2Fe] mimics allowed for the observation of this effect.[8,21]

However, for other selenium substituted cluster mimics, no influence on the catalytic bias was noted.[7,45] The lack of increased catalytic activity is often reasoned by outweighing the effects of the electron donor capability of selenium and the concurrent increase of the Fe–Fe bond length, which turns the catalytic rotated state energetically disfavorable. Contrary to the molecular [2Fe] mimics, within the protein the sulfur to selenium exchange clearly does not hinder the formation of the catalytically relevant rotated state as crystal structure analysis revealed a bridging CO-ligand and an open coordination site at the Fe_d. This might be due to the fact that the [2Fe] binding site is very rigid and only allows the [2Fe] mimic integration in the rotated configuration.[28]

The influence of the more electropositive selenium was clearly reflected in the IR spectroscopy of [2Fe] mimics as overall red shifts of 8 to 11 cm^{-1} were observed when S was exchanged for Se.[21,46] Herein, the better electron-donating capability of selenium results in an increased electron density at the iron atoms which leads to stronger π-backbonding of the CO- and CN^--ligands. Since the CN^--ligands are weaker π-acceptors compared to CO-ligands, the red shifts of the CN^- bands are less prominent than those of the CO-bands. The very same effect was observed here for ADSe incorporated into HydA1 and CpI. Comparison of the CO-inhibited spectra of CpI-ADT and CpI-ADSe clearly shows red shifts of 4 to 9 cm^{-1} for the CO signals. This behavior is in contrast to the results recently obtained for a sulfur to selenium exchange within the [4Fe–4S] subcluster of HydA1. Here, no changes in the corresponding FT-IR spectra were observed.[19] Thus contrary to corresponding alterations in the [4Fe–4S] cluster, the sulfur to selenium exchange within the [2Fe] cluster significantly modulates the electronic fine-structure at the catalytic active site.

As oxygen induced degradation of the H-cluster remains a challenge in the biotechnical use of hydrogenases, we thus further questioned the altered stability of HydA1-ADSe and CpI-ADSe in the presence of oxygen as compared to their native counterparts. [FeFe]-hydrogenases are damaged by O_2 but the mechanism of inactivation is still under debate.[47–49] A drastic decrease in oxygen stability was observed for CpI-ADSe, as well as for HydA1-ADSe. While the O_2 stability of the enzymes attached to electrodes is different to the *in vitro* assays, similar observations were recently reported and explained by differences in the proton/electron availability between both experimental setups causing a variability in the nature of the degradation products.[50] A similar decrease in oxygen stability upon sulfur to selenium exchange was shown previously for a [4Fe–4S] cluster within a ferredoxin from *C. pasteurianum*.[51]

Conclusions

In conclusion, we herein presented the first study allowing for variation of the H-cluster with a non-naturally relevant synthetic cofactor within two structurally different [FeFe]-hydrogenases maintaining native-like enzymatic activities. We therefore extended the possibilities of sulfide to selenide exchanges beyond simple electron transfer systems to the active site of enzymatic catalysis. As such, this study shows the high potential of combining biological and chemical methods to design and tune the properties of enzymes.

Experimental

All reactions were performed under dry Ar atmosphere using standard Schlenk techniques or in a Glovebox (*MBraun*). $Fe_3Se_2(CO)_9$ [24] and $Fe_2Se_2(CO)_6$ [52] were synthesized according to literature procedures. All other compounds were obtained from commercial vendors and used without further purification. All solvents were dried prior to use according to standard methods. ^1H, $^{13}C\{^1H\}$, and $^{77}Se\{^1H\}$ NMR spectra were recorded with a Bruker DPX-200 NMR or a *Bruker* DPX-250 NMR spectrometer at room temperature. Peaks were referenced to residual ^1H signals from the deuterated solvent and are reported in ppm. $^{77}Se\{^1H\}$ NMR spectra were recorded by using Ph_2Se_2 (δ = 463 ppm) as an external reference and are reported in ppm. IR spectra were measured with a *Bruker* Tensor 27 FT-IR spectrometer in solution and are reported in cm^{-1}.

$(ClCH_2)_2NC(O)OCH_2Ph$ (1a)

Benzyl carbamate (5 g, 33 mmol), paraformaldehyde (2 g, 66 mmol) and potassium hydroxide (20 mg, 0.35 mmol) were combined in small flask and fused at 150 °C. The clear melt was then added to freshly distilled, stirring $SOCl_2$ (10 mL) resulting in strong gas development. The reaction mixture was stirred until the gas development stopped (about 3–4 h) and excess $SOCl_2$ was removed under reduced pressure to yield a viscous clear oil. **IR** (ATR, cm^{-1}): 1725. **^1H NMR** (200 MHz, $CDCl_3$): δ 7.36 (s, 5H, aromat.), 5.37 (s, 4H, $ClCH_2$), 2.17 (s, 2H, OCH_2Ph). **$^{13}C\{^1H\}$ NMR** (51 MHz, $CDCl_3$): δ 153.1 (carbonyl), 135.0 (quart. aromat.), 128.6 (aromat.), 128.5 (aromat.), 128.0 (aromat.), 69.0 (O-CH_2), 57.5 (–CH_2Cl,), 57.2 (–CH_2Cl).

$(ClCH_2)_2NC(O)OCH_2CH_3$ (1b)

Prepared as **1a**, starting with 5 g (56 mmol) ethyl carbamate and 3.7 g (123 mmol) paraformaldehyde. **IR** (ATR, cm^{-1})

ν(C═O): 1722. **^{1}H NMR** (200 MHz, $CDCl_3$): δ 5.28 (s, 4H, $ClCH_2$), 4.21 (q, 2H, OCH_2), 1.25 (t, 3H, CH_3). **^{13}C{^{1}H} NMR** (51 MHz, $CDCl_3$): δ 153.2 (carbonyl), 63.6 (N-CH_2), 63.2 (O-CH_2,), 14.3 (CH_3).

$[Fe_2\{\mu(SeCH_2)_2N(Cbz)\}(CO)_6]$ (2a)

$Fe_2(CO)_6Se_2$ (244 mg, 0.56 mmol) was dissolved in 10 mL dry THF and cooled to −78 °C. Subsequently, 1.23 mL Li $(Et)_3BH$ (0.123 mmol, 1 M in THF) were added dropwise leading to a color change to brownish red. The solution was then stirred for 15 minutes under these conditions. Afterwards, **1** (208 mg, 0.84 mmol) was slowly added *via* syringe. The solution was stirred for 13 h while it achieves room temperature. The solvent was removed, the crude brownish red solid dissolved in a small amount of PE/DCM (1 : 3) and transferred to a chromatography column (SiO_2, PE/DCM (1 : 3)). The second band contained 60 mg (0.11 mmol, 20%) of ($Fe_2(CO)_6Se_2(CH_2)_2$N-Cbz). **IR** (ATR in Hexane, cm^{-1}): 2064, 2026, 1974, 1710. **^{1}H NMR** (200 MHz, $CDCl_3$): δ 7.37 (s, 5H, aromat.), 5.18 (s, 2H, OCH_2), 4.24 (broad, 4H, $SeCH_2$). **^{13}C{^{1}H} NMR** (63 MHz, $CDCl_3$): δ 207.9 (CO), 152.5 (carbamate), 135.0 (quart. aromat.), 128.7 (aromat.), 128.4 (aromat.), 128.0 (aromat.), 69.1 (O-CH_2), 36.9 (Se-CH_2,), 36.5 (Se-CH_2). **^{77}Se-NMR** (48 MHz, $CDCl_3$): δ 783.

$[Fe_2\{\mu(SeCH_2)_2N(COOCH_2CH_3)\}(CO)_6]$ (2b)

Prepared as **2a**, starting with 200 mg (0.46 mmol) $Fe_2(CO)_6Se_2$ and 94 mg (0.51 mmol) **1b**. **IR** (ATR, cm^{-1}) ν(CO): 2066, 2023, 1980; ν(C═O): 1709. **^{1}H NMR** (200 MHz, $CDCl_3$): δ 4.24 (broad, 4H, $SeCH_2$), 4.22 (q, 2H, OCH_2), 1.31 (t, 3H, $-CH_3$). **^{13}C{^{1}H} NMR** (63 MHz, $CDCl_3$,): δ 208.0 (CO), 152.8 (carbamate), 63.6 (O-CH_2), 37.0 (Se-CH_2,), 36.7 (Se-CH_2), 14.5 ($-CH_3$).

$[Fe_2\{\mu(SeCH_2)_2NH\}(CO)_6]$ (3)

$[Fe_2\{\mu(SeCH_2)_2N(Cbz)\}(CO)_6]$ (**2a**) (40 mg, 73 μmol) was dissolved in 1.5 mL dry DCM. To the red solution, 185 μL $BF_3{\cdot}OEt_2$ (99.6 mg, 48% in DCM) and 214 μL Me_2S (1.98 mmol) were added. The mixture was then stirred for 1.5 hours, before additional 118 μL (1.62 mmol) Me_2S were added and stirred for further 2 hours. The solution was transferred into a flask containing 1.5 mL degassed H_2O *via* a syringe. To the orange solution 1.5 mL degassed NH_4OH (10%) were added. The mixture was then transferred into a Schlenk separating funnel and extracted with 3 × 5 mL $CHCl_3$. The organic phases were combined, washed with water (2 mL), brine (5 mL) and dried over $MgSO_4$. The solvent was removed and the residue purified by column chromatography (SiO_2, PE → PE/DCM (3 : 1)) under inert conditions. The pure PE phase contained decomposition products and was discarded. The second band after changing to the PE/DCM mixture contains 7 mg (14.5 μmol, 20%) of $[Fe_2(CO)_6\{(SeCH_2)_2NH\}]$ (**3**). **IR** (ATR in Hexane, cm^{-1}): 2062, 2021, 1981. **^{1}H NMR** (250 MHz, $CDCl_3$): δ 3.83 (d, 4H, $SeCH_2$). **^{77}Se-NMR** (48 MHz, $CDCl_3$): δ 784.

$[Fe_2\{\mu(SeCH_2)_2NH\}(CO)_4(CN)_2](N(Et)_4)_2$ (ADSe)

In a 10 ml Schlenk flask, compound **2** (7 mg, 14.5 μmol) was dissolved in 2 mL acetonitrile. In a separate flask, $N(Et)_4CN$ (5 mg, 30 μmol) was dissolved in 0.5 mL acetonitrile. Both solutions were cooled to 0 °C and combined *via* a syringe. The mixture was then stirred for 3 hours at room temperature before the solvent was removed. The flask was transferred into a glovebox and the residue washed with diethyl ether/MeCN (20 : 1) and dried under reduced pressure to yield 7 mg (9.5 μmol, 65%) of ADSe. **IR** (ATR, cm^{-1}) ν(CO): 2022, 1991, 1940; ν(CN): 2075. **^{1}H NMR** (250 MHz, $CDCl_3$): δ 3.2 (d, 4H, $SeCH_2$). **^{13}C{^{1}H} NMR** (63 MHz, $CDCl_3$): δ 215.4 (CO), 53.3 (Se-CH_2). **^{77}Se-NMR** (48 MHz, $CDCl_3$): δ 783.

Protein expression and purification

[FeFe]-hydrogenases HydA1 from *Chlamydomonas reinhardtii*[53] (48 kDa) and CpI from *Clostridium pasteurianum* (65 kDa) with C-terminal fused strep-tagII were heterologously expressed in *Escherichia coli* BL21(DE3)ΔiscR[54] in absence of specific maturases therefore lacking the [2Fe] cluster (apoHydA1 and apoCpI).[27] Strep-tactin affinity chromatography (*iba*, Göttingen, Germany) was used for protein purification under strictly anaerobic conditions using 100 mM Tris-HCl buffer (pH 8.0) with 2 mM sodium dithionite (NaDT).[55] Protein concentrations were determined by the method of Bradford using bovine serum albumin as standard and protein purity was assessed by SDS-PAGE.[56] Bovine serum albumin was obtained commercially (*Carl Roth*, Karlsruhe, Germany).

In vitro maturation

$[Fe_2\{\mu(SeCH_2)_2NH\}(CN)_2(CO)_4][Et_4N]_2$ (ADSe) was dissolved in 100 mM K_2HPO_4/KH_2PO_4 buffer (pH 6.8) to concentrations of 3.9 to 6.7 mM. A threefold molar excess of ADSe was added to 130 to 275 μm apoHydA1 initiating the maturation process in a final volume of 500 μL 100 mM K_2HPO_4/KH_2PO_4 buffer (pH 6.8) with 2 mM NaDT at RT for 1 h.[3] Subsequently the excess of ADSe was removed *via* size exclusion chromatography using a NAP5™ column (*GE Healthcare*) equilibrated with 50 mM M K_2HPO_4/KH_2PO_4 buffer 100 mM KCl (pH 8.0). For maturation of 90 μM apoCpI a fivefold excess of ADSe was used and chromatography was performed with 10 mM Tris-HCl buffer (pH 8.0) with 2 mM NaDT. Protein preparations were concentrated up to 1 mM using 30 kDa Amicon Ultra centrifugal filter unit (*Millipore*) and stored anaerobically at −80 °C. Enzymatic activity was assayed for each protein preparation in order to ensure protein quality.

Enzymatic assay for hydrogen evolution

A standard *in vitro* enzymatic activity assay of the variants of HydA1 and CpI[57] was performed within 8 mL anaerobically sealed vials (Suba-seal septa, *Sigma-Aldrich*, Munich, Germany) using 400 ng of *in vitro* maturated hydrogenase, 100 mM NaDT and 10 mM methylviologen in 100 mM K_2HPO_4/KH_2PO_4 buffer (pH 6.8) in a final volume of 2 mL. Hydrogen evolution was detected *via* gas chromatography after incubation at 37 °C for 30 min.

Enzymatic assay for hydrogen uptake

Hydrogen uptake was assayed based on procedures described in literature.[4,27] A sealed 1 mL UV-cuvette was flushed with H_2 before adding 955 μL 100 mM K_2HPO_4/KH_2PO_4 buffer (pH 6.8) containing 40 mM MV (HydA1) or 10 mM MV (CpI) and 5 μL *in vitro* maturated protein corresponding to 5 to 80 ng of total protein *via* a syringe. MV reduction was followed spectrophotometrically at 604 nm at 25 °C using a Beckman Coulter PARADIGM™ absorbance detection platform. Activity was estimated based on the initial slope of absorbance *versus* time determined using linear regression.

Oxygen exposure of CpI-ADSe and HydA1-ADSe to air saturated buffer

Influence of oxygen on CpI-ADT and HydA1-ADT in comparison to CpI-ADSe and HydA1-ADSe was tested by exposing *in vitro* maturated hydrogenase to air saturated buffer prior to a hydrogen evolution assay. Within a 2 mL reaction tube 50 ng of *in vitro* maturated hydrogenase, anaerobic 100 mM K_2HPO_4/KH_2PO_4 buffer (pH 6.8) and increasing amounts of air saturated 100 mM K_2HPO_4/KH_2PO4 buffer (pH 6.8) yielding a total volume of 140 μL were mixed. After incubation for 5 min the reaction was quenched adding 60 μL of a NaDT/MV premixture leading to final concentrations of 200 mM and 10 mM respectively. Hydrogen evolution was detected *via* gas chromatography after anaerobic incubation at 37 °C for 20 min.

FT-IR spectroscopy

All measurements were done anaerobically. Transmission FT-IR spectra were recorded on a Bruker Vertex 80v spectrometer with a mercury cadmium telluride (MCT) detector at a spectral resolution of 2 cm^{-1}. The measuring cell with CaF_2 windows was cooled to 15 °C controlled by a *Huber* Minichiller. Baseline correction was facilitated with home written routines in MATLAB. A water cooled Harrick/Bruker BioATR cell II was used with a Bruker Tensor 27 spectrometer equipped with a MCT detector in a continuously purged glovebox.

Electrochemistry

Electrochemical testing of the complexes was conducted in acetonitrile using a standard three-electrode setup using a GAMRY Reference 600 potentiostate. A glassy carbon (GC) electrode was used as working electrode. $Ag/AgNO_3$ (0.1 M in CH_3CN) and a Pt wire were used as reference and counter electrode, respectively. If not otherwise stated, 0.05 M $TBAPF_6$ was used as the electrolyte and the measured potential was referenced to the ferrocene/ferrocenium couple (Fc/Fc^+) and transferred *vs.* SHE. Cyclic voltammetric measurements were then performed at a scan rate of 100 mV s^{-1}.

Protein film electrochemistry

A typical three electrode setup with a pyrolytic graphite (PGE) working electrode, a platinum wire as counter electrode and saturated Calomel reference electrode was used. The PGE electrode (homemade using pyrolytic graphite from *Momentive Materials*, 0.031 cm^2) was polished with aluminia MasterPrep Polishing Suspension (0.05 mm, Buehler), rinsed and sonicated for 5 min in Milli-Q water. All experiments were done in a N_2 filled glovebox from *MBraun*. The temperature of the electrochemical cell was controlled with a water-jacket system and water circuit pump (*Lauda*). All data are referred to the standard hydrogen electrode using a conversion of +241 mV.

The PGE electrode surface was polished under anaerobic conditions and afterwards covered with 4 μL diluted proteins for some minutes to perform adsorption. Proteins were diluted with 10 mM MES, 2 mM NaDT pH 5.8 to a concentration of 3 μM. About 5 mL pH 7 mixed buffer (100 mM NaCl, 25 mM NaOAc, 15 mM each MES, HEPES, TAPS, CHES) was used in the measuring cell. All measurements are performed at 25 °C, under 100% hydrogen with working electrode rotation of 2000 rpm and scan rate of 20 mV s^{-1}. A Parstat MC potentiostat (*Princeton Applied Research*) was used. In the amperometric oxygen tolerance tests (−0.039 V) same amounts of the oxygen saturated mixed buffer were added at two time points and the current was recorded for at least 700 s. For low currents the traces were smoothed.

Crystallography

A 1 : 1 mixture of 150 μM CpI-ADSe and 100 mM MES pH 6.5, 0.2 M MgCl2 19% PEG 4000 21% Glycerol buffer was used in a hanging drop vapor diffusion experiment leading to rod shaped brown crystals within 7 days at 4 °C. Crystals were mounted into Cryo-Loops™ (*Hampton Research*) and flash-frozen with liquid N_2 under anaerobic conditions.[28] The presence of Se in the crystals was confirmed by measurements of the X-ray fluorescence spectrum (Fig. S7†) and fluorescence-detected X-ray absorption around the Se-edge at 12 656 eV (Fig. 3B). Collection of diffraction data took place at the beamline ID-30A (FIPS) of the ESRF (Grenoble, France) at 100 K with incident beam wavelength of 12 644 eV. The dataset was processed with the space group *P*21 using the software package XDS[58] and structure optimization was performed with the help of software packages PHENIX[59] and COOT.[60] The available structure of CpI-ADT (PDB 4XDC) with a resolution of 1.63 Å was used as starting model for refinement, whereas the S of the [2Fe] cluster was replaced by Se in the model as well as in the restraint file for the cluster. The anomalous data was not used for the refinement. Initially six rounds of refinement of the protein scaffold were performed omitting the [2Fe] cluster by setting its occupancy to 0 (R_{work} 0.2245; R_{free} 0.2582). This model was used to introduce the selenium containing [2Fe] cluster by setting its initial occupancy to 0.9 and performing three rounds of rigid body, *B*-factor and occupancy refinement of the [2Fe] cluster only, because the resolution did not allow for *xyz* coordinate refinement of the [2Fe] cluster itself. In between these cycles, the *xyz* coordinates, *B*-factor and occupancies of the protein scaffold were refined. In these final rounds of refinement the Fe to ligand distances within the accessory [4Fe–4S] and [2Fe–2S] cluster were custom restraint

using values obtained from the starting model (PDB: 4XDC). This led to a model refined to 2.05 Å resolution with R_{work} and R_{free} values of 0.2321 and 0.2685 (PDB: 5OEF), respectively. Simulated annealing omit maps were calculated with PHENIX, omitting the [2Fe] cluster and the complete H-cluster with the bridging cysteine residue as well as all aminoacids within the central cavity (Fig. S8 and S9†).

Author contributions

LK, MW and TH designed and performed the maturation experiments. FW and UPA performed the syntheses of the materials. CS, EJR and WL performed the spectroscopic investigations. Electrochemical analysis was performed by CS and OR. LK, JE and EH were responsible for protein crystallography. MW, TH and UPA coordinated the project. All authors contributed in writing the manuscript.

Funding sources

This work was supported by the Max Planck Society. The authors are grateful for support by the Cluster of Excellence RESOLV (EXC1069) and the DIP Programme (LU 315/17-1) funded by the Deutsche Forschungsgemeinschaft (DFG). We thank the Fond der Chemischen Industrie for supporting LK by a Kekulé Mobility Fellowship and U.-P. A. by a Liebig grant. U.-P. A. was further supported by the DFG (Emmy Noether grant AP242/2-1).

Conflicts of interest

The authors declare no competing financial interest.

Abbrevations

ADSe	$[Fe_2\{\mu(SeCH_2)_2NH\}(CO)_4(CN)_2]^{2-}$
ADT	$[Fe_2\{\mu(SCH_2)_2NH\}(CO)_4(CN)_2]^{2-}$
apoCpI	Apoform of CpI only harboring the [4Fe–4S] subcluster
apoHydA1	Apoform of HydA1 only harboring the [4Fe–4S] subcluster
CpI	[FeFe]-hydrogenases CpI from *Clostridium pasteurianum*
CpI-ADSe	CpI maturated with ADSe
CpI-ADT	CpI maturated with ADT
CV	Cyclic voltammograms
Fe_d	Distal iron atom of the [2Fe] cluster relative to the [4Fe–4S] moiety
FT-IR	Fourier-transform infrared
holoCpI	Holoform of CpI harboring the [4Fe–4S] and [2Fe] cluster
holoHydA1	Holoform of HydA1 harboring the [4Fe–4S] and [2Fe] cluster
HydA1	[FeFe]-hydrogenases HydA1 from *Chlamydomonas reinhardtii*
HydA1-ADSe	HydA1 maturated with ADSe
HydA1-ADT	HydA1 maturated with ADT
MV	Methyl viologen
NaDT	Sodium dithionite
PGE	Pyrolytic graphite edge
WT	Wild-type

Acknowledgements

We thank the staff of beamline ID-30A (FIPS) of the ESRF (Grenoble, France) for technical support during X-ray data collection.

References

1 W. Lubitz, H. Ogata, O. Rüdiger and E. Reijerse, *Chem. Rev.*, 2014, **114**, 4081–4148.
2 M. C. Marques, C. Tapia, O. Gutiérrez-Sanz, A. R. Ramos, K. L. Keller, J. D. Wall, A. L. De Lacey, P. M. Matias and I. A. C. Pereira, *Nat. Chem. Biol.*, 2017, **13**, 544–550.
3 J. Esselborn, C. Lambertz, A. Adamska-Venkatesh, T. Simmons, G. Berggren, J. Noth, J. Siebel, A. Hemschemeier, V. Artero, E. Reijerse, M. Fontecave, W. Lubitz and T. Happe, *Nat. Chem. Biol.*, 2013, **9**, 607–609.
4 J. F. Siebel, A. Adamska-Venkatesh, K. Weber, S. Rumpel, E. Reijerse and W. Lubitz, *Biochemistry*, 2015, **54**, 1474–1483.
5 M. Bourrez, R. Steinmetz and F. Gloaguen, *Inorg. Chem.*, 2014, **53**, 10667–10673.
6 U.-P. Apfel, H. Görls, G. A. Felton, D. H. Evans, R. S. Glass, D. L. Lichtenberger and W. Weigand, *Helv. Chim. Acta*, 2012, **95**, 2168–2175.
7 M. K. Harb, U.-P. Apfel, J. Kübel, H. Görls, G. A. N. Felton, T. Sakamoto, D. H. Evans, R. S. Glass, D. L. Lichtenberger, M. El-khateeb and W. Weigand, *Organometallics*, 2009, **28**, 6666–6675.
8 U.-P. Apfel, Y. Halpin, M. Gottschaldt, H. Görls, J. G. Vos and W. Weigand, *Eur. J. Inorg. Chem.*, 2008, **2008**, 5112–5118.
9 L.-C. Song, Z.-Y. Yang, H.-Z. Bian, Y. Liu, H.-T. Wang, X.-F. Liu and Q.-M. Hu, *Organometallics*, 2005, **24**, 6126–6135.
10 L.-C. Song, Z.-Y. Yang, Y.-J. Hua, H.-T. Wang, Y. Liu and Q.-M. Hu, *Organometallics*, 2007, **26**, 2106–2110.
11 J. W. Peters, W. N. Lanzilotta, B. J. Lemon and L. C. Seefeldt, *Science*, 1998, **282**, 1853–1858.
12 B. Ginovska-Pangovska, M.-H. Ho, J. C. Linehan, Y. Cheng, M. Dupuis, S. Raugei and W. J. Shaw, *Biochim. Biophys. Acta, Bioenerg.*, 2014, **1837**, 131–138.

13 A. J. Cornish, B. Ginovska, A. Thelen, J. C. S. da Silva, T. A. Soares, S. Raugei, M. Dupuis, W. J. Shaw and E. L. Hegg, *Biochemistry*, 2016, **55**, 3165–3173.
14 A. J. Cornish, K. Gartner, H. Yang, J. W. Peters and E. L. Hegg, *J. Biol. Chem.*, 2011, **286**, 38341–38347.
15 O. Sode and G. A. Voth, *J. Chem. Phys.*, 2014, **141**, 22D527.
16 D. W. Mulder, Y. Guo, M. W. Ratzloff and P. W. King, *J. Am. Chem. Soc.*, 2017, **139**, 83–86.
17 E. J. Reijerse, C. C. Pham, V. Pelmenschikov, R. Gilbert-Wilson, A. Adamska-Venkatesh, J. F. Siebel, L. B. Gee, Y. Yoda, K. Tamasaku, W. Lubitz, T. B. Rauchfuss and S. P. Cramer, *J. Am. Chem. Soc.*, 2017, **139**, 4306–4309.
18 B. J. Lemon and J. W. Peters, *Biochemistry*, 1999, **38**, 12969–12973.
19 J. Noth, J. Esselborn, J. Güldenhaupt, A. Brünje, A. Sawyer, U.-P. Apfel, K. Gerwert, E. Hofmann, M. Winkler and T. Happe, *Angew. Chem., Int. Ed.*, 2016, **55**, 8396–8400.
20 W. Gao, L.-C. Song, B.-S. Yin, H.-N. Zan, D.-F. Wang and H.-B. Song, *Organometallics*, 2011, **30**, 4097–4107.
21 W. Gao, J. Liu, W. Jiang, M. Wang, L. Weng, B. Åkermark and L. Sun, *Comptes Rendus Chimie*, 2008, **11**, 915–921.
22 M. K. Harb, U.-P. Apfel, T. Sakamoto, M. El-khateeb and W. Weigand, *Eur. J. Inorg. Chem.*, 2011, **2011**, 986–993.
23 H. Li and T. B. Rauchfuss, *J. Am. Chem. Soc.*, 2002, **124**, 726–727.
24 W. Hieber and J. Gruber, *Z. Anorg. Allg. Chem.*, 1958, **296**, 91–103.
25 L. Sun, B. Akermark and S. Ott, *Coord. Chem. Rev.*, 2005, **249**, 1653–1663.
26 K. Fuji, K. Ichikawa, M. Node and E. Fujita, *J. Org. Chem.*, 1979, **44**, 1661–1664.
27 J. M. Kuchenreuther, C. S. Grady-Smith, A. S. Bingham, S. J. George, S. P. Cramer and J. R. Swartz, *PLoS One*, 2010, **5**, e15491.
28 J. Esselborn, N. Muraki, K. Klein, V. Engelbrecht, N. Metzler-Nolte, U.-P. Apfel, E. Hofmann, G. Kurisu and T. Happe, *Chem. Sci.*, 2016, **7**, 959–968.
29 J.-F. Capon, S. Ezzaher, F. Gloaguen, F. Y. Pétillon, P. Schollhammer and J. Talarmin, *Chem. – Eur. J.*, 2008, **14**, 1954–1964.
30 A. Adamska-Venkatesh, D. Krawietz, J. Siebel, K. Weber, T. Happe, E. Reijerse and W. Lubitz, *J. Am. Chem. Soc.*, 2014, **136**, 11339–11346.
31 S. V. Hexter, F. Grey, T. Happe, V. Climent and F. A. Armstrong, *Proc. Natl. Acad. Sci. U. S. A.*, 2012, **109**, 11516–11521.
32 G. Goldet, C. Brandmayr, S. T. Stripp, T. Happe, C. Cavazza, J. C. Fontecilla-Camps and F. A. Armstrong, *J. Am. Chem. Soc.*, 2009, **131**, 14979–14989.
33 C. Baffert, K. Sybirna, P. Ezanno, T. Lautier, V. Hajj, I. Meynial-Salles, P. Soucaille, H. Bottin and C. Léger, *Anal. Chem.*, 2012, **84**, 7999–8005.
34 V. Fourmond, C. Greco, K. Sybirna, C. Baffert, P.-H. Wang, P. Ezanno, M. Montefiori, M. Bruschi, I. Meynial-Salles, P. Soucaille, J. Blumberger, H. Bottin, L. De Gioia and C. Léger, *Nat. Chem.*, 2014, **6**, 336–342.
35 C. Léger, S. J. Elliott, K. R. Hoke, L. J. C. Jeuken, A. K. Jones and F. A. Armstrong, *Biochemistry*, 2003, **42**, 8653–8662.
36 J. C. M. Tsibris, M. J. Namtvedt and I. C. Gunsalus, *Biochem. Biophys. Res. Commun.*, 1968, **30**, 323–327.
37 W. H. Orme-Johnson, R. E. Hansen, H. Beinert, J. C. Tsibris, R. C. Bartholomaus and I. C. Gunsalus, *Proc. Natl. Acad. Sci. U. S. A.*, 1968, **60**, 368–372.
38 J. Meyer, J.-M. Moulis, J. Gaillard and M. Lutz, in *Advances in Inorganic Chemistry*, Elsevier, 1992, vol. 38, pp. 73–115.
39 P. C. Hallenbeck, G. N. George, R. C. Prince and R. N. F. Thorneley, *JBIC, J. Biol. Inorg. Chem.*, 2009, **14**, 673–682.
40 J. L. Breton, J. A. Farrar, M. C. Kennedy, H. Beinert and A. J. Thomson, *Biochem. J.*, 1995, **311**, 197–202.
41 B. Tse Sum Bui, T. A. Mattioli, D. Florentin, G. Bolbach and A. Marquet, *Biochemistry*, 2006, **45**, 3824–3834.
42 G. Berggren, A. Adamska, C. Lambertz, T. R. Simmons, J. Esselborn, M. Atta, S. Gambarelli, J.-M. Mouesca, E. Reijerse, W. Lubitz, T. Happe, V. Artero and M. Fontecave, *Nature*, 2013, **499**, 66–69.
43 M. K. Harb, T. Niksch, J. Windhager, H. Görls, R. Holze, L. T. Lockett, N. Okumura, D. H. Evans, R. S. Glass, D. L. Lichtenberger, M. El-khateeb and W. Weigand, *Organometallics*, 2009, **28**, 1039–1048.
44 H. Abul-Futouh, M. El-khateeb, H. Gorls, K. J. Asali and W. Weigand, *Dalton Trans.*, 2017, **46**, 2937–2947.
45 M. K. Harb, H. Görls, T. Sakamoto, G. A. N. Felton, D. H. Evans, R. S. Glass, D. L. Lichtenberger, M. El-khateeb and W. Weigand, *Eur. J. Inorg. Chem.*, 2010, **2010**, 3976–3985.
46 M. K. Harb, J. Windhager, T. Niksch, H. Görls, T. Sakamoto, E. R. Smith, R. S. Glass, D. L. Lichtenberger, D. H. Evans, M. El-khateeb and W. Weigand, *Tetrahedron*, 2012, **68**, 10592–10599.
47 S. T. Stripp, *Proc. Natl. Acad. Sci. U. S. A.*, 2009, **106**, 17331–17336.
48 A. Kubas, D. De Sancho, R. B. Best and J. Blumberger, *Angew. Chem., Int. Ed.*, 2014, **53**, 4081–4084.
49 K. D. Swanson, M. W. Ratzloff, D. W. Mulder, J. H. Artz, S. Ghose, A. Hoffman, S. White, O. A. Zadvornyy, J. B. Broderick, B. Bothner, P. W. King and J. W. Peters, *J. Am. Chem. Soc.*, 2015, **137**, 1809–1816.
50 A. Kubas, C. Orain, D. De Sancho, L. Saujet, M. Sensi, C. Gauquelin, I. Meynial-Salles, P. Soucaille, H. Bottin, C. Baffert, V. Fourmond, R. B. Best, J. Blumberger and C. L?ger, *Nat. Chem.*, 2017, **9**, 88–95.
51 J. Meyer and J.-M. Moulis, *Biochem. Biophys. Res. Commun.*, 1981, **103**, 667–673.
52 L. E. Bogan, D. A. Lesch and T. B. Rauchfuss, *J. Organomet. Chem.*, 1983, **250**, 429–438.
53 T. Happe and J. D. Naber, *Eur. J. Biochem.*, 1993, **214**, 475–481.
54 M. K. Akhtar and P. R. Jones, *Appl. Microbiol. Biotechnol.*, 2008, **78**, 853–862.

55 G. Vonabendroth, S. Stripp, A. Silakov, C. Croux, P. Soucaille, L. Girbal and T. Happe, *Int. J. Hydrogen Energy*, 2008, **33**, 6076–6081.
56 M. M. Bradford, *Anal. Biochem.*, 1976, **72**, 248–254.
57 A. Hemschemeier, A. Melis and T. Happe, *Photosynth. Res.*, 2009, **102**, 523–540.
58 W. Kabsch, *Acta Crystallogr., Sect. D: Biol. Crystallogr.*, 2010, **66**, 125–132.
59 P. V. Afonine, R. W. Grosse-Kunstleve, N. Echols, J. J. Headd, N. W. Moriarty, M. Mustyakimov, T. C. Terwilliger, A. Urzhumtsev, P. H. Zwart and P. D. Adams, *Acta Crystallogr., Sect. D: Biol. Crystallogr.*, 2012, **68**, 352–367.
60 P. Emsley, B. Lohkamp, W. G. Scott and K. Cowtan, *Acta Crystallogr., Sect. D: Biol. Crystallogr.*, 2010, **66**, 486–501.

Supporting Information

Chalcogenide substitution in the [2Fe]-cluster of [FeFe]-hydrogenases conserves high enzymatic activity

Leonie Kertess[a‡], Florian Wittkamp[b‡], Constanze Sommer[c‡], Julian Esselborn[a], Olaf Rüdiger[c], Edward J. Reijerse[c], Eckhard Hofmann[d], Wolfgang Lubitz[c], Martin Winkler[a], Thomas Happe[a]*, Ulf-Peter Apfel[b]*

[a] Ruhr-Universität Bochum, Lehrstuhl für Biochemie der Pflanzen, AG Photobiotechnologie, Universitätsstraße 150, 44801 Bochum

[b] Ruhr-Universität Bochum, Anorganische Chemie I / Bioanorganische Chemie, Universitätsstraße 150, 44801 Bochum

[c] Max-Planck-Institut für Chemische Energiekonversion, Stiftstraße 34-36, 45470 Mülheim an der Ruhr

[d] Ruhr-Universität Bochum, Lehrstuhl für Biophysik, AG Röntgenstrukturanalyse an Proteinen, Universitätsstraße 150, 44801 Bochum

Additional catalytic activity data

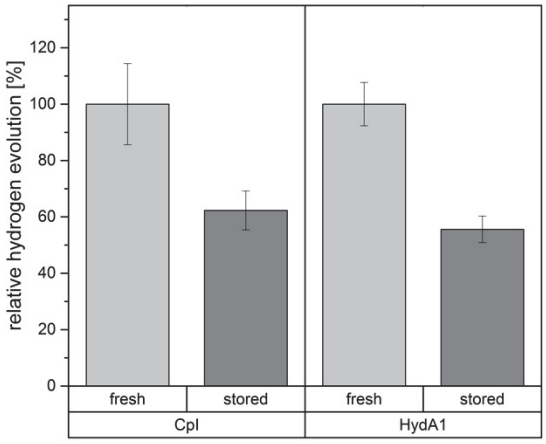

Figure S1. Comparison of relative hydrogen evolution activity of fresh and stored CpI-ADSe and HydA1-ADSe. Initial activities represent values obtained just after *in vitro* maturation. For shelf life tests CpI-ADSe sample was stored for 7 months at -80 °C while and HydA1-ADSe was stored for 1 month at -80 °C and thawed twice. Measurements were done in triplicates. Activity tests for methyl viologen dependent H_2 production was carried out in 100 mM K_2HPO_4/KH_2PO_4 buffer (pH 6.8), 10 mM methyl viologen with the addition of 100 mM sodium dithionite. Activities are presented relative to initial HydA1-ADT and CpI-ADT activity (both set to 100 %). Error bars indicate standard deviation.

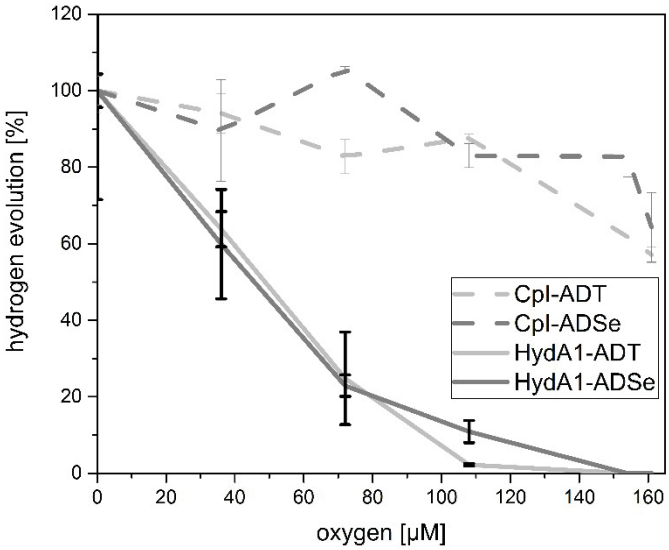

Figure S2. Oxygen exposure of CpI-ADT, CpI-ADSe, HydA1-ADT and HydA1-ADSe to air saturated buffer. Increasing amounts of air saturated buffer corresponding to 0 to 161 µM oxygen were added to 50 ng of *in vitro* maturated hydrogenases and incubated for 5 min at RT in order to compare the influence of oxygen on CpI-ADT, CpI-ADSe, HydA1-ADT and HydA1-ADSe. Data was obtained from parallel measurements in duplicate. Initial activities of CpI-ADT, CpI-ADSe, HydA1-ADT and HydA1-ADSe e were set to 100 %. Error bars indicate standard deviation.

Table S1. H_2 production activities of CpI-ADSe, HydA1-ADSe, CpI-ADT and HydA1-ADT in [µmol H_2 per min per mg enzyme]. Activity tests for methyl viologen dependent H_2 production was carried out in 100 mM K_2HPO_4/KH_2PO_4 buffer (pH 6.8), 10 mM methyl viologen with the addition of 100 mM sodium dithionite. Representative data of HydA1-ADSe and CpI-ADSe from two independent preparations for at least two measurements in triplicates from samples analyzed by FT-IR spectroscopy in parallel.

[FeFe]-hydrogenase	ADSe	ADT
CpI	1240 ± 178	1453 ± 225
HydA1	1198 ± 93	983 ± 82

Table S2. H_2 production and uptake activities of CpI-ADSe, HydA1-ADSe, CpI-ADT and HydA1-ADT. Activities given in [µmol H2 per min per mg enzyme] using MV as electron mediator. Ratio of MV dependent H_2 uptake to H_2 production is given as ratio. Activity tests for MV dependent H_2 production were carried out in 100 mM K_2HPO_4/KH_2PO_4 buffer (pH 6.8), 10 mM MV with the addition of 100 mM NaDT. The activity tests for MV dependent H_2 uptake were carried out in 100 mM K_2HPO_4/KH_2PO_4 buffer (pH 6.8), 40 mM MV (HydA1) or 10 mM MV (CpI) using 5 to 80 ng enzyme under 100 % H_2. H_2 production and uptake were determined on the same day from identical protein preparations.

Sample	H_2 evolution [µmol H_2 per min per mg protein]	H_2 uptake [µmol H_2 per min per mg protein]	Ratio uptake/evolution
CpI-ADT	2335 ± 86	410 ± 47	17.6×10^{-2}
CpI-ADSe	1582 ± 207	79 ± 36	5.0×10^{-2}
HydA1-ADT	728 ± 5	281 ± 3	$38.6\ 10^{-2}$
HydA1-ADSe	199 ± 62	19 ± 3	9.5×10^{-2}

It should be noted that for exact comparison of activities, ideally the same amount of protein and electron mediator should be used in the measurement, which, however, was not possible for the oxidation assays due to the diversity of activities and the need to stay within the linear range of the spectrometer. Since this analysis was done about one year after the initial measurements presented in Table S1, the overall higher hydrogen evolution activities might be reasoned by a different batch of chemicals and slight modifications in the detection method. However, the values reflect the same trends as seen before and are still within the range reported in literature.[1]

Additional Spectroscopy Data

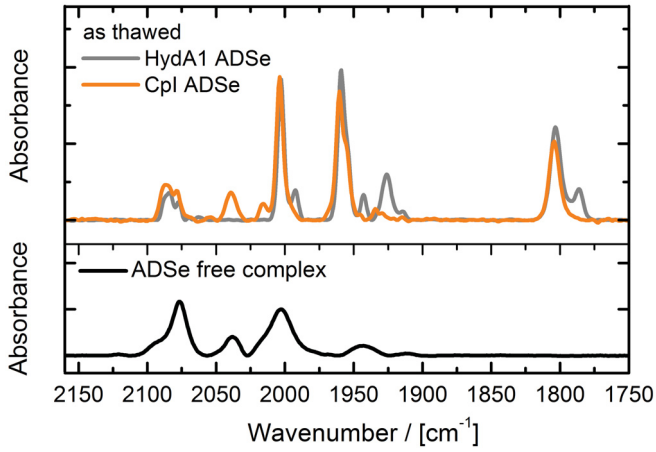

Figure S3. Transmission FT-IR spectra of CpI-ADSe and HydA1-ADSe (350 µM) as thawed and ADSe free complexes. Samples were in 100 mM Tris-HCl, 150 mM NaCl (pH 8). Spectra were taken at 15°C with 2 cm^{-1} resolution.

The free ADSe complex in aqueous solution shows an IR pattern different from that of ADT. The shifts are rather large, suggesting that the complex adopts a different conformation. The observed bands for ADSe do not fit to any known ADT variants.[2]

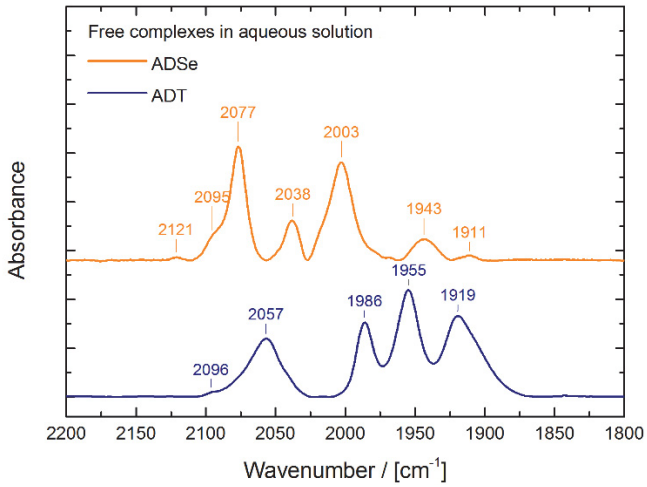

Figure S4. Transmission FT-IR spectra of free complexes in aqueous solution. ADSe complex in solution shows a blue shift compared to ADT in its CO and CN^- vibrations.

In the FTIR of CpI-ADT as well as CpI-ADSe (Figure 2) two CO vibrations strongly overlap. In Figure S5 these bands are deconvoluted using two Gaussian line shapes. For the fits following equations were used:

$$y = a \cdot \exp\left(\frac{-(x-x_0)^2}{2 \cdot b^2}\right) \quad (1)$$

$$\mathrm{FWHM} = 2 \cdot \sqrt{2 \cdot \ln(2)} \cdot b \quad (2)$$

For CpI-ADT the fits result in peak positions of 1974 and 1970 cm^{-1} which is consistent with the data reported in literature.[3]

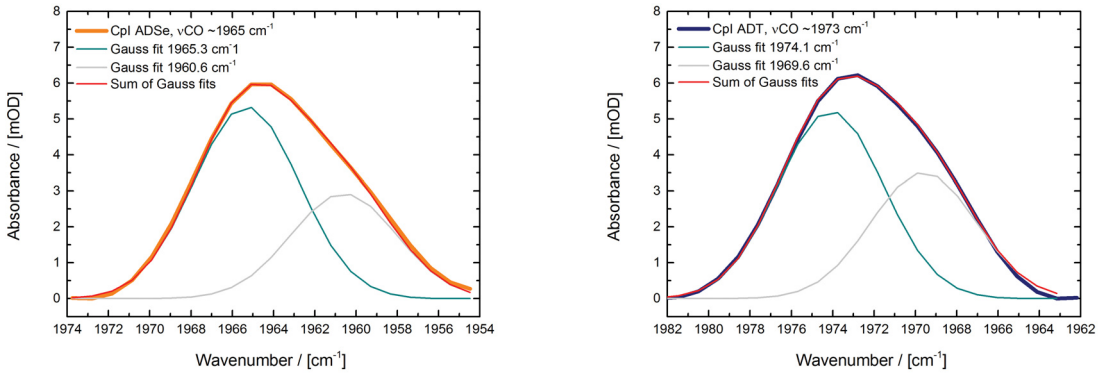

Figure S5. Gauss fits of overlapping CO bands of CpI-ADSe (left) and CpI-ADT (right). Left: Following parameters are used: 1965.3 cm^{-1}, a1= 5.35 (corresponding to 64%); 1960.6 cm^{-1}, a2= 2.93 with FWHM 6.0 for both fits. Right: 1974.1 cm^{-1}, a1= 5.23 (60%), 1969.6 cm^{-1}, a2= 3.52 with FWHM 6.0 each. Gauss fits are calculated in the same spectral resolution as the experimental spectra.

Additional Structural Data

Table S3. Crystal data and structure refinement for 2a and 2b.

Property	Value	
Identification code	**2a**	**2b**
Empirical formula	$C_{24}HN_{13}O_{10}FeSe_4$	$C_{11}H_9NO_8Fe_2Se_2$
Formula weight	614.88	552.81
Temperature/K	114(4)	111(1)
Crystal system	triclinic	monoclinic
Space group	P-1	$P2_1/n$
a/Å	7.8537(2)	9.78531(10)
b/Å	9.3351(2)	8.65801(11)
c/Å	14.4434(4)	20.60799(20)
α/°	100.188(2)	90
β/°	100.216(2)	102.8436(10)
γ/°	100.918(2)	90
Volume/$Å^3$	998.70(5)	1702.25(3)
Z	2	4
$\rho_{calc}g/cm^3$	2.0446	2.157
μ/mm^{-1}	16.229	18.940
F(000)	589.9	1064.0
Crystal size/mm^3	0.1744 × 0.1349 × 0.1	0.23 × 0.1027 × 0.0791
Radiation	Cu Kα (λ = 1.54184)	CuKα (λ = 1.54184)
2Θ range for data collection/°	9.88 to 152.36	8.802 to 152.814
Index ranges	-9 ≤ h ≤ 9, -11 ≤ k ≤ 11, -17 ≤ l ≤ 17	-12 ≤ h ≤ 12, -10 ≤ k ≤ 10, -25 ≤ l ≤ 25
Reflections collected	19982	25880
Independent reflections	4105 [R_{int} = 0.0249, R_{sigma} = 0.0164]	3540 [R_{int} = 0.0262, R_{sigma} = 0.0126]
Data/restraints/parameters	4105/0/261	3540/0/218
Goodness-of-fit on F^2	1.054	1.048
Final R indexes [I>=2σ (I)]	R_1 = 0.0236, wR_2 = 0.0628	R_1 = 0.0171, wR_2 = 0.0420
Final R indexes [all data]	R_1 = 0.0248, wR_2 = 0.0633	R_1 = 0.0181, wR_2 = 0.0424
Largest diff. peak/hole / e $Å^{-3}$	0.61/-0.45	0.38/-0.47
CCDC reference	1570441	1570440

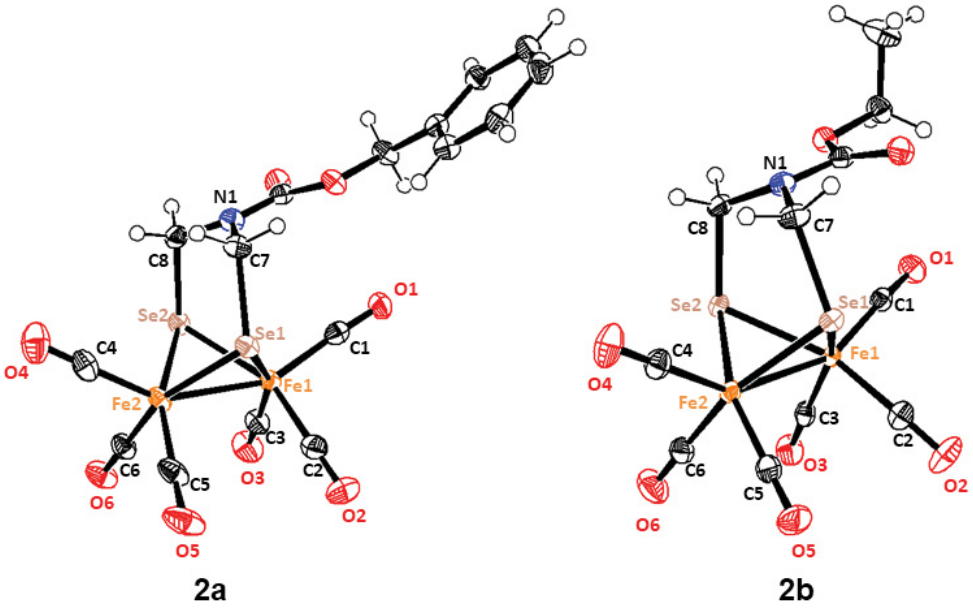

Figure S6. ORTEP representation of the asymmetric unit of $[Fe_2\{\mu(SeCH_2)_2NCO(O)CH_2Ph\}(CO)_6]$ (2a) and $[Fe_2\{\mu(SeCH_2)_2NCO(O)CH_2CH_3\}(CO)_6]$ (2b). Ellipsoids displayed at 50% probability.

Table S4. Selected bond lengths and angles of 2a and 2b.

Atoms	Bond length [Å] / Bond angle [°]	
	2a	**2b**
Fe1-Fe2	2.5405(5)	2.5296(4)
Fe1-Se1	2.3733(4)	2.3906(3)
Fe1-Se2	2.3859(4)	2.3765(3)
Fe2-Se1	2.3882(4)	2.3766(3)
Fe2-Se2	2.3768(4)	2.3901(3)
Se1-C7	2.008(2)	1.9946(18)
Se2-C8	1.996(2)	2.0058(17)
Se1-Fe1-Se2	87.063(13)	86.964(10)
Se1-Fe1-Fe2	58.040(11)	57.684(9)
Se2-Fe1-Fe2	57.591(12)	58.208(9)
Se1-Fe2-Fe1	57.471(11)	58.223(9)
Se1-Fe2-Se2	86.932(13)	86.964(10)
Se2-Fe2-Fe1	57.939(12)	57.689(9)
Fe1-Se1-Fe2	64.489(12)	64.093(10)
Fe1-Se2-Fe2	64.471(13)	64.103(10)

Table S5. Crystal data and refinement statistics.

Property	Value
Wavelength (eV)	12644
Space group	P 1 2_1 1
Unit cell parameters	90.35 72.88 103.10
a, b, c, α, β, γ	90.0 98.7 90.0
Resolution range (Å)	47.50 - 2.05 (2.10 - 2.05)[a]
Total reflections	615226 (46457)
Unique reflections	162396 (12146)
Multiplicity	3.78843 (3.8248)
Completeness (%)	99.5 (99.7)
R_{meas} **(%)**	16.9 (119.9)
I/σ **(I)**	7.15 (1.50)
CC 1/2	99.3 (72.3)[b]
Resolution (Å)	2.05
R_{work}	0.2321 (0.3328)
R_{free}	0.2685 (0.3757)
No. atoms (except H)	9760
Protein	8933
Ligand	106
Solvent/ion	716/5
RMSD from ideal bond lengths (Å)	0.004
RMSD from ideal bond angles (°)	0.59
Ramachandran favored (%)	96.0
Ramachandran allowed (%)	4.0
Ramachandran outliers (%)	0.0
Clashscore	1.12
Average B factor	39.10
Wilson B factor (Å^2)	27.07

[a] Numbers in the parenthesis represent values for the highest resolution bin.

[b] Correlation coefficient CC 1/2 as defined in Karplus and Diederichs, 2012.[4]

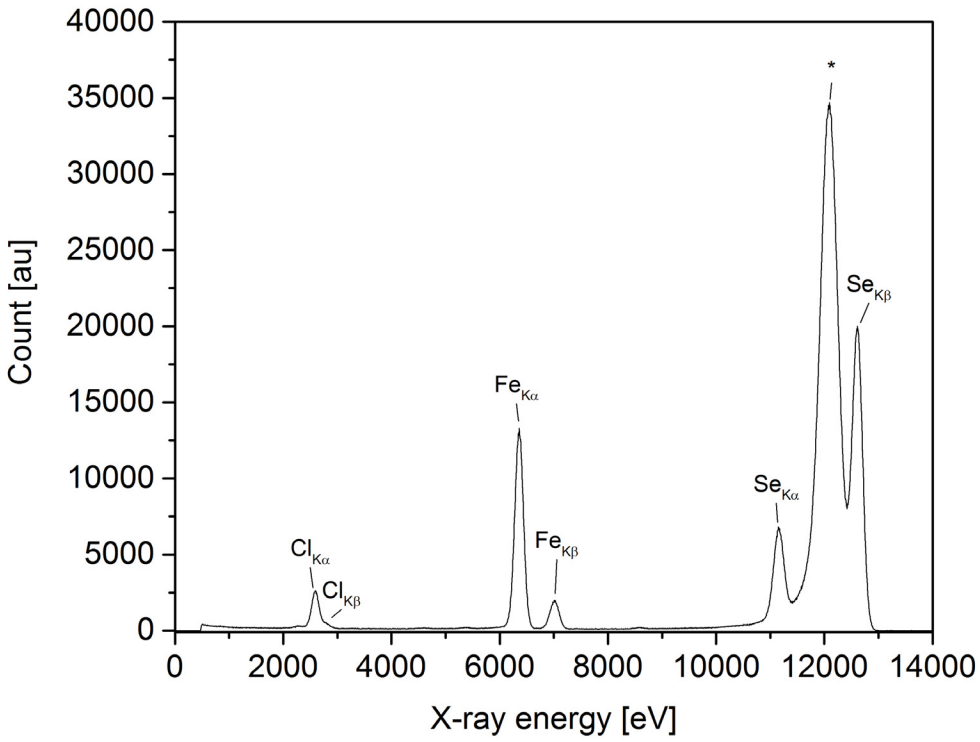

Figure S7. X-ray fluorescence of the CpI-ADSe crystal. Excitation at 12656 eV. * indicates back-scattering.

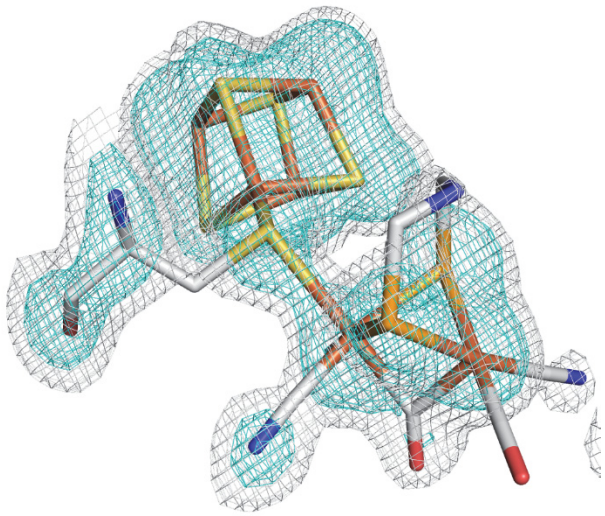

Figure S8. Model of the H-cluster of CpI-ADSe. Stick model of CpI-ADSe (PDB 50EF) F_o - F_c simulated annealing omit map contoured at 1.5 (cyan) and 3.5 (grey) σ.

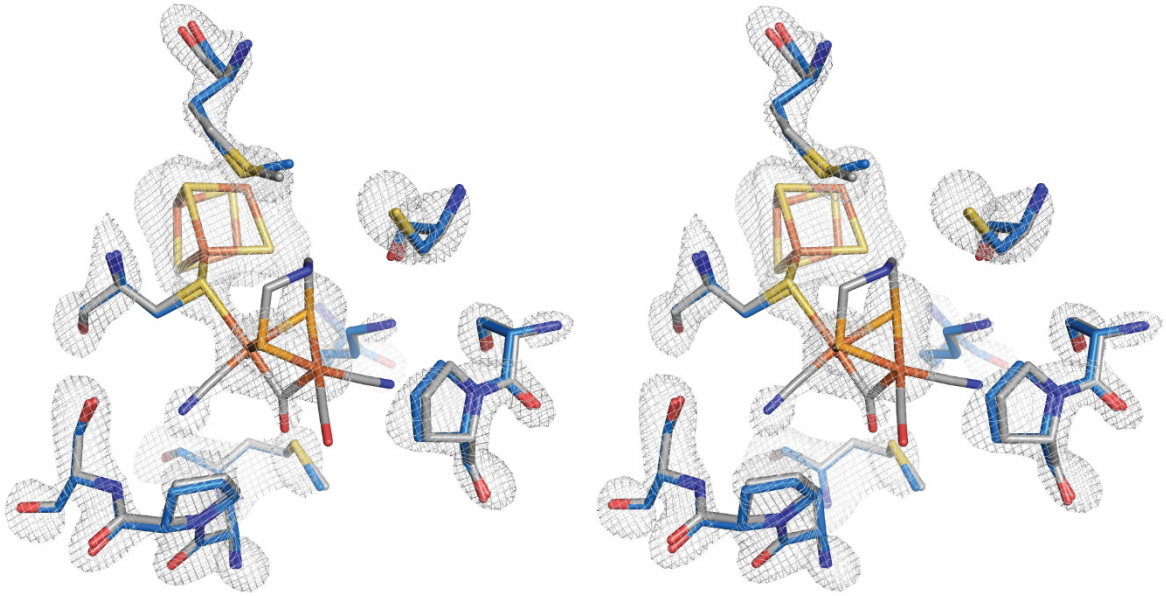

Figure S9. The central cavity of CpI-ADSe. Stereo view of a stick model of the central cavity of CpI-ADSe (PDB 5OEF; carbon atoms in grey) with F_o - F_c simulated annealing omit map contoured at 3.0 σ. A stick model of amino acids lining the central cavity of CpI-ADT is superposed (PDB 4XDC; carbon atoms in marine).

Additional electrochemistry data

Direct comparison on the absolute currents revealed that for CpI-ADSe the catalytic current for hydrogen production is 10 fold less than for CpI-ADT. For HydA1-ADSe the current is about three times less.

For electrochemistry experiments it was inevitable to freeze and thaw the samples. To test if a further freeze/thaw cycle leads to an additional loss of activity, further CVs were recorded. However, no further loss in activity was found. In solution, a similar behavior after storage of ADSe samples was observed. Eventually, CO inhibition of the enzyme during storage protects a fraction of the sample from degradation and upon CO release under catalytic conditions this fraction displays full activity.

It should be kept in mind that the comparison of the absolute magnitude is meaningless due to the unknown electroactive coverage on the electrode. However, the ratio of the oxidation over reduction currents can be used to reveal a bias to either direction compared to the WT as done in our study.[5]

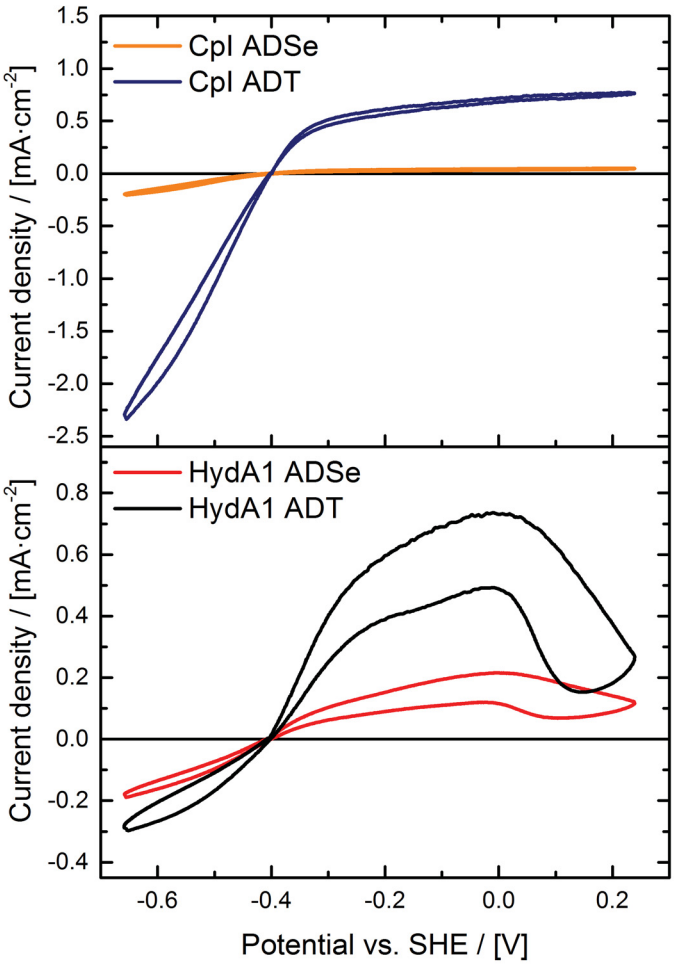

Figure S10. Cyclovoltammograms of CpI and HydA1 maturated with ADT and ADSe. Samples were thawed, diluted to 3 µM (10 mM MES, 2 mM NaDT, pH 5.8) and adsorbed to the PG electrode. Measurements are carried out at 25°C, 100 % H_2 with 20 mV/s scan rate, electrode rotation of 2000 rpm in buffer at pH 7.0.

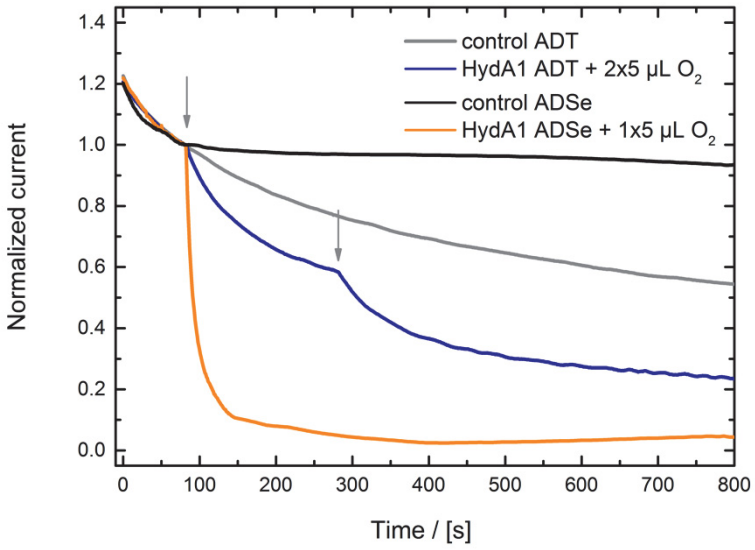

Figure S11. Chronoamperometry (CA) of HydA1-ADSe and HydA1-ADT upon addition of O2 saturated buffer to compare their level of oxygen sensitivity. Currents were normalized to the value just before the first O_2 addition. Each arrow indicates the addition of 5 µL O_2 saturated buffer to a total volume of 5 mL, respectively. CA was recorded at -39 mV vs. SHE, 25°C, 100% H_2, pH 7.0 and during an electrode rotation of 2000 rpm. Individual protein films were used for the oxygen exposed and control experiments.

1 Esselborn e*t al*., Nat. Chem. Biol., 2013, 9, 607–609.

2 J. F. Siebel, A. Adamska-Venkatesh, K. Weber, S. Rumpel, E. Reijerse and W. Lubitz, Biochemistry, 2015, 54, 1474–1483.

3 Z. Chen, B.J., Lemon, S. Huang, D.J. Swartz, J.W. Peters and K.A. Bagley, Biochemistry, 2002, 41, 2036–2043.

4 P. A. Karplus and K. Diederichs, Science, 2012, 336, 1030–1033.

5 A. Abou Hamdan, S. Dementin, P.-P. Liebgott, O. Gutierrez-Sanz, P. Richaud, A.L. De Lacey, M. Rousset, P. Bertrand, L. Cournac and C. Léger, J. Am. Chem. Soc., 2012, 134, 8368–8371.

4.3 Paper III

^{1}H NMR Spectroscopy of [FeFe] Hydrogenases: Insight into the Electronic Structure of the Active Site

S. Rumpel, E. Ravera, C. Sommer, E. Reijerse, C. Farès, C. Luchinat, W. Lubitz

J. Am. Chem. Soc. 2018, 140, 131-134.

DOI: 10.1021/jacs.7b11196

Journal name: Journal of the American Chemical Society

Author: Third author

Contribution: – 15 %

– I recorded most and analyzed all FTIR data

– I was involved in writing the manuscript

S. Rumpel measured all ^{1}H NMR data and wrote most of the manuscript. E. Ravera measured the NOE spectrum together with S. Rumpel and helped analyzing the data. All others discussed the results and were involved in writing the manuscript.

JACS
JOURNAL OF THE AMERICAN CHEMICAL SOCIETY
Communication
Cite This: J. Am. Chem. Soc. 2018, 140, 131−134
pubs.acs.org/JACS

^{1}H NMR Spectroscopy of [FeFe] Hydrogenase: Insight into the Electronic Structure of the Active Site

Sigrun Rumpel,*[,†] Enrico Ravera,[‡] Constanze Sommer,[†] Edward Reijerse,[†] Christophe Farès,[§] Claudio Luchinat,[‡] and Wolfgang Lubitz*[,†]

[†]Max-Planck-Institut für Chemische Energiekonversion, Stiftstrasse 34-36, 45470 Mülheim an der Ruhr, Germany
[‡]Department of Chemistry "Ugo Schiff" and Magnetic Resonance Center (CERM), University of Florence and Interuniversity Consortium for Magnetic Resonance of Metallo Proteins (CIRMMP), Via L. Sacconi 6, 50019 Sesto Fiorentino, Italy
[§]Max-Planck-Institut für Kohlenforschung, Kaiser-Wilhelm Platz 1, 45470 Mülheim an der Ruhr, Germany

Supporting Information

ABSTRACT: The [FeFe] hydrogenase HydA1 from *Chlamydomonas reinhardtii* has been studied using ^{1}H NMR spectroscopy identifying the paramagnetically shifted ^{1}H resonances associated with both the $[4Fe\text{-}4S]_H$ and the $[2Fe]_H$ subclusters of the active site "H-cluster". The signal pattern of the unmaturated HydA1 containing only $[4Fe\text{-}4S]_H$ is reminiscent of bacterial-type ferredoxins. The spectra of maturated HydA1, with a complete H-cluster in the active H_{ox} and the CO-inhibited H_{ox}−CO state, reveal additional upfield and downfield shifted ^{1}H resonances originating from the four methylene protons of the azadithiolate ligand in the $[2Fe]_H$ subsite. The two axial protons are affected by positive spin density, while the two equatorial protons experience negative spin density. These protons can be used as important probes sensing the effects of ligand-binding to the catalytic site of the H-cluster.

Hydrogenases are metalloenzymes that catalyze the reversible conversion of dihydrogen into protons and electrons with the class of [FeFe] hydrogenases being the most active hydrogen producers.[1] The unique [6Fe] active site of these enzymes, the so-called "H-cluster", serves as inspiration for the development of inorganic catalysts for production of solar fuels or as part of fuel cells. The H-cluster consists of a $[4Fe\text{-}4S]_H$ cluster connected to the protein via four cysteines, one of which bridges to a unique binuclear Fe subsite $[2Fe]_H$ containing a proximal (Fe_p) and a distal iron (Fe_d) (Figure 1). In contrast to most [FeFe] hydrogenases, HydA1 from *Chlamydomonas reinhardtii* with a molecular weight of about 48 kDa contains no accessory iron sulfur clusters and is thus particularly well suited for spectroscopic investigations of structure and function of the H-cluster. Large quantities of fully active HydA1 can be prepared by the addition of the synthesized inorganic cofactor precursor $[Fe_2(adt)(CO)_4(CN)_2]$ (adt = azadithiolate) to recombinant HydA1 containing only the $[4Fe\text{-}4S]_H$ cluster (apo-HydA1) (Figure 1).[2,3] The active site and its highly conserved protein environment are suggested to act synergistically for efficient hydrogen evolution. The electronic structure of the different redox states of the H-cluster has been well characterized by

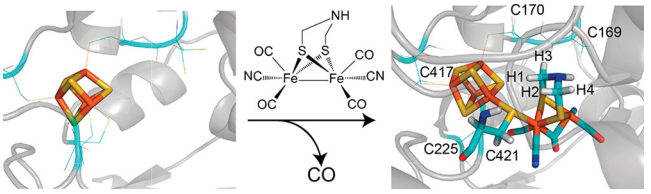

Figure 1. Maturation of HydA1 containing only the $[4Fe\text{-}4S]_H$ cluster with the synthetic precursor $[Fe_2(adt)(CO)_4(CN)_2]$ of the binuclear Fe subsite results in fully functional HydA1. The images of the $[4Fe\text{-}4S]_H$ cluster and the H-cluster are based on PDB entries 3LX4 and 3C8Y, respectively. The metal clusters and the bridging cysteine are shown as sticks with the following color coding; iron, orange; sulfur, yellow; carbon, cyan; oxygen, red; nitrogen, blue.

EPR and FTIR spectroscopy.[4−9] Electronic coupling between the $[4Fe\text{-}4S]_H$ and $[2Fe]_H$ subclusters is of central importance to the electron flow during catalysis.[10] The intimate contact between $[4Fe\text{-}4S]_H$ and $[2Fe]_H$ sites translates into magnetic exchange coupling, which has been demonstrated at low temperatures by Mössbauer and EPR/ENDOR spectroscopy.[11,12] However, the spin density distribution over the H-cluster and the influence of the protein environment have never been studied in solution at room temperature. Here, the method of choice is solution NMR spectroscopy, which can reveal sign and magnitude of the spin density at each NMR active nucleus. Protons are the most sensitive ones, although other magnetic nuclei, e.g., ^{13}C and ^{15}N, could also be studied easily by NMR techniques.[13] For hydrogenases, protons are of particular importance since they are substrate and product of the reversible enzymatic reaction. In principle, NMR allows one in a unique way to directly follow the hydrogen species during the catalytic cycle under physiological conditions.

Here, we present the first NMR spectroscopic investigation of a hydrogenase enzyme, the [FeFe] hydrogenase HydA1. Similar to other iron sulfur proteins, magnetic coupling among iron centers reduces the NMR line widths and renders the spectroscopic investigation feasible.[14] The β-CH_2 protons of the four cysteines coordinating $[4Fe\text{-}4S]_H$ as well as the protons within the $[2Fe]_H$ site are contact shifted out of the diamagnetic envelope (−1 to 11 ppm). Size and sign of the

Received: October 27, 2017
Published: December 6, 2017

DOI: 10.1021/jacs.7b11196
J. Am. Chem. Soc. 2018, 140, 131−134

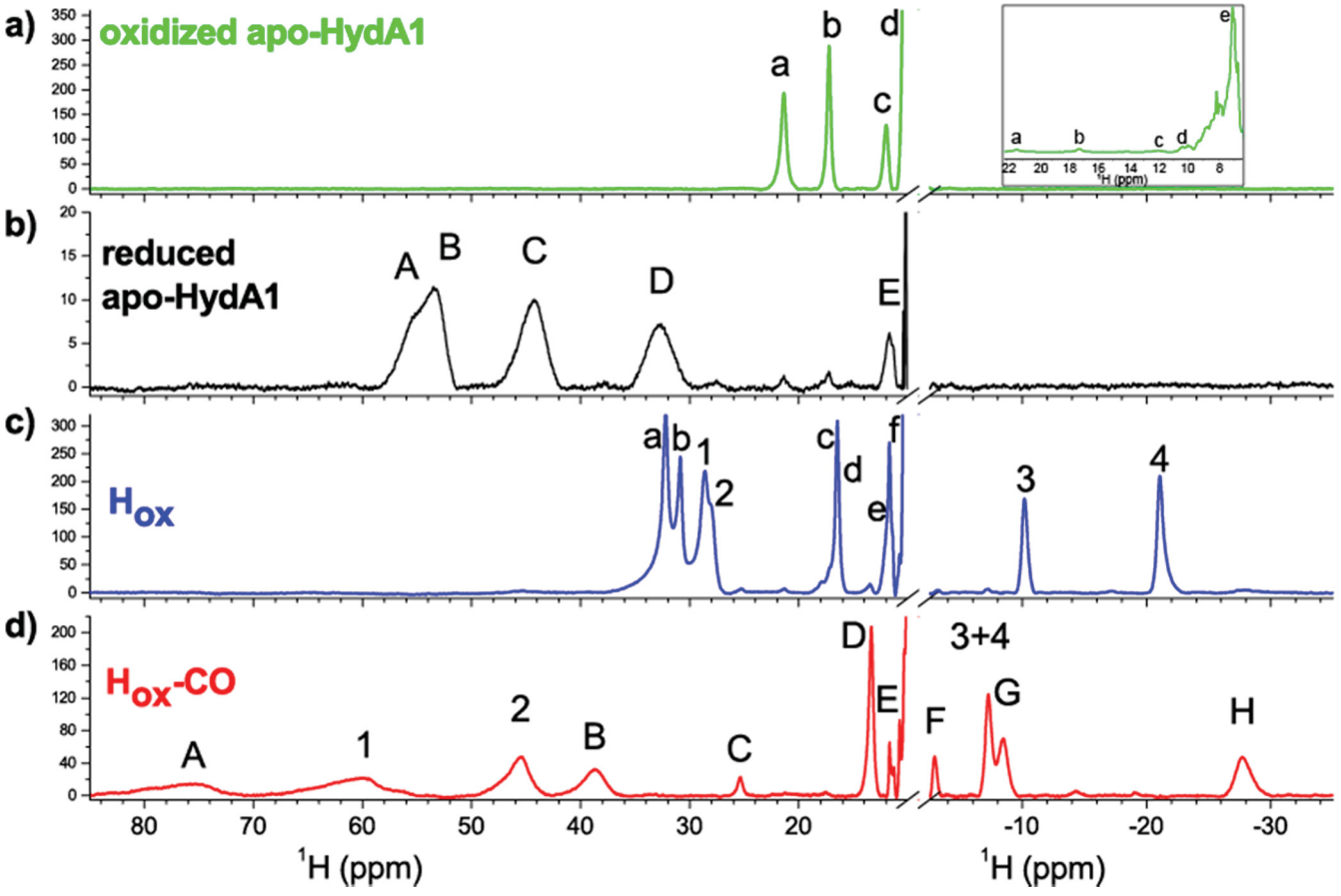

Figure 2. Downfield and upfield region of the 1D ^{1}H NMR spectra (600 MHz) at 298 K of (a) oxidized apo-HydA1 (green line), (b) reduced apo-HydA1 (black line), (c) oxidized HydA1 (blue line, H_{ox}), and (d) CO-inhibited oxidized HydA1 (red line, H_{ox}–CO). Downfield region and upfield region are shown from 85 to 10 ppm and −2.5 to −35 ppm, respectively. Contact shifted cysteine resonances are labeled a–e in (a), A–E in (b), a–f in (c), and A–H in (d). Labels 1, 2, 3, and 4 indicate ^{1}H resonances of $[2Fe]_H$. The inset of (a) shows the spectrum of oxidized apo-HydA1 from 6 to 22 ppm.

contact shift depend on (i) the spin state of the Fe in the cluster to which the cysteine is attached, (ii) the spin density at the nucleus, which largely depends on the Fe–S–Cβ–βCH$_2$ dihedral angle θ, and (iii) temperature.[15] Although the hyperfine shifted signals are significantly broadened due to the interaction of the unpaired electron(s) with the resonating nucleus, they provide a distinctive fingerprint of the cluster environment and protons inherent in the H-cluster. To our knowledge, the only other iron sulfur proteins of high molecular weight studied by NMR are the homodimeric nitrogenase Fe-protein[16] and the hemeprotein subunit of sulfite reductase.[17] The results presented here provide unique insight into structure and function of [FeFe] hydrogenases in solution at room temperature including an exclusive view of the catalytically active H_{ox} state. These data open new prospects to unravel intimate details about geometric and electronic structure of the H-cluster and the influence of the surrounding amino acids.

The amenability of HydA1 to a high-resolution NMR study is demonstrated on oxidized apo-HydA1. The measured ^{1}H NMR spectra reveal three contact shifted resonances downfield of 11 ppm with line width up to 300 Hz (Figure 2a and Table S2). Their pattern resembles bacterial-type ferredoxins in the oxidized $[4Fe\text{-}4S]^{2+}$ form,[18−20] which can be viewed as two antiferromagnetically coupled Fe(II)Fe(III) pairs that form a diamagnetic ground state with a total spin state $S = 0$.[21] Paramagnetism arises at room temperature due to population of low-lying excited states with $S = 1$, 2, etc. Consistent with an oxidized $[4Fe\text{-}4S]^{2+}_H$, all contact shifted resonances exhibit anti-Curie temperature dependence (Table S2 and Figure S1a).[18−20]

Reduction of the $[4Fe\text{-}4S]^{2+}_H$ cluster to the $[4Fe\text{-}4S]^{+}_H$ form is accompanied by about four-fold increased contact shifts and line widths, which is in agreement with a paramagnetic $S = 1/2$ ground state (Figure 2b). For reduced apo-HydA1, the downfield shifted resonances A and D exhibit Curie, whereas B and C show anti-Curie temperature dependence (Figure S1b). Based on their chemical shifts and line widths, signals A to D belong most likely to β-CH$_2$ protons of cysteinyl ligands. Signal E was assigned as a cysteine α-CH proton as its line width is smaller when compared to signals A to D (Figure 2b and Table S2).

Maturation of apo-HydA1 with $[Fe_2(adt)(CO)_4(CN)_2]$ yields HydA1 with a fully functional H-cluster (see Supporting Information SI1). In this [6Fe] system, spin coupling is in effect. For H_{ox} and CO-inhibited H_{ox}–CO state, the H-cluster contains the cubane in the oxidized 2+ state. According to a theoretical model, $[4Fe\text{-}4S]^{2+}_H$ is composed of two valence-delocalized Fe pairs, $[2Fe]_A$ and $[2Fe]_B$, which are antiferromagnetically coupled to each other via the strong intracluster coupling J_{cube} ($\approx$ 200 cm^{-1}).[12] In addition, $[4Fe\text{-}4S]_H^{2+}$ is coupled through $[2Fe]_B$ to $[2Fe]_H$ in the $[Fe_p^{I}Fe_d^{II}]$

DOI: 10.1021/jacs.7b11196
J. Am. Chem. Soc. 2018, 140, 131−134

redox configuration via the intercluster exchange coupling j (Figure 3).

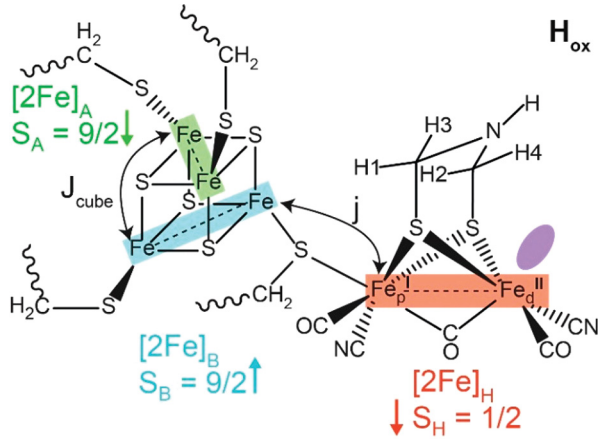

Figure 3. Schematic representation of the active site H-cluster of [FeFe] hydrogenases in the H_{ox} state. The exchange interactions of the H-cluster are indicated. $[4Fe\text{-}4S]_H^{2+}$ is composed of two valence-delocalized Fe(II)−Fe(III) pairs with $S = 9/2$ that are antiferromagnetically coupled by J_{cube}. $[2Fe]_H$ consists of a low-spin Fe(I)−Fe(II) pair with ground state $S = 1/2$, which is coupled via the coupling constant j to $[4Fe\text{-}4S]_H^{2+}$. The violet sphere indicates the open coordination site at Fe_d where substrate or CO bind.

This coupling, previously investigated by ENDOR and Mössbauer spectroscopy, has been found to be about 25 cm^{-1} for H_{ox} and 95 cm^{-1} for H_{ox}−CO.[11,12,22] The 4-fold increased j in the H_{ox}−CO state causes the spin density to be strongly localized on Fe_p, while it is more evenly distributed over Fe_d and Fe_p in the H_{ox} state.[11] Nevertheless, both j values are small compared to J_{cube}. J_{cube} leads to an orientation of S_A antiparallel to S_B and j orients S_H antiparallel to S_B. Hence, S_H is oriented parallel to S_A (Figure 3). Magnitude and sign of the spin density are reflected by the observed proton hyperfine shifts that depend mainly on the Fe−S−C−H dihedral angle θ. The angular dependence of the chemical shift δ follows the general Karplus relationship $\delta = a \cos^2\theta + b \cos\theta + c$ with b and c being small and often neglected.[15] As the remaining angular term $\cos^2\theta$ is always positive, solely the sign of the spin density on the coordinated Fe determines the direction of the paramagnetic shift.

After preparation of HydA1 in the H_{ox} state (see Supporting Information S1 and Figure S4), six downfield shifted resonances are observed in the ^1H NMR spectrum between 11 and 33 ppm and also two upfield shifted resonances at −10 and −21 ppm (Figure 2c). The downfield shifted signals a, b, 1, and 2 exhibit Curie and signals c to f anti-Curie temperature dependence (Table S2 and Figure S2). The two upfield shifted resonances show pseudo-Curie temperature dependence. No hyperfine-shifted signals were detected at positions observed in the spectrum for apo-HydA1. This demonstrates the influence of the $[2Fe]_H$ on the $[4Fe\text{-}4S]_H^{2+}$ cluster via exchange coupling in solution. In order to distinguish the methylene proton resonances originating from the cysteines coordinating $[4Fe\text{-}4S]_H^{2+}$ from those of adt, H_{ox} was also prepared using a deuterated $[2Fe]_H$ site (^{2}H-adt). Thus, the downfield shifted signals 1 and 2 and the upfield shifted signals 3 and 4 (Figures 2c) have been unambiguously assigned to the four methylene protons of $[2Fe]_H$ (Figure S5). They can be attributed to two pairs of geometrically and electronically similar protons. Based on their distances to Fe_p and Fe_d, line widths, and observed ^1H NOE connectivities, signals 1 and 2 are assigned to the axial and signals 3 and 4 to the equatorial protons (Figure 1 and Table S2). Further details are provided in the Supporting Information (SI4, Figure S6 and Table S1).

By flushing active HydA1 with CO, pure H_{ox}−CO state is prepared (see Supporting Information S1 and Figure S7). This CO-inhibited state is an important source of information reporting about the redistribution of spin density in the H-cluster upon binding of an electron donating external ligand to the open coordination site at Fe_d. In its ^1H NMR spectrum, seven downfield and four upfield shifted resonances are observed in the range 11 to 85 ppm and −2 to −30 ppm, respectively (Figure 2d). The downfield shifted signals A, 1, 2, B, C, and D show Curie and E weak anti-Curie temperature dependence. As for the H_{ox} state, all upfield shifted resonances show pseudo Curie temperature dependence (Figure S4). In agreement with an increased j due to coordination of the external CO ligand at Fe_d, ^1H resonances were broader (as much as 4 kHz) and more dispersed than those for all other HydA1 states investigated here (Figure 2 and Table S2). In contrast, the line widths of the contact shifted proton signals of H_{ox} are ∼300 Hz similar to oxidized apo-HydA1. For the H_{ox}−CO state, signals 1 to 4 have been assigned analogous to the H_{ox} state to axial and equatorial protons (Figure S8). Although the temperature dependence of signals 1 to 4 is weak in the H_{ox}−CO state, their temperature-dependence in the H_{ox} state is the strongest of all observed hyperfine shifted resonances in that state (Figures S2 and SI3). This large temperature dependence of the adt methylene protons in the H_{ox} state indicates that the energies of the populated excited states of $[2Fe]_H$ are closer than those of $[4Fe\text{-}4S]_H^{2+}$ and agrees well with j, determined to be small for this state. One possible explanation for the relatively small temperature dependence of the adt methylene protons in the H_{ox}−CO state is that binding of the external CO ligand increases not only j but also the energies of the levels populated at room temperature. The assignment of the methylene protons of the adt bridge provides insight into the spin density at four additional positions of the $[2Fe]_H$ site. Large negative hyperfine shifts are observed for signals 3 and 4 in the H_{ox}, and large positive hyperfine shifts are detected for signals 1 and 2 in the H_{ox}−CO state (Figure 2cd). These hyperfine shifts reflect the larger $[2Fe]_H$ spin density for H_{ox} when compared to H_{ox}−CO, resulting from the different ratio of j and J_{cube}. The NMR spectra observed for the H_{ox} and H_{ox}−CO states can be interpreted based on the spin coupling model described above (Figure 3). Spin-polarization mechanisms will transmit positive and negative spin density to the ^1H atoms of the cysteines coordinating $[2Fe]_A$ and $[2Fe]_B$, respectively. Thus, ligation of $[2Fe]_A$ results in downfield and ligation of $[2Fe]_B$ in upfield shifted ^1H resonances. However, the bridging cysteine experiences not only positive spin density from $[2Fe]_B$ but also negative spin density from $[2Fe]_H$. Taking into account the larger spin density at $[4Fe\text{-}4S]_H^{2+}$ and the lower spin density at $[2Fe]_H$ in the H_{ox}−CO as compared to the H_{ox} state, a net upfield shift is expected for the β-CH_2 protons of the bridging cysteine. Accordingly, peaks F, G, and H can be assigned to the β-CH_2 protons of the bridging and nonbridging cysteine coordinating $[2Fe]_B$ (Figure 2d). For the H_{ox} state, only two upfield shifted resonances are observed because of the smaller spin density at $[4Fe\text{-}4S]_H^{2+}$ resulting from j, which is four-fold smaller than for the H_{ox}−CO state (Figure 2c).

DOI: 10.1021/jacs.7b11196
J. Am. Chem. Soc. 2018, 140, 131−134

We show here that paramagnetic NMR can be applied to the important class of [FeFe] hydrogenases. The derived assignments of the axial and equatorial protons of the unique $[2Fe]_H$ help to reveal intimate details of the different electronic states of the active site required for efficient catalytic H_2 evolution under near-native conditions. Solution NMR titration experiments of HydA1 with its native electron donor PetF[23] are foreseen to provide also experimental insight of HydA1's complex interface as well as dynamics related to complex formation as recently reported for cytochrome P450 and b_5.[24,25] Furthermore, NMR spectroscopy allows for the investigation of HydA1 states with a diamagnetic ground state like H_{red} and $H_{red}H^+$ that are EPR silent. Most importantly, the terminal hydride intermediate, which already has been discussed based on FTIR,[26,27] Mössbauer,[28] and NRVS spectroscopy,[29,30] can be accessed directly at ambient temperatures using solution NMR spectroscopy.

■ ASSOCIATED CONTENT

Supporting Information

The Supporting Information is available free of charge on the ACS Publications website at DOI: 10.1021/jacs.7b11196.

Methods, supplementary NMR and FTIR, and figures and tables (PDF)

■ AUTHOR INFORMATION

Corresponding Authors

*sigrun.rumpel@cec.mpg.de
*wolfgang.lubitz@cec.mpg.de

ORCID

Enrico Ravera: 0000-0001-7708-9208
Claudio Luchinat: 0000-0003-2271-8921
Wolfgang Lubitz: 0000-0001-7059-5327

Notes

The authors declare no competing financial interest.

■ ACKNOWLEDGMENTS

We thank Nina Breuer, Patricia Malkowski, and Inge Heise for sample preparation and synthesis of unlabeled and deuterated $[Fe_2(adt)(CO)_4(CN)_2]$. This work has been supported by iNEXT, grant number 653706, funded by the Horizon 2020 programme of the European Union and COST action FeSBioNet CA15133.

■ REFERENCES

(1) Lubitz, W.; Ogata, H.; Rüdiger, O.; Reijerse, E. *Chem. Rev.* **2014**, *114*, 4081.
(2) Esselborn, J.; Lambertz, C.; Adamska-Venkatesh, A.; Simmons, T.; Berggren, G.; Noth, J.; Siebel, J.; Hemschemeier, A.; Artero, V.; Reijerse, E.; Fontecave, M.; Lubitz, W.; Happe, T. *Nat. Chem. Biol.* **2013**, *9*, 607.
(3) Berggren, G.; Adamska, A.; Lambertz, C.; Simmons, T. R.; Esselborn, J.; Atta, M.; Gambarelli, S.; Mouesca, J. M.; Reijerse, E.; Lubitz, W.; Happe, T.; Artero, V.; Fontecave, M. *Nature* **2013**, *499*, 66.
(4) Adamska, A.; Silakov, A.; Lambertz, C.; Rüdiger, O.; Happe, T.; Reijerse, E.; Lubitz, W. *Angew. Chem., Int. Ed.* **2012**, *51*, 11458.
(5) Adamska-Venkatesh, A.; Krawietz, D.; Siebel, J.; Weber, K.; Happe, T.; Reijerse, E.; Lubitz, W. *J. Am. Chem. Soc.* **2014**, *136*, 11339.
(6) Roseboom, W.; De Lacey, A. L.; Fernandez, V. M.; Hatchikian, E. C.; Albracht, S. P. J. *JBIC, J. Biol. Inorg. Chem.* **2006**, *11*, 102.
(7) Silakov, A.; Wenk, B.; Reijerse, E.; Albracht, S. P. J.; Lubitz, W. *JBIC, J. Biol. Inorg. Chem.* **2009**, *14*, 301.
(8) Silakov, A.; Wenk, B.; Reijerse, E.; Lubitz, W. *Phys. Chem. Chem. Phys.* **2009**, *11*, 6592.
(9) Mulder, D. W.; Ratzloff, M. W.; Shepard, E. M.; Byer, A. S.; Noone, S. M.; Peters, J. W.; Broderick, J. B.; King, P. W. *J. Am. Chem. Soc.* **2013**, *135*, 6921.
(10) Sommer, C.; Adamska-Venkatesh, A.; Pawlak, K.; Birrell, J. A.; Rüdiger, O.; Reijerse, E. J.; Lubitz, W. *J. Am. Chem. Soc.* **2017**, *139*, 1440.
(11) Silakov, A.; Reijerse, E. J.; Albracht, S. P. J.; Hatchikian, E. C.; Lubitz, W. *J. Am. Chem. Soc.* **2007**, *129*, 11447.
(12) Popescu, C. V.; Munck, E. *J. Am. Chem. Soc.* **1999**, *121*, 7877.
(13) Bertini, I.; Luchinat, C.; Parigi, G.; Ravera, E. *NMR of Paramagnetic Molecules*; Elsevier Amsterdam, 2017.
(14) Bertini, I.; Turano, P.; Vila, A. J. *Chem. Rev.* **1993**, *93*, 2833.
(15) Bertini, I.; Capozzi, F.; Luchinat, C.; Piccioli, M.; Vila, A. J. *J. Am. Chem. Soc.* **1994**, *116*, 651.
(16) Lanzilotta, W. N.; Holz, R. C.; Seefeldt, L. C. *Biochemistry* **1995**, *34*, 15646.
(17) Kaufman, J.; Spicer, L. D.; Siegel, L. M. *Biochemistry* **1993**, *32*, 2853.
(18) Bertini, I.; Briganti, F.; Luchinat, C.; Scozzafava, A. *Inorg. Chem.* **1990**, *29*, 1874.
(19) Donaire, A.; Gorst, C. M.; Zhou, Z. H.; Adams, M. W. W.; Lamar, G. N. *J. Am. Chem. Soc.* **1994**, *116*, 6841.
(20) Lebrun, E.; Simenel, C.; Guerlesquin, F.; Delepierre, M. *Magn. Reson. Chem.* **1996**, *34*, 873.
(21) Beinert, H.; Holm, R. H.; Munck, E. *Science* **1997**, *277*, 653.
(22) Silakov, A.; Reijerse, E. J.; Lubitz, W. *Eur. J. Inorg. Chem.* **2011**, *2011*, 1056.
(23) Rumpel, S.; Siebel, J. F.; Diallo, M.; Fares, C.; Reijerse, E. J.; Lubitz, W. *ChemBioChem* **2015**, *16*, 1663.
(24) Ravula, T.; Barnaba, C.; Mahajan, M.; Anantharamaiah, G. M.; Im, S.-C.; Waskell, L.; Ramamoorthy, A. *Chem. Commun.* **2017**, *53*, 12798.
(25) Barnaba, C.; Gentry, K.; Sumangala, N.; Ramamoorthy, A. *F1000Research* **2017**, *6*, 662.
(26) Mulder, D. W.; Ratzloff, M. W.; Bruschi, M.; Greco, C.; Koonce, E.; Peters, J. W.; King, P. W. *J. Am. Chem. Soc.* **2014**, *136*, 15394.
(27) Winkler, M.; Senger, M.; Duan, J. F.; Esselborn, J.; Wittkamp, F.; Hofmann, E.; Apfel, U. P.; Stripp, S. T.; Happe, T. *Nat. Commun.* **2017**, *8*, 16115.
(28) Mulder, D. W.; Guo, Y. S.; Ratzloff, M. W.; King, P. W. *J. Am. Chem. Soc.* **2017**, *139*, 83.
(29) Reijerse, E. J.; Pham, C. C.; Pelmenschikov, V.; Gilbert-Wilson, R.; Adamska-Venkatesh, A.; Siebel, J. F.; Gee, L. B.; Yoda, Y.; Tamasaku, K.; Lubitz, W.; Rauchfuss, T. B.; Cramer, S. P. *J. Am. Chem. Soc.* **2017**, *139*, 4306.
(30) Pelmenschikov, V.; Birrell, J. A.; Pham, C. C.; Mishra, N.; Wang, H.; Sommer, C.; Reijerse, E.; Richers, C. P.; Tamasaku, K.; Yoda, Y.; Rauchfuss, T. B.; Lubitz, W.; Cramer, S. P. *J. Am. Chem. Soc.* **2017**, *139*, 16894.

■ NOTE ADDED AFTER ASAP PUBLICATION

This paper was published on December 14, 2017. The abstract has been corrected and the revised version was re-posted on December 19, 2017.

DOI: 10.1021/jacs.7b11196
J. Am. Chem. Soc. 2018, 140, 131−134

Supporting Information

^{1}H NMR Spectroscopy of [FeFe] Hydrogenase: Insight into the Electronic Structure of the Active Site

Sigrun Rumpel,[†] Enrico Ravera,[‡] Constanze Sommer,[†] Edward Reijerse,[†] Christophe Farès,[§] Claudio Luchinat,[‡] and Wolfgang Lubitz[†]

[†] Max-Planck-Institut für Chemische Energiekonversion, Stiftstrasse 34-36, 45470 Mülheim an der Ruhr, Germany

[‡] Department of Chemistry “Ugo Schiff” and Magnetic Resonance Center (CERM), University of Florence and Interuniversi-ty Consortium for Magnetic Resonance of Metallo Proteins (CIRMMP), Via L. Sacconi 6, 50019 Sesto Fiorentino, Italy

[§] Max-Planck-Institut für Kohlenforschung, Kaiser-Wilhelm Platz 1, 45470 Mülheim an der Ruhr, Germany

Table of Contents

SI1. Sample preparation

Apo-HydA1 was expressed and purified as described previously[1]. The bacteria suspension was shaken at 37°C aerobically till an OD600 (optical density at a wavelength of 600 nm) of 0.6 was reached. After pH correction to 7.4 and transfer in a glass bottle with Teflon membrane, protein expression was induced with 0.5 M IPTG (isopropyl β-D-thiogalactopyranoside). The suspension was gassed with argon for one hour and expression was continued for 25 h at room temperature. Unless indicated, all samples were handled under strictly anaerobic conditions in a glove box (COY) using a palladium catalyst and forming gas with 1-2.5% hydrogen.

All NMR samples were prepared in NMR buffer 1 (25 mM potassium phosphate pH* 7.4 and 100% D_2O) or 2 (25 mM potassium phosphate pH* 6.4 and 100% D_2O).

Preparation of pure states for NMR spectroscopy:

(1) The first sample had a concentration of 1.7 mM and contained >95% oxidized apo-HydA1. This sample was purified in the absence of sodium dithionite and the NMR tube was flame sealed.
(2) The second sample had a concentration of 4.2 mM and contained >95% reduced apo-HydA1. It was purified in the presence of 2 mM sodium dithionite. The buffer was exchanged directly before the measurement to remove sodium dithionite and the NMR tube was flame sealed.
(3) To prepare the third sample, a two-fold excess of a 50 mM $[Fe_2(adt)(CO)_3(CN)_2]$ solution in DMSO was added to 0.53 ml of 2.65 mM apo-HydA1 in 25 mM Tris/HCl pH 8.0, 25 mM KCl and 2 mM NaDT diluted to 2.5 ml with NMR buffer 1. The maturation and removal of excess $[Fe_2(adt)(CO)_3(CN)_2]$ was performed as described previously.[1,2] After concentrating the sample to approximately 3.5 mM, it was flashed with argon for 20.5 h. All following steps were performed in a glove box (MBRAUN) filled with N_2 in the absence of hydrogen. Addition of 2.45 mM thionine acetate to remove residual H_{red} and H_{sred} resulted in >95% HydA1 in the H_{ox} state (Figure S4, bottom). The sample was measured in a flame sealed NMR tube.
(4) The fourth sample was prepared by CO-flushing about 4 mM maturated apo-HydA1 for 1 h and keeping the sample in the CO-filled closed vial for about 1 h. The FTIR spectrum confirmed HydA1 to be present to >95% in the H_{ox}-CO state (Figure S7). This sample was measured in a 5 mm medium wall precision quick pressure valve NMR tube.
(5) For the NOE-based assignment of the methylene protons of the dithiolate bridge, apo-HydA1 was maturated with $Fe_2(pdt)(CO)_3(CN)_2$ (pdt = propanedithiolate). The resulting HydA1-pdt has been shown to exist only in an oxidized and reduced state and is much more stable than HydA1-adt. Furthermore, the oxidized form of HydA1-pdt has revealed basically the same electronic structure.[3] The sample used for measuring the transient NOE had a concentration of about 3.6 mM, contained about 50% oxidized and 50% reduced HydA1-pdt and was measured in a flame-sealed NMR tube.

SI2. FTIR measurements of H_{ox} and H_{ox}-CO

An aliquot of 8 µl of the NMR samples (3) and (4) was employed to assess the purity of the H_{ox} and H_{ox}-CO redox states using FTIR spectroscopy.[4] FTIR measurements were carried out on a Bruker IFS 66v/S or a Bruker VERTEX 80v spectrometer with a resolution of 2 cm^{-1} in forward-backward measuring mode for 1000 scans at room temperature. Baseline correction was performed using a self-written routine in MATLAB.

SI3. NMR experiments

1D ^{1}H NMR spectra shown in Figure 2 were acquired at 298 K on a Bruker AVANCE 600 spectrometer equipped with a cryogenic TCI probehead using the normal one pulse experiments with ^1H_2O presaturation or using the super-WEFT pulse sequence.[5] Relaxation delay times were 200 ms. In case of HydA1 in the H_{ox} and H_{ox}-CO state, methylene protons of the $[2Fe]_H$ site were identified by comparison of the ^{1}H 1D spectra of samples maturated with deuterated and non-deuterated $[Fe_2(adt)(CO)_4(CN)_2]$.

1D NOE (Figure S6)

The 1D NOE experiments of HydA1-pdt were acquired at 298 K on a Bruker AVANCE 600 equipped with a cryogenic TCI probehead. For the measurement of the NOE, a modified super-WEFT sequence including CW irradiation off resonance from the carrier position was used.[6] To minimize the artifacts the following irradiation scheme was used as follows: the spectrum with CW irradiation on resonance with the target signal is acquired twice and co-added, then the spectra with the CW irradiation symmetrically off-resonance with respect to the target signals are acquired and subtracted. The used on and off resonance frequencies are summarized in the following table.

Table S1. Summary of the used on and off resonance frequencies to measure the NOE at 600 MHz

	Signal	Off resonance (downfield) frequency (Hz) subtracted	On resonance frequency (Hz) acquired twice	Off resonance (upfield) frequency (Hz) subtracted
oxidized HydA1-pdt	1+2	6999.64	6711.60	6430.56
	3	-12932.45	-13208.90	-15329.66
	4	-15329.66	-15600.77	-15871.88

Temperature-dependence of the hyperfine shifted resonances of oxidized and reduced apo-HydA1

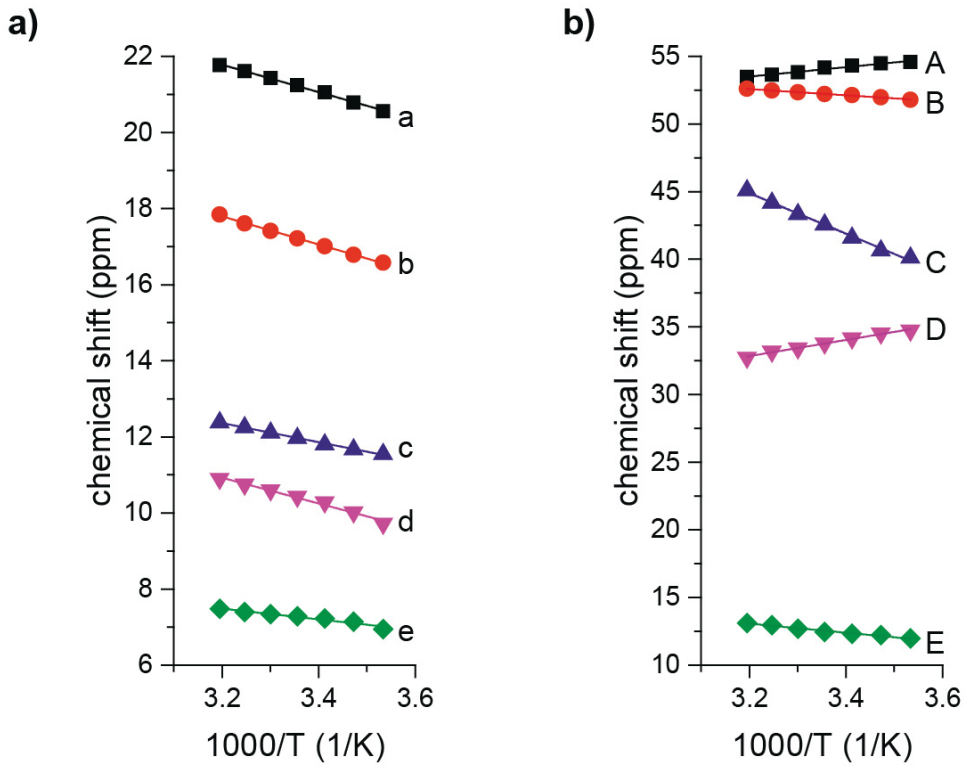

Figure S1. Plot of the observed chemical shifts versus the reciprocal temperature for the assigned contact shifted Cys resonances from oxidized (a) and reduced (b) HydA1 containing only the $[4Fe\text{-}4S]_H$ cluster. The peaks are labeled as in Figure 2.

Temperature-dependence of the hyperfine shifted resonances of H_{ox}

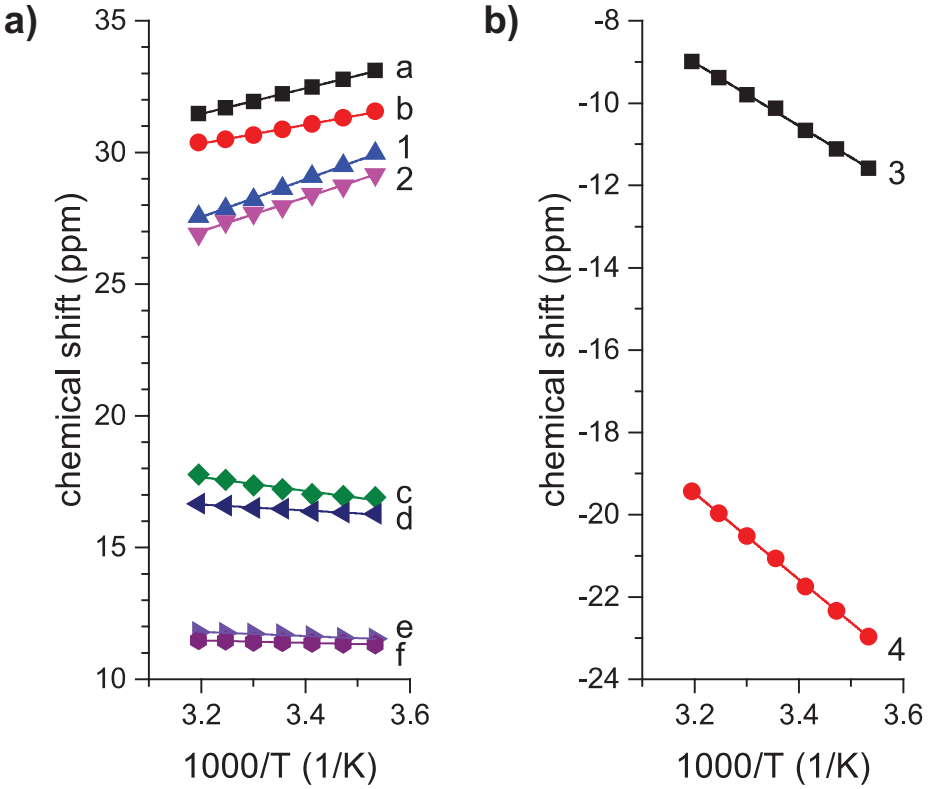

Figure S2. Plot of the observed chemical shifts versus the reciprocal temperature for the contact shifted resonances from HydA1 in the H_{ox} state. The peaks are labeled as in Figure 2. The downfield shifted resonances are displayed in a) and the upfield shifted resonances are shown in b).

Temperature-dependence of the hyperfine shifted resonances of H_{ox}-CO

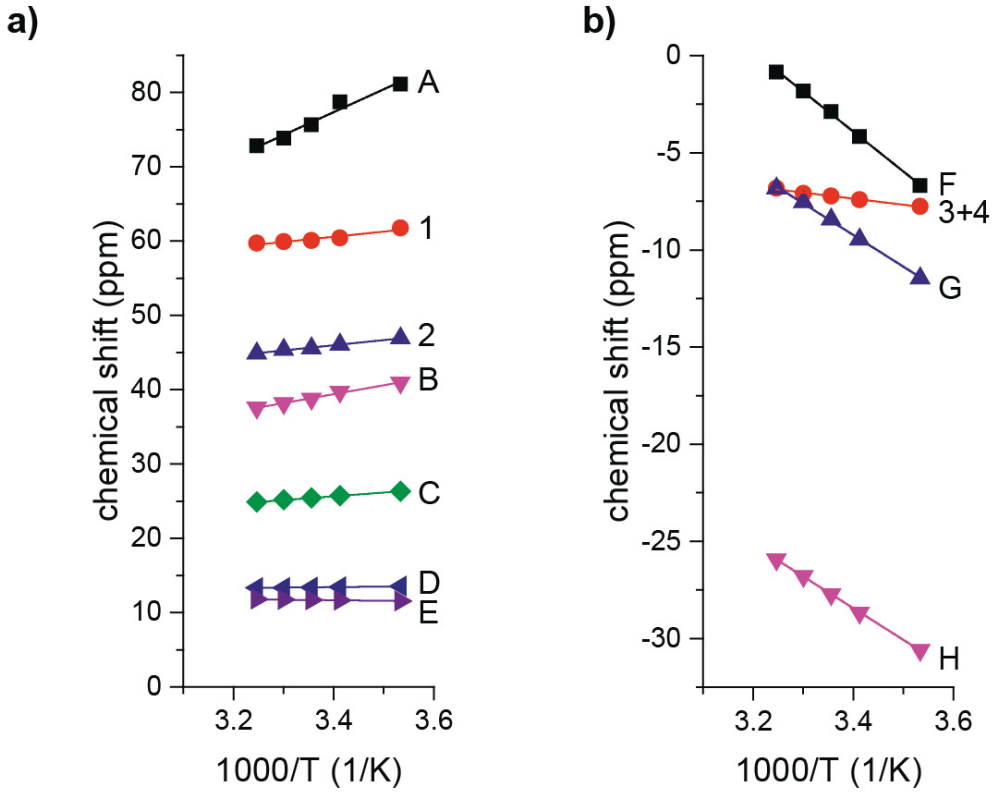

Figure S3. Plot of the observed chemical shifts versus the reciprocal temperature for the contact shifted resonances from HydA1 in the H_{ox}-CO state. The peaks are labeled as in Figure 2. The downfield shifted resonances are displayed in a) and the upfield shifted resonances are shown in b).

Table S2. ^{1}H NMR spectral parameters for the hyperfine shifted resonances for different forms of HydA1.

peak label	assign-ment	chem. shift (ppm)	line-width (Hz)[a]	temp. dep.	rela-tive area	peak label	assign-ment	chem. shift (ppm)	line-width (Hz)[a]	temp. dep.	rela-tive area
oxidized apo-HydA1						reduced apo-HydA1					
a	β-CH_2	21.38	300	aC	1	A	β-CH_2	55.59	1500	C	2
b	β-CH_2	17.23	200	aC	1	B	β-CH_2	53.54	1500	aC	2
c	β-CH_2	11.97	300	aC	1	C	β-CH_2	44.38	1800	aC	2
d	β-CH_2	10.4	200	aC	1	D	β-CH_2	33.98	1600	C	2
e	β-CH_2	7.11	200	n. d.	n. d.	E	α-CH_2	11.74	400	aC	1
H_{ox} state						H_{ox}-CO state					
a	β-CH_2	32.22	300	C	1	A	β-CH_2	75.66	4000	C	n. d.
b	β-CH_2	30.87	300	C	1	1	adt-CH_2	60.09	4000	C	n. d.
1	adt-CH_2	28.63	600	C	1	2	adt-CH_2	45.48	1800	C	n. d.
2	adt-CH_2	27.95	400	C	1	B	β-CH_2	38.71	1400	C	n. d.
c	β-CH_2	17.22	200	aC	1	C	α-CH_2	25.39	300	C	n. d.
d	β-CH_2	16.47	200	aC	1	D	α-CH_2	13.36	300	C	n. d.
3	adt-CH_2	-10.13	200	pC	1	E	α-CH_2	11.69	300	aC	n. d.
4	adt-CH_2	-21.07	200	pC	1	F	α-CH_2	-2.92	300	pC	1
e	α-CH_2	11.7	200	aC	1	3+4	adt-CH_2	-7.25	300	pC	2
f	α-CH_2	11.4	100	aC	1	G	β-CH_2	-8.48	400	pC	1
						H	β-CH_2	-27.78	800	pC	1

[a] full-width at half-maximum, n. d. = not determined, C = Curie, aC = anti-Curie, pC = pseudo-Curie

FTIR spectra of HydA1 in the H_{ox} state

Due to the appearance of the active site (with a free ligand site at Fe_d), there are two terminal –CO vibrations and one bridging –CO as well as two $–CN^-$ vibrations expected in FTIR spectrum. For the [FeFe] hydrogenase HydA1 from *Chlamydomonas reinhardtii* in the H_{ox} state, bands at 2088/2070 cm^{-1} corresponding to the $–CN^-$ vibrations and bands at 1964/ 1939/ 1803 cm^{-1} for the –CO vibrations are described.[1] With small deviations these vibrations can be detected for the used NMR samples for the H_{ox} state (Figure S4). The deuteration of methylene protons of adt does not affect the band positions in the H_{ox} state. Impurities, mainly H_{ox}-CO state (see asterisk Figure S4 and compare Figure S7), are slightly more pronounced in the sample maturated with ^{2}H-adt. Based on the FTIR spectra the purity of both freshly prepared NMR samples in the H_{ox} state has been estimated as >95 %.

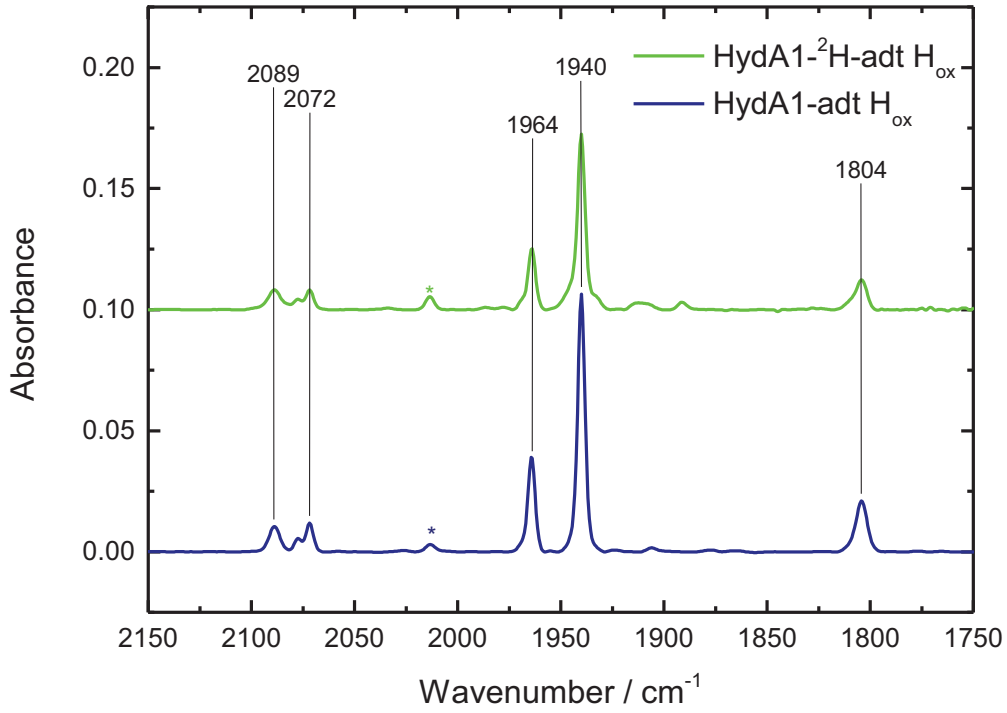

Figure S4. FTIR spectra of HydA1 in the H_{ox} state at room temperature. The spectrum of the unlabeled sample is shown in blue and the sample with the deuterated $[2Fe]_H$ site (^{2}H-adt) is shown in green. The marker band of the H_{ox}-CO state at 2013 cm^{-1} is indicated by *.

Assignment of the adt methylene protons in the H_{ox}-CO state

In order to distinguish the methylene protons of the $[4Fe\text{-}4S]_H$ cluster-coordinating cysteines and of the adt in the $[2Fe]_H$ cluster of the H_{ox} state, apo-HydA1 was maturated using ^{2}H-adt. By comparison of the ^{1}H spectra of unlabeled H_{ox} with H_{ox} containing ^{2}H-adt, signals labelled 1 to 4 in Figure 2c have been unambiguously assigned to the four methylene protons of $[2Fe]_H$. The amine proton of adt exchanges with water and is thus not present in the ^{1}H NMR spectra when 100% D_2O is used as the solvent.

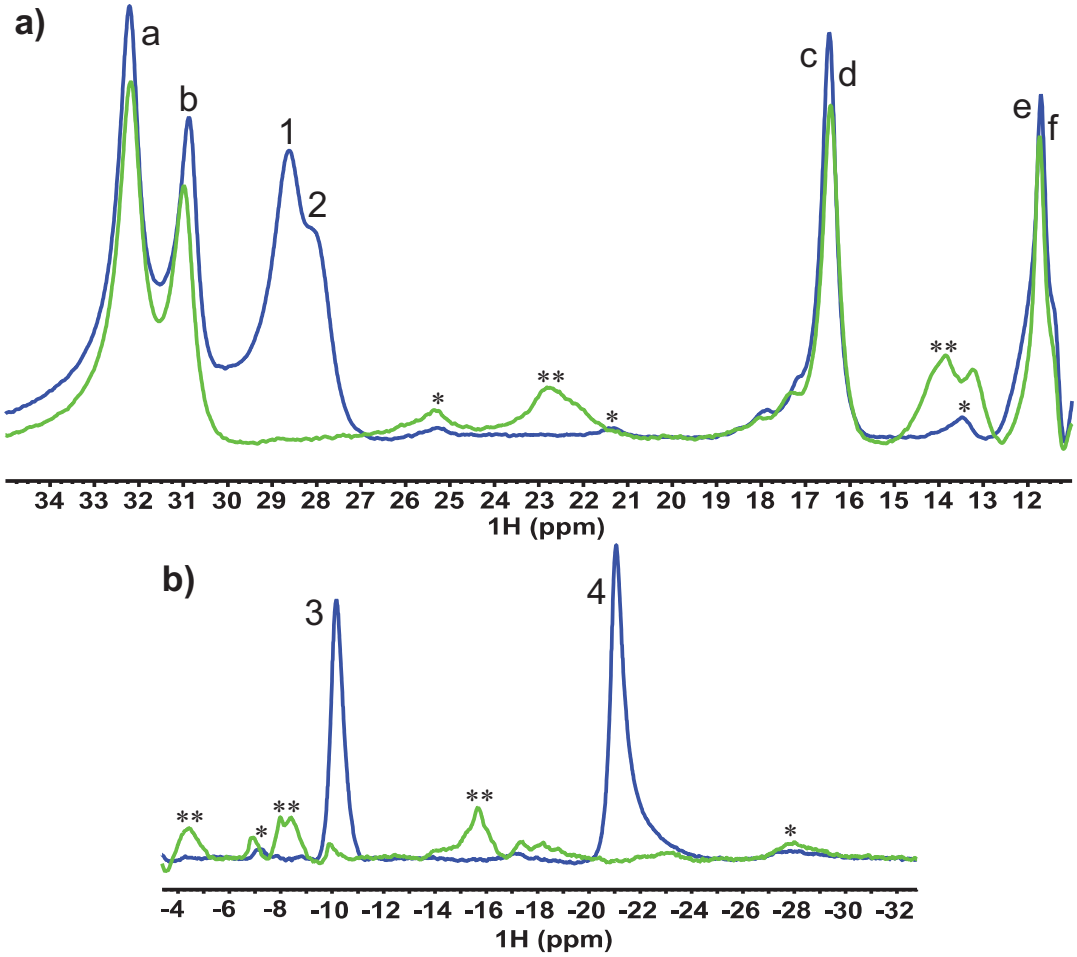

Figure S5. 1D ^{1}H NMR spectra (600 MHz) at 298 K of unlabeled oxidized HydA1 (blue, H_{ox}) and oxidized HydA1 maturated with deuterated adt (green, H_{ox}-^{2}H-adt). a) Downfield region from 35 to 11 ppm and b) upfield region from -3 to -33 ppm. Peaks that belong to other HydA1 states investigated here are labelled with *. Resonances marked with ** originate probably from reduced HydA1 states present in the sample. The contaminations constitute about 5 % of the total sample for unlabeled H_{ox} and about 20 % for H_{ox}-^{2}H-adt. As the FTIR spectra for H_{ox} and H_{ox}-^{2}H-adt are almost identical (Figure S4), the sample maturated with ^{2}H-adt appears to be less stable than the sample maturated with adt.

SI4 Assignment of the axial and equatorial methylene protons of adt

a) Distance and linewidth considerations

In the X-ray structure[7] with protons added, the axial protons are closer to $[4Fe\text{-}4S]_H$ as well as to the proximal and distal Fe sites (Fe_p and Fe_d) compared to the equatorial protons (Figure 1 (right) and Table S2). Since the paramagnetic relaxation enhancement also depends on the inverse sixth power of the distance between metal ion and nuclear spin, in general the closer a proton is to an Fe, the larger is its line width of the corresponding ^1H signal.[8]

Table S3. Distances of the methylene protons of adt to Fe_d and Fe_p

	distance to Fe_p (Å)	distance to Fe_d (Å)
H1	3.54	3.98
H2	3.44	4.07
H3	4.40	4.19
H4	4.37	4.12

b) Experimentally observed characteristic NOE patterns for axial and equatorial protons

In addition to $[Fe_2(adt)(CO)_4(CN)_2]$ other synthesized inorganic cofactors can be incorporated into recombinant HydA1 containing only the $[4Fe\text{-}4S]_H$ cluster. The resulting analogues of HydA1 have a reduced or no activity but may have other advantages over fully active HydA1.[1] Using the propanedithiolate (pdt) analogue $Fe_2(pdt)(CO)_4(CN)_2$ for maturation to prepare the "so-called" HydA1-pdt provides the advantage of high sample stability concomitant with only an oxidized and a reduced state. Importantly, the oxidized form of HydA1-pdt has revealed basically the same electronic structure as fully active HydA1 in the H_{ox} state.[3] Hence the H_{ox} state of HydA1-pdt has been used to obtain ^1H NOEs connectivities between the methylene protons of the dithiolate bridge of $[2Fe]_H$. These ^1H NOE connectivities present another strong evidence for signals 1+2 to correspond to the axial and for signals 3+4 to correspond to the equatorial protons. The measured ^1H NOE spectra revealed NOEs between signals 3 and 1+2 as well as between signals 4 and 1+2. In addition, no NOE was observed between signal 3 and 4 (Figure S6). Accordingly, the downfield shifted signals 1+2 with a line width of about 500 Hz have been tentatively assigned to the axial protons H1 and H2 and signals 3+4 with a line width of about 200 Hz have been assigned to the equatorial protons H3 and H4 (Figure 1 and Table 1). The NOE experiments were carried out with the mixture of 50% oxidized and 50% reduced HydA1-pdt to observe any possible saturation transfer from one oxidation state to the other.

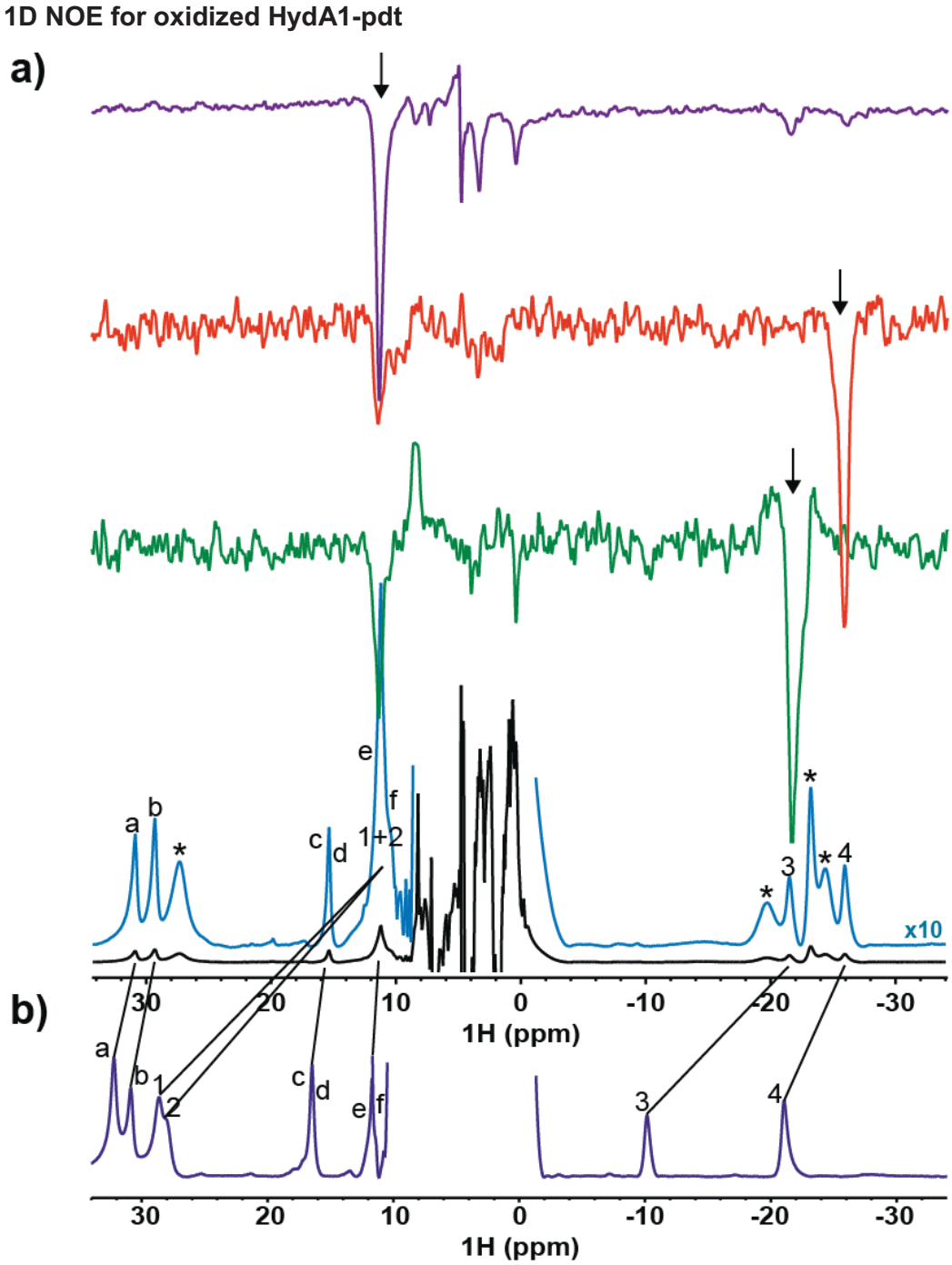

Figure S6. a) Overlay of the NOE spectra obtained upon irradiating the hyperfine shifted resonances and the full spectrum of an about 1:1 mixture of oxidized and reduced HydA1-pdt (black). The trace in light blue indicates a x10 multiplication of the intensity. Upon irradiating signal 3 (green trace) or signal 4 (red trace), a signal at about 11.2 ppm responds (signal 1+2). Signal 1+2 (violet trace) is coupled to signal 3 and also signal 4. The arrows indicate the irradiation frequencies. Irradiation is performed to minimize the artifacts as shown in Figure S1. The resonances originating from the reduced portion of the sample are indicated by *. b) The 1D ^{1}H NMR spectrum of H_{ox} as also shown in Figure 1c. The black lines connect the corresponding resonances of H_{ox} in b) and oxidized HydA1-pdt in a). The strong chemical shift differences of signals 1-4 observed when comparing the ^{1}H 1D NMR spectra of HydA1-adt and HydA1-pdt in the H_{ox} state are caused by the presence of a methylene group instead of a secondary amine in the bridgehead position of the dithiolate ligand connecting the two irons of $[2Fe]_H$.

FTIR spectra of HydA1 in the H_{ox}-CO state

In the H_{ox}-CO state an additional –CO ligand is bound to the open coordination site at Fe_d. Thus, four instead of three –CO vibrations occur. In the literature band positions at 2092/2084/2013/1970/1964 and 1810 cm^{-1} are described[9] and the detected signals for the used NMR samples in H_{ox}-CO state are almost identical. The rather broad contributions in the HydA1-^{2}H-adt H_{ox}-CO spectrum (Figure S7, green line) are impurities (^{v}) and do not belong to a second redox state. For the unlabelled sample, a tiny amount of H_{ox} (1939 cm^{-1}) and $H_{red}H^+$ (1891 cm^{-1}) estimated as less than 5 % of the total sample were detected (Figure S7).

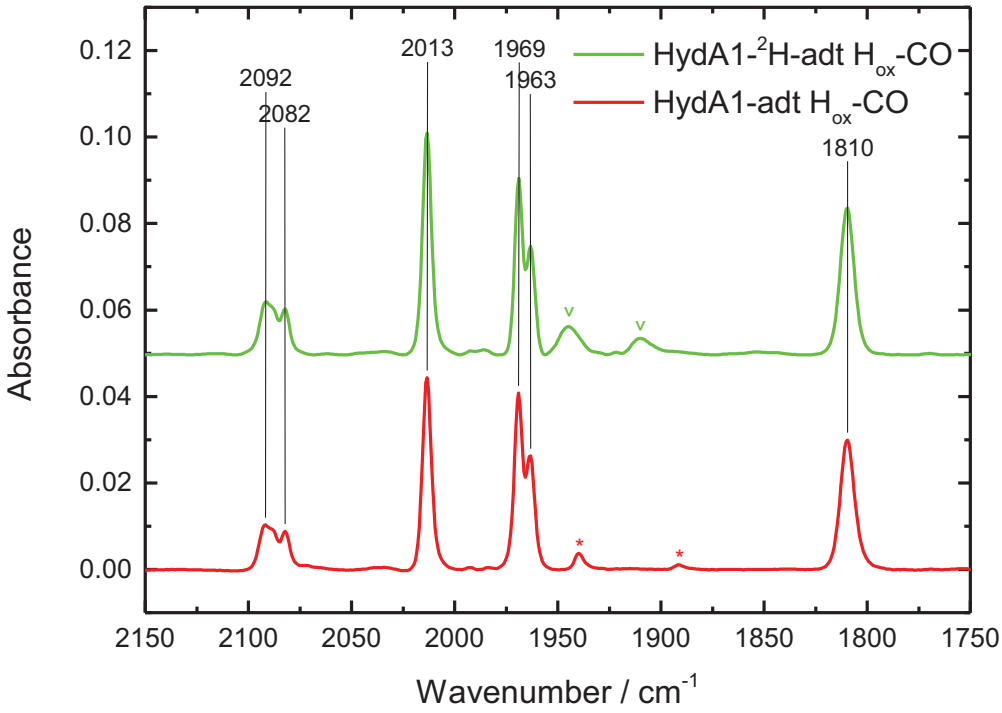

Figure S7. FTIR spectra of HydA1 in the H_{ox}-CO state at room temperature. The spectrum of the unlabeled sample is shown in red and the sample with the deuterated [2Fe] site (^{2}H-adt) is shown in green. Impurities are indicated by ^{v} and other redox states are indicated by *.

Assignment of the adt methylene protons in the H_{ox}-CO state

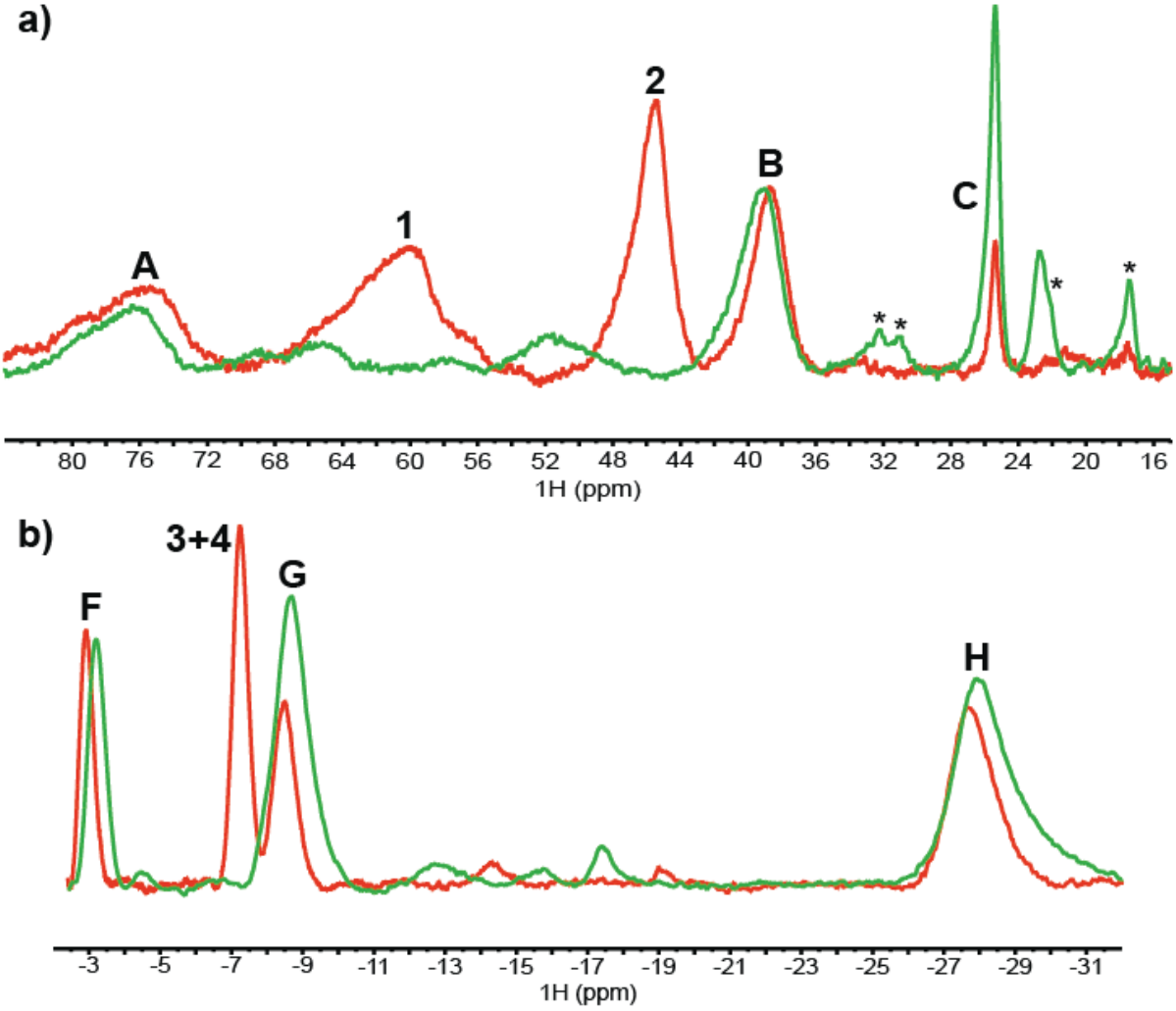

Figure S8. 1D ^{1}H NMR spectra (600 MHz) at 298 K of unlabeled HydA1 in the H_{ox}-CO state (red) and H_{ox}-CO after maturation with deuterated ADT (green). a) Downfield region from 84 to 15 ppm and b) upfield region from -2 to -32 ppm. Peaks that belong to other HydA1 states investigated here are labelled with *. The contaminations constitute about 5 % of the total sample.

Three of the hyperfine shifted signals observed for unlabeled HydA1 in the H_{ox}-CO state are not present when deuterated $[Fe_2(adt)(CO)_4(CN)_2]$ has been used for maturation. Given that the integral of the disappearing upfield peak at -7.25 ppm suggests that it consists of two proton signals (3+4), all four methylene protons of $[2Fe]_H$ could thus also be identified for H_{ox}-CO (Figure 2c).

References

(1) Siebel, J. F.; Adamska-Venkatesh, A.; Weber, K.; Rumpel, S.; Reijerse, E.; Lubitz, W. *Biochemistry* **2015**, *54*, 1474.

(2) Esselborn, J.; Lambertz, C.; Adamska-Venkatesh, A.; Simmons, T.; Berggren, G.; Noth, J.; Siebel, J.; Hemschemeier, A.; Artero, V.; Reijerse, E.; Fontecave, M.; Lubitz, W.; Happe, T. *Nat. Chem. Biol.* **2013**, *9*, 607.

(3) Adamska-Venkatesh, A.; Simmons, T. R.; Siebel, J. F.; Artero, V.; Fontecave, M.; Reijerse, E.; Lubitz, W. *Phys. Chem. Chem. Phys.* **2015**, *17*, 5421.

(4) Lubitz, W.; Ogata, H.; Rüdiger, O.; Reijerse, E. *Chem. Rev.* **2014**, *114*, 4081.

(5) Inubushi, T.; Becker, E. D. *J. Magn. Reson.* **1983**, *51*, 128.

(6) Bertini, I.; Luchinat, C.; Parigi, G.; Ravera, E. *NMR of Paramagnetic Molecules*; Elsevier Amsterdam 2017.

(7) Pandey, A. S.; Harris, T. V.; Giles, L. J.; Peters, J. W.; Szilagyi, R. K. *J. Am. Chem. Soc.* **2008**, *130*, 4533.

(8) Bertini, I.; Luchinat, C.; Parigi, G.; Pierattelli, R. *Chembiochem* **2005**, *6*, 1536.

(9) Adamska-Venkatesh, A.; Krawietz, D.; Siebel, J.; Weber, K.; Happe, T.; Reijerse, E.; Lubitz, W. *J. Am. Chem. Soc.* **2014**, *136*, 11339.

4.4 Paper IV

Spectroscopic Investigations of a semi-synthetic [FeFe] hydrogenase with propane di-selenol as bridging ligand in the bi-nuclear subsite

C. Sommer, S. Rumpel, S. Roy, V. Artero, M. Fontecave, E.J. Reijerse and W. Lubitz

JBIC submitted

Journal: Journal of Biological and Inorganic Chemistry

Published 07.04.2018, DOI: 10.1007/s00775-018-1558-4

Author: First Author

Contribution: 60 %

- I prepared all biological samples and measured the activities

- I measured, analyzed and fitted all FTIR and FTIR-spectroelectrochemistry experiments

- I was involved analyzing the ^{1}H NMR data

- I was largely involved in writing the manuscript

S. Rumpel measured the ^{1}H NMR spectra, S. Roy synthesized the [2Fe]-PDSe precursor complex, E. J. Reijerse measured and simulated the EPR data and calculated the zero field splitting constant. All others discussed the results and were involved in writing the manuscript.

Spectroscopic Investigations of a semi-synthetic [FeFe] hydrogenase with propane di-selenol as bridging ligand in the binuclear subsite

C. Sommer[1], S. Rumpel[1], S. Roy[2], C. Farès[3], V. Artero[2], M. Fontecave[4], E. Reijerse[1], W. Lubitz[1]

1 Max-Planck-Institut für Chemische Energiekonversion, Stiftstrasse 34-36, 45470 Mülheim an der Ruhr, Germany.

2 Laboratoire de Chimie et Biologie des Métaux, Université Grenoble Alpes, CEA/BIG, CNRS, 17 rue des martyrs, 38000 Grenoble, France.

3 Max-Planck-Institut für Kohlenforschung, Kaiser-Wilhelm Platz 1, 45470 Mülheim an der Ruhr, Germany

4 Laboratoire de Chimie des Processus Biologiques, Collège de France, Université Pierre et Marie Curie, CNRS UMR 8229, PSL Research University, 11 place Marcelin Berthelot, 75005 Paris, France.

✉ Wolfgang.Lubitz@cec.mpg.de

Abbreviations and nomenclature

MV Methyl viologen, **NMR** Nuclear Magnetic Resonance, **EPR** Electron Paramagnetic Resonance, **FTIR** Fourier Transform Infrared Spectroscopy.

*Bridging ligands***: ADT** aza-propane-dithiolate ($\mu(CH_2S)_2NH$), **ADSe** aza-propane-diselenate ($\mu(CH_2Se)_2NH$), **PDT** propane-dithiolate ($\mu(CH_2S)_2CH_2$), **PDSe** propane-diselenate, ($\mu(CH_2Se)_2CH_2$).
Synthetic precursors: [2Fe]-ADT/-ADSe/-PDT/-PDSe, where [2Fe]=$Fe_2(CO)_4(CN^-)_2$
Enzymes: apo-HydA1: *Cr*HydA1 containing only the $[4Fe\text{-}4X]_H$ subsite; HydA1-XDT: *Cr*HydA1 maturated with [2Fe]-XDT; *Cr*: *Chlamydomonas reinhardtii*

Subsites/complexes: $[2Fe]_H$: $Fe_2(CO)_3(CN^-)_2$XDT subsite of [FeFe] hydrogenase

Abstract

[FeFe] hydrogenases catalyze the reversible conversion of H_2 into electrons and protons. Their catalytic site, the H-cluster, contains a generic $[4Fe\text{-}4S]_H$ cluster coupled to a $[2Fe]_H$ subsite $[Fe_2(ADT)(CO)_3(CN)_2]^{2-}$, ADT = $\mu(CH_2S)_2NH$. Heterologously expressed [FeFe] hydrogenases (apo-hydrogenase) lack the $[2Fe]_H$ unit but this can be incorporated through artificial maturation with a synthetic precursor $[Fe_2(ADT)(CO)_4(CN)_2]^{2-}$. Maturation with a [2Fe] complex in which the essential ADT amine moiety has been replaced by CH_2 (PDT=propane-dithiolate) results in a low activity enzyme with structural and spectroscopic properties similar to those of the native enzyme but with simplified redox behavior. Here we study the effect of sulfur-to-selenium (S-to-Se) substitution in the bridging PDT ligand incorporated in the [FeFe] hydrogenase HydA1 from *Chlamydomonas reinhardtii* using magnetic resonance (EPR, NMR), FTIR and spectroelectrochemistry. The resulting HydA1-PDSe enzyme shows the same redox behavior as the parent HydA1-PDT. In addition, a state is observed in which extraneous CO is bound to the open coordination site of the $[2Fe]_H$ unit. This state was previously observed only in the native enzyme HydA1-ADT and not in HydA1-PDT. We also studied the effect of S-to-Se substitution in the [4Fe-4S] subcluster. The reduced form of HydA1 containing only the $[4Fe\text{-}4Se]_H$ cluster shows a characteristic S=7/2 spin state which converts back into the S=1/2 spin state upon maturation with a [2Fe]-XDT complex. The spectroscopic features and redox behavior of HydA1-PDSe, resulting from maturation with $[Fe_2(PDSe)(CO)_4(CN)_2]^{2-}$ are discussed in terms of spin and charge density shifts and provide interesting insight into the electronic structure of the H-cluster.

Keywords [FeFe] Hydrogenase, chalcogenic substitution, Nuclear Magnetic Resonance, Electron Paramagnetic Resonance, FTIR spectroelectrochemistry

Introduction

The reversible heterolytic splitting of hydrogen into protons and electrons is one of the most basic reactions in chemistry. In nature, hydrogen is part of the energy metabolism of several single cellular organisms which are spread over all three domains of life.[1, 2] [FeFe] Hydrogenases catalyze the conversion of protons and electrons into hydrogen in a very efficient way with turnover frequencies over 10.000 H_2/s.[3, 4] The active site in these enzymes, the so called H-cluster, consists of a generic $[4Fe\text{-}4S]_H$ cluster linked to a bi-nuclear iron complex $[2Fe]_H$ carrying 3 CO and 2 CN^- ligands as well as a bridging aza-propane-dithiolate (ADT) ligand (see fig. 1) that serves as proton relay of the protein´s proton transport pathway.[5] Often, additional [4Fe-4S] clusters are present that form an electron transport chain connecting the H-cluster with the protein surface where redox partners of the enzyme can bind.

The small hydrogenase from *Chlamydomonas reinhardtii* HydA1 is used as prototype for [FeFe] hydrogenases since it contains only the H-cluster and can be overexpressed in *Escherichia coli*[6] with high yields.[7] However, since the host organism lacks the maturation factors that built the $[2Fe]_H$ subsite, the resulting enzyme (called apo-HydA1) only contains the $[4Fe\text{-}4S]_H$ cluster and is inactive in hydrogen conversion. Through artificial maturation using synthetic precursors of the $[2Fe]_H$ subsite, the active enzyme can be obtained.[8, 9] This process can be conveniently followed using FTIR spectroscopy since the CO and CN^- stretches of the H-cluster are found in a frequency range that does not overlap with the strong protein amide bands.[10] The use of synthetic precursors of the $[2Fe]_H$ subsite opens the possibility to introduce modified complexes into the enzyme and label these with different nuclear isotopes .[11-13] In addition, the generic $[4Fe\text{-}4S]_H$ cluster can be modified through classical reconstitution.[7, 14]

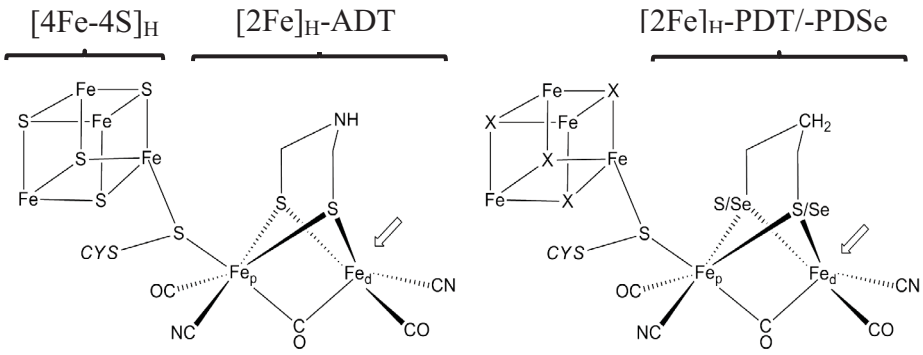

Fig. 1: The native active site of [FeFe] hydrogenase and applied modifications. The iron atoms are labeled as proximal (Fe_p) and distal (Fe_d) with respect to their position to the $[4Fe\text{-}4S]_H$ cluster. Left: Native H-cluster that consists of the $[4Fe\text{-}4S]_H$ cluster and $[2Fe]_H$-ADT subsite. Right: Modified H-cluster with $[2Fe]_H$-PDT or $[2Fe]_H$-PDSe. Additionally bridging sulfides in the cubane cluster (here marked with X) can be exchanged to Se

Native HydA1 shows a variety of redox states. The $[2Fe]_H$ site can be reduced $[Fe^I\,Fe^I]$ or oxidized $[Fe^I\,Fe^{II}]$. Likewise, the $[4Fe\text{-}4S]_H$ subcluster can be present in reduced (1+) or oxidized (2+) forms. Additionally, the bridgehead amino group can be protonated (NH_2^+) or unprotonated (NH).[15] It is assumed that, for the doubly reduced state of the H-cluster, transfer of an NH_2^+ proton to the distal iron Fe_d affords a terminal hydride that upon reprotonation forms H_2.[16-18]

The enzyme is inhibited by external CO, which binds to the open coordination site at Fe_d. This additional donor ligand has a strong effect on the electronic structure of the H-cluster as observed by EPR and FTIR.[19] Furthermore, it has been shown that the redox and catalytic behavior of the active enzyme in various organisms is sensitive to pH[15] and the presence of accessory [4Fe-4S] clusters.[20] In order to affect, and possibly, improve the activity and oxygen resistance of [FeFe] hydrogenases the bridging ADT ligand in the $[2Fe]_H$ subsite has been extensively modified through artificial maturation with appropriate synthetic precursors.[21, 22] However, these attempts did not lead to improved enzymatic properties (activity, O_2 resistance); however, it did provide useful insight into the structure/function relations of the H-cluster. By substituting the bridgehead amino group to a methylene group, using the [2Fe]-PDT precursor, the number of accessible redox states in HydA1-PDT is

reduced to two: H_{ox} and H_{red}.[23] The spectroscopic signatures (FTIR/EPR) of these states are virtually identical to the corresponding states in the native enzyme suggesting a very similar electronic and geometric structure. Both are characterized by a mixed valence binuclear site and differ only in the redox state of the cubane $\left[4\text{Fe-}4\text{S}\right]_{\text{H}}^{2+/+}$. Interestingly, despite the structural similarities with the native enzyme[24], in HydA1-PDT, binding of extrinsic CO to the open coordination site has not been observed.

Inspired by selenium's role in oxidative protection in [NiFeSe] hydrogenases[25], variants of the H-cluster were recently reported in which the sulfurs in both $[4\text{Fe-}4\text{S}]_{\text{H}}$ and $[2\text{Fe}]_{\text{H}}$ subclusters were changed to selenium. The atomic mass of Se is more than twice that of sulfur. It has a ≈15% increased atomic radius and forms more polarized bonds based on its stronger metallic character compared to sulfur. It has been shown that $[4\text{Fe-}4\text{Se}]_{\text{H}}$ reconstituted HydA1-ADT does not show any decrease in activity nor does it change the vibrational characteristics of the CO and CN^- ligands.[7] A S-to-Se substitution in the $[2\text{Fe}]_{\text{H}}$ subsite generates an enzyme which shows similar activity but is less stable under laboratory conditions.[22] Therefore, the individual redox states are more difficult to stabilize preventing most of the spectroscopic investigations.

To bypass this limitation and be able to study the effect of S-to-Se substitutions on the electronic structure of the H-cluster, we turned to the more stable HydA1-PDSe enzyme, produced via maturation of apo-HydA1 with the [2Fe]-PDSe precursor. HydA1-PDSe, in analogy to HydA1-PDT, shows a stable H_{ox} and a singly reduced H_{red} state. However, in contrast to HydA1-PDT, a H_{ox}-CO state could be observed in HydA1-PDSe. Since the structural properties of HydA1-PDSe are expected to be very similar to those of the native enzyme as found for HydA1-PDT, HydA1-PDSe was used to study the effect of S-to-Se exchange on the electronic structure of the H-cluster, using FTIR-spectroelectrochemistry, EPR and NMR spectroscopy, and on the catalytic activity. ^{1}H NMR in solution has recently

been introduced as technique to study the hydrogenase active site.[26] For these enzymes ^{1}H NMR is extremely useful since the active site with its reactants as well as the protein surrounding can be studied simultaneously with atomic (nuclear) resolution under near physiological conditions. NMR has frequently been used as a tool to study paramagnetic iron-sulfur proteins[27, 28] to resolve the electron distribution and the magnetic couplings; for unknown systems it can help to identify the cluster type.[29]

We have also studied S-to-Se substitution in the $[4Fe\text{-}4S]_H$ subcluster using the unmaturated apo-enzyme. This substitution often leads to high spin multiplicity in the reduced state of the cluster and is well documented for ferredoxins.[30-33]

Materials and Methods

Synthesis of active site mimics

All reactions were carried out under an inert atmosphere of argon using standard Schlenk and vacuum-line techniques. Solvents were freshly distilled under argon using appropriate drying agents and the distilled solvents were degassed by three freeze-pump-thaw cycles. FTIR spectra of the complexes were recorded on a Perkin Elmer Spectrum-100 spectrometer via a thin film solution using a stainless steel sealed liquid spectrophotometer cell with CaF_2 windows. $[Fe_2(\mu(CH_2Se)_2CH_2)(CO)_6]$ was synthesized according to literature procedure.[34]

$(Et_4N)_2[Fe_2(\mu(CH_2Se)_2CH_2)(CO)_4(C^{14}N)_2]$

To a solution of $Fe_2[(\mu(CH_2Se)_2CH_2)(CO)_6]$ (0.146 g, 0.3 mmol) in acetonitrile (15 mL), tetraethylammonium cyanide (0.105 g, 0.62 mmol) was added under positive argon flow. After stirring at room temperature for 3 h, the reaction mixture was cannula-filtered to a Schlenk-flask and the red solution was concentrated to approximately 7 mL. This solution was layered with diethyl ether (20 mL) and cooled to 253 K to yield

$(Et_4N)_2[Fe_2(\mu(CH_2Se)_2CH_2)(CO)_4(C^{14}N)_2]$ as dark red solid. IR (CH_3CN, cm^{-1}): 2075 (CN^-), 1955, 1918, 1879 (CO).

$(Et_4N)_2[Fe_2(\mu(CH_2Se)_2CH_2)(CO)_4(C^{15}N)_2]$

A solution of $KC^{15}N$ (0.016 g, 0.24 mmol) in methanol (5 mL) was added dropwise via a cannula to a solution of $[Fe_2(\mu(CH_2Se)_2CH_2)(CO)_6]$ (0.045 g, 0.1 mmol) in acetonitrile (5 mL). After stirring the reaction mixture for 30 min at room temperature, a solution of $[Et_4N]Br$ (0.05 g, 0.24 mmol) in acetonitrile (4 mL) was added, and the dark red solution was allowed to stir for 3 h. The solvent was removed under reduced pressure to yield a dark red oily solid. This residue was redissolved in acetonitrile (5 mL) and filtered via cannula to give a dark red filtrate. This solution

was layered with diethyl ether (15 mL) and cooled to 253 K to produce $(Et_4N)_2[Fe_2(\mu(CH_2Se)_2CH_2)(CO)_4(C^{15}N)_2]$ as a dark red solid (0.028 g, 25%). IR (CH_3CN, cm^{-1}): 2044 ($C^{15}N^-$), 1956, 1917, 1879 (CO).

Protein purification and maturation Apo-HydA1 protein expression and maturation are based on a slightly modified previously published protocol.[8, 35] The pH was adjusted prior to induction of the protein expression and the purification was performed without any dithionite. 30 mg/L Kanamycin was used as selection antibiotic. For maturation the apo protein was diluted to 350 µM in 0.1 M Tris/HCl, 0.15 M NaCl pH 8.0 and a three times excess of [2Fe]-PDSe/-PDT dissolved in DMSO was added for one hour. For maturation of $[4Fe\text{-}4Se]_H$ apo-HydA1 with [2Fe]-PDT/-PDSe a temperature of 310-311 K and an incubation time of 2-3 h was used. Unbound complexes were removed by a desalting column (PD-10, GE Healthcare) and the maturated proteins were concentrated (Merck Millipore, Amicon Ultra-15, 30 kDa).

Substitution of $[4Fe\text{-}4S]_H$ with $[4Fe\text{-}4Se]_H$ through reconstitution

All steps for cluster reconstitution were performed anaerobically. $[4Fe\text{-}4S]_H$ apo-HydA1 was unfolded with 6 M guanidinium chloride to extract the bound cubane cluster. To remove the chaotropic agent the sample was desalted three times over a PD-10 column (GE Healthcare). While removing the chaotropic agent, apo-HydA1 refolds in the used 0.1 M Tris/HCl, 0.15 M NaCl pH 8.0 buffer. The protein was prepared for the new cluster assembly by reduction with 5 mM dithiothreitol. After reduction, a 12-16 fold excess of $FeCl_3$ was added followed after 10 min by the same excess of reduced $NaSe_2$ into the continuously stirred solution. After incubation for 90 min at room temperature the solution was dark brown and the reconstitution was stopped. After two consecutive desalting steps the $[4Fe\text{-}4Se]_H$ apo-HydA1 was concentrated and used for further applications.

H_2 oxidation assay

The hydrogen oxidation assay was performed based on methyl viologen (MV) reduction under strictly anaerobic conditions as previously described.[35] The photometric assay (578 nm) was performed with 100 µg HydA1-PDT/-PDSe in a reaction volume of 1 mL with hydrogen saturated 100 mM $K_xH_yPO_4$, 10 mM MV pH 6.8 buffer. The slope was determined and the activities were calculated based on an extinction coefficient for the MV radical of 9780 $\frac{L}{mol \cdot cm}$.

H_2 production

Hydrogen production was examined analogous to Winkler *et al.* 2002[36] using gas chromatography. In a 2 mL gas tight vial, 400 µL reaction volume containing 10 µg HydA1-PDT/-PDSe, 300 mM $K_xH_yPO_4$ pH 6.8, 10 mM MV and 100 mM sodium dithionite (NaDT) was flushed with argon for 5 min. Samples were incubated at 310 K for 20 min. A gaschromatogram of 300 µL headspace was recorded at 313 K with a RT-MSieve 5 Å

column. Given are the mean values with standard deviations calculated from three measurements per sample in triplicate.

FTIR spectroscopy and FTIR spectroelectrochemistry

Transmission FTIR spectra were obtained using a Vertex 80v FTIR spectrometer from Bruker Optics with a N_2 cooled mercury cadmium telluride (MCT) detector. All sample preparations were performed under strict anaerobic conditions. Samples were immobilized between CaF_2 windows and measured in a continuously purged sample chamber. Spectra were recorded with 20 kHz velocity in double-sided forward backward mode with phase resolution of 16, zero filling factor of 2 and Blackman-Harris-3-term apodization. Final data processing was performed using home-written scripts in the Matlab® programming environment. FTIR spectroelectrochemistry was carried out as previously described but without use of redox mediators.[15] Spectra were recorded on a Bruker IFS 66v/s spectrometer with N_2 cooled MCT detector with an aperture of 2.5–3 mm and thermostated sample (278 K). An equilibration time of 40-60 min was used between two applied potentials (Autolab PGSTAT101; NOVA software).

Sample preparation and NMR spectroscopy

For proton NMR spectroscopy samples were maturated as described and then three times rebuffered to a low salt D_2O buffer (25 mM $K_xH_yPO_4$, pD 6.8) and subsequently concentrated up to 2.5 mM. Finally the required redox states were titrated with NaDT or thionine acetate and monitored by FTIR spectroscopy. All NMR spectra were acquired on a Bruker AVANCE 600 spectrometer equipped with a cryogenic TCI probehead. The 1D spectra were recorded with 2048 scans, a relaxation delay of 0.2 s and a spectral width of 200 ppm. Spectra were processed and analyzed using Topspin 2.1 and Mnova 10.0.2.

EPR spectroscopy

X-band CW-EPR spectra were recorded on a Bruker Elexsys 500 EPR spectrometer equipped with a standard TE102 rectangular resonator and an Oxford ESR900 helium flow cryostat.

Pulse echo detected EPR spectra were obtained using a Bruker Elexsys 580 X-band pulsed EPR spectrometer. Samples were accommodated in a Bruker MD5 dielectric resonator inserted into an Oxford CF935 helium flow cryostat. Q-band Echo detected experiments were conducted on a Bruker Elexsys 580 Q-band pulsed EPR spectrometer using a homebuilt Q-band resonator.[37] Low temperatures were reached using a closed cycle Helium cryostat from Cryogenic Ltd.[38]

Results and discussion

For all artificial enzymes no catalytic activity for hydrogen production or oxidation was observed (see fig. S1). This is surprising since HydA1-ADSe was reported to be fully active.[22] Therefore, it was anticipated that HydA1-PDSe would at least show an activity similar to that of HydA1-PDT.

The H_{ox} and H_{red} states

The successful maturation with [2Fe]-PDSe and the charge distribution of the two main states H_{ox} and H_{red} from HydA1-PDT and –PDSe was studied with FTIR spectroscopy using the CO and CN^- vibrations as probes.

FTIR spectroscopy

The incorporation of the [2Fe]-PDSe precursor into apo-HydA1 was confirmed by FTIR spectroscopy showing narrow CO and CN^- bands as compared to those of the free synthetic precursor in solution (see fig. S2A).

As shown in figure 2 the signal pattern for CN^- and CO bands of the H_{ox} state of HydA1-PDSe is red shifted by 3-8 cm^{-1} compared to HydA1-PDT which is in good agreement with the red shifts found for the [2Fe]-ADSe complex incorporated into HydA1 from *Chlostridium pasteurianum* (*Cp*) by Kertess *et al*.[22] compared to HydA1-ADT. This can be explained by the donation from the Se lone pair to the Fe σ*-orbital that enhances π-back-donation from Fe to CO/CN^- and weakens the CO/CN^- internal ligand bond strength.

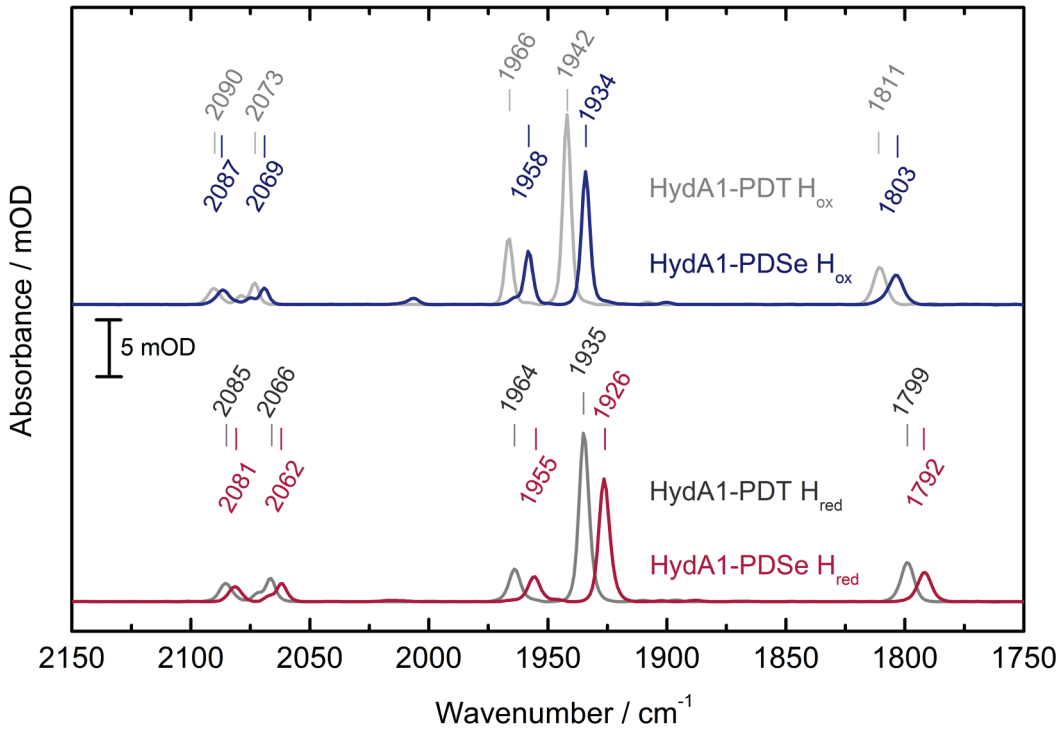

Fig. 2 Comparison of the H_{ox} and H_{red} states of $[4Fe\text{-}4S]_H$ HydA1-PDT/-PDSe in FTIR spectroscopy. The smaller contribution at 2005 cm^{-1} in the spectrum of HydA1-PDSe H_{ox} originates from the oxidized CO-inhibited state (see fig 5). Spectra are taken at 288 K with a spectral resolution of 2 cm^{-1}

Reduction with 5 mM NaDT results in HydA1-PDSe H_{red} with small red shifts in the FTIR spectrum compared to the oxidized state (see table 1) similar to the ones observed for HydA1-PDT upon reduction (see fig. 2). Both terminal CO's are red shifted by -9 cm^{-1} whereas the bridging μCO is red shifted by -7 cm^{-1} compared to HydA1-PDT H_{red} (see table 1). The cyanide ligand vibration frequencies are lowered by 3-4 cm^{-1}. The small red shifts in HydA1-PDSe from the oxidized to the reduced state indicate that the reduction takes place at the $[4Fe\text{-}4S]_H$ subcluster leading to $[4Fe\text{-}4S]_H^+$ HydA1-PDSe with a $[Fe_p(I)Fe_d(II)]$ configuration. A reduction at the $[2Fe]_H$ subsite would lead to larger shifts, e.g. as can be observed in the sensing hydrogenase HydS-ADT from *Thermotoga maritima* upon conversion from the H_{ox} into the H_{red*} state.[39]

These observations show that the two enzyme variants show a similar charge distribution with only minor effects caused the larger mass of selenium as compared to sulfur.

Table 2 FTIR vibrations in cm^{-1} of HydA1-PDT and -PDSe in their oxidized and reduced states.

	-CN^-	**-CO**	**-CO**	**-μCO**
PDT H_{ox}	2090/2073	1966	1942	1811
PDSe H_{ox}	2087/2069	1958	1934	1803
PDT H_{red}	2085/2066	1964	1935	1799
PDSe H_{red}	2081/2062	1955	1926	1792

EPR spectroscopy

The singly reduced states H_{red} in HydA1-PDT and -PDSe are EPR silent although both the reduced $[4Fe\text{-}4S]_H$ and mixed valence $[2Fe]_H$ subclusters formally carry unpaired spin density. The anti-ferromagnetic intercluster spin coupling, however, leads to a $S_{total}=0$ ground state.

The oxidized HydA1-PDSe was additionally analyzed with EPR spectroscopy. The H_{ox} state is expected to have an electronic configuration $[4Fe\text{-}4S]_H^{2+}$ $[Fe_p(I)Fe_d(II)]$ which has an S=1/2 ground state. It indeed shows a rhombic EPR spectrum very similar to that of HydA1-PDT H_{ox} (see fig. 3). The g-values of HydA1-PDSe are, however, significantly shifted towards higher values (in particular g_y) which can be explained by the larger spin-orbit contribution of selenium as compared to sulfur.

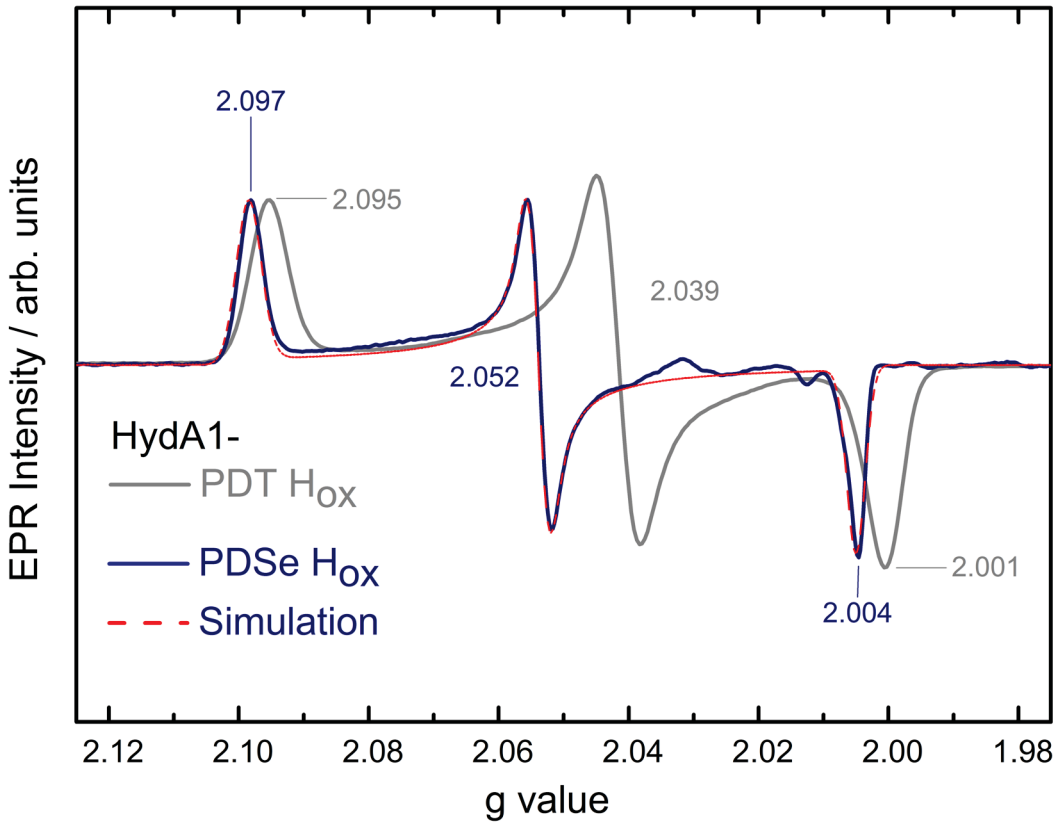

Fig. 3: Superimposed EPR spectra of HydA1-PDT H_{ox} and HydA1-PDSe H_{ox} with simulation. HydA1-PDT H_{ox} is shown in grey, HydA1-PDSe H_{ox} is shown is dark blue. The small additional signals in HydA1-PDSe H_{ox} are from a contribution of H_{ox}-CO state (see table S2). Spectra are taken at 20 K

^{1}H NMR spectroscopy

^{1}H NMR spectroscopy can provide information about the electronic spin density delocalization of the H-cluster in two otherwise structurally similar enzymatic states. For the measurements, usually performed at room temperature, a stable redox state of the sample is required as was shown for H_{ox} and H_{ox}-CO state of the native HydA1.[26]

In contrast to HydA1-ADSe, HydA1-PDSe is very stable in the H_{ox} state and can be used for ^{1}H NMR solution studies at room temperature to investigate the effect of selenium substitution. Figure 4 shows the ^{1}H NMR spectra of the oxidized states of HydA1-PDT and HydA1-PDSe in comparison. The characteristic contact shifted signals originate from the

methylene protons of the PDT/PDSe bridge and the β-CH_2 protons of the cysteines ligating the $[4Fe\text{-}4S]_H$ cluster (see fig. S3) as recently described by Rumpel *et al*.[26]

Both spectra show a very similar pattern with four downfield and two upfield shifted resonances (see fig. 4). The two upfield (negative shift) resonances **3+4**, and also **3′+4′,** originate, based on the earlier assignment achieved for HydA1-ADT H_{ox}[26], from the methylene protons of the PDT/PDSe bridge pointing away from the $[4Fe\text{-}4S]_H$ subcluster ($H_{equatorial}$, see fig. S3). The downfield shifted resonances (**a-f**) and (**a'-f'**) can be assigned to the methylene protons of the β-CH_2 protons of the cysteines coordinating the $[4Fe\text{-}4S]_H$ subcluster.[26]

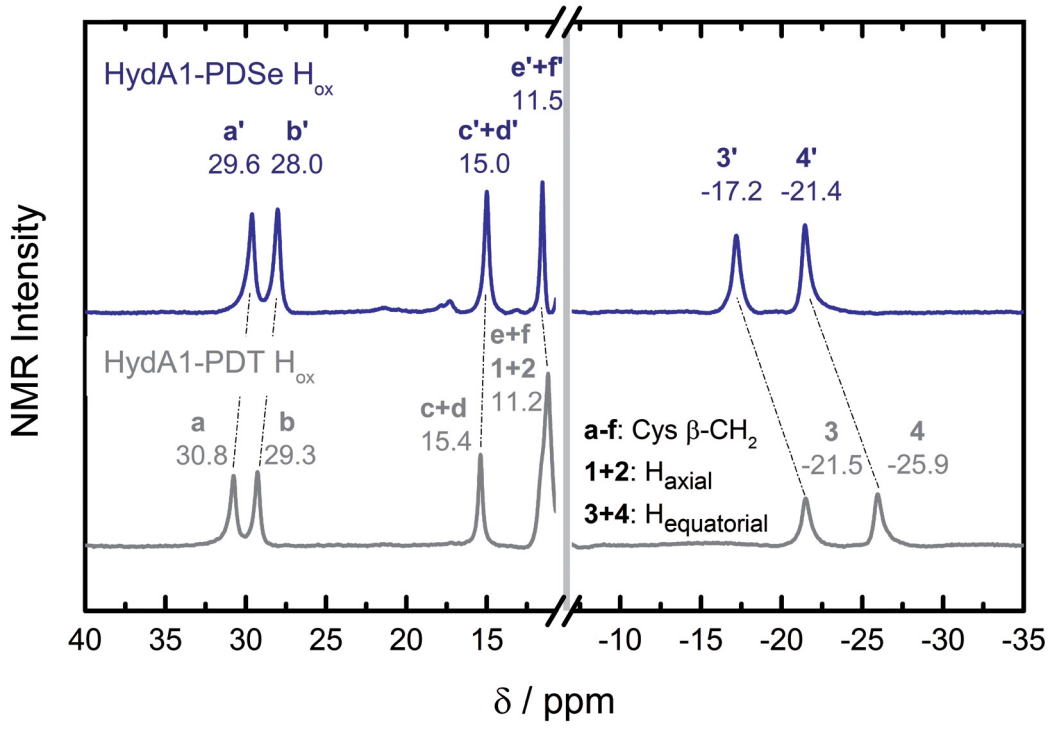

Fig. 4 Liquid state ^{1}H NMR spectra for HydA1-PDT/-PDSe in the H_{ox} state. Spectra were recorded with 600 MHz at 298 K**.** Nomenclature used is based on Rumpel *et al*. 2017

In comparison to HydA1-PDT H_{ox} the ^{1}H NMR spectrum of HydA1-PDSe H_{ox} shows a chemical shift for these equatorial methylene protons **3′+4′** of approximately +4.5 ppm. The axial protons **1+2** pointing towards the $[4Fe\text{-}4S]_H$ cluster resonate downfield around 11.2 ppm

in HydA1-PDT [26], overlapping with the peak of the β-CH_2 pair **e+f** resulting in an increased signal width of 400 Hz (see also table S1). The smaller linewidth of the e'+f' feature (200 Hz) suggest that the **1'+2'** feature (originating from the axial PDSe methylene protons) is no longer overlapping and probably located within the diamagnetic envelope. The smaller shifts in HydA1-PDSe show that the protons experience a reduced spin density at the $[2Fe]_H$ subsite as well as in the $[4Fe\text{-}4S]_H$ cluster. The downfield resonances **a-f** from HydA1-PDT H_{ox} are assigned to the β-methylene protons of the cysteine side-chains coordinating the $[4Fe\text{-}4S]_H$ cluster. In HydA1-PDSe H_{ox} the β-CH_2 protons (**a′-f′**) are only slightly shifted by approximately -0.5 to -1 ppm compared HydA1-PDT H_{ox}.

The electronic spin state and the distance of the observed nucleus to the iron in combination with the local spin density is correlated with the broadening of the resonance.[40] The similarity in signal width between HydA1-PDT H_{ox} to HydA1-PDSe H_{ox} (see table S1) indicates that there is no difference in spin state and spin density distribution.

For the reduced proteins the obtained ^1H NMR spectra in solution show more proton signals over an extended chemical shift range (80 to -25 ppm) with broader line widths due to a reduced cubane cluster with S=1/2 (see fig. S4). Although the $[4Fe\text{-}4S]_H$ cluster is coupled with the $[2Fe]_H$ subsite to an EPR silent H_{red} state at low temperatures, at room temperature higher spin states are populated that induce the large chemical shifts. The data are collected and compared in table S1.

FTIR Spectroelectrochemistry

As inferred from the magnetic resonance and FTIR experiments the substitution of sulfur to selenium in the bridging position slightly changes the electronic structure of the altered active

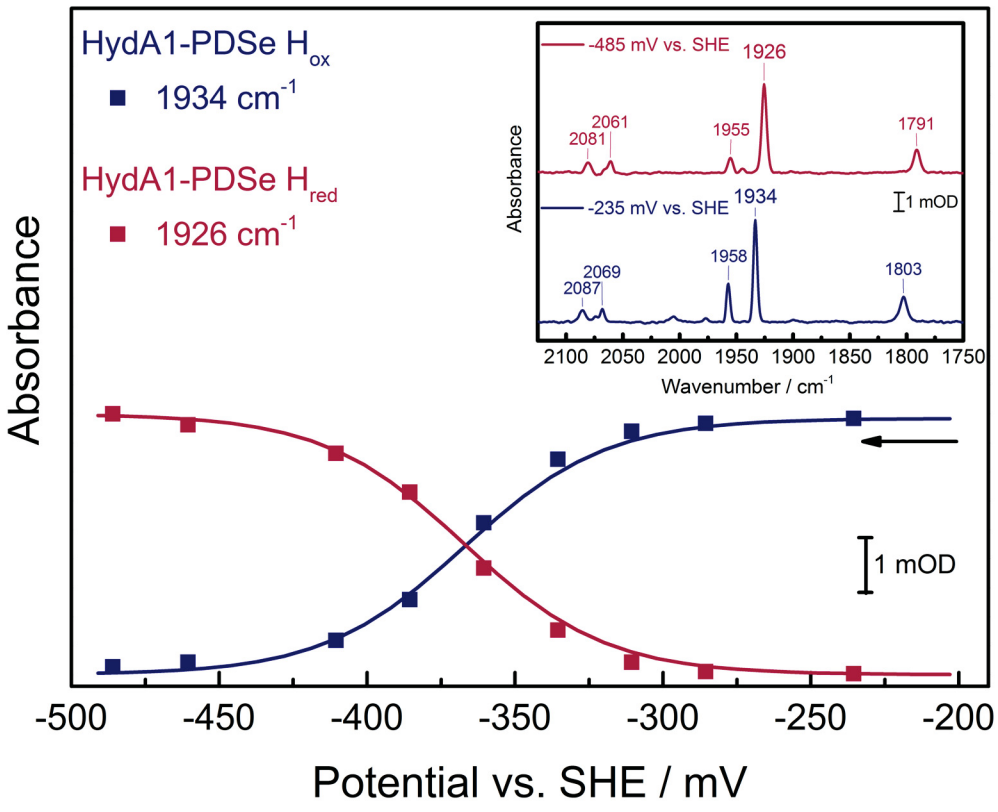

Fig. 5 Reductive titration of HydA1-PDSe monitored by FTIR spectroelectrochemistry with selected FTIR spectra. Blue squares represent the intensities of the marker band for the H_{ox} state, red squares for the H_{red} state (see inset). Data are collected at 278 K with 2 cm^{-1} resolution. Solid lines correspond to Nernstian fits with n=1 and give a midpoint potential of $E_{red/ox}$=-367 mV±20 mV vs SHE, the arrow indicates the titration direction

site bringing more charge density to the $[2Fe]_H$ subsite. The small red shift of the FTIR pattern indicates that the redox reaction takes place at the $[4Fe\text{-}4S]_H$ cluster.

To analyze the redox properties of the $[4Fe\text{-}4S]_H$ subcluster in HydA1-PDSe in detail, FTIR spectro-electrochemistry was performed to determine the mid-point potential of the ox/red transition (see fig. 5). The redox titration of HydA1-PDSe shows the main transition from H_{ox} to H_{red}. The plotted absorbance of the two chosen marker bands 1934 and 1926 cm^{-1} against the applied potential are fitted with one electron Nernstian curves. They give a midpoint-potential of -367 mV±20 mV vs SHE which is 22 mV lower than that of HydA1-PDT.[23] Although this difference is small, a slightly more negative redox potential is consistent with the increased electron density at the $[2Fe]_H$ core[19] which is coupled to the cubane cluster.

The H_{ox}-CO state

In contrast to HydA1-PDT, a CO-inhibited state is formed under CO gas exposure in HydA1-PDSe. It can only be stabilized in the oxidized state (see fig. S2A) and will be compared to HydA1-ADT H_{ox}-CO.

FTIR spectroscopy and FTIR spectroelectrochemistry

The FTIR spectra of the two H_{ox}-CO states show the same peak pattern (see fig. 6). In comparison to HydA1-ADT H_{ox}-CO (2012, 1972, 1964 cm^{-1}) the FTIR vibrations of the CO ligands in HydA1-PDSe H_{ox}-CO state (2006, 1964, 1958 cm^{-1}) are slightly red shifted as it was also observed for the H_{ox} state.

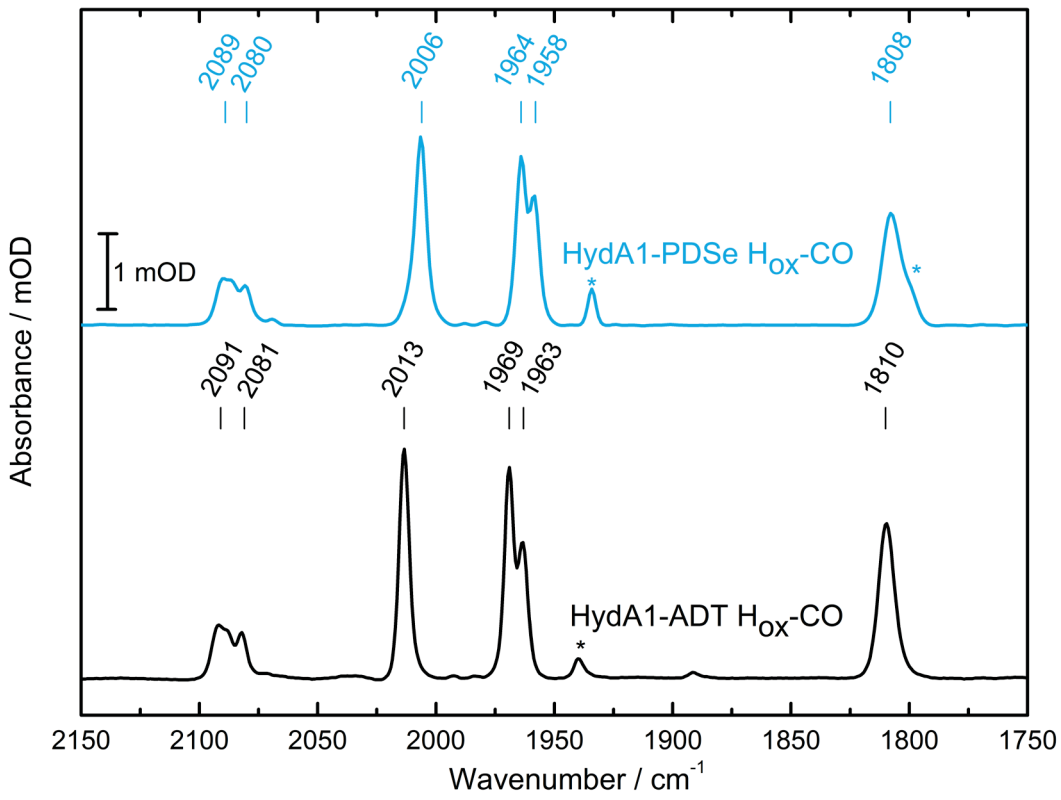

Fig. 6 Comparison of H_{ox}-CO states of HydA1-ADT and HydA1-PDSe in FTIR spectroscopy. The asterisks indicate minor contributions from the H_{ox} state in the samples. Spectra are taken at 288 K with 2 cm^{-1} resolution

Reductive treatment (2 mM NaDT) of HydA1-PDSe H_{ox}-CO partly converts it into the H_{red} state with simultaneous FTIR band broadening from ≈6 cm^{-1} to ≈15 cm^{-1} (FWHM) indicating a partial detachment from the protein scaffold (see fig.S1 A1-A4). Due to the lack of a reduced product from the H_{ox}-CO state the corresponding FTIR spectroelectrochemistry (see fig. S6) shows only vibrational peaks decreasing in intensity during reduction. This behavior was also observed for the native [FeFe] hydrogenase from *D. desulfuricans*.[41]

In native HydA1 from *C. reinhardtii*, however, the H_{ox}-CO state is readily reduced to a pure H_{red}-CO state at -470 mV (pH 8.0).[23] Since the apparent midpoint potential for HydA1-PDSe H_{ox}-CO reduction (approximately -337 mV, see fig. S6) is even more positive than $E_{red/ox}$ for HydA1-PDSe (-367 mV, see fig. 5) we must conclude that the CO inhibited state of HydA1-PDSe is much less stable than that in the native enzyme.

EPR spectroscopy

Since HydA1-PDT is not inhibited by CO the native enzyme is again used for comparison. HydA1-PDSe H_{ox}-CO gives a rhombic EPR spectrum with rather broad lines, whereas the known HydA1-ADT H_{ox}-CO state is characterized by an axial EPR spectrum with narrower lines[42] (see fig. 7). Two of the g-values are significantly shifted towards higher values which, as for the HydA1-PDSe H_{ox} state, can be explained by the larger spin-orbit contribution of selenium compared to sulfur. Thus the EPR spectrum suggests that the spin distribution of the iron core in HydA1-PDSe H_{ox}-CO deviates significantly from that in the native H_{ox}-CO state.

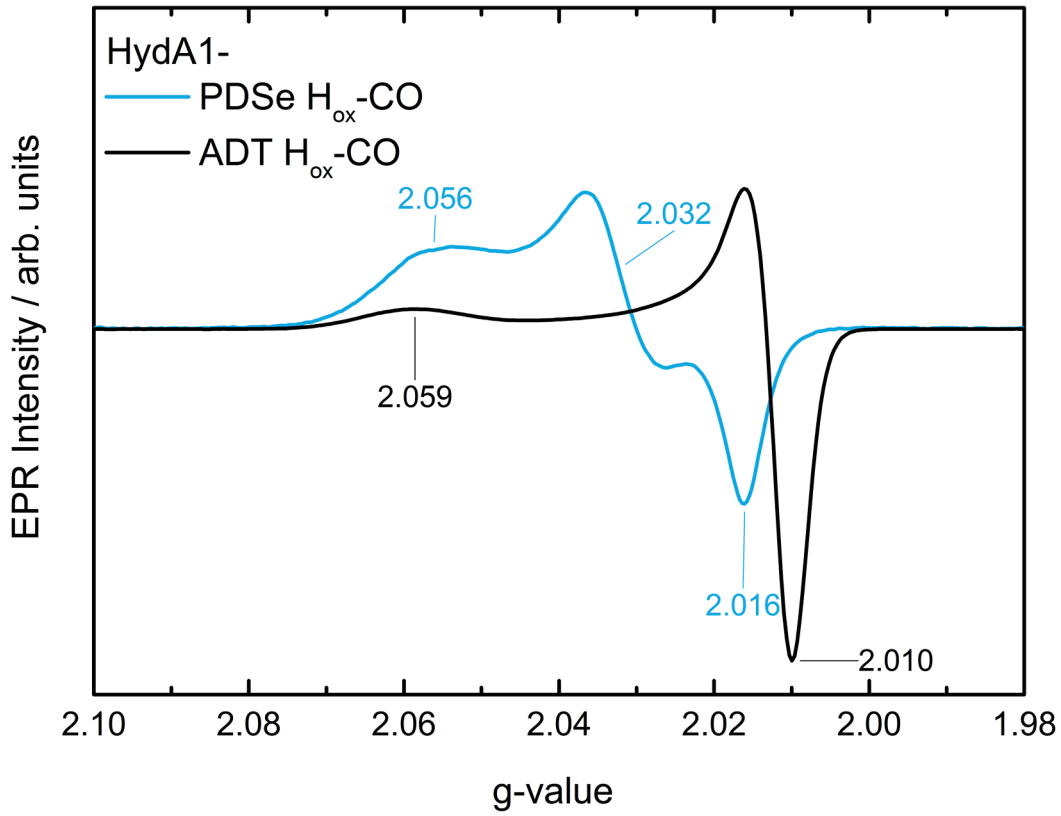

Fig. 7: Superimposed EPR spectra of HydA1-ADT H_{ox}-CO and HydA1-PDSe H_{ox}-CO. Spectra are taken at 20 K

Reconstitution of apo-HydA1 with $[4Fe\text{-}4Se]_H$

Owing to the possibility of heterologous expression, the cubane cluster of apo-HydA1 could also be reconstituted with selenium (see materials and methods) leading to a stable $[4Fe\text{-}4Se]_H$ hydrogenase which was analyzed with EPR and NMR spectroscopy.

^{1}H NMR spectroscopy

The ^{1}H NMR spectra of apo-HydA1 containing either the native $[4Fe\text{-}4S]_H$ or the $[4Fe\text{-}4Se]_H$ subcluster in their oxidized (2+) state show a similar pattern of the contact-shifted β-CH_2 proton resonances (**a-d** and **a′-e′**) in the downfield region. They originate from the Fe coordinating cysteines confirming a successful reconstitution with no significant difference between the two structures (see fig. 8). In the oxidized state of apo-HydA1 with the $[4Fe\text{-}4S]_H$ cluster the two S=9/2 Fe(II)Fe(III) pairs in the cubane cluster are antiferromagnetically

coupled to form a diamagnetic S=0 ground state. At room temperature paramagnetism arises from population of the excited states[43], explaining the anti-Curie temperature dependence of the ^{1}H chemical shifts.[26] S to Se exchange in the cubane cluster increases the chemical shift of the hyperfine shifted proton resonances in the range from 2.8 to 5.2 ppm being indicative of a stronger magnetic interaction. The overall larger chemical shifts in the [4Fe-4Se]$_{H}$ substituted enzyme uncover an additional proton signal at 11.6 ppm, labelled with **e′**.

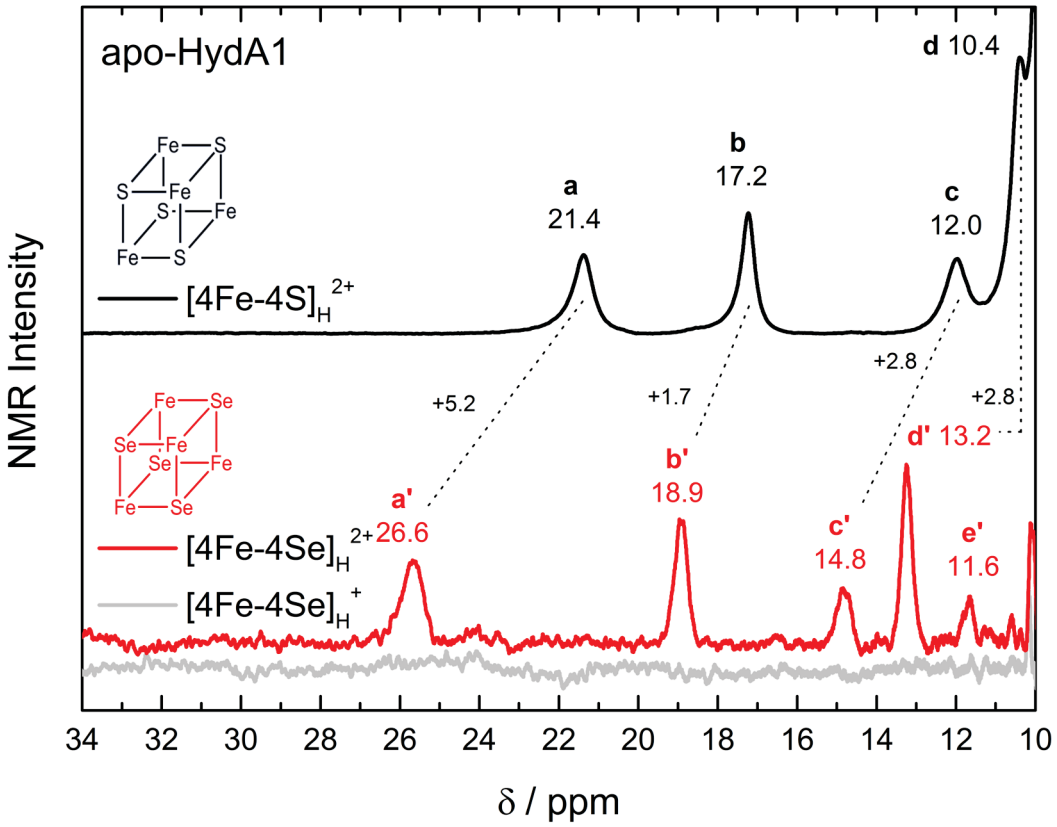

Fig. 8 Scaled ^{1}H NMR spectra of apo-HydA1 with a [4Fe-4S]$_{H}$ or a [4Fe-4Se]$_{H}$ cluster. For apo-HydA1 with [4Fe-4S]$_{H}$ cluster only the oxidized sate (black) and for the selenium substituted enzyme the oxidized (red) and reduced state (grey) are shown in the range of 34 to 10 ppm. Spectra are measured at 298 K with 600 MHz

For the dithionite reduced cubane cluster the effect of Se substitution is dramatic. Whereas the $[4\text{Fe-4S}]_{H}^{+}$ cluster shows a classical S=1/2 ground state with broad resonances occurring over a more extended field range (down to 55 ppm)[26], the $[4\text{Fe-4Se}]_{H}^{+}$ apo-HydA1 seems to be

in a high spin state with ^{1}H NMR features that are broadened beyond detection (see grey trace fig. 8). For the small bacterial ferredoxins (≈6 kDa) the selenium substitution resulted in higher spin systems with peaks from -45 to 160 ppm but the extreme broadening was not observed due to the about 8 times smaller size of the ferredoxins compared to apo-HydA1.[24]

EPR spectroscopy on reduced [4Fe-4Se]$_H$ apo-HydA1

EPR spectroscopy can contribute to understanding the lack of ^{1}H NMR signals introduced by high electron spin states in combination with the large size of ≈50 kDa of [4Fe-4Se]$_H$ apo-HydA1.

The EPR spectra of the reduced [4Fe-4Se]$_H$ apo-HydA1shown in fig. 9a with EPR features at g=5.17 and g=5.6 are indicative of a mixed high spin state. These high spin states have been described earlier for Se substituted ferredoxins.[30, 32, 33] The derivative feature at g=5.17 is assigned to the excited S=3/2 Kramers doublet of the S=7/2 ground state assuming a rhombicity of E/D=0.117.[44] The temperature dependence of the amplitude of this feature is consistent with a D = -1.07 cm^{-1} (see fig. 9b). The absorptive feature at g=5.63 is assigned to anisotropic components of both S=1/2 and S=3/2 Kramers doublets of an S=3/2 ground state.[33] It is assumed that the occurrence of high spin components of the Se substituted cubane cluster is related to its coordination environment which is modulating the intra-cluster exchange coupling(s).

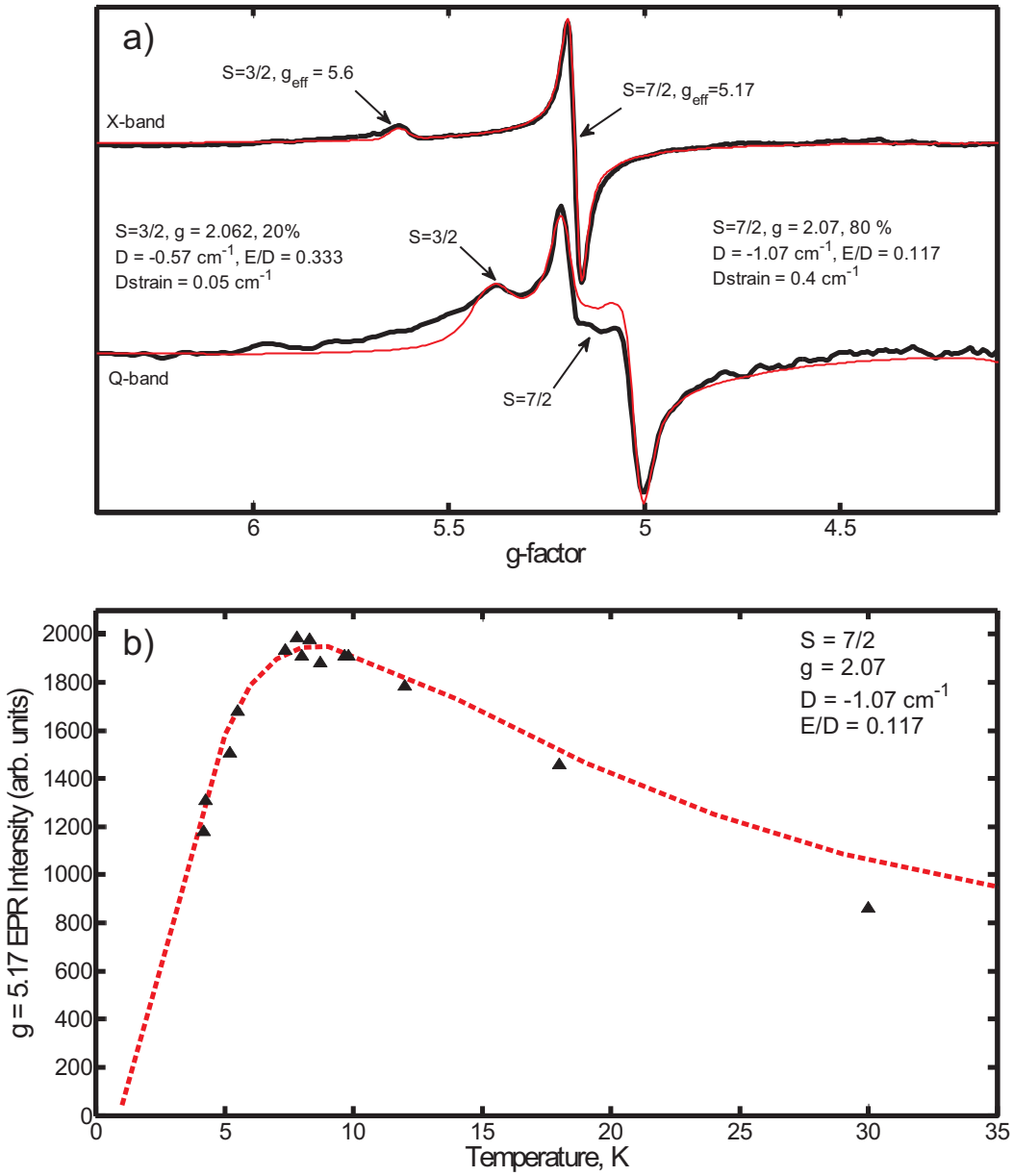

Fig. 9 CW X-band EPR of reduced $[4Fe\text{-}4Se]_H$ apo-HydA1 with temperature dependence. a) CW X- and Q-band EPR spectra (black) with corresponding simulations (red) showing S=3/2 and S=7/2 species. b) Temperature dependence of the signal at g=5.17, amplitudes were recorded at X-band frequency with corresponding fit to determine the zero field splitting parameter D

Modification of the protein surrounding by binding interactions e.g. in photosystem I (PSI) have led to a spin crossover.[33] We observed a similar effect when the $[4Fe\text{-}4Se]_H$ apo-HydA1 enzyme is maturated with [2Fe]-ADT/-PDT/-PDSe. The familiar S=1/2 species of the H_{ox} state can be identified (see fig. S6). This shows that, at least, the oxidized $[4Fe\text{-}4Se]^{2+}$

cluster is in a low spin configuration. The ^{1}H NMR spectrum of the $[4Fe\text{-}4Se]_H$ HydA1-PDT H_{red} state in figure S4 shows paramagnetic shifts very similar to the $[4Fe\text{-}4S]_H$ HydA1-PDT H_{red} state. This indicates that the reduced $\left[4Fe\text{-}4Se\right]_H^+$ cluster in HydA1-PDT H_{red} is also in a low spin state (formally S=1/2) and couples antiferromagnetically to the S=1/2 state of the $[2Fe]_H$ binuclear subcluster to generate a diamagnetic ground state. Further changes are not observed for the $[4Fe\text{-}4Se]_H$ HydA1 maturated samples as expected from the previous results of Noth *et.al.*[7] (see fig. S6 and S7).

Summary and Conclusions

In this work we have shown that S-to-Se substitution in the bridging ligand of the binuclear subsite in the H-cluster of the [FeFe] hydrogenase from *Chlamydomonas reinhardtii* induces distinct changes in the electronic structure of the enzyme's active site. According to the FTIR signatures of the H_{ox} and H_{red} states, the charge density on the $[2Fe]_H$ site in HydA1-PDSe is increased. Part of the charge density is transported onto the $[4Fe\text{-}4S]_H$ subcluster explaining the slightly lower midpoint potential of the H_{ox}/H_{red} transition. The increased charge density lowers the reduction potential and may also contribute to the increased oxygen sensitivity of the active *Cp*HydA1-ADSe observed in an earlier study.[22]

The observed reduced paramagnetic shift of the methylene protons in the bridging ligand in ^{1}H NMR spectroscopy shows that less spin density remains on the PDSe ligand than on the PDT ligand. The increased size of Se with respect to S causes the Fe-Se bond to be somewhat longer than the corresponding Fe-S bond. This reduces the steric bulk of the $-CH_2$ bridgehead at the open coordination site and may be a contributing factor allowing an external CO to bind at Fe_d in HydA1-PDSe in contrast to the situation in HydA1-PDT. The extraneous CO ligand significantly affects the spin distribution of the $[2Fe]_H$ subcluster as apparent from the rhombic EPR spectrum of HydA1-PDSe H_{ox}-CO that strongly deviates from that of HydA1-ADT H_{ox}-CO. Although the reduced steric bulk of the $-CH_2$ bridgehead allows formation of

the H_{ox}-CO state, it still destabilizes this state sufficiently such that the HydA1-PDSe H_{ox}-CO state cannot be reduced without detaching the extraneous CO or the $[2Fe]_H$ subsite as a whole from the H-cluster.[41]

The effect of substituting selenium for the inorganic sulfides in the $[4Fe\text{-}4S]_H$ cluster is different from the effect of PDT to PDSe substitution in the $[2Fe]_H$ subsite. In the oxidized $[4Fe\text{-}4Se]^{2+}$ protein more spin-density is transported to the Fe ions leading to large chemical shifts in the NMR spectrum. In the reduced $[4Fe\text{-}4Se]^{+}$ protein the spin coupling between the iron ions becomes critically dependent on the first coordination sphere and leads to a mixed spin state S=3/2 and S=7/2. Maturation of the $[4Fe\text{-}4Se]^{2+}$ apo-protein, however, restores the coordination environment to that of the native enzyme resulting in a low spin configuration with S=1/2. The FTIR patterns of the $[4Fe\text{-}4Se]_H$ HydA1-PDT/-PDSe samples do not differ from the $[4Fe\text{-}4S]_H$ cluster containing samples at pH 8.0. At pH 6.0 most likely a protonation event occurs in the reduced state of the samples, leading to a red shift of 3 cm^{-1}.

These effects illustrate the intricate balance of spin interactions and charge density distributions within the H-cluster governing the electronic structure and catalytic behavior of the enzyme´s active site.

Acknowledgments

The Max Planck Society is gratefully acknowledged for financial support.

The French State Program ‘Investissements d’Avenir (Grants “LABEX DYNAMO”, ANR-11-LABX-0011, and “LABEX ARCANE”, ANR-11-LABX-0003-01) supported this work.

Reference List

1. Lubitz W, Ogata H, Rüdiger O, Reijerse E (2014) Chem.Rev. 114:4081-4148
2. Vignais PM, Billoud B (2007) Chem.Rev. 107:4206-4272
3. Glick BR, Martin WG, Martin SM (1980) Canadian Journal of Microbiology 26:1214-1223
4. Madden C, Vaughn MD, Díez-Pérez I, Brown KA, King PW, Gust D, Moore AL, Moore TA (2012) J. Am. Chem. Soc. 134:1577-1582
5. Cornish AJ, Gärtner K, Yang H, Peters JW, Hegg EL (2011) Journal of Biologial Chemistry 286:38341-38347
6. Kuchenreuther JM, George SJ, Grady-Smith CS, Cramer SP, Swartz JR (2011) Plos one 6:1-8
7. Noth J, Esselborn J, Güldenhaupt J, Brünje A, Sawyer A, Apfel UP, Gerwert K, Hofmann E, Winkler M, Happe T (2016) Angew.Chem.Int.Ed. 55:8396-8400
8. Berggren G, Adamska A, Lambertz C, Simmons TR, Esselborn J, Atta M, Mouesca J.M F, Reijerse E, Lubitz W, Happe T, Artero V, Fontecave M (2013) Nature 499:66-70
9. Esselborn J, Lambertz CF, Adamska-Venkatesh AF, Simmons TF, Berggren GF, Noth JF, Siebel JF, Hemschemeier AF, Artero VF, Reijerse E Fau - Fontecave M, Fontecave MF, Lubitz WF, Happe T (2013) Nature Chemical Biology 9:607-610
10. Barth A (2007) Biochimica et Biophysica Acta 1767:1073-1101
11. Li H, Rauchfuss TB (2002) Journal of American Chemical Society 124:726-727
12. Gilbert-Wilson R, Siebel JF, Adamska-Venkatesh A, Pham CC, Reijerse E, Wang H, Cramer SP, Lubitz W (2015) J Am Chem Soc. 137:8998-9005
13. Adamska-Venkatesh A, Simmons TR, Siebel JF, Artero V, Fontecave M, Reijerse E, Lubitz W (2015) Phys.Chem.Chem.Phys 17:5421-5430
14. Meyer J, Moulis JM (1981) Biochemical and Biophysical Research Communications 103:667-673
15. Sommer C, Adamska-Venkatesh A, Pawlak K, Birrell JA, Rüdiger O, Reijerse EJ, Lubitz W (2017) Journal of American Chemical Society 139:1440-1443
16. Reijerse EJ, Pham CC, Pelmenschikov V, Gilbert-Wilson R, Adamska-Venkatesh A, Siebel JF, Gee LB, Yoda Y, Tamasaka K, Lubitz W, Rauchfuss TB, Cramer SP (2017) Journal of American Chemical Society 139:4306-4309
17. Winkler M, Senger M, Duan J, Esselborn J, Wittkamp F, Hofmann E, Apfel UP, Stripp ST, Happe T (2017) Nat.Commun. 8:16115
18. Pelmenschikov V, Birrell JA, Pham CC, Mishra N, Wang H, Sommer C, Reijerse E, Richers CP, Tamasaku K, Yoda Y, Rauchfuss TB, Lubitz W, Cramer SP (2017) J Am Chem Soc. 139:16894-16902
19. Silakov A, Wenk B, Reijerse E, Albracht SPJ, Lubitz W (2009) J Biol Inorg Chem 14:301-313
20. Rodríguez-Maciá P, Pawlak K, Rüdiger O, Reijerse E, Lubitz W, Birrell JA (2017) JACS 139:15122-15134
21. Siebel JF, Adamska-Venkatesh A, Reijerse E, Lubitz W (2015) Biochemistry 54:1474-1483
22. Kertess L, Wittkamp F, Sommer C, Esselborn J, Rüdiger O, Reijerse EJ, Hofmann E, Lubitz W, Winkler M, Happe T, Apfel UP (2017) Dalton Trans 46:16947-16958
23. Adamska-Venkatesh A, Krawietz D, Siebel JF, Weber K, Happe T, Reijerse E, Lubitz W (2014) J.Am.Chem.Soc. 136:11339-11346
24. Esselborn J, Muraki N, Klein K, Engelbrecht V, Metzler-Nolte N, Apfel UP, Hofmann E, Kurisu G, Happe T (2016) Chem.Sci. 7:959
25. Marques MC, Tapia C, Gutiérrez-Sanz O, Ramos AR, Keller KL, Wall JD, De Lacey AL, Matias PM, Pereira IAC (2017) Nat.Chem.Biol. 13:544-550
26. Rumpel S, Ravera E, Sommer C, Reijerse E, Farès C, Luchinat C, Lubitz W (2017) J Am Chem Soc.
27. Gaillard J, Moulis JM, Meyer J (1987) Inorg.Chem. 26:320-324
28. Banci L, Bertini I, Briganti F, Luchinat C, Scozzafava A (1991) In: E.Rizzarelli, T.Theophanides (eds) Chemistry and Properties of Biomolecular Systems. Kluwer Academic Publishers, pp. 73-90
29. Nagayama K, Ozaki Y, Kyojoku Y, Hase T, Matsubara H (1983) J Biol Chem. 94:893-902
30. Gaillard J, Moulis JM, Auric P, Meyer J (1986) Biochemistry 25:464-468

31. Moulis JM, Meyer J (1982) Biochemistry 21:4762-4771
32. Moulis JM, Auric P, Meyer J (1984) J Biol Chem. 259:11396-11402
33. Jung YS, Vassiliev IR, Golbeck JH (1997) Journal of Biological Inorganic Chemistry 2:209-217
34. Harb MK, Niksch T, Windhager J, Görls H, Holze R, Lockett LT, Okumura N, Evans DH, Glass RS, Lichtenberger DL, El-khateeb M, Weigand W (2009) Organometallics 28:1039-1048
35. Kuchenreuther JM, Grady-Smith CS, Bingham AS, George SJ, Cramer SP, Swartz JR (2010) Plos one 5:1-7
36. Winkler M, Hemschemeier A, Gotor C, Melis A, Happe T (2002) International Journal of Hydrogen Energy 27:1431-1439
37. Reijerse E, Lendzian F, Isaacson R, Lubitz W (2012) Journal of Magnetic Resonance 214:237-243
38. Reijerse E, Savitsky A (2017) eMagRes 6:187-205
39. Chongdar N, Birrell JA, Pawlak K, Sommer C, Reijerse EJ, Rüdiger O, Lubitz W, Ogata H (2017) J. Am. Chem Soc. DOI 10.1021/jacs.7b11287
40. Bertini I, Luchinat C, Parigi G (2002) Concepts in Magnetic Resonance 14:259-286
41. Rodríguez-Maciá P, Reijerse E, Lubitz W, Birrell JA, Rüdiger O (2017) J Phys Chem Lett. 8:3834-3839
42. Kamp C, Silakov A, Winkler M, Reijerse EJ, Lubitz W, Happe T (2008) Biochim Biophys Acta. 1777:410-416
43. Poe M, Phillips WD, McDonald CC, Lovenberg W (1990) Proc.N.A.S. 65:797-804
44. Hagen WR (2009) Biomolecular EPR Spectroscopy. CRC Press Taylor and Francis, Boca Raton, Florida

4.4.1 Supporting Information

Supporting Information

Spectroscopic Investigations of a semi-synthetic [FeFe] hydrogenase with propane di-selenol as bridging ligand in the bi-nuclear sub-site

C. Sommer[1], S. Rumpel[1], S. Roy[2], C. Farès[3], V. Artero[2], M. Fontecave[4], E. Reijerse[1], W. Lubitz[1]

1 Max-Planck-Institut für Chemische Energiekonversion, Stiftstrasse 34-36, 45470 Mülheim an der Ruhr, Germany.

2 Laboratoire de Chimie et Biologie des Métaux, Université Grenoble Alpes, CEA/BIG, CNRS, 17 rue des martyrs, 38000 Grenoble, France.

3 Max-Planck-Institut für Kohlenforschung, Kaiser-Wilhelm Platz 1, 45470 Mülheim an der Ruhr, Germany

4 Laboratoire de Chimie des Processus Biologiques, Collège de France, Université Pierre et Marie Curie, CNRS UMR 8229, PSL Research University, 11 place Marcelin Berthelot, 75005 Paris, France.

✉ Wolfgang.Lubitz@cec.mpg.de

1. Catalytic activity of HydA1-PDSe as compared to that of HydA1-PDT

Although HydA1 incorporates the [2Fe]-PDSe complex no activity could be measured, neither in hydrogen production nor in hydrogen oxidation (see fig.S1). For HydA1-PDT a residual activity in both tests can be measured that are 0.49 H_2/s for H_2 production and 0.06 H_2/s for H_2 consumption, which is less than 1% of WT activity. HydA1-PDSe shows no activity.

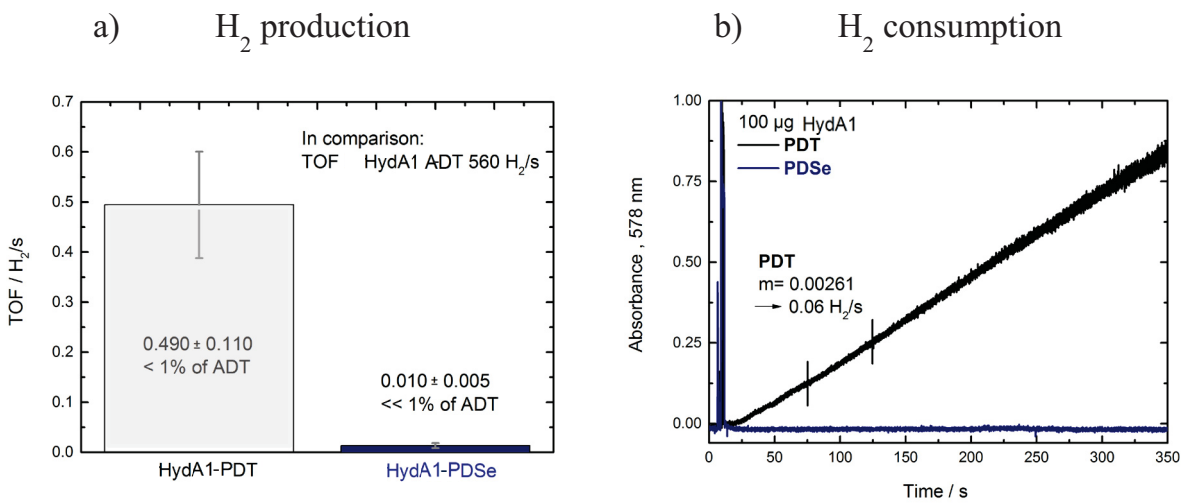

Fig. S1 Activities of H_2 production and H_2 consumption for HydA1-PDT/-PDSe. a) H_2 production was measured with GC analysis after incubation of 10 µg protein for 20 min at 310 K with 10 mM MV/100 mM NaDT. b) H_2 consumption was measured with 100 µg protein, 10 mM MV and hydrogen saturated buffer at room temperature

2. Maturation of apo-HydA1 with $[Fe_2(PDSe)(CO)_4(CN)_2)]^{2-}$

FTIR spectroscopy was used to demonstrate that the [2Fe]-PDSe cofactor was incorporated into the protein scaffold. The spectrum of the free complex in aqueous solution is shown in figure S1 part B and is characterized by its three broad CO bands (1972/1943/1906 cm^{-1}) and an even broader contribution in the region of the CN^- bands (2050 cm^{-1}). This finger pattern is very similar to the one observed for free [2Fe]-PDT.[1] With ^{15}N labeled CN^- ligands a wavenumber shift of -30 cm^{-1} occurs for the CN^- bands while the CO peaks are only slightly

shifted indicating weak vibrational coupling to the CN^- ligands. No additional changes occur. Figure S2B shows the FTIR spectrum obtained after maturation of apo-HydA1 with [2Fe]-PDSe and exposure to CO. The clear band narrowing to 6-8 cm^{-1} indicates successful incorporation of the binuclear cofactor into the hydrogenase.

Additionally, figure S2 shows how the active site is disassembled by trying to reduce the H_{ox}-CO state (A2-A4). With minor amounts of dithionite (DT) the reduced state H_{red} (1926/1792 cm^{-1}) and peaks related to an unknown species appear. Already with 0.5 mM DT all H_{ox}-CO peaks disappeared. With 10 mM DT only broad, unidentified contributions are detected that most likely arise from partly detached [2Fe]-PDSe.

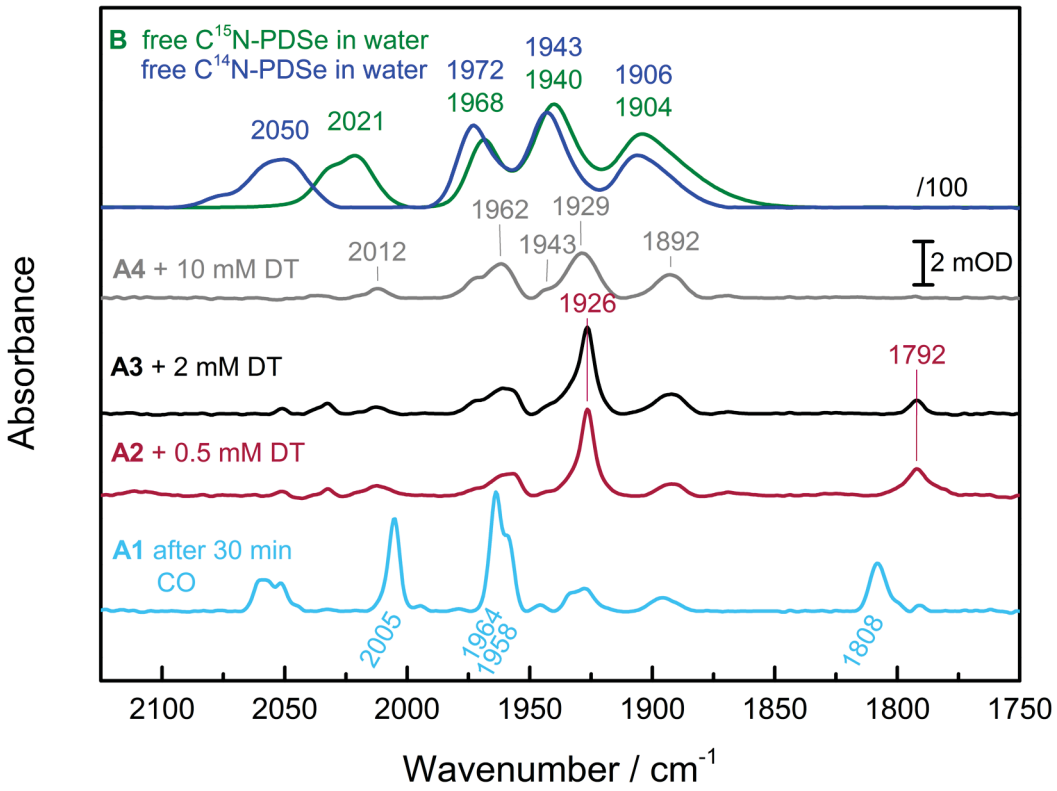

Fig. S2 FTIR spectra of HydA1-$C^{15}N$-PDSe in the H_{ox}-CO state with reductive titration and a comparison with the free complexes dissolved in water. Spectra labeled with A show HydA1-$C^{15}N$-PDSe after 30 min exposure to 1 bar CO(g) (A1) and addition of different concentrations of dithionite (A2-A4). Superimposed FTIR spectra in B show the $C^{15}N$ labeled

free complex compared to the free complex with $C^{14}N$ in aqueous buffer (0.1 M TRIS, 0.15 M NaCl, pH 8.0). Spectra are taken at 288 K with a resolution of 2 cm^{-1}

3. ^{1}H NMR of HydA1-PDSe H_{ox}/H_{red} in comparison to HydA1-PDT

In the 3D structure of the active site (see fig.S3) the difference of the methylene proton pairs in the bridge become obvious. The axial oriented protons (H_{ax}) are located above Fe_p with a distances of about 3.44 Å. The equatorial protons (H_{eq}) have a distance to Fe_p of ≈4.37 Å.[2] These distances are of interest because in the H_{ox}-CO state the spin density is assumed to be located at Fe_p.[3]

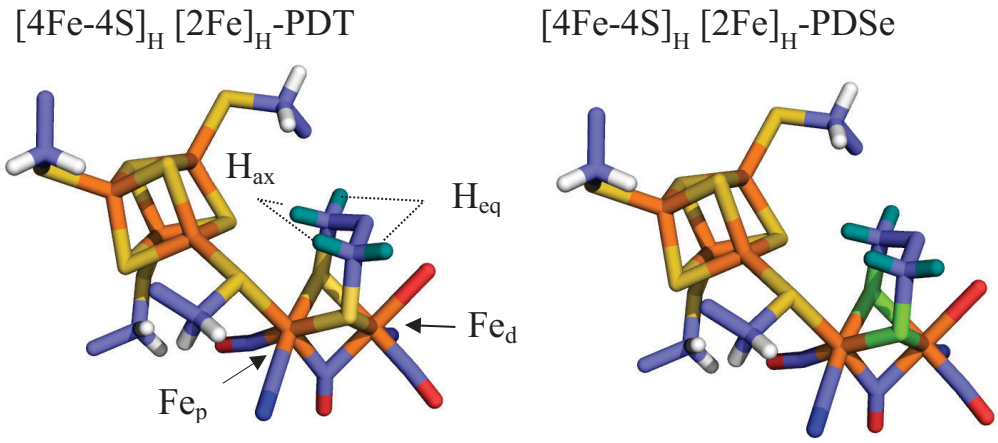

Fig. S3 H-Cluster of PDT (left) and PDSe (right) maturated [FeFe] hydrogenase with β-CH_2 protons (white) of Fe ligating cysteines and methylene protons (aqua blue) of the bridge. The figure was made using PYMOL with PDB 3C8Y[4]. Note that the figure shows the originally –NH bridgehead but colored as carbon to indicate –CH_2 and that a hydride is bound in at Fe_d. Color code: white β-CH_2 protons, purple: C, yellow: S, orange: Fe, blue: O, red: N, aqua blue: methylene protons in bridge, lime: Se

In the reduced states the resonances of Cys β-CH_2 protons are more downfield shifted (down to 62 ppm) and broader than in the oxidized state due to the paramagnetic S=1/2 ground state of the cubane cluster (compare fig.3 and S4).[5] The signal pattern for reduced HydA1-PDT

and HydA1-PDSe are very similar and show only a minor effect upon S-to-Se substitution (fig. S4). The upfield shift can be explained by a decreased spin density on the PDSe bridge that affects the methylene protons. The β-CH_2 protons of the ligating cysteines are hardly affected. The $[4Fe\text{-}4Se]_H$ HydA1-PDT H_{red} with its far less shifted Cys β-CH_2 protons follows the described tendency of lower spin density for selenium substituted samples. More interestingly $[4Fe\text{-}4Se]_H$ HydA1-PDT H_{red} shows that even in the reduced state there is no high spin system (for the oxidized state see EPR in fig. S7).

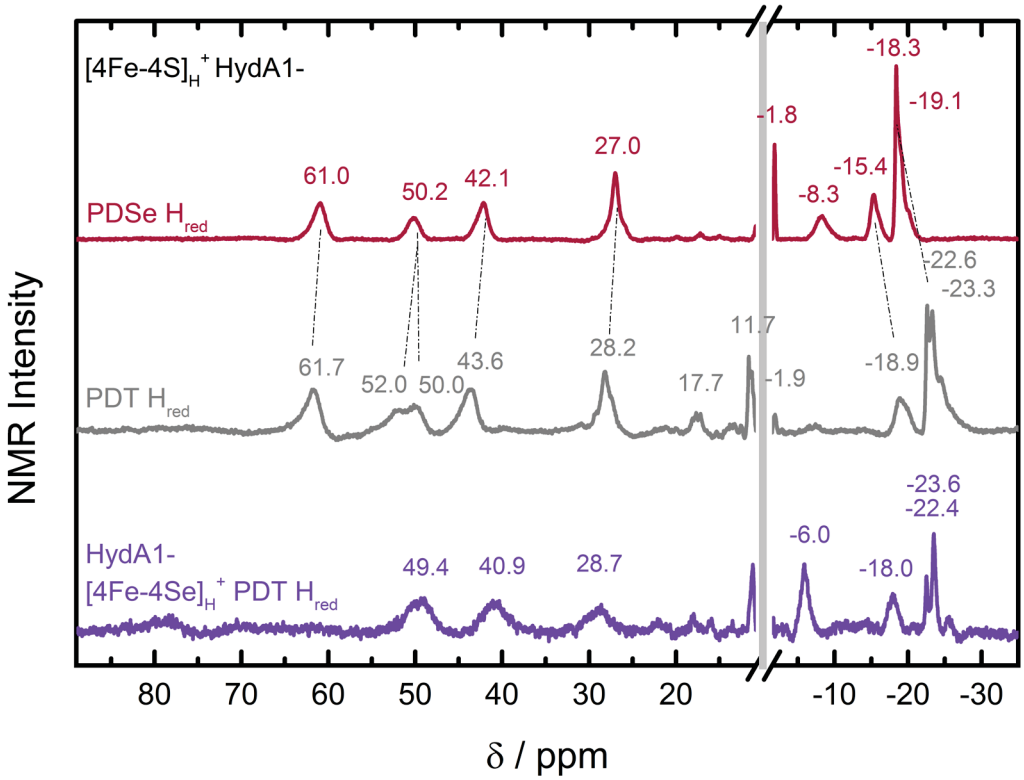

Fig. S4 ^{1}H NMR spectra of HydA1-PDT/-PDSe in the reduced state. The cubane clusters are reduced (paramagnetic) leading to broader linewidths. In HydA1-PDSe H_{red} small contributions of the H_{ox} can be seen as shoulders/little peaks at around 30, 28 and 15 ppm. Spectra are measured at 600 MHz and 298 K. The downfield region is shown from 90 to 10.8 ppm and the upfield region from -1.5 to -35 ppm

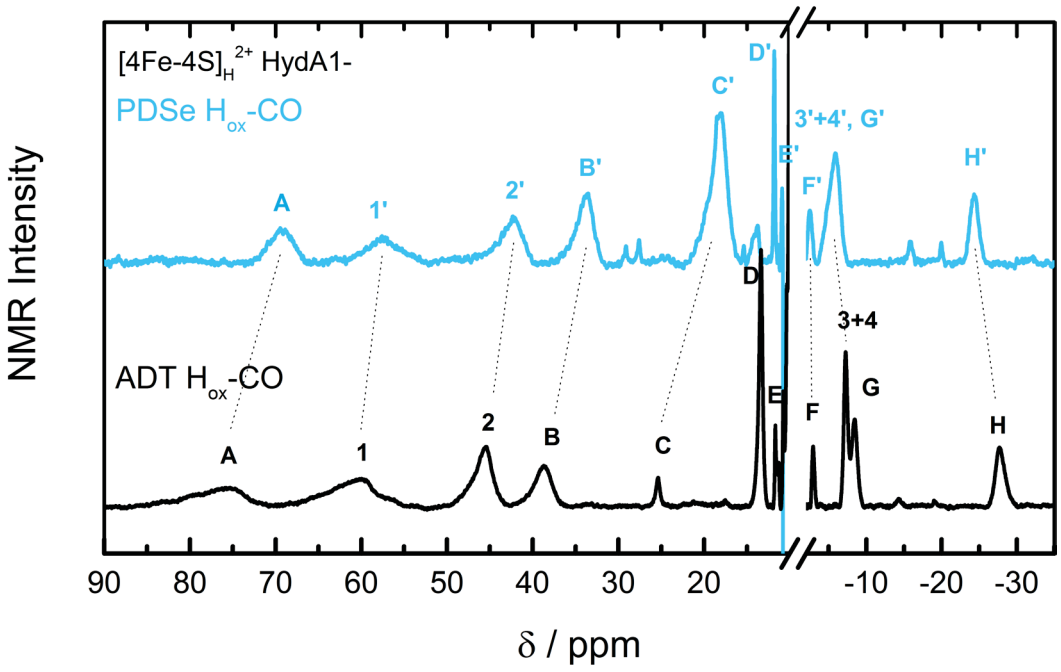

Fig. S5 ^{1}H NMR spectra of HydA1-ADT and HydA1-PDSe in the oxidized CO inhibited state. Spectra are measured at 600 MHz and 298 K. The downfield region is shown from 90 to 10 ppm and the upfield region from -2 to -35 ppm

Figure S5 presents a comparison of the ^{1}H NMR spectra of HydA1-PDSe H_{ox}-CO and ADT H_{ox}-CO as a reference system since HydA1-PDT is lacking a stable CO-inhibited state. In general, the observed Cys β-CH_2 signals of the CO-inhibited samples show larger downfield and smaller upfield shifts than the H_{ox} samples.[2] In the H_{ox} state the spin is distributed more equally over the $[2Fe]_H$ site while in the H_{ox}-CO state it is localized at Fe_p[3] which is the reason for the large shift of the axial protons **1**, **2** of the bridge. The labeling of the peaks in HydA1-PDSe H_{ox}-CO is carried out based on homology to the assigned HydA1-ADT H_{ox}-CO state. For HydA1-PDSe H_{ox}-CO the effect of localization on Fe_p seems to be diminished, suggesting an overall reduction of the spin density at the $[2Fe]_H$ site due to the presence of selenium (see fig. 7).

Table S1: ^{1}H NMR data collection with peak labels, putative assignments, chemical shifts and line width of the resonances. Data are recorded at 298 K with 600 MHz. Data marked with * are taken from Rumpel *et al*[2], n.d. not determined.

Peak label	Assignment	Chemical Shift/ Ppm	Width / Hz	Peak label	Assignment	Chemical Shift/ ppm	Width/ Hz
$[4Fe\text{-}4S]_H$ HydA1-PDT H_{ox}				**$[4Fe\text{-}4S]_H$ HydA1-PDSe H_{ox}**			
a	β-CH_2	30.8	300	**a'**	β-CH_2	29.6	300
b	β-CH_2	29.3	300	**b'**	β-CH_2	28.0	300
c+d	β-CH_2	15.4	200	**c'+d'**	β-CH_2	15.0	200
e+f 1+2	β-CH, H_{ax}, H_{ax}	11.2	400	**e'+f'**	β-CH_2	11.5	200
3	H_{eq}	-21.5	360	**3'**	H_{eq}	-17.2	310
4	H_{eq}	-25.9	350	**4'**	H_{eq}	-21.4	310
$[4Fe\text{-}4S]_H$ HydA1-ADT Hox-CO*				**$[4Fe\text{-}4S]_H$ HydA1-PDSe Hox-CO**			
A	β-CH_2	75.3	4000	**A'**	β-CH_2	69.0	1500
1	H_{ax}	60.0	4000	**1'**	H_{ax}	57.3	5400
2	H_{ax}	45.4	1800	**2'**	H_{ax}	42.0	1100
B	β-CH_2	38.6	1400	**B'**	β-CH_2	33.7	1400
C	β-CH_2	25.4	300	**C'**	β-CH_2	18.0	800
D	β-CH_2	13.4	300	**D'**	β-CH_2	14.0	1000
E	β-CH_2	11.7	300	**E'**	β-CH_2	11.8	100
F	β-CH_2	-2.9	300	**F'**	β-CH_2	-2.5	400
3+4	H_{eq}	-7.3	300	**3'+4'**	H_{eq}	-5.8	700
G	β-CH_2	-8.5	400	**G'**	β-CH_2	-5.8	700
H	β-CH_2	-27.8	800	**H'**	β-CH_2	-24.4	1000
$[4Fe\text{-}4S]_H$ apo HydA1 oxidized*				**$[4Fe\text{-}4Se]_H$ apo HydA1 oxidized**			
a	β-CH_2	21.2	300	**a'**	β-CH_2	25.5	400
b	β-CH_2	17.2	200	**b'**	β-CH_2	18.9	300
c	β-CH_2	12.0	300	**c'**	β-CH_2	14.8	300
d	β-CH_2	10.4	200	d'	β-CH_2	13.2	200
				e'	β-CH_2	11.6	200
$[4Fe\text{-}4Se]_H$ HydA1-PDT H_{ox}				**$[4Fe\text{-}4Se]_H$ HydA1-PDSe H_{ox}**			
		32.9	270			30.8	270
		31.5	290			29.3	240
		17.0	190			15.4	180
		15.0	160			11.2	400
		11.4	330			10.3	280
		-21.7	330			9.6	n.d.
		-26.2	300			-21.5	350

Peak label	Assignment	Chemical Shift/ Ppm	Width / Hz	Peak label	Assignment	Chemical Shift/ ppm	Width/ Hz
$[4Fe\text{-}4Se]_H$ HydA1-PDT H_{red}							
		49.4	1800				
		40.9	1600				
		28.7	2000				
		-6.00	1100				
		-18.0	1000				
		-22.4	300				
		-23.6	300				
$[4Fe\text{-}4S]_H$ HydA1-PDT H_{red}				**$[4Fe\text{-}4S]_H$ HydA1-PDSe H_{red}**			
		61.7	1100			61.0	1100
		52.0	1000			50.2	1000
		50.0	1000			42.1	1000
		43.6	1100			27.0	900
		28.2	900				
		17.7	700				
		11.7	200				
		-1.9	n.d.			-1.8	200
		-18.9	1100			-8.3	800
		-22.6	250			-15.4	900
		-23.3	400			-18.3	200
						-19.1	200

4. FTIR spectroelectrochemistry of HydA1-PDSe H_{ox}-CO

The reductive potential titration of the H_{ox}-CO state of HydA1-PDSe shows the disappearing of the typical H_{ox}-CO signals but no conversion into a CO inhibited reduced state. Instead, the H_{red} state as well as an unidentified species is formed (see fig. S2 A1-A4).

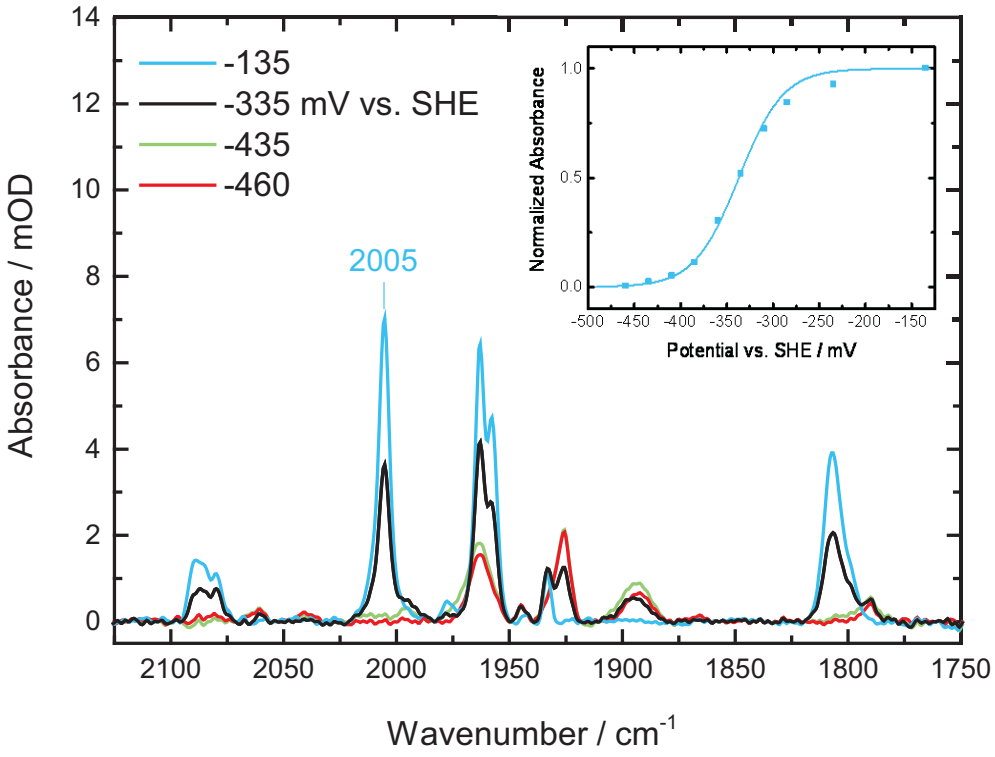

Fig. S6 Reductive FTIR spectro-electrochemistry of HydA1-PDSe H_{ox}-CO with normalized marker bands for the H_{ox}-CO state (2005 cm^{-1}). Inset: Blue squares represent the intensities of the marker band for the H_{ox}-CO state. The solid line corresponds to a Nernstian fit with a midpoint-potential of -337 mV vs. SHE and n=1. Data are collected at 278 K with 2 cm^{-1} resolution

Taking into account only the disappearance of the H_{ox}-CO state an apparent mid-point potential of -337 mV vs. SHE can be calculated that is by 130 mV higher than the corresponding midpoint potential for HydA1-ADT.[6] Due to the different composition of the bridging ligand, the properties of the CO bound state of HydA1-PDSe cannot be directly

compared to the native enzyme. From our observations one must conclude that the CO bound state in HydA1-PDSe is much less stable than that in the native HydA1-ADT.

5. EPR of $[4Fe\text{-}4Se]_H$ HydA1-ADT, -PDT and -PDSe

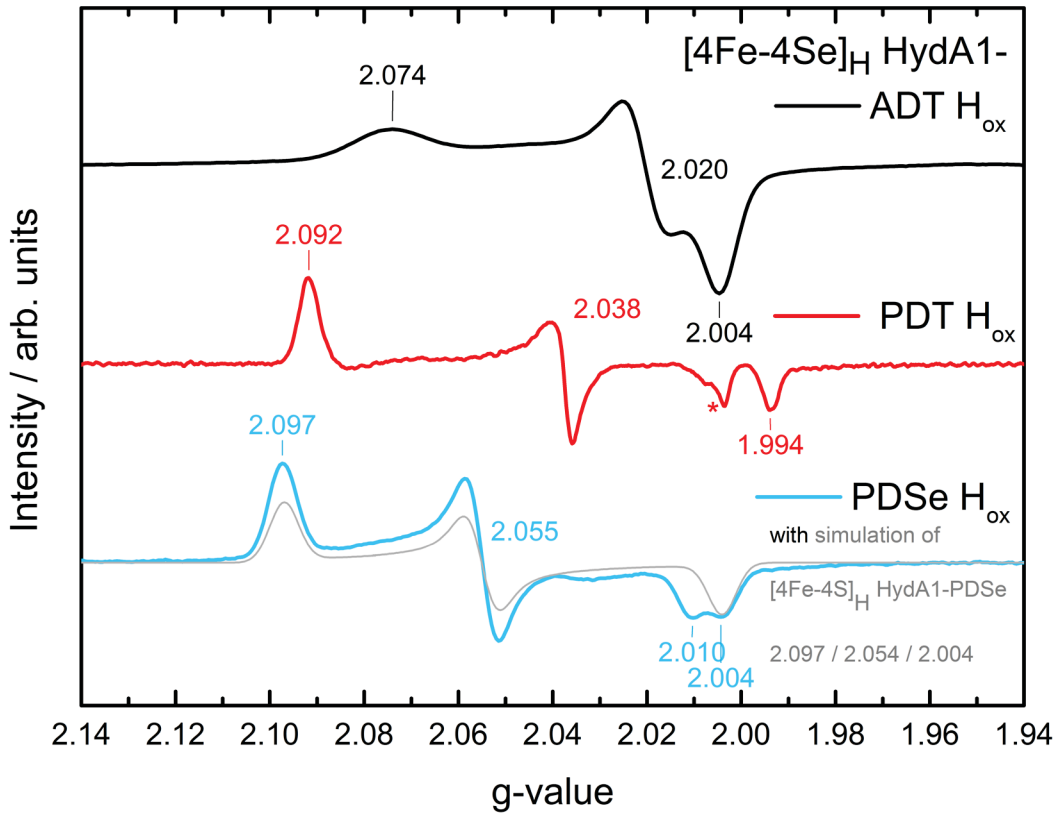

Fig. S7 CW X-band EPR spectra of $[4Fe\text{-}4Se]_H$ HydA1-ADT/-PDT/-PDSe at pH 8. The $[4Fe\text{-}4Se]_H$ HydA1-PDSe sample shows a contamination by the sulfur containing cubane $[4Fe\text{-}4S]_H$ HydA1-PDSe as confirmed by the simulation with g-values from fig.3. The additional signals marked with an asterisk in HydA1-PDT H_{ox} are background signals from the resonator

Figure S7 shows the EPR spectra of the $[4Fe\text{-}4Se]_H$ reconstituted enzyme with the native [2Fe]-ADT cofactor as well as with the -PDT and -PDSe variants. All mimics lead to a S=1/2 spin state when the $[4Fe\text{-}4Se]_H$ apo-enzyme was successfully maturated. The differences in g-values between the three active sites is larger than that between the same mimics in combination with the native $[4Fe\text{-}4S]_H$ subcluster (see table 2). As discussed in the main text, the S-to-Se substitution in the $[4Fe\text{-}4S]_H$ cluster reduces the intracluster exchange interactions

and, in general, the competing exchange mechanisms (Heisenberg, double exchange, super exchange) attain comparable contributions complicating the magnetic structure of the H-cluster significantly.

Table 2: g-values of HydA1-ADT/-PDT/-PDSe with either the $[4Fe\text{-}4S]_H$ or a $[4Fe\text{-}4Se]_H$ cluster.

HydA1-	$[4Fe\text{-}4S]_H$			$[4Fe\text{-}4Se]_H$		
ADT	2.102	2.040	1.998	2.074	2.020	2.004
PDT	2.095	2.039	2.001	2.094	2.038	1.994
PDSe	2.097	2.052	2.004	2.097	2.055	2.010

6. pH dependence of $[4Fe\text{-}4Se]_H$ HydA1-PDT/-PDSe

For $[4Fe\text{-}4Se]_H$ HydA1-PDT and -PDSe a proton coupled event at low pH (e.g. pH 6.0) was observed in FTIR (see fig. S8). Interestingly only in the reduced state this pH effect can be detected. It results in a blue shift of 1-3 cm^{-1} with respect to the H_{red} state at pH 8.0. Because of the small shift the proton coupled event occurs most likely at the $[4Fe\text{-}4Se]_H$ subcluster. Whether this involves a direct protonation of a ligating cysteine or an amino acid proximal to the subcluster, remains unknown. Senger *et al.* analyzed $[4Fe\text{-}4S]_H$ HydA1-PDT and suggested a protonation at a coordinating cysteine (C417) of the reduced $[4Fe\text{-}4S]_H$ cluster with an overall configuration of: $H^+[4Fe\text{-}4S]_H^+$ $[Fe_p(I)Fe_d(II)]$.[7]

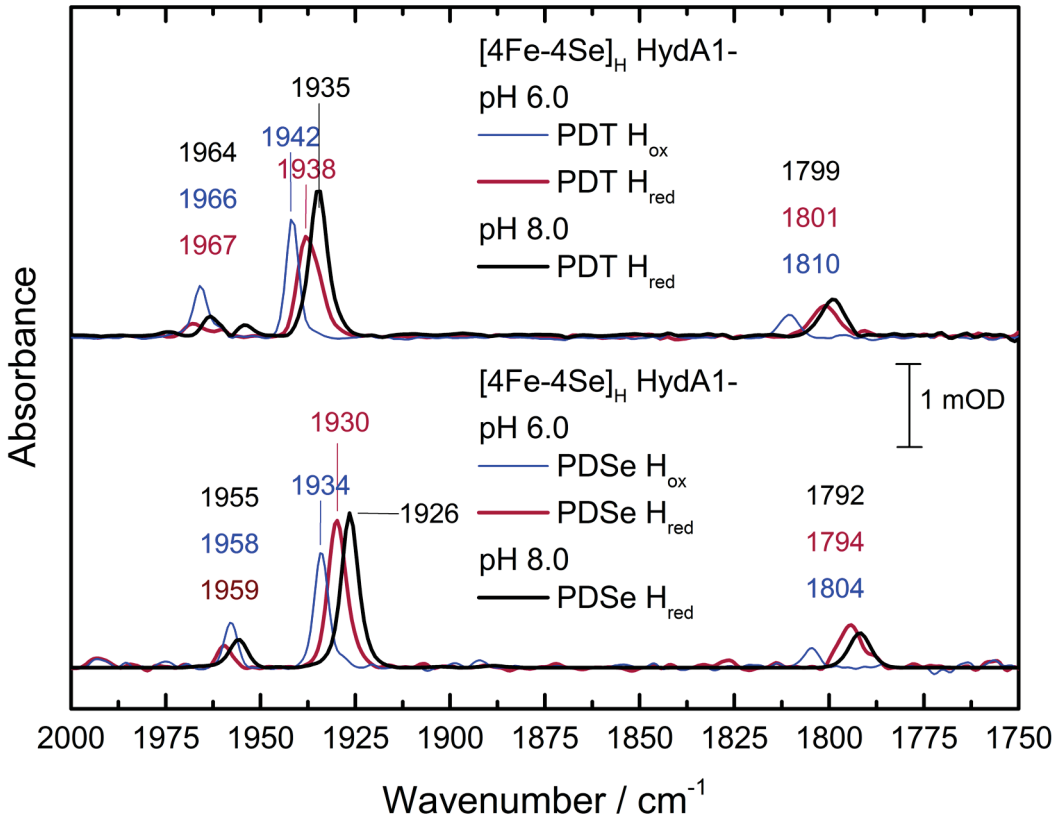

Fig S8: FTIR spectra of $[4Fe\text{-}4Se]_H$ HydA1-PDT and -PDSe at pH 6.0 and pH 8.0. The oxidized (blue) and reduced (red) spectra at pH 6.0 of the two variants are shown. To emphasize the observed blue shift in $[4Fe\text{-}4Se]_H$ HydA1-PDT/-PDSe H_{red} the corresponding reduced spectrum at pH 8.0 is superimposed (black). Spectra are taken at 288 K with a resolution of 2 cm^{-1}

Reference List

1. Siebel JF, Adamska-Venkatesh A, Reijerse E, Lubitz W (2015) Biochemistry 54:1474-1483
2. Rumpel S, Ravera E, Sommer C, Reijerse E, Farès C, Luchinat C, Lubitz W (2017) J. Am. Chem. Soc. 140:131-134
3. Silakov A, Wenk B, Reijerse E, Albracht SPJ, Lubitz W (2009) J Biol Inorg Chem 14:301-313
4. Pandey AS, Harris TV, Giles LJ, Peters JW, Szilagyi RK (2007) J Am Chem Soc. 130:4533-4540
5. Gaillard J, Moulis JM, Auric P, Meyer J (1986) Biochemistry 25:464-468
6. Adamska-Venkatesh A, Krawietz D, Siebel JF, Weber K, Happe T, Reijerse E, Lubitz W (2014) J.Am.Chem.Soc. 136:11339-11346
7. Senger M, Laun K, Wittkamp F, Duan J, Haumann M, Happe T, Winkler M, Apfel UP, Stripp ST (2017) Angew. Chem. Int. Ed. 56:16503-16506

4.5 Paper V

Direct Detection of the Terminal Hydride Intermediate in [FeFe] Hydrogenase by NMR Spectroscopy

S. Rumpel, C. Sommer, E. Reijerse, C. Farès and W. Lubitz

JACS communication, under revision

Journal: Journal of the American Chemical Society

Published 09.03.2018, DOI: 10.1021/jacs.8b00459

Author: Second author

Contribution: 25 %

- I established the protein expression for HydA1-C169A

- I prepared the wild-type enzyme in the hydride state

- I measured most and analyzed all FTIR spectra

- I was involved in preparing the manuscript

S. Rumpel measured all ^{1}H NMR data and wrote most of the manuscript. All others discussed the results and were involved in writing the manuscript.

JACS
JOURNAL OF THE AMERICAN CHEMICAL SOCIETY
Communication
Cite This: J. Am. Chem. Soc. 2018, 140, 131−134
pubs.acs.org/JACS

^{1}H NMR Spectroscopy of [FeFe] Hydrogenase: Insight into the Electronic Structure of the Active Site

Sigrun Rumpel,*[,†] Enrico Ravera,[‡] Constanze Sommer,[†] Edward Reijerse,[†] Christophe Farès,[§] Claudio Luchinat,[‡] and Wolfgang Lubitz*[,†]

[†]Max-Planck-Institut für Chemische Energiekonversion, Stiftstrasse 34-36, 45470 Mülheim an der Ruhr, Germany
[‡]Department of Chemistry "Ugo Schiff" and Magnetic Resonance Center (CERM), University of Florence and Interuniversity Consortium for Magnetic Resonance of Metallo Proteins (CIRMMP), Via L. Sacconi 6, 50019 Sesto Fiorentino, Italy
[§]Max-Planck-Institut für Kohlenforschung, Kaiser-Wilhelm Platz 1, 45470 Mülheim an der Ruhr, Germany

Supporting Information

ABSTRACT: The [FeFe] hydrogenase HydA1 from *Chlamydomonas reinhardtii* has been studied using ^{1}H NMR spectroscopy identifying the paramagnetically shifted ^{1}H resonances associated with both the $[4Fe\text{-}4S]_H$ and the $[2Fe]_H$ subclusters of the active site "H-cluster". The signal pattern of the unmaturated HydA1 containing only $[4Fe\text{-}4S]_H$ is reminiscent of bacterial-type ferredoxins. The spectra of maturated HydA1, with a complete H-cluster in the active H_{ox} and the CO-inhibited H_{ox}−CO state, reveal additional upfield and downfield shifted ^{1}H resonances originating from the four methylene protons of the azadithiolate ligand in the $[2Fe]_H$ subsite. The two axial protons are affected by positive spin density, while the two equatorial protons experience negative spin density. These protons can be used as important probes sensing the effects of ligand-binding to the catalytic site of the H-cluster.

Hydrogenases are metalloenzymes that catalyze the reversible conversion of dihydrogen into protons and electrons with the class of [FeFe] hydrogenases being the most active hydrogen producers.[1] The unique [6Fe] active site of these enzymes, the so-called "H-cluster", serves as inspiration for the development of inorganic catalysts for production of solar fuels or as part of fuel cells. The H-cluster consists of a $[4Fe\text{-}4S]_H$ cluster connected to the protein via four cysteines, one of which bridges to a unique binuclear Fe subsite $[2Fe]_H$ containing a proximal (Fe_p) and a distal iron (Fe_d) (Figure 1). In contrast to most [FeFe] hydrogenases, HydA1 from *Chlamydomonas reinhardtii* with a molecular weight of about 48 kDa contains no accessory iron sulfur clusters and is thus particularly well suited for spectroscopic investigations of structure and function of the H-cluster. Large quantities of fully active HydA1 can be prepared by the addition of the synthesized inorganic cofactor precursor $[Fe_2(adt)(CO)_4(CN)_2]$ (adt = azadithiolate) to recombinant HydA1 containing only the $[4Fe\text{-}4S]_H$ cluster (apo-HydA1) (Figure 1).[2,3] The active site and its highly conserved protein environment are suggested to act synergistically for efficient hydrogen evolution. The electronic structure of the different redox states of the H-cluster has been well characterized by

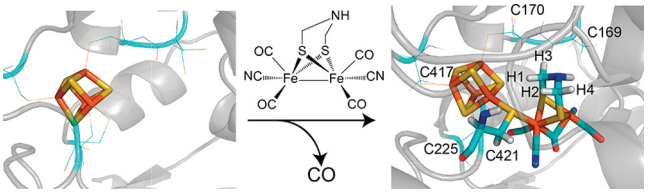

Figure 1. Maturation of HydA1 containing only the $[4Fe\text{-}4S]_H$ cluster with the synthetic precursor $[Fe_2(adt)(CO)_4(CN)_2]$ of the binuclear Fe subsite results in fully functional HydA1. The images of the $[4Fe\text{-}4S]_H$ cluster and the H-cluster are based on PDB entries 3LX4 and 3C8Y, respectively. The metal clusters and the bridging cysteine are shown as sticks with the following color coding; iron, orange; sulfur, yellow; carbon, cyan; oxygen, red; nitrogen, blue.

EPR and FTIR spectroscopy.[4−9] Electronic coupling between the $[4Fe\text{-}4S]_H$ and $[2Fe]_H$ subclusters is of central importance to the electron flow during catalysis.[10] The intimate contact between $[4Fe\text{-}4S]_H$ and $[2Fe]_H$ sites translates into magnetic exchange coupling, which has been demonstrated at low temperatures by Mössbauer and EPR/ENDOR spectroscopy.[11,12] However, the spin density distribution over the H-cluster and the influence of the protein environment have never been studied in solution at room temperature. Here, the method of choice is solution NMR spectroscopy, which can reveal sign and magnitude of the spin density at each NMR active nucleus. Protons are the most sensitive ones, although other magnetic nuclei, e.g., ^{13}C and ^{15}N, could also be studied easily by NMR techniques.[13] For hydrogenases, protons are of particular importance since they are substrate and product of the reversible enzymatic reaction. In principle, NMR allows one in a unique way to directly follow the hydrogen species during the catalytic cycle under physiological conditions.

Here, we present the first NMR spectroscopic investigation of a hydrogenase enzyme, the [FeFe] hydrogenase HydA1. Similar to other iron sulfur proteins, magnetic coupling among iron centers reduces the NMR line widths and renders the spectroscopic investigation feasible.[14] The β-CH_2 protons of the four cysteines coordinating $[4Fe\text{-}4S]_H$ as well as the protons within the $[2Fe]_H$ site are contact shifted out of the diamagnetic envelope (−1 to 11 ppm). Size and sign of the

Received: October 27, 2017
Published: December 6, 2017

DOI: 10.1021/jacs.7b11196
J. Am. Chem. Soc. 2018, 140, 131−134

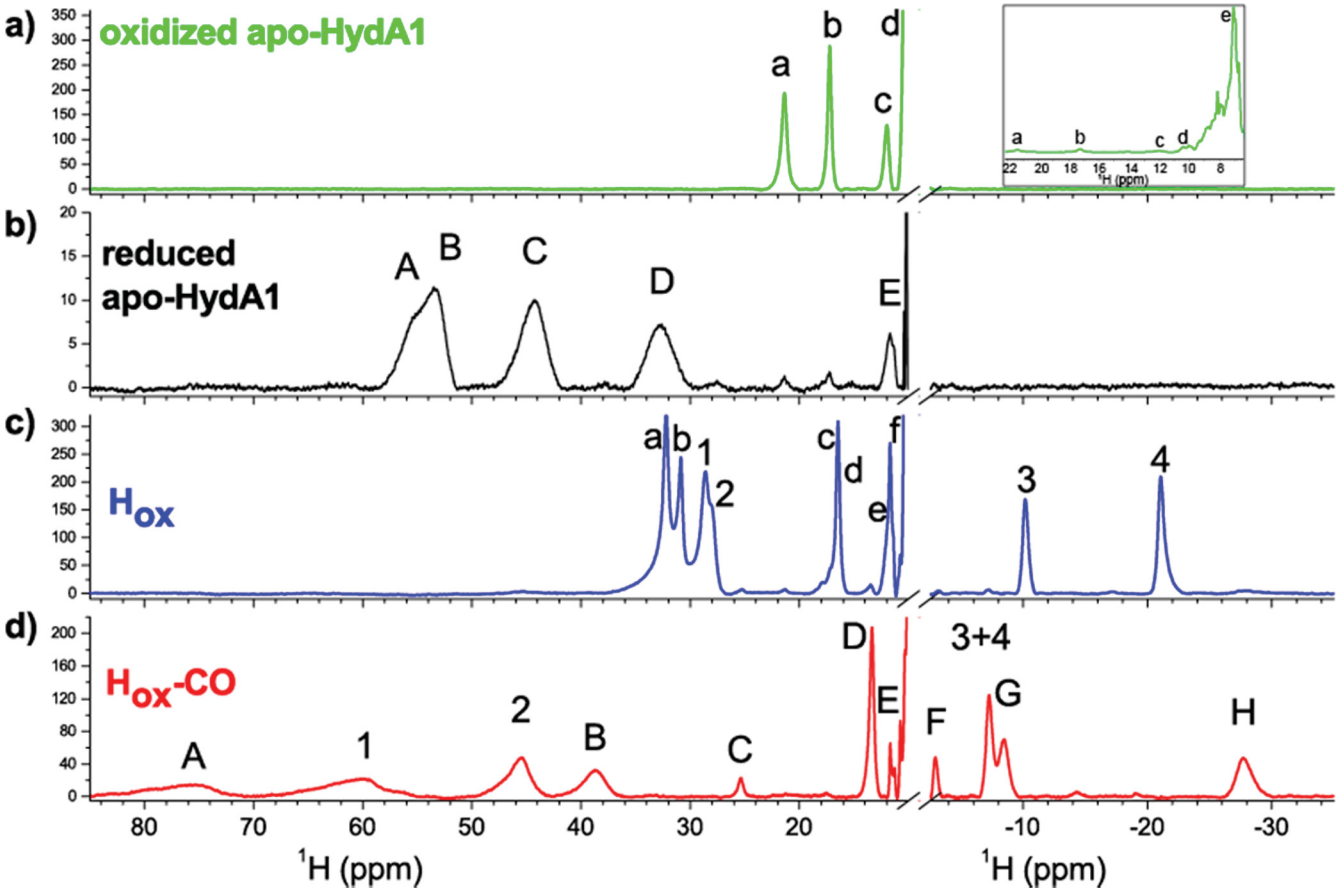

Figure 2. Downfield and upfield region of the 1D ^{1}H NMR spectra (600 MHz) at 298 K of (a) oxidized apo-HydA1 (green line), (b) reduced apo-HydA1 (black line), (c) oxidized HydA1 (blue line, H_{ox}), and (d) CO-inhibited oxidized HydA1 (red line, H_{ox}–CO). Downfield region and upfield region are shown from 85 to 10 ppm and −2.5 to −35 ppm, respectively. Contact shifted cysteine resonances are labeled a–e in (a), A–E in (b), a–f in (c), and A–H in (d). Labels 1, 2, 3, and 4 indicate ^{1}H resonances of $[2Fe]_H$. The inset of (a) shows the spectrum of oxidized apo-HydA1 from 6 to 22 ppm.

contact shift depend on (i) the spin state of the Fe in the cluster to which the cysteine is attached, (ii) the spin density at the nucleus, which largely depends on the Fe–S–Cβ–βCH$_2$ dihedral angle θ, and (iii) temperature.[15] Although the hyperfine shifted signals are significantly broadened due to the interaction of the unpaired electron(s) with the resonating nucleus, they provide a distinctive fingerprint of the cluster environment and protons inherent in the H-cluster. To our knowledge, the only other iron sulfur proteins of high molecular weight studied by NMR are the homodimeric nitrogenase Fe-protein[16] and the hemeprotein subunit of sulfite reductase.[17] The results presented here provide unique insight into structure and function of [FeFe] hydrogenases in solution at room temperature including an exclusive view of the catalytically active H_{ox} state. These data open new prospects to unravel intimate details about geometric and electronic structure of the H-cluster and the influence of the surrounding amino acids.

The amenability of HydA1 to a high-resolution NMR study is demonstrated on oxidized apo-HydA1. The measured ^{1}H NMR spectra reveal three contact shifted resonances downfield of 11 ppm with line width up to 300 Hz (Figure 2a and Table S2). Their pattern resembles bacterial-type ferredoxins in the oxidized $[4Fe\text{-}4S]^{2+}$ form,[18−20] which can be viewed as two antiferromagnetically coupled Fe(II)Fe(III) pairs that form a diamagnetic ground state with a total spin state $S = 0$.[21] Paramagnetism arises at room temperature due to population of low-lying excited states with $S = 1$, 2, etc. Consistent with an oxidized $[4Fe\text{-}4S]^{2+}_H$, all contact shifted resonances exhibit anti-Curie temperature dependence (Table S2 and Figure S1a).[18−20]

Reduction of the $[4Fe\text{-}4S]^{2+}_H$ cluster to the $[4Fe\text{-}4S]^{+}_H$ form is accompanied by about four-fold increased contact shifts and line widths, which is in agreement with a paramagnetic $S = 1/2$ ground state (Figure 2b). For reduced apo-HydA1, the downfield shifted resonances A and D exhibit Curie, whereas B and C show anti-Curie temperature dependence (Figure S1b). Based on their chemical shifts and line widths, signals A to D belong most likely to β-CH$_2$ protons of cysteinyl ligands. Signal E was assigned as a cysteine α-CH proton as its line width is smaller when compared to signals A to D (Figure 2b and Table S2).

Maturation of apo-HydA1 with $[Fe_2(adt)(CO)_4(CN)_2]$ yields HydA1 with a fully functional H-cluster (see Supporting Information SI1). In this [6Fe] system, spin coupling is in effect. For H_{ox} and CO-inhibited H_{ox}–CO state, the H-cluster contains the cubane in the oxidized 2+ state. According to a theoretical model, $[4Fe\text{-}4S]^{2+}_H$ is composed of two valence-delocalized Fe pairs, $[2Fe]_A$ and $[2Fe]_B$, which are antiferromagnetically coupled to each other via the strong intracluster coupling J_{cube} ($\approx$ 200 cm^{-1}).[12] In addition, $[4Fe\text{-}4S]_H^{2+}$ is coupled through $[2Fe]_B$ to $[2Fe]_H$ in the $[Fe_p^{I}Fe_d^{II}]$

DOI: 10.1021/jacs.7b11196
J. Am. Chem. Soc. 2018, 140, 131−134

redox configuration via the intercluster exchange coupling j (Figure 3).

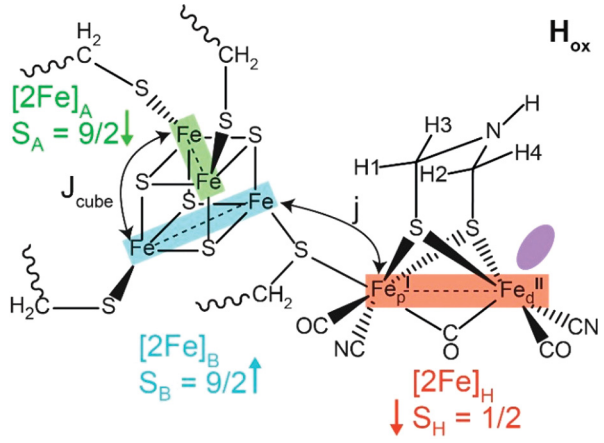

Figure 3. Schematic representation of the active site H-cluster of [FeFe] hydrogenases in the H_{ox} state. The exchange interactions of the H-cluster are indicated. $[4Fe\text{-}4S]_H^{2+}$ is composed of two valence-delocalized Fe(II)−Fe(III) pairs with $S = 9/2$ that are antiferromagnetically coupled by J_{cube}. $[2Fe]_H$ consists of a low-spin Fe(I)−Fe(II) pair with ground state $S = 1/2$, which is coupled via the coupling constant j to $[4Fe\text{-}4S]_H^{2+}$. The violet sphere indicates the open coordination site at Fe_d where substrate or CO bind.

This coupling, previously investigated by ENDOR and Mössbauer spectroscopy, has been found to be about 25 cm^{-1} for H_{ox} and 95 cm^{-1} for H_{ox}−CO.[11,12,22] The 4-fold increased j in the H_{ox}−CO state causes the spin density to be strongly localized on Fe_p, while it is more evenly distributed over Fe_d and Fe_p in the H_{ox} state.[11] Nevertheless, both j values are small compared to J_{cube}. J_{cube} leads to an orientation of S_A antiparallel to S_B and j orients S_H antiparallel to S_B. Hence, S_H is oriented parallel to S_A (Figure 3). Magnitude and sign of the spin density are reflected by the observed proton hyperfine shifts that depend mainly on the Fe−S−C−H dihedral angle θ. The angular dependence of the chemical shift δ follows the general Karplus relationship $\delta = a \cos^2\theta + b \cos\theta + c$ with b and c being small and often neglected.[15] As the remaining angular term $\cos^2\theta$ is always positive, solely the sign of the spin density on the coordinated Fe determines the direction of the paramagnetic shift.

After preparation of HydA1 in the H_{ox} state (see Supporting Information S1 and Figure S4), six downfield shifted resonances are observed in the ^1H NMR spectrum between 11 and 33 ppm and also two upfield shifted resonances at −10 and −21 ppm (Figure 2c). The downfield shifted signals a, b, 1, and 2 exhibit Curie and signals c to f anti-Curie temperature dependence (Table S2 and Figure S2). The two upfield shifted resonances show pseudo-Curie temperature dependence. No hyperfine-shifted signals were detected at positions observed in the spectrum for apo-HydA1. This demonstrates the influence of the $[2Fe]_H$ on the $[4Fe\text{-}4S]_H^{2+}$ cluster via exchange coupling in solution. In order to distinguish the methylene proton resonances originating from the cysteines coordinating $[4Fe\text{-}4S]_H^{2+}$ from those of adt, H_{ox} was also prepared using a deuterated $[2Fe]_H$ site (^{2}H-adt). Thus, the downfield shifted signals 1 and 2 and the upfield shifted signals 3 and 4 (Figures 2c) have been unambiguously assigned to the four methylene protons of $[2Fe]_H$ (Figure S5). They can be attributed to two pairs of geometrically and electronically similar protons. Based on their distances to Fe_p and Fe_d, line widths, and observed ^1H NOE connectivities, signals 1 and 2 are assigned to the axial and signals 3 and 4 to the equatorial protons (Figure 1 and Table S2). Further details are provided in the Supporting Information (SI4, Figure S6 and Table S1).

By flushing active HydA1 with CO, pure H_{ox}−CO state is prepared (see Supporting Information S1 and Figure S7). This CO-inhibited state is an important source of information reporting about the redistribution of spin density in the H-cluster upon binding of an electron donating external ligand to the open coordination site at Fe_d. In its ^1H NMR spectrum, seven downfield and four upfield shifted resonances are observed in the range 11 to 85 ppm and −2 to −30 ppm, respectively (Figure 2d). The downfield shifted signals A, 1, 2, B, C, and D show Curie and E weak anti-Curie temperature dependence. As for the H_{ox} state, all upfield shifted resonances show pseudo Curie temperature dependence (Figure S4). In agreement with an increased j due to coordination of the external CO ligand at Fe_d, ^1H resonances were broader (as much as 4 kHz) and more dispersed than those for all other HydA1 states investigated here (Figure 2 and Table S2). In contrast, the line widths of the contact shifted proton signals of H_{ox} are ∼300 Hz similar to oxidized apo-HydA1. For the H_{ox}−CO state, signals 1 to 4 have been assigned analogous to the H_{ox} state to axial and equatorial protons (Figure S8). Although the temperature dependence of signals 1 to 4 is weak in the H_{ox}−CO state, their temperature-dependence in the H_{ox} state is the strongest of all observed hyperfine shifted resonances in that state (Figures S2 and SI3). This large temperature dependence of the adt methylene protons in the H_{ox} state indicates that the energies of the populated excited states of $[2Fe]_H$ are closer than those of $[4Fe\text{-}4S]_H^{2+}$ and agrees well with j, determined to be small for this state. One possible explanation for the relatively small temperature dependence of the adt methylene protons in the H_{ox}−CO state is that binding of the external CO ligand increases not only j but also the energies of the levels populated at room temperature. The assignment of the methylene protons of the adt bridge provides insight into the spin density at four additional positions of the $[2Fe]_H$ site. Large negative hyperfine shifts are observed for signals 3 and 4 in the H_{ox}, and large positive hyperfine shifts are detected for signals 1 and 2 in the H_{ox}−CO state (Figure 2cd). These hyperfine shifts reflect the larger $[2Fe]_H$ spin density for H_{ox} when compared to H_{ox}−CO, resulting from the different ratio of j and J_{cube}. The NMR spectra observed for the H_{ox} and H_{ox}−CO states can be interpreted based on the spin coupling model described above (Figure 3). Spin-polarization mechanisms will transmit positive and negative spin density to the ^1H atoms of the cysteines coordinating $[2Fe]_A$ and $[2Fe]_B$, respectively. Thus, ligation of $[2Fe]_A$ results in downfield and ligation of $[2Fe]_B$ in upfield shifted ^1H resonances. However, the bridging cysteine experiences not only positive spin density from $[2Fe]_B$ but also negative spin density from $[2Fe]_H$. Taking into account the larger spin density at $[4Fe\text{-}4S]_H^{2+}$ and the lower spin density at $[2Fe]_H$ in the H_{ox}−CO as compared to the H_{ox} state, a net upfield shift is expected for the β-CH_2 protons of the bridging cysteine. Accordingly, peaks F, G, and H can be assigned to the β-CH_2 protons of the bridging and nonbridging cysteine coordinating $[2Fe]_B$ (Figure 2d). For the H_{ox} state, only two upfield shifted resonances are observed because of the smaller spin density at $[4Fe\text{-}4S]_H^{2+}$ resulting from j, which is four-fold smaller than for the H_{ox}−CO state (Figure 2c).

DOI: 10.1021/jacs.7b11196
J. Am. Chem. Soc. 2018, 140, 131−134

We show here that paramagnetic NMR can be applied to the important class of [FeFe] hydrogenases. The derived assignments of the axial and equatorial protons of the unique $[2Fe]_H$ help to reveal intimate details of the different electronic states of the active site required for efficient catalytic H_2 evolution under near-native conditions. Solution NMR titration experiments of HydA1 with its native electron donor PetF[23] are foreseen to provide also experimental insight of HydA1's complex interface as well as dynamics related to complex formation as recently reported for cytochrome P450 and b_5.[24,25] Furthermore, NMR spectroscopy allows for the investigation of HydA1 states with a diamagnetic ground state like H_{red} and $H_{red}H^+$ that are EPR silent. Most importantly, the terminal hydride intermediate, which already has been discussed based on FTIR,[26,27] Mössbauer,[28] and NRVS spectroscopy,[29,30] can be accessed directly at ambient temperatures using solution NMR spectroscopy.

■ ASSOCIATED CONTENT

Supporting Information

The Supporting Information is available free of charge on the ACS Publications website at DOI: 10.1021/jacs.7b11196.

Methods, supplementary NMR and FTIR, and figures and tables (PDF)

■ AUTHOR INFORMATION

Corresponding Authors

*sigrun.rumpel@cec.mpg.de
*wolfgang.lubitz@cec.mpg.de

ORCID

Enrico Ravera: 0000-0001-7708-9208
Claudio Luchinat: 0000-0003-2271-8921
Wolfgang Lubitz: 0000-0001-7059-5327

Notes

The authors declare no competing financial interest.

■ ACKNOWLEDGMENTS

We thank Nina Breuer, Patricia Malkowski, and Inge Heise for sample preparation and synthesis of unlabeled and deuterated $[Fe_2(adt)(CO)_4(CN)_2]$. This work has been supported by iNEXT, grant number 653706, funded by the Horizon 2020 programme of the European Union and COST action FeSBioNet CA15133.

■ REFERENCES

(1) Lubitz, W.; Ogata, H.; Rüdiger, O.; Reijerse, E. *Chem. Rev.* **2014**, *114*, 4081.
(2) Esselborn, J.; Lambertz, C.; Adamska-Venkatesh, A.; Simmons, T.; Berggren, G.; Noth, J.; Siebel, J.; Hemschemeier, A.; Artero, V.; Reijerse, E.; Fontecave, M.; Lubitz, W.; Happe, T. *Nat. Chem. Biol.* **2013**, *9*, 607.
(3) Berggren, G.; Adamska, A.; Lambertz, C.; Simmons, T. R.; Esselborn, J.; Atta, M.; Gambarelli, S.; Mouesca, J. M.; Reijerse, E.; Lubitz, W.; Happe, T.; Artero, V.; Fontecave, M. *Nature* **2013**, *499*, 66.
(4) Adamska, A.; Silakov, A.; Lambertz, C.; Rüdiger, O.; Happe, T.; Reijerse, E.; Lubitz, W. *Angew. Chem., Int. Ed.* **2012**, *51*, 11458.
(5) Adamska-Venkatesh, A.; Krawietz, D.; Siebel, J.; Weber, K.; Happe, T.; Reijerse, E.; Lubitz, W. *J. Am. Chem. Soc.* **2014**, *136*, 11339.
(6) Roseboom, W.; De Lacey, A. L.; Fernandez, V. M.; Hatchikian, E. C.; Albracht, S. P. J. *JBIC, J. Biol. Inorg. Chem.* **2006**, *11*, 102.
(7) Silakov, A.; Wenk, B.; Reijerse, E.; Albracht, S. P. J.; Lubitz, W. *JBIC, J. Biol. Inorg. Chem.* **2009**, *14*, 301.
(8) Silakov, A.; Wenk, B.; Reijerse, E.; Lubitz, W. *Phys. Chem. Chem. Phys.* **2009**, *11*, 6592.
(9) Mulder, D. W.; Ratzloff, M. W.; Shepard, E. M.; Byer, A. S.; Noone, S. M.; Peters, J. W.; Broderick, J. B.; King, P. W. *J. Am. Chem. Soc.* **2013**, *135*, 6921.
(10) Sommer, C.; Adamska-Venkatesh, A.; Pawlak, K.; Birrell, J. A.; Rüdiger, O.; Reijerse, E. J.; Lubitz, W. *J. Am. Chem. Soc.* **2017**, *139*, 1440.
(11) Silakov, A.; Reijerse, E. J.; Albracht, S. P. J.; Hatchikian, E. C.; Lubitz, W. *J. Am. Chem. Soc.* **2007**, *129*, 11447.
(12) Popescu, C. V.; Munck, E. *J. Am. Chem. Soc.* **1999**, *121*, 7877.
(13) Bertini, I.; Luchinat, C.; Parigi, G.; Ravera, E. *NMR of Paramagnetic Molecules*; Elsevier Amsterdam, 2017.
(14) Bertini, I.; Turano, P.; Vila, A. J. *Chem. Rev.* **1993**, *93*, 2833.
(15) Bertini, I.; Capozzi, F.; Luchinat, C.; Piccioli, M.; Vila, A. J. *J. Am. Chem. Soc.* **1994**, *116*, 651.
(16) Lanzilotta, W. N.; Holz, R. C.; Seefeldt, L. C. *Biochemistry* **1995**, *34*, 15646.
(17) Kaufman, J.; Spicer, L. D.; Siegel, L. M. *Biochemistry* **1993**, *32*, 2853.
(18) Bertini, I.; Briganti, F.; Luchinat, C.; Scozzafava, A. *Inorg. Chem.* **1990**, *29*, 1874.
(19) Donaire, A.; Gorst, C. M.; Zhou, Z. H.; Adams, M. W. W.; Lamar, G. N. *J. Am. Chem. Soc.* **1994**, *116*, 6841.
(20) Lebrun, E.; Simenel, C.; Guerlesquin, F.; Delepierre, M. *Magn. Reson. Chem.* **1996**, *34*, 873.
(21) Beinert, H.; Holm, R. H.; Munck, E. *Science* **1997**, *277*, 653.
(22) Silakov, A.; Reijerse, E. J.; Lubitz, W. *Eur. J. Inorg. Chem.* **2011**, *2011*, 1056.
(23) Rumpel, S.; Siebel, J. F.; Diallo, M.; Fares, C.; Reijerse, E. J.; Lubitz, W. *ChemBioChem* **2015**, *16*, 1663.
(24) Ravula, T.; Barnaba, C.; Mahajan, M.; Anantharamaiah, G. M.; Im, S.-C.; Waskell, L.; Ramamoorthy, A. *Chem. Commun.* **2017**, *53*, 12798.
(25) Barnaba, C.; Gentry, K.; Sumangala, N.; Ramamoorthy, A. *F1000Research* **2017**, *6*, 662.
(26) Mulder, D. W.; Ratzloff, M. W.; Bruschi, M.; Greco, C.; Koonce, E.; Peters, J. W.; King, P. W. *J. Am. Chem. Soc.* **2014**, *136*, 15394.
(27) Winkler, M.; Senger, M.; Duan, J. F.; Esselborn, J.; Wittkamp, F.; Hofmann, E.; Apfel, U. P.; Stripp, S. T.; Happe, T. *Nat. Commun.* **2017**, *8*, 16115.
(28) Mulder, D. W.; Guo, Y. S.; Ratzloff, M. W.; King, P. W. *J. Am. Chem. Soc.* **2017**, *139*, 83.
(29) Reijerse, E. J.; Pham, C. C.; Pelmenschikov, V.; Gilbert-Wilson, R.; Adamska-Venkatesh, A.; Siebel, J. F.; Gee, L. B.; Yoda, Y.; Tamasaku, K.; Lubitz, W.; Rauchfuss, T. B.; Cramer, S. P. *J. Am. Chem. Soc.* **2017**, *139*, 4306.
(30) Pelmenschikov, V.; Birrell, J. A.; Pham, C. C.; Mishra, N.; Wang, H.; Sommer, C.; Reijerse, E.; Richers, C. P.; Tamasaku, K.; Yoda, Y.; Rauchfuss, T. B.; Lubitz, W.; Cramer, S. P. *J. Am. Chem. Soc.* **2017**, *139*, 16894.

■ NOTE ADDED AFTER ASAP PUBLICATION

This paper was published on December 14, 2017. The abstract has been corrected and the revised version was re-posted on December 19, 2017.

DOI: 10.1021/jacs.7b11196
J. Am. Chem. Soc. 2018, 140, 131−134

Supporting Information

^{1}H NMR Spectroscopy of [FeFe] Hydrogenase: Insight into the Electronic Structure of the Active Site

Sigrun Rumpel,[†] Enrico Ravera,[‡] Constanze Sommer,[†] Edward Reijerse,[†] Christophe Farès,[§] Claudio Luchinat,[‡] and Wolfgang Lubitz[†]

[†] Max-Planck-Institut für Chemische Energiekonversion, Stiftstrasse 34-36, 45470 Mülheim an der Ruhr, Germany

[‡] Department of Chemistry “Ugo Schiff” and Magnetic Resonance Center (CERM), University of Florence and Interuniversi-ty Consortium for Magnetic Resonance of Metallo Proteins (CIRMMP), Via L. Sacconi 6, 50019 Sesto Fiorentino, Italy

[§] Max-Planck-Institut für Kohlenforschung, Kaiser-Wilhelm Platz 1, 45470 Mülheim an der Ruhr, Germany

Table of Contents

SI1. Sample preparation

Apo-HydA1 was expressed and purified as described previously[1]. The bacteria suspension was shaken at 37°C aerobically till an OD600 (optical density at a wavelength of 600 nm) of 0.6 was reached. After pH correction to 7.4 and transfer in a glass bottle with Teflon membrane, protein expression was induced with 0.5 M IPTG (isopropyl β-D-thiogalactopyranoside). The suspension was gassed with argon for one hour and expression was continued for 25 h at room temperature. Unless indicated, all samples were handled under strictly anaerobic conditions in a glove box (COY) using a palladium catalyst and forming gas with 1-2.5% hydrogen.

All NMR samples were prepared in NMR buffer 1 (25 mM potassium phosphate pH* 7.4 and 100% D_2O) or 2 (25 mM potassium phosphate pH* 6.4 and 100% D_2O).

Preparation of pure states for NMR spectroscopy:

(1) The first sample had a concentration of 1.7 mM and contained >95% oxidized apo-HydA1. This sample was purified in the absence of sodium dithionite and the NMR tube was flame sealed.
(2) The second sample had a concentration of 4.2 mM and contained >95% reduced apo-HydA1. It was purified in the presence of 2 mM sodium dithionite. The buffer was exchanged directly before the measurement to remove sodium dithionite and the NMR tube was flame sealed.
(3) To prepare the third sample, a two-fold excess of a 50 mM $[Fe_2(adt)(CO)_3(CN)_2]$ solution in DMSO was added to 0.53 ml of 2.65 mM apo-HydA1 in 25 mM Tris/HCl pH 8.0, 25 mM KCl and 2 mM NaDT diluted to 2.5 ml with NMR buffer 1. The maturation and removal of excess $[Fe_2(adt)(CO)_3(CN)_2]$ was performed as described previously.[1,2] After concentrating the sample to approximately 3.5 mM, it was flashed with argon for 20.5 h. All following steps were performed in a glove box (MBRAUN) filled with N_2 in the absence of hydrogen. Addition of 2.45 mM thionine acetate to remove residual H_{red} and H_{sred} resulted in >95% HydA1 in the H_{ox} state (Figure S4, bottom). The sample was measured in a flame sealed NMR tube.
(4) The fourth sample was prepared by CO-flushing about 4 mM maturated apo-HydA1 for 1 h and keeping the sample in the CO-filled closed vial for about 1 h. The FTIR spectrum confirmed HydA1 to be present to >95% in the H_{ox}-CO state (Figure S7). This sample was measured in a 5 mm medium wall precision quick pressure valve NMR tube.
(5) For the NOE-based assignment of the methylene protons of the dithiolate bridge, apo-HydA1 was maturated with $Fe_2(pdt)(CO)_3(CN)_2$ (pdt = propanedithiolate). The resulting HydA1-pdt has been shown to exist only in an oxidized and reduced state and is much more stable than HydA1-adt. Furthermore, the oxidized form of HydA1-pdt has revealed basically the same electronic structure.[3] The sample used for measuring the transient NOE had a concentration of about 3.6 mM, contained about 50% oxidized and 50% reduced HydA1-pdt and was measured in a flame-sealed NMR tube.

SI2. FTIR measurements of H_{ox} and H_{ox}-CO

An aliquot of 8 µl of the NMR samples (3) and (4) was employed to assess the purity of the H_{ox} and H_{ox}-CO redox states using FTIR spectroscopy.[4] FTIR measurements were carried out on a Bruker IFS 66v/S or a Bruker VERTEX 80v spectrometer with a resolution of 2 cm^{-1} in forward-backward measuring mode for 1000 scans at room temperature. Baseline correction was performed using a self-written routine in MATLAB.

SI3. NMR experiments

1D ^{1}H NMR spectra shown in Figure 2 were acquired at 298 K on a Bruker AVANCE 600 spectrometer equipped with a cryogenic TCI probehead using the normal one pulse experiments with ^1H_2O presaturation or using the super-WEFT pulse sequence.[5] Relaxation delay times were 200 ms. In case of HydA1 in the H_{ox} and H_{ox}-CO state, methylene protons of the $[2Fe]_H$ site were identified by comparison of the ^{1}H 1D spectra of samples maturated with deuterated and non-deuterated $[Fe_2(adt)(CO)_4(CN)_2]$.

1D NOE (Figure S6)

The 1D NOE experiments of HydA1-pdt were acquired at 298 K on a Bruker AVANCE 600 equipped with a cryogenic TCI probehead. For the measurement of the NOE, a modified super-WEFT sequence including CW irradiation off resonance from the carrier position was used.[6] To minimize the artifacts the following irradiation scheme was used as follows: the spectrum with CW irradiation on resonance with the target signal is acquired twice and co-added, then the spectra with the CW irradiation symmetrically off-resonance with respect to the target signals are acquired and subtracted. The used on and off resonance frequencies are summarized in the following table.

Table S1. Summary of the used on and off resonance frequencies to measure the NOE at 600 MHz

	Signal	Off resonance (downfield) frequency (Hz) subtracted	On resonance frequency (Hz) acquired twice	Off resonance (upfield) frequency (Hz) subtracted
oxidized HydA1-pdt	1+2	6999.64	6711.60	6430.56
	3	-12932.45	-13208.90	-15329.66
	4	-15329.66	-15600.77	-15871.88

Temperature-dependence of the hyperfine shifted resonances of oxidized and reduced apo-HydA1

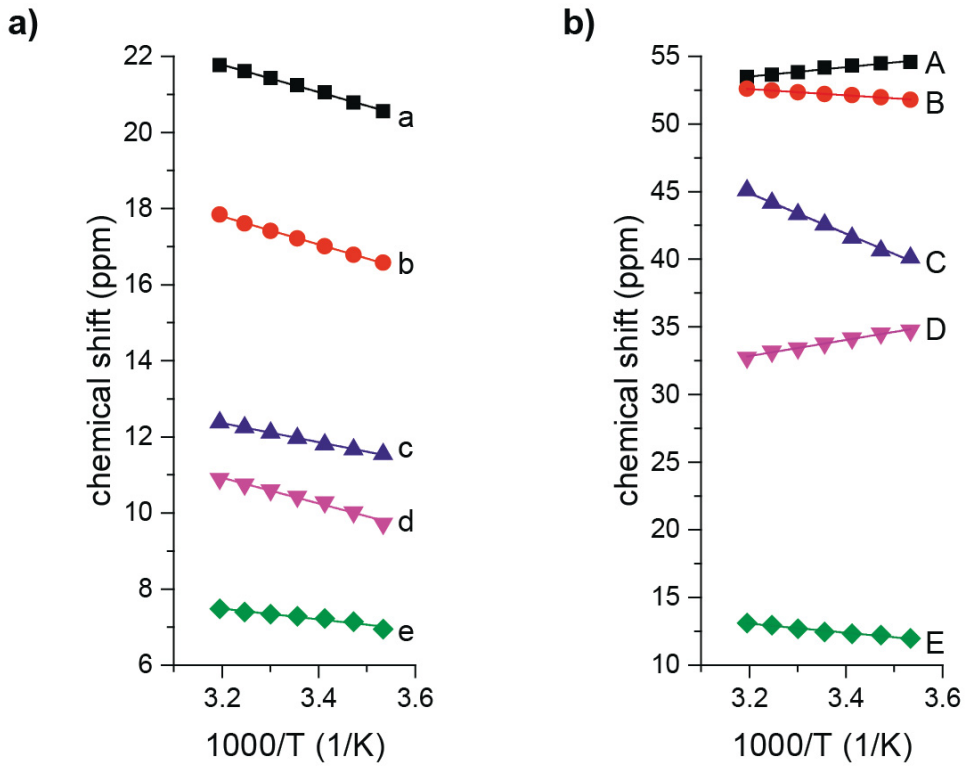

Figure S1. Plot of the observed chemical shifts versus the reciprocal temperature for the assigned contact shifted Cys resonances from oxidized (a) and reduced (b) HydA1 containing only the $[4Fe\text{-}4S]_H$ cluster. The peaks are labeled as in Figure 2.

Temperature-dependence of the hyperfine shifted resonances of H_{ox}

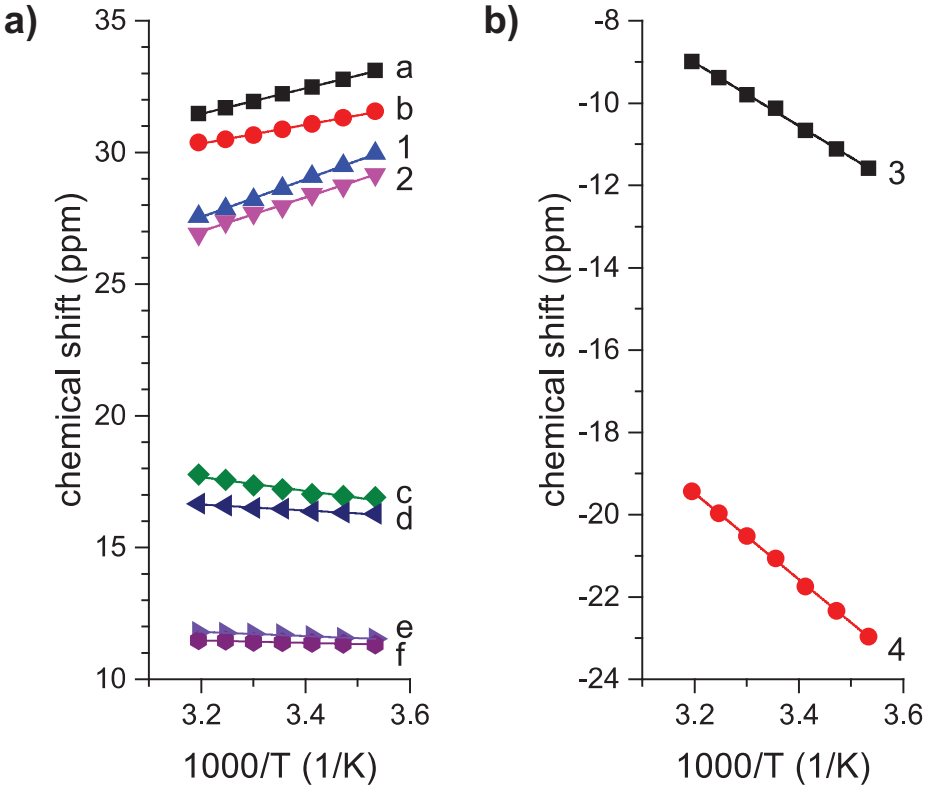

Figure S2. Plot of the observed chemical shifts versus the reciprocal temperature for the contact shifted resonances from HydA1 in the H_{ox} state. The peaks are labeled as in Figure 2. The downfield shifted resonances are displayed in a) and the upfield shifted resonances are shown in b).

Temperature-dependence of the hyperfine shifted resonances of H_{ox}-CO

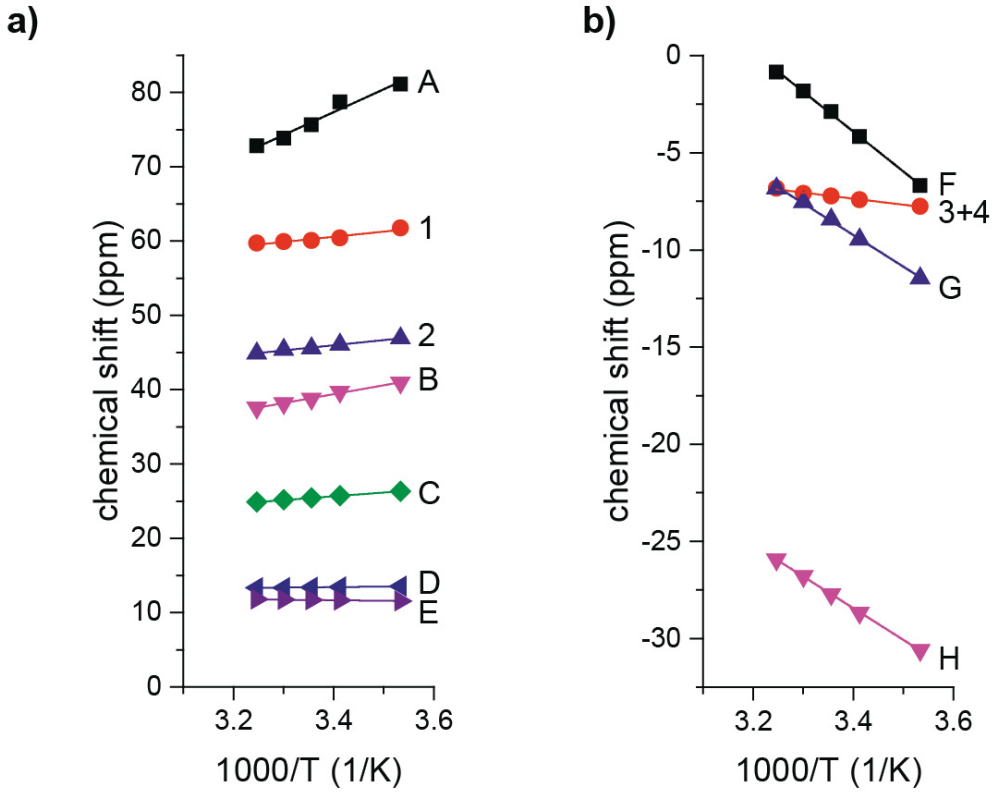

Figure S3. Plot of the observed chemical shifts versus the reciprocal temperature for the contact shifted resonances from HydA1 in the H_{ox}-CO state. The peaks are labeled as in Figure 2. The downfield shifted resonances are displayed in a) and the upfield shifted resonances are shown in b).

Table S2. ^{1}H NMR spectral parameters for the hyperfine shifted resonances for different forms of HydA1.

peak label	assign-ment	chem. shift (ppm)	line-width (Hz)[a]	temp. dep.	rela-tive area	peak label	assign-ment	chem. shift (ppm)	line-width (Hz)[a]	temp. dep.	rela-tive area
oxidized apo-HydA1						reduced apo-HydA1					
a	β-CH_2	21.38	300	aC	1	A	β-CH_2	55.59	1500	C	2
b	β-CH_2	17.23	200	aC	1	B	β-CH_2	53.54	1500	aC	2
c	β-CH_2	11.97	300	aC	1	C	β-CH_2	44.38	1800	aC	2
d	β-CH_2	10.4	200	aC	1	D	β-CH_2	33.98	1600	C	2
e	β-CH_2	7.11	200	n. d.	n. d.	E	α-CH_2	11.74	400	aC	1
H_{ox} state						H_{ox}-CO state					
a	β-CH_2	32.22	300	C	1	A	β-CH_2	75.66	4000	C	n. d.
b	β-CH_2	30.87	300	C	1	1	adt-CH_2	60.09	4000	C	n. d.
1	adt-CH_2	28.63	600	C	1	2	adt-CH_2	45.48	1800	C	n. d.
2	adt-CH_2	27.95	400	C	1	B	β-CH_2	38.71	1400	C	n. d.
c	β-CH_2	17.22	200	aC	1	C	α-CH_2	25.39	300	C	n. d.
d	β-CH_2	16.47	200	aC	1	D	α-CH_2	13.36	300	C	n. d.
3	adt-CH_2	-10.13	200	pC	1	E	α-CH_2	11.69	300	aC	n. d.
4	adt-CH_2	-21.07	200	pC	1	F	α-CH_2	-2.92	300	pC	1
e	α-CH_2	11.7	200	aC	1	3+4	adt-CH_2	-7.25	300	pC	2
f	α-CH_2	11.4	100	aC	1	G	β-CH_2	-8.48	400	pC	1
						H	β-CH_2	-27.78	800	pC	1

[a] full-width at half-maximum, n. d. = not determined, C = Curie, aC = anti-Curie, pC = pseudo-Curie

FTIR spectra of HydA1 in the H_{ox} state

Due to the appearance of the active site (with a free ligand site at Fe_d), there are two terminal –CO vibrations and one bridging –CO as well as two $–CN^-$ vibrations expected in FTIR spectrum. For the [FeFe] hydrogenase HydA1 from *Chlamydomonas reinhardtii* in the H_{ox} state, bands at 2088/2070 cm^{-1} corresponding to the $–CN^-$ vibrations and bands at 1964/ 1939/ 1803 cm^{-1} for the –CO vibrations are described.[1] With small deviations these vibrations can be detected for the used NMR samples for the H_{ox} state (Figure S4). The deuteration of methylene protons of adt does not affect the band positions in the H_{ox} state. Impurities, mainly H_{ox}-CO state (see asterisk Figure S4 and compare Figure S7), are slightly more pronounced in the sample maturated with ^{2}H-adt. Based on the FTIR spectra the purity of both freshly prepared NMR samples in the H_{ox} state has been estimated as >95 %.

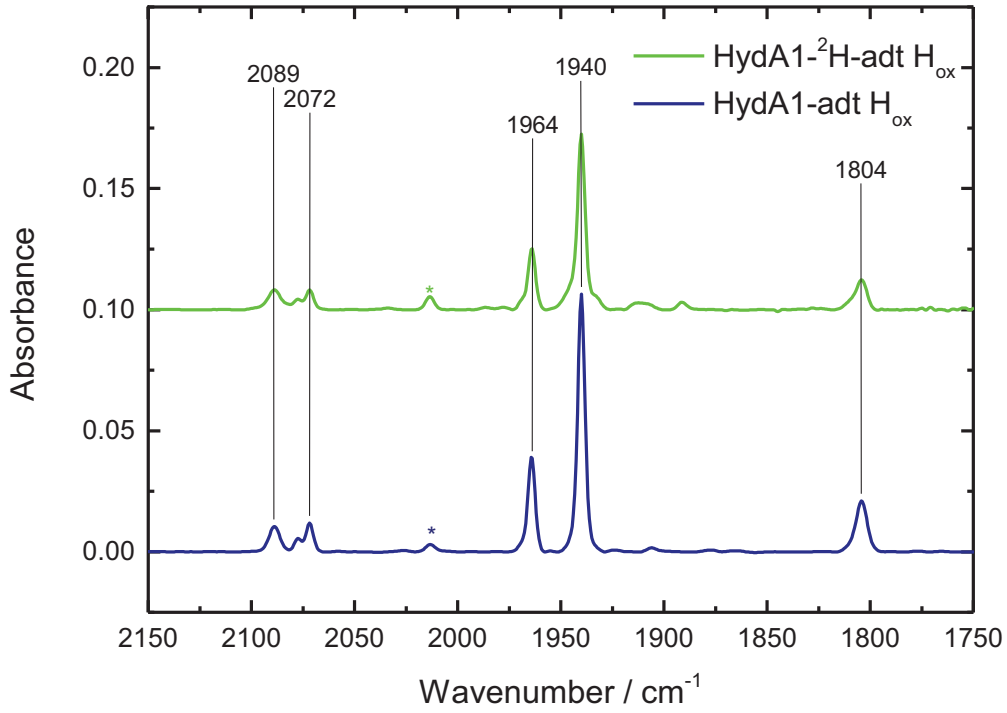

Figure S4. FTIR spectra of HydA1 in the H_{ox} state at room temperature. The spectrum of the unlabeled sample is shown in blue and the sample with the deuterated $[2Fe]_H$ site (^{2}H-adt) is shown in green. The marker band of the H_{ox}-CO state at 2013 cm^{-1} is indicated by *.

Assignment of the adt methylene protons in the H_{ox}-CO state

In order to distinguish the methylene protons of the $[4Fe\text{-}4S]_H$ cluster-coordinating cysteines and of the adt in the $[2Fe]_H$ cluster of the H_{ox} state, apo-HydA1 was maturated using ^{2}H-adt. By comparison of the ^{1}H spectra of unlabeled H_{ox} with H_{ox} containing ^{2}H-adt, signals labelled 1 to 4 in Figure 2c have been unambiguously assigned to the four methylene protons of $[2Fe]_H$. The amine proton of adt exchanges with water and is thus not present in the ^{1}H NMR spectra when 100% D_2O is used as the solvent.

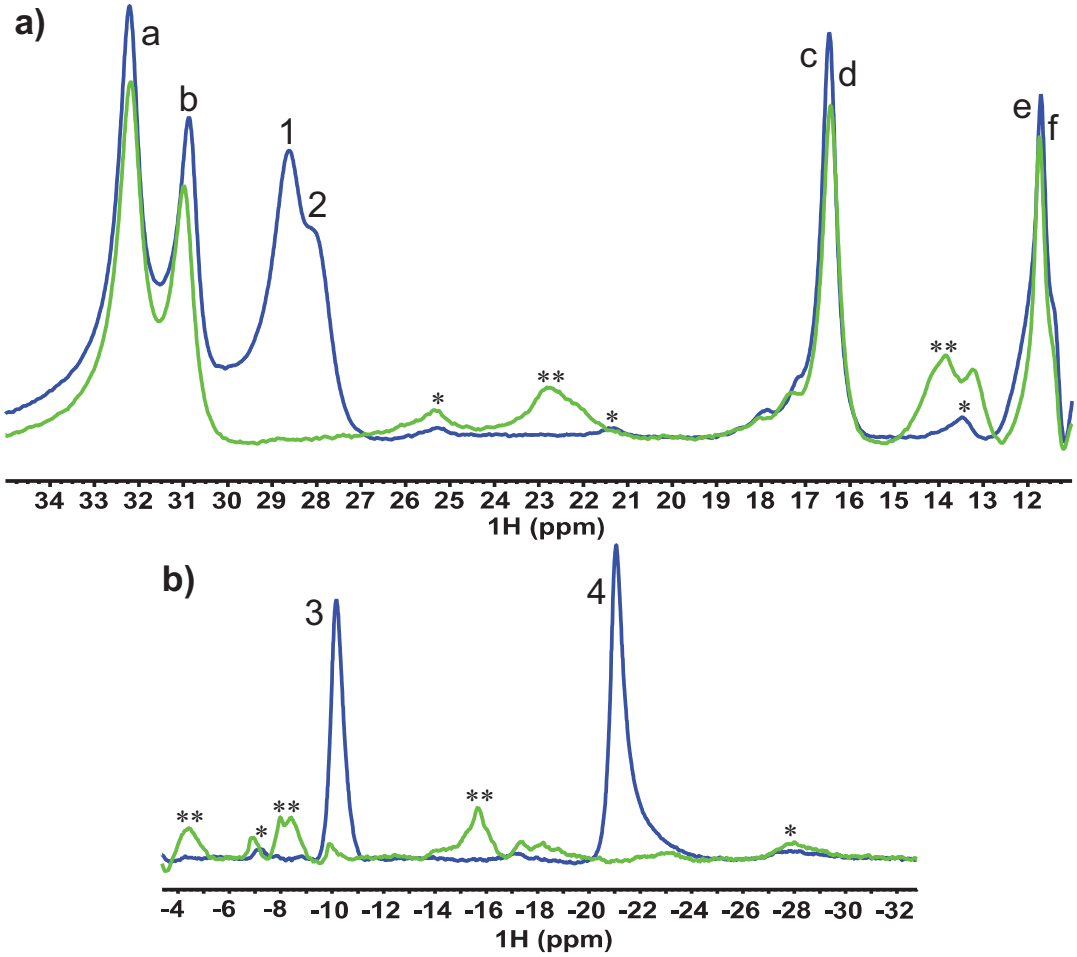

Figure S5. 1D ^{1}H NMR spectra (600 MHz) at 298 K of unlabeled oxidized HydA1 (blue, H_{ox}) and oxidized HydA1 maturated with deuterated adt (green, H_{ox}-^{2}H-adt). a) Downfield region from 35 to 11 ppm and b) upfield region from -3 to -33 ppm. Peaks that belong to other HydA1 states investigated here are labelled with *. Resonances marked with ** originate probably from reduced HydA1 states present in the sample. The contaminations constitute about 5 % of the total sample for unlabeled H_{ox} and about 20 % for H_{ox}-^{2}H-adt. As the FTIR spectra for H_{ox} and H_{ox}-^{2}H-adt are almost identical (Figure S4), the sample maturated with ^{2}H-adt appears to be less stable than the sample maturated with adt.

SI4 Assignment of the axial and equatorial methylene protons of adt

a) Distance and linewidth considerations

In the X-ray structure[7] with protons added, the axial protons are closer to $[4Fe\text{-}4S]_H$ as well as to the proximal and distal Fe sites (Fe_p and Fe_d) compared to the equatorial protons (Figure 1 (right) and Table S2). Since the paramagnetic relaxation enhancement also depends on the inverse sixth power of the distance between metal ion and nuclear spin, in general the closer a proton is to an Fe, the larger is its line width of the corresponding ^1H signal.[8]

Table S3. Distances of the methylene protons of adt to Fe_d and Fe_p

	distance to Fe_p (Å)	distance to Fe_d (Å)
H1	3.54	3.98
H2	3.44	4.07
H3	4.40	4.19
H4	4.37	4.12

b) Experimentally observed characteristic NOE patterns for axial and equatorial protons

In addition to $[Fe_2(adt)(CO)_4(CN)_2]$ other synthesized inorganic cofactors can be incorporated into recombinant HydA1 containing only the $[4Fe\text{-}4S]_H$ cluster. The resulting analogues of HydA1 have a reduced or no activity but may have other advantages over fully active HydA1.[1] Using the propanedithiolate (pdt) analogue $Fe_2(pdt)(CO)_4(CN)_2$ for maturation to prepare the "so-called" HydA1-pdt provides the advantage of high sample stability concomitant with only an oxidized and a reduced state. Importantly, the oxidized form of HydA1-pdt has revealed basically the same electronic structure as fully active HydA1 in the H_{ox} state.[3] Hence the H_{ox} state of HydA1-pdt has been used to obtain ^1H NOEs connectivities between the methylene protons of the dithiolate bridge of $[2Fe]_H$. These ^1H NOE connectivities present another strong evidence for signals 1+2 to correspond to the axial and for signals 3+4 to correspond to the equatorial protons. The measured ^1H NOE spectra revealed NOEs between signals 3 and 1+2 as well as between signals 4 and 1+2. In addition, no NOE was observed between signal 3 and 4 (Figure S6). Accordingly, the downfield shifted signals 1+2 with a line width of about 500 Hz have been tentatively assigned to the axial protons H1 and H2 and signals 3+4 with a line width of about 200 Hz have been assigned to the equatorial protons H3 and H4 (Figure 1 and Table 1). The NOE experiments were carried out with the mixture of 50% oxidized and 50% reduced HydA1-pdt to observe any possible saturation transfer from one oxidation state to the other.

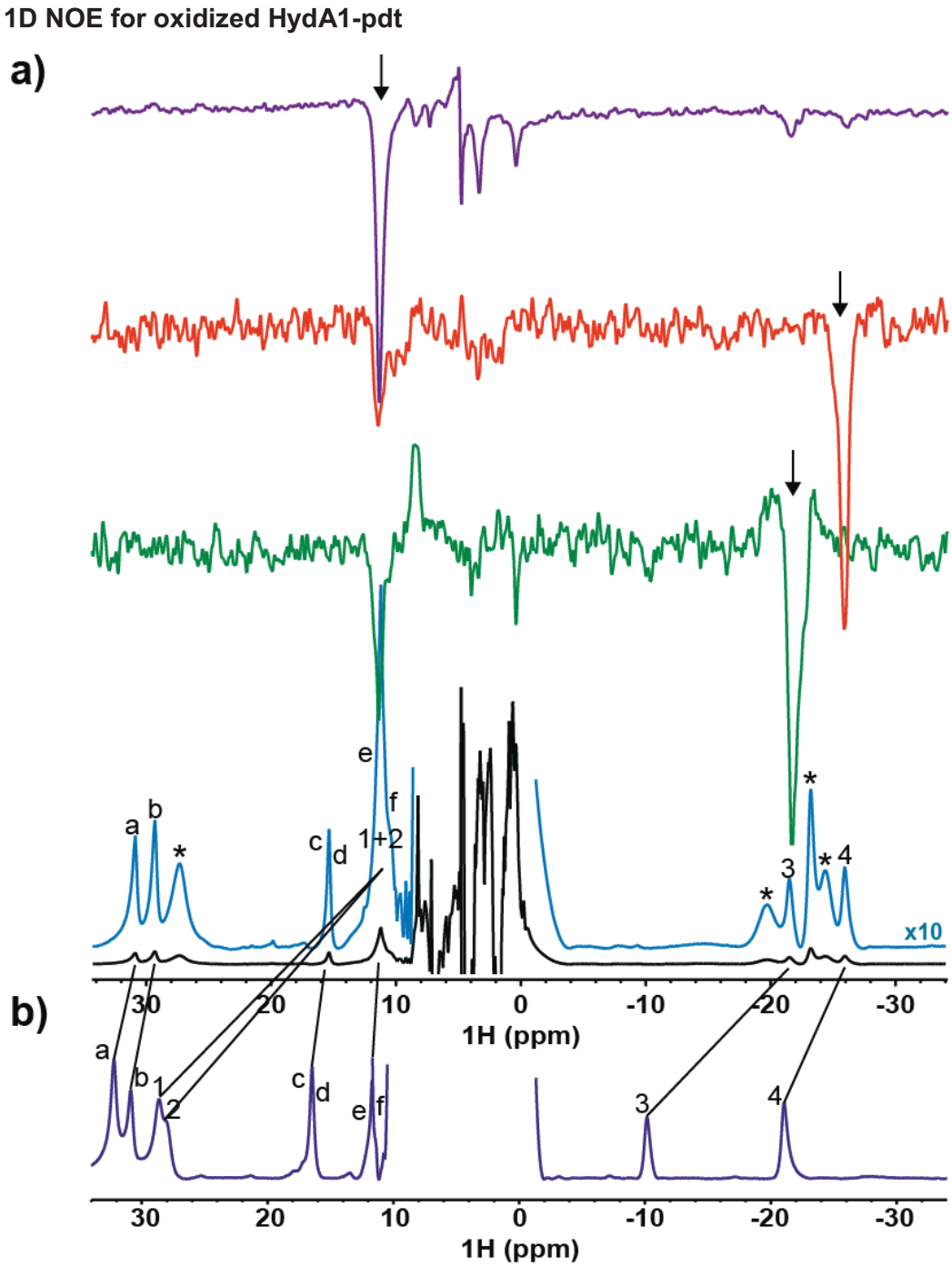

Figure S6. a) Overlay of the NOE spectra obtained upon irradiating the hyperfine shifted resonances and the full spectrum of an about 1:1 mixture of oxidized and reduced HydA1-pdt (black). The trace in light blue indicates a x10 multiplication of the intensity. Upon irradiating signal 3 (green trace) or signal 4 (red trace), a signal at about 11.2 ppm responds (signal 1+2). Signal 1+2 (violet trace) is coupled to signal 3 and also signal 4. The arrows indicate the irradiation frequencies. Irradiation is performed to minimize the artifacts as shown in Figure S1. The resonances originating from the reduced portion of the sample are indicated by *. b) The 1D ^{1}H NMR spectrum of H_{ox} as also shown in Figure 1c. The black lines connect the corresponding resonances of H_{ox} in b) and oxidized HydA1-pdt in a). The strong chemical shift differences of signals 1-4 observed when comparing the ^{1}H 1D NMR spectra of HydA1-adt and HydA1-pdt in the H_{ox} state are caused by the presence of a methylene group instead of a secondary amine in the bridgehead position of the dithiolate ligand connecting the two irons of $[2Fe]_H$.

FTIR spectra of HydA1 in the H_{ox}-CO state

In the H_{ox}-CO state an additional –CO ligand is bound to the open coordination site at Fe_d. Thus, four instead of three –CO vibrations occur. In the literature band positions at 2092/2084/2013/1970/1964 and 1810 cm^{-1} are described[9] and the detected signals for the used NMR samples in H_{ox}-CO state are almost identical. The rather broad contributions in the HydA1-^{2}H-adt H_{ox}-CO spectrum (Figure S7, green line) are impurities (^{v}) and do not belong to a second redox state. For the unlabelled sample, a tiny amount of H_{ox} (1939 cm^{-1}) and $H_{red}H^+$ (1891 cm^{-1}) estimated as less than 5 % of the total sample were detected (Figure S7).

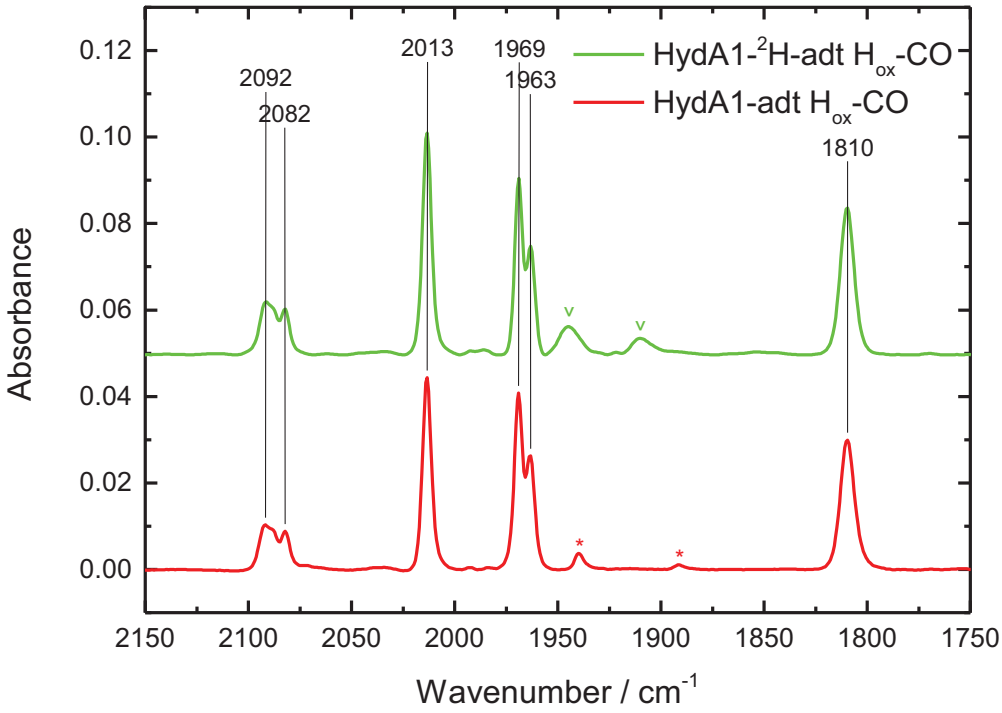

Figure S7. FTIR spectra of HydA1 in the H_{ox}-CO state at room temperature. The spectrum of the unlabeled sample is shown in red and the sample with the deuterated [2Fe] site (^{2}H-adt) is shown in green. Impurities are indicated by ^{v} and other redox states are indicated by *.

Assignment of the adt methylene protons in the H_{ox}-CO state

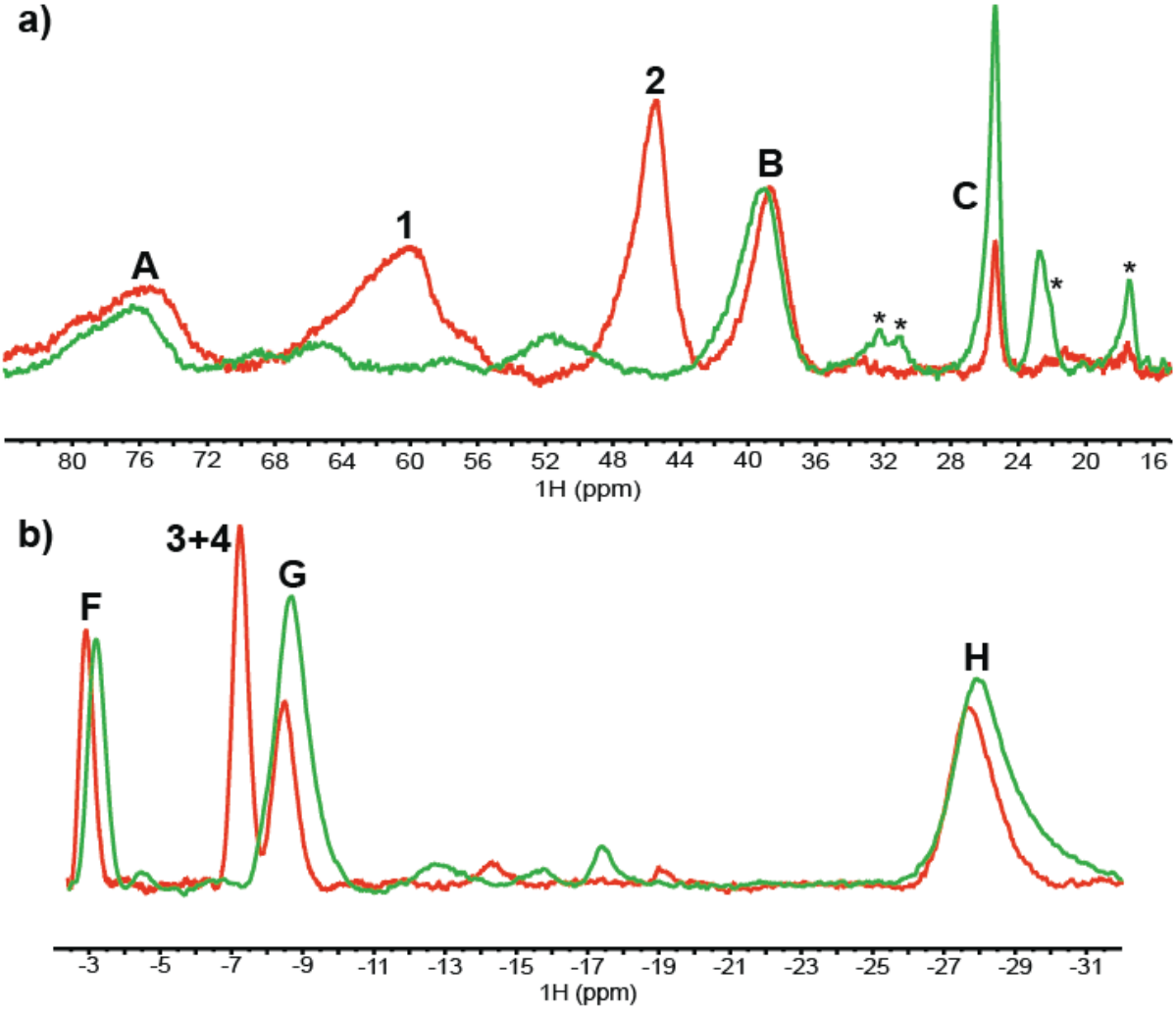

Figure S8. 1D ^{1}H NMR spectra (600 MHz) at 298 K of unlabeled HydA1 in the H_{ox}-CO state (red) and H_{ox}-CO after maturation with deuterated ADT (green). a) Downfield region from 84 to 15 ppm and b) upfield region from -2 to -32 ppm. Peaks that belong to other HydA1 states investigated here are labelled with *. The contaminations constitute about 5 % of the total sample.

Three of the hyperfine shifted signals observed for unlabeled HydA1 in the H_{ox}-CO state are not present when deuterated $[Fe_2(adt)(CO)_4(CN)_2]$ has been used for maturation. Given that the integral of the disappearing upfield peak at -7.25 ppm suggests that it consists of two proton signals (3+4), all four methylene protons of $[2Fe]_H$ could thus also be identified for H_{ox}-CO (Figure 2c).

References

(1) Siebel, J. F.; Adamska-Venkatesh, A.; Weber, K.; Rumpel, S.; Reijerse, E.; Lubitz, W. *Biochemistry* **2015**, *54*, 1474.

(2) Esselborn, J.; Lambertz, C.; Adamska-Venkatesh, A.; Simmons, T.; Berggren, G.; Noth, J.; Siebel, J.; Hemschemeier, A.; Artero, V.; Reijerse, E.; Fontecave, M.; Lubitz, W.; Happe, T. *Nat. Chem. Biol.* **2013**, *9*, 607.

(3) Adamska-Venkatesh, A.; Simmons, T. R.; Siebel, J. F.; Artero, V.; Fontecave, M.; Reijerse, E.; Lubitz, W. *Phys. Chem. Chem. Phys.* **2015**, *17*, 5421.

(4) Lubitz, W.; Ogata, H.; Rüdiger, O.; Reijerse, E. *Chem. Rev.* **2014**, *114*, 4081.

(5) Inubushi, T.; Becker, E. D. *J. Magn. Reson.* **1983**, *51*, 128.

(6) Bertini, I.; Luchinat, C.; Parigi, G.; Ravera, E. *NMR of Paramagnetic Molecules*; Elsevier Amsterdam 2017.

(7) Pandey, A. S.; Harris, T. V.; Giles, L. J.; Peters, J. W.; Szilagyi, R. K. *J. Am. Chem. Soc.* **2008**, *130*, 4533.

(8) Bertini, I.; Luchinat, C.; Parigi, G.; Pierattelli, R. *Chembiochem* **2005**, *6*, 1536.

(9) Adamska-Venkatesh, A.; Krawietz, D.; Siebel, J.; Weber, K.; Happe, T.; Reijerse, E.; Lubitz, W. *J. Am. Chem. Soc.* **2014**, *136*, 11339.

4.6 Paper VI

The [RuRu] analogue of [FeFe] hydrogenase traps the key metal bound hydride intermediate in the enzyme's catalytic cycle

C. Sommer, C. Richers, W. Lubitz, E. Reijerse, T. Rauchfuss

Journal name: Angewandte Chemie International Edition

Published 26.03.2018, DOI: 10.1002/anie.201801914

Author: First author

Contribution: – 65 %

– I prepared all biological samples

– I recorded, analyzed and fitted all FTIR (-spectroelectrochemistry) data

– I was largely involved in writing the manuscript

S. Richers measured synthesized the ruthenium containing precursor complexes. E. Reijerse measured the CW EPR spectrum and performed the DFT calculations. All others discussed the results and were involved in writing the manuscript.

[RuRu] Analogue of [FeFe]-Hydrogenase Traps the Key Hydride Intermediate in the Enzyme's Catalytic Cycle

Constanze Sommer,[a] Casseday P. Richers,[b] Wolfgang Lubitz,[a] Thomas B. Rauchfuss*[b] Edward J. Reijerse*[a]

Abstract: The active site of the [FeFe]-hydrogenases features a binuclear $[2Fe]_H$ subcluster that contains a unique bridging amine moiety close to an exposed iron center. Heterologous splitting of H_2 results in formation of a transient terminal hydride at this iron site which, however, is difficult to stabilize. Here, we show that the hydride intermediate forms immediately when $[2Fe]_H$ is replaced by $[2Ru]_H$ analogues through artificial maturation. Outside the protein the $[2Ru]_H$ analogues form bridging hydrides, which rearrange to terminal hydrides after insertion into the apo-protein. H/D exchange of the hydride only occurs for $[2Ru]_H$ analogues containing the bridging amine moiety.

[FeFe]-Hydrogenases catalyze the fundamental reaction: $H_2 \rightleftharpoons 2H^+ + 2e$.[1] The active site (H-cluster) contains a binuclear iron complex $[Fe_2(ADT)(CO)_3(CN)_2]^{2-}$, (ADT = $HN(CH_2S^-)_2$), referred to as $[2Fe]_H$, linked to a generic $[4Fe\text{-}4S]_H$ cluster. The distal iron features an open coordination site close to the pendant amine base of the bridging ADT (azadithiolate) ligand, which shuttles protons in and out of the active site via the intermediacy of hydride intermediates (Figure 1).[2] The detailed properties of these hydride states are of great interest.

Mechanistic analysis of the [FeFe]-hydrogenases has greatly benefited from the discovery of "artificial maturation"[3] whereby the apo-enzyme lacking the $[2Fe]_H$ subsite but still containing the $[4Fe\text{-}4S]_H$ cluster is heterologously expressed in *E. coli* and subsequently reconstituted with $[Fe_2(ADT)(CO)_4(CN)_2]^{2-}$.[4] While many variants of $[2Fe]_H$ have been introduced, focused on modified dithiolate cofactors[3a, 5] [6] the question remains, could $[2Fe]_H$ be replaced with non-native metals? In this report, we address this question and describe the unexpected consequences. Specifically, we report the characterization of apo-HydA1 from *Chlamydomonas reinhardtii* maturated with $[2Ru]_H$ affording an artificial [RuRu]-hydrogenase.

As precursor of $[2Ru]_H$ we prepared $[Ru_2(ADT)(CO)_4(CN)_2]^{2-}$ by cyanation of $[Ru_2(ADT)(CO)_6]$, following the protocol for preparing $[Ru_2(PDT)(CO)_4(CN)_2]^{2-}$ (PDT = $CH_2(CH_2S^-)_2$)).[7] The intermediate $[Ru_2(ADT)(CO)_6]$ was obtained using carboxybenzyl protected ADT, Cbz $N(CH_2SH)_2$ according to Scheme 1.

[a] C. Sommer, Prof. Dr. W. Lubitz, Dr. E.J.Reijerse
Max-Planck-Institut für Chemische Energiekonversion
Stiftstrasse 34-36,
45470 Mülheim an der Ruhr, Germany
E-mail: Edward.reijerse@cec.mpg.de
[b] Dr. C.P. Richers, Prof. Dr. T.B. Rauchfuss
School of Chemical Sciences
600 S. Goodwin Ave.
University of Illinois at Urbana-Champaign
Urbana, IL 61801, USA
E-mail: rauchfuz@illinois.edu

Supporting information for this article is given via a link at the end of the document.

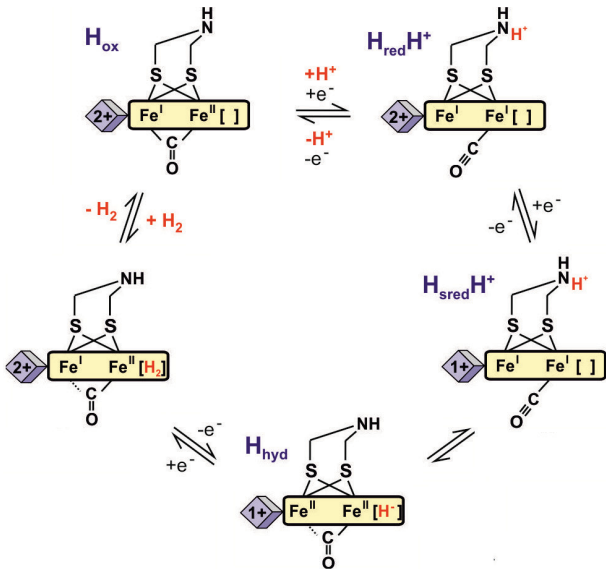

Figure 1 Scheme of potential catalytic states of the H-cluster in [FeFe]-hydrogenases highlighting protonation and hydride formation at the reduced $[2Fe]_H$ subsite in combination with a redox event at the $[4Fe\text{-}4S]_H$ cluster. The two terminal CO and two CN^- ligands are omitted for clarity.

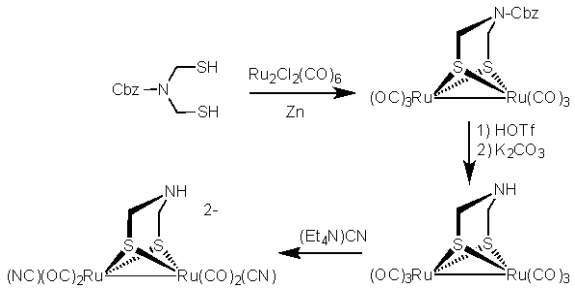

Scheme 1. Synthesis of $[Ru_2(ADT)(CO)_4(CN)_2]^{2-}$.

Dissolution of $[Ru_2(ADT)(CO)_4(CN)_2]^{2-}$ in water resulted in a color change from orange to pale yellow over the course of 15 min. yielding $[(\mu\text{-}H)Ru_2(ADT)(CO)_4(CN)_2]^-$. The protonation reaction causes ν_{CO} bands to shift 63-82 cm^{-1} towards higher energy (figure 2B and also figure S8). The ^1H NMR spectrum of the product exhibits a signal at δ = -13.9 ppm, a region characteristic of a bridging hydride ligands.[8] Similar IR and ^1H NMR signals were observed when a DMSO solution of $(Et_4N)_2[Ru_2(ADT)(CO)_4(CN)_2]$ was treated with one equivalent of trichloroacetic acid (see figure S7). In contrast to the behavior of $[(\mu\text{-}H)Ru_2(ADT)(CO)_4(CN)_2]^-$, the analogous $[(\mu\text{-}H)Fe_2(ADT)(CO)_4(CN)_2]^-$ is unstable in solution at room temperature.[9] We observed no evidence for the formation of terminal hydrides, in complete contrast to our observations of the ruthenated protein (vide infra).

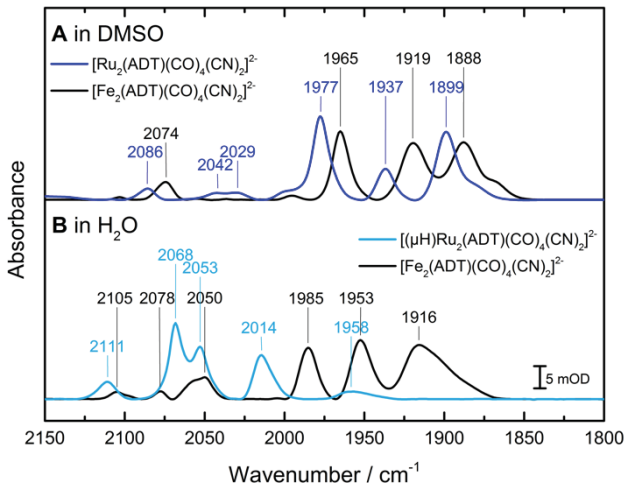

Figure 2. FTIR of $[Ru_2(ADT)(CO)_4(CN)_2]^{2-}$ and $[Fe_2(ADT)(CO)_4(CN)_2]^{2-}$ in **A** DMSO and **B** in H_2O where the complex is protonated forming a bridging hydride (μH) (light blue trace).

Initial maturation experiments were conducted with $[Ru_2(PDT)(CO)_4(CN)_2]^{2-}$. This precursor lacks the amine function of ADT. Figure 3A,B presents the FTIR spectrum of HydA1 maturated with $[Ru_2(PDT)(CO)_4(CN)_2]^{2-}$ dissolved in DMSO added 2:1 to the apo-enzyme in aqueous buffer at pH 8 and rebuffered to pH 6. Maturation proceeds very cleanly. Five FTIR bands are observed for the HydA1-$[2Ru]_H$-PDT, two at higher wavenumbers arising from CN^- ligands and three carbonyl stretches between 1990-1850 cm^{-1}. The narrow spectral linewidth of these bands is characteristic for insertion of the complex into the protein (compare spectra in figures 2 and 3). Interestingly, the enzyme can also be maturated with the [2Ru]-PDT complex predissolved in aqueous buffer in which it, similar to the ADT complex, forms a bridging hydride (figure S8), i.e. $[(\mu\text{-}H)Ru_2(PDT)(CO)_4(CN)_2]^-$.[7] However, the FTIR spectrum of the inserted [2Ru]-PDT complex is *identical* to that of the enzyme maturated with the precursor pre-dissolved in DMSO.

Just like the HydA1-$[2Fe]_H$-PDT H-cluster analogue,[10] the HydA1-$[2Ru]_H$-PDT complex shows two redox states (figure 3A,B). The oxidized and reduced states are distinguished by relative small (≈10 cm^{-1}) shifts in the corresponding FTIR spectra. The small shift suggest that only the $[4Fe\text{-}4S]_H$ subcluster is participating in this redox event.[10] The HydA1-$[2Ru]_H$-PDT subsite seems to be trapped in a single redox state which is different from the mixed valence state [Fe(I)Fe(II)] found for the PDT variant of HydA1.[10] The FTIR spectra of HydA1-$[2Ru]_H$-PDT strongly resemble those of the recently identified terminal hydride state (H_{hyd}).[11] In particular, the blue shifted bridging CO band at 1860 cm^{-1} is characteristic of an H-cluster state with an oxidized [Ru(II)Ru(II)]core and an electron donating ligand (i.e. H^-) in the open coordination site. Due to the coupling of the bridging CO and metal hydride stretch vibration, the presence of a hydride state can be identified through H/D exchange (figure S9 and S10).[12] Figure 3C shows the FTIR of HydA1-$[2Ru]_H$-PDT maturated in D_2O (pD=8.0) The ν(μCO) feature shows an additional peak which is 10 cm^{-1} blue shifted with respect to its position in H_2O buffer. The incomplete conversion of the ν(μCO) band suggests that the hydride is partly formed through equilibration of the buffer with the 2.0% H_2 atmosphere present in the anaerobic chamber. Indeed, when the atmosphere is exchanged for 2.5% D_2 the ν(μCO) band of the hydride species at 1852 cm^{-1} decreases in intensity (figure 3C). The occurrence of the characteristic bridging CO band (1853-1863 cm^{-1}) and its sensitivity to H/D exchange signifies that the hydride is required to be terminal. Insertion of the complex into the protein therefore induces a rearrangement of the bridging hydride into a terminal hydride.

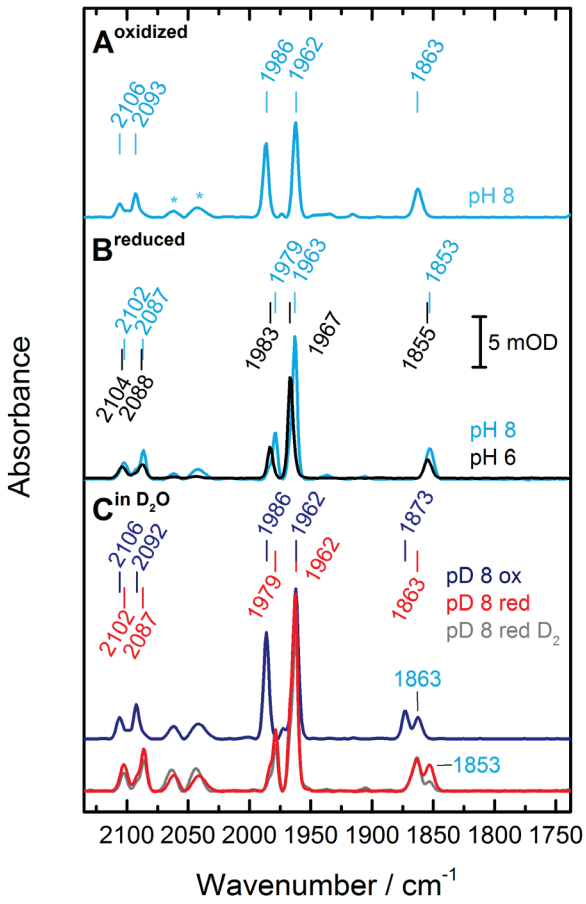

Figure 3. FTIR spectra of HydA1-$[2Ru]_H$-PDT. **A** shows the oxidized state at pH 8 adjusted with a 1:1 ratio protein:thionin, in **B** the reduced state is shown as prepared with three fold excess of sodium dithionite at pH 8 and 6 respectively. In **C** the effect of H/D exchange is demonstrated through artificial maturation in D_2O with 2.0% H_2 atmosphere or 2.5% D_2 atmosphere at pD 8. All FTIR spectra are taken at room temperature with a spectral resolution of 2 cm^{-1}.

These experiments also establish that the Ru-H/D species do not readily exchange with buffer. Indeed, rebuffering the in D_2O maturated enzyme in H_2O did not alter the FTIR spectrum of the $[2Ru]_H$ unit at all (see figure S11). This result leads us to conclude that the terminal hydride in HydA1-$[2Ru]_H$-PDT is very stable and unreactive and does not exchange with the solvent. The two redox states observed in the HydA1-$[2Ru]_H$-PDT variant of the enzyme can thus be represented as $[4Fe\text{-}4S]^{2+}$ $[Ru(II)Ru(II)](H^-)$ and $[4Fe\text{-}4S]^+[Ru(II)Ru(II)](H^-)$. The latter state has a reduced $[4Fe\text{-}4S]_H$ subcluster as is also evidenced by its EPR spectrum (figure S12). Interestingly, at pH 6 its FTIR bands show a blue shift of ≈3 cm^{-1} (figure 3B) with respect to the spectrum recorded at pH 8 suggesting a protonation event close to the H-cluster but not on the HydA1-$[2Ru]_H$-PDT subsite itself.

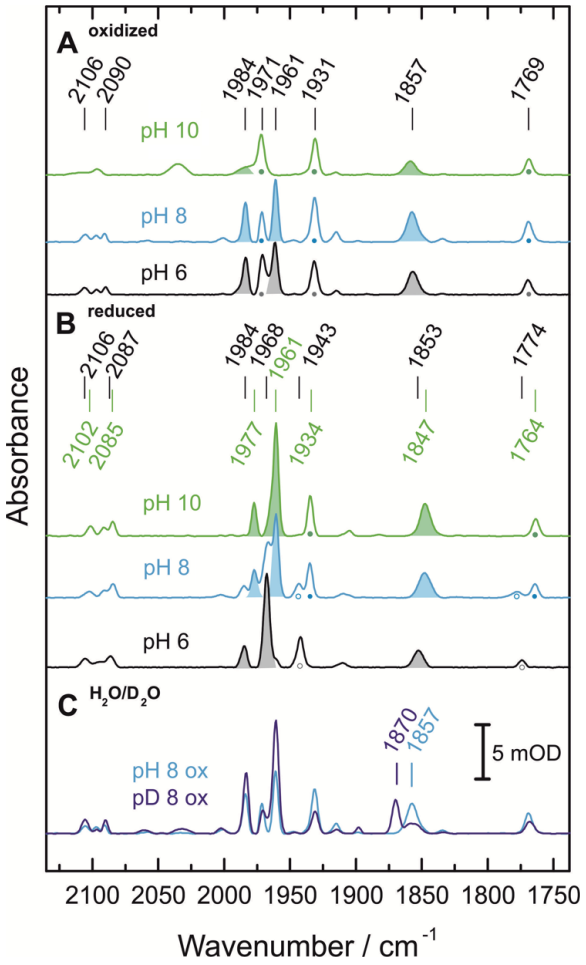

Figure 4 FTIR spectra of HydA1-$[2Ru]_H$-ADT. **A** shows the oxidized state at pH 6 (black)/8 (blue) /10 (green) adjusted with thionin 1:1 ratio, in **B** the samples are all reduced with three times excess of dithionite at pH 6/8/10 indicating two pH dependent reduced states. The bands of the hydride state are colored while the bands of the reduced state are indicated by closed (high pH) or open (low pH) bullets. Part **C** shows two oxidized samples, one maturated in H_2O (light blue) and the other in D_2O (dark blue) at pH/pD 8. All FTIR spectra are taken at room temperature with a spectral resolution of 2 cm^{-1}.

The same maturation experiments were subsequently conducted using $[Ru_2(ADT)(CO)_4(CN)_2]^{2-}$ (pre-dissolved in DMSO) as well as $[(\mu\text{-H})Ru_2(ADT)(CO)_4(CN)_2]^-$ (pre-dissolved in H_2O). Both precursors maturated the enzyme which, however, turned out to be inactive in hydrogen conversion. With the ADT derivative, a mixture of two states is obtained, which is dominated by the terminal hydride state H_{hyd} (CO bands 1984, 1961, 1857 cm^{-1} at pH 8, oxidized) that was also observed for the PDT-containing precursor (compare figure 3A,B and 4A,B). The new species, associated with FTIR bands 1971, 1931, 1769 cm^{-1} (pH 8, oxidized), is tentatively assigned to a state that lacks the hydride but is presumably protonated at the ADT amine moiety. This assignment is based on the strongly red shifted FTIR signature (suggesting a [Ru(I)Ru(I)] configuration) and the similarity to the recently reported H_{red}* state observed in a sensory [FeFe]-hydrogenase, which is characterized by a [Fe(I)Fe(I)] core coordinated by a bridging CO ligand.[13] Small model DFT calculations predict that amine protonation of the reduced HydA1-$[2Fe]_H$-ADT subsite induces the opening of the bridging CO[14] as is also observed experimentally.[15] The same type of calculation also predicts that for the ruthenium substituted subsite the bridging CO is retained upon amine protonation (see figure S14). Analogous to the [Ru(II)Ru(II)] hydride state, the [Ru(I)Ru(I)] species shows two redox states characterized by small (10 cm^{-1}) shifts of the CO bands, again suggesting a redox event on the $[4Fe\text{-}4S]_H$ subcluster. Therefore, these redox states can be represented as $[4Fe\text{-}4S]^{2+}$[Ru(I)Ru(I)] and $[4Fe\text{-}4S]^{+}$[Ru(I)Ru(I)].

The H/D exchange experiment presented in figure 4C indicates that for the HydA1-$[2Ru]_H$-ADT variant, in contrast to HydA1-$[2Ru]_H$-PDT, the hydride fully exchanges with the solvent. Maturation in D_2O buffer leads to a blue shifted ν(μCO) peak (figure 4C), which is restored to its original position upon rebuffering in H_2O (figure S13). The [Ru(I)Ru(I)] species is, however, unaffected by H/D exchange confirming that no hydride is associated with this state. Given the simultaneous occurrence of both hydride and [Ru(I)Ru(I)] states in the ADT enzyme with a ratio largely independent of pH and redox potential, it is tempting to assume that both states are protonated, i.e. either at the ADT amine or at Ru_d. The two states are in rapid exchange (see figure S15) explaining the fact that for the HydA1-$[2Ru]_H$-ADT enzyme H/D exchange of the hydride is possible through buffer exchange while exchange is not observed for the HydA1-$[2Ru]_H$-PDT maturated enzyme (see also figure S16). Figure S17 shows the FTIR-spectroelectrochemistry of HydA1-$[2Ru]_H$-ADT at pH 6. Both hydride and [Ru(I)Ru(I)] states show a reduction event, assigned to the $[4Fe\text{-}4S]_H$ sub-cluster. The hydride state with its formally oxidized [Ru(II)Ru(II)] core shows the highest redox potential (≈-270 mV), while the [Ru(I)Ru(I)] state is reduced at ≈-370 mV. Therefore, hydride formation and concomitant oxidation of the [2Ru] core increases the redox potential of the $[4Fe\text{-}4S]_H$ subcluster by ≈100 mV. This signifies that the strong electronic contact between the two subclusters is retained in the HydA1-$[2Ru]_H$-ADT H-cluster analogue.

In summary, deep mechanistic insight is provided when the periphery of the $[2Fe]_H$ cofactor in [FeFe]-hydrogenase is left intact but the metals are changed. This work exploits the stability characteristic of ruthenium hydrides.[16] Interestingly, both protonated and unprotonated precursors maturate apo-[FeFe]-hydrogenase and produce identical $[2Ru]_H$ analogues. This μ-hydride → terminal-hydride transformation demonstrates the profound influence of the protein on the stereochemistry of the hydride, an effect yet to be replicated in models.[8] Although the $[4Fe\text{-}4S]_H$ subcluster functions normally in these ruthenated proteins, the $[2Ru]_H$ is redox-inactive hence catalysis does not proceed. Thus the high activity of FeFe-based active sites reflects the advantages of mild redox potentials of the Fe^I/Fe^{II} couple. Finally, the work allows the first interrogation of a protein-metal hydride with and without the ADT cofactor, showing that the amine constitutes a critical proton relay.[2-3]

Acknowledgements

Research was supported by the Max Planck Society and the U.S. National Institutes of Health.

Keywords: hydrogenase • iron • ruthenium • hydride • FT-IR

[1] W. Lubitz, H. Ogata, O. Rüdiger, E. Reijerse, *Chem. Rev.* **2014**, *114*, 4081-4148.

[2] a. Y. Nicolet, A. L. de Lacey, X. Vernede, V. M. Fernandez, E. C. Hatchikian, J. C. Fontecilla-Camps, *J Am Chem Soc* **2001**, *123*, 1596-1601; b. T. B. Rauchfuss, *Acc. Chem. Res.* **2015**, *48*, 2107–2116.

[3] a. V. Artero, G. Berggren, M. Atta, G. Caserta, S. Roy, L. Pecqueur, M. Fontecave, *Acc. Chem. Res.* **2015**, *48*, 2380-2387; b. J. A. Birrell, O. Rüdiger, E. J. Reijerse, W. Lubitz, *Joule* **2017**, *1*, 61-76.

[4] a. G. Berggren, A. Adamska, C. Lambertz, T. R. Simmons, J. Esselborn, M. Atta, S. Gambarelli, J.-M. Mouesca, E. Reijerse, W. Lubitz, T. Happe, V. Artero, M. Fontecave, *Nature* **2013**, *499*, 66–69; b. J. Esselborn, C. Lambertz, A. Adamska-Venkatesh, T. Simmons, G. Berggren, J. Nothl, J. Siebel, A. Hemschemeier, V. Artero, E. Reijerse, M. Fontecave, W. Lubitz, T. Happe, *Nat. Chem. Biol.* **2013**, *9*, 607–609.

[5] J. F. Siebel, A. Adamska-Venkatesh, K. Weber, S. Rumpel, E. Reijerse, W. Lubitz, *Biochem.* **2015**, *54*, 1474-1483.

[6] J. Noth, J. Esselborn, J. Güldenhaupt, A. Brünje, A. Sawyer, U.-P. Apfel, K. Gerwert, E. Hofmann, M. Winkler, T. Happe, *Angew. Chem. Int. Ed.* **2016**, *55*, 8396-8400.

[7] A. K. Justice, R. C. Linck, T. B. Rauchfuss, *Inorg. Chem.* **2006**, *45*, 2406-2412.

[8] D. Schilter, J. M. Camara, M. T. Huynh, S. Hammes-Schiffer, T. B. Rauchfuss, *Chem. Rev.* **2016**, *116*, 8693-8749.

[9] X. Zhao, I. P. Georgakaki, M. L. Miller, J. C. Yarbrough, M. Y. Darensbourg, *J Am Chem Soc* **2001**, *123*, 9710–9711.

[10] A. Adamska-Venkatesh, D. Krawietz, J. Siebel, K. Weber, T. Happe, E. Reijerse, W. Lubitz, *J Am Chem Soc* **2014**, *136*, 11339-11346.

[11] a. E. J. Reijerse, C. C. Pham, V. Pelmenschikov, R. Gilbert-Wilson, A. Adamska-Venkatesh, J. F. Siebel, L. B. Gee, Y. Yoda, K. Tamasaku, W. Lubitz, T. B. Rauchfuss, S. P. Cramer, *J Am Chem Soc* **2017**, *139*, 4306-4309; b. M. Winkler, M. Senger, J. Duan, J. Esselborn, F. Wittkamp, E. Hofmann, U.-P. Apfel, S. T. Stripp, T. Happe, *Nature Commun.* **2017**, *8*, 16115; c. V. Pelmenschikov, J. A. Birrell, C. C. Pham, N. Mishra, H. Wang, C. Sommer, E. Reijerse, C. P. Richers, K. Tamasaku, Y. Yoda, T. B. Rauchfuss, W. Lubitz, S. P. Cramer, *J Am Chem Soc* **2017**, *139*, 16894-16902.

[12] a. D. W. Mulder, Y. Guo, M. W. Ratzloff, P. W. King, *J Am Chem Soc* **2017**, *139*, 83-86; b. D. W. Mulder, M. W. Ratzloff, M. Bruschi, C. Greco, E. Koonce, J. W. Peters, P. W. King, *J Am Chem Soc* **2014**, *136*, 15394-15402; c. H. D. Kaesz, R. B. Saillant, *Chem. Rev.* **1972**, *72*, 231-281.

[13] N. Chongdar, J. A. Birrell, K. Pawlak, C. Sommer, E. J. Reijerse, O. Rüdiger, W. Lubitz, H. Ogata, *J Am Chem Soc* **2018**, *140*, 1057-1068.

[14] L. Yu, C. Greco, M. Bruschi, U. Ryde, L. De Gioia, M. Reiheet, *Inorg. Chem.* **2011**, *50*, 3888-3900.

[15] C. Sommer, A. Adamska-Venkatesh, K. Pawlak, J. A. Birrell, O. Rüdiger, E. J. Reijerse, W. Lubitz, *J Am Chem Soc* **2017**, *139*, 1440-1443.

[16] a. S. E. Clapham, A. Hadzovic, R. H. Morris, *Coord. Chem. Rev.* **2004**, *248*, 2201-2237; b. J. Zhang, G. Leitus, Y. Ben-David, D. Milstein, *Angew. Chem., Int. Ed.* **2006**, *45*, 1113-1115; c. A. Boddien, B. Loges, H. Junge, M. Beller, *Chemsuschem* **2008**, *1*, 751-758; d. M. Creus, A. Pordea, T. Rossel, A. Sardo, C. Letondor, A. Ivanova, I. LeTrong, R. E. Stenkamp, T. R. Ward, *Angew. Chem., Int. Ed.* **2008**, *47*, 1400-1404.

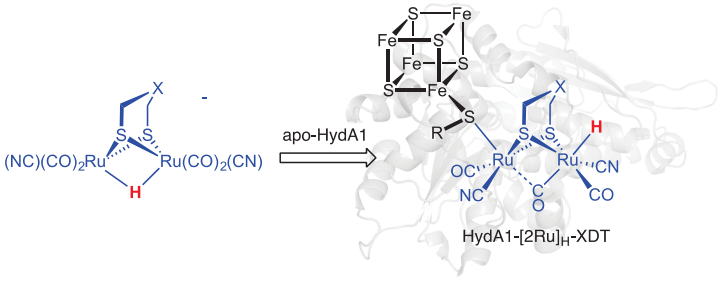

Constanze Sommer, Casseday P. Richers, Wolfgang Lubitz, Thomas B. Rauchfuss, Edward J. Reijerse**

0000 – 0000

[RuRu] Analogue of [FeFe]-Hydrogenase Traps the Key Metal Bound Hydride Intermediate in the Enzyme's Catalytic Cycle

Engine change gives the hydride: By combining artificial maturation and synthetic organoruthenium chemistry, an Ru_2 center has been installed at the active site in the [FeFe]-hydrogenase. The work reveals that the protein favors formation of terminal hydrides, that the amine cofactor uniquely allows hydrides to undergo isotopic exchange, and that the dimetallic hydrides must be redox-active for catalysis.

Supporting information

[RuRu] Analogue of [FeFe]-Hydrogenase Traps the Key Hydride Intermediate in the Enzyme's Catalytic Cycle

Constanze Sommer, Casseday P. Richers, Wolfgang Lubitz, Thomas B. Rauchfuss*, Edward J. Reijerse*

Contents

Extended experimental details: Organometallic Synthesis

$CbzN(CH_2SAc)_2$. A CH_2Cl_2 (50 mL) solution of $CbzN(CH_2Cl)_2$ (9.36 g, 3.77 x 10^{-2} mol) and solid KSAc (8.62 g, 7.54 X 10^{-2} mol) was stirred for 18 h. The crude mixture was filtered and concentrated on a rotary evaporator, leaving 11.37 g, 3.47 x 10^{-2} mol (92%) colorless oil. ^1H NMR ($CDCl_3$): δ 7.44-7.29 (m, 5H), 5.16 (s, 2H), 4.97-4.84 (overlapping singlets, 4H), 2.37 (s, 3H), 2.32 (s, 3H). $^{13}C\{^1H\}$ NMR ($CDCl_3$): δ 194.9, 194.2, 154.7, 135.5, 128.4, 128.1, 127.9, 68.04, 47.69, 47.16. Anal. Calcd for $C_{14}H_{17}NO_4S_2$: C, 51.36; H, 5.23; N, 4.28. Found: C, 51.00; H, 5.14; N 4.20. The sample for elemental analysis was purified by column chromatography.

$CbzN(CH_2SH)_2$. A MeOH (50 mL) solution of $CbzN(CH_2SAc)_2$ (11.37 g, 3.47 x 10^{-2} mol) was treated with a MeOH (50 mL) solution of NaOMe (3.75 g, 6.94 x 10^{-2} mol) at room temperature for 6 h before treating with HOAc (19.8 mL, 20.8 g, 3.47 x 10^{-1} mol). Solvent was removed, and the residual solid was extracted into Et_2O (3 x 50 mL) and re-evaporated to yield 8.36 g, 3.44 x 10^{-2} mol (99%) of a colorless oil ^1H NMR ($CDCl_3$, 20 °C): δ 7.49-7.31 (m, 5H), 5.23 (s, 2H), 4.60 (d, *J* = 9.1 Hz, 2H), 4.59 (d, *J* = 8.9 Hz, 2H), 2.30 (t, *J* = 8.7 Hz, 1H), 2.16 (t, *J* = 8.6 Hz, 1H). $^{13}C\{^1H\}$ NMR (CD_2Cl_2, 20 °C): δ 154.5, 136.7, 129.0, 128.7, 128.4, 68.31, 43.29, 42.62. Anal. Calcd for $C_{10}H_{13}NO_2S_2$: C, 49.36; H, 5.39; N, 5.76. Found: C, 49.36; H, 5.34; N, 5.56. The sample for elemental analysis was purified by column chromatography.

$Ru_2[(SCH_2)_2NCbz](CO)_6$. This preparation followed the literature procedure for the synthesis of $Ru_2(PDT)(CO)_6$ (A. K. Justice, R. C. Linck, T. B. Rauchfuss, *Inorg. Chem.* **2006**, *45*, 2406) ^1H NMR (CD_2Cl_2, 500 MHz, 20 °C): δ 7.50-7.23 (m, 5H), 5.16 (s, 2H), 4.14 (s, br, 4H). $^{13}C\{^1H\}$ NMR ($CDCl_3$, 126 MHz, 20 °C): δ 194.1, 189.1, 153.3, 135.3, 128.6, 128.5, 128.3, 68.75, 46.12, 45.99. IR (CH_2Cl_2): ν_{CO} = 2089, 2059, 2013, 1995 (sh), 1711 cm^{-1}. Anal. Calcd for $C_{16}H_{11}NO_8Ru_2S_2$: C, 31.43; H, 1.81; N, 2.29. Found: C, 31.1; H, 1.74; N, 2.26. The sample for elemental analysis was purified by column chromatography.

Deprotection of $Ru_2[(SCH_2)_2NCbz](CO)_6$ to $\{Ru_2[(SCH_2)_2NH_2](CO)_6\}OTf$. A CH_2Cl_2 (5 mL) solution of $Ru_2[(SCH_2)_2NCbz](CO)_6$ (240 mg, 3.92 x 10^{-4} mol) was treated with anisole (1.27 mL, 1.27 g, 1.18 x 10^{-2} mol) followed by triflic acid (346 µL, 589 mg, 3.92 x 10^{-3} mol). The mixture was stirred at room temperature for 18 h. Dry Et_2O (15 mL) was added to the mixture, and the reaction stirred at room temperature for an additional 3 h to convert the sticky solid to a powder. The reaction mixture was collected on a glass frit and washed with additional Et_2O (2 x 10 mL) to give 182 mg (2.90 x 10^{-4} mol (74%). ^1H NMR (CD_3CN, 500 MHz, 20 ºC): δ 7.00 (s, br, 2H), 3.77 (s, 4H). $^{13}C\{^1H\}$ NMR (CD_3CN, 126 MHz, 20 °C): δ 193.70 (br), 42.60. IR (CH_3CN): ν_{CO}

= 2099, 2071, 2024, 2008 (sh) cm^{-1}. Anal. Calcd for $C_9H_6F_3NO_9Ru_2S_3$: C, 17.23; H, 0.96; N, 2.23. Found: C, 17.40; H, 1.05; N, 2.20.

$Ru_2(ADT)(CO)_6$. A THF solution (3 mL) of $\{Ru_2[(SCH_2)_2NH_2](CO)_6\}OTf$ (100. mg, 1.59 x 10^{-4} mol) was treated with a THF solution of 1,8-bis(dimethylamino)naphthalene (34.2 mg, 1.59 x 10^{-4} mol) for 30 min. The mixture was filtered through Celite, and the solvent removed under vacuum. The orange solid was extracted with pentane, and the pentane removed under vacuum to give a yellow solid. Yield: 36.4 mg, 7.62 x 10^{-5} mol (48%). ^1H NMR (CD_3CN): δ 3.88 (m, 2H), 3.66 (m, 2H), 2.47 (s, 1H). $^{13}C\{^1H\}$ NMR (CD_3CN): δ 195.3 (br), 45.93. IR (MeCN): ν_{CO} = 2086, 2055, 2011, 1990 (sh) cm^{-1}. IR (pentane): ν_{CO} = 2086, 2056, 2015, 2003, 1993 cm^{-1}. Anal. Calcd for $C_8H_5NO_6Ru_2S_2$: C, 20.13; H, 1.06; N, 2.93. Found: C, 20.09; H, 1.02; N, 2.67.

$(Et_4N)_2[Ru_2(ADT)(CN)_2CO)_4]$. Under an inert atmosphere, a MeCN solution (3 mL) of $Ru_2(ADT)(CO)_6$ (206 mg, 4.32 x 10^{-4} mol) was treated with a MeCN solution (2 mL) of $(Et_4N)CN$ (135 mg, 8.64 x 10^{-4} mol). Gas evolved immediately, and the solution darkened. After 20 min., solvent was removed, leaving a red oily solid, which was repeatedly triturated with THF and with Et_2O to yield 201 mg, 2.74 x 10^{-4} mol (63.5%) solid. ^1H NMR (CD_3CN, 500 MHz, 20 °C): δ 3.60 (br, s, 2H), 3.38 (br, s, 2H), 3.22 (q, J = 7.3 Hz, 16H), 1.26-1.20 (m, 24H). $^{13}C\{^1H\}$ NMR (CD_3CN, 126 MHz, 20 °C): δ 209, 207.9, 140.2, 137.9, 53.4, 45.8, 8.24. IR (CH_3CN): ν_{CN} = 2086 cm^{-1}. ν_{CO} = 1980, 1938, 1902 cm^{-1}. Anal. Calcd for $C_{24}H_{45}N_5O_4Ru_2S_2$: C, 39.28; H, 6.18; N, 9.54. Found: C, 39.63; H, 6.09; N, 9.37.

Extended experimental details: Protein purification and maturation

Protein overexpression in *E.coli* and maturation of HydA1 from *Chlamydomonas reinhardtii* are based on a slightly modified previously published protocol.[1-2] The pH was adjusted prior to induction of the protein expression and the purification was performed without any dithionite. 30 mg/L Kanamycin was used as selection antibiotic throughout the expression. For the maturation the apo-protein was diluted to about 350 µM in 0.1 M Tris/HCl, 0.15 M NaCl pH 8.0 or pD 8.0. The [2Ru]-ADT/-PDT precursor was dissolved in DMSO or H_2O and added as a 2-3 times excess for 60 min. Unbound complexes were removed by a desalting column (PD-10, GE Healthcare) and the maturated proteins were concentrated (Merck Millipore, Amicon Ultra-15, 30 kDa).

Maturation under D_2 gas was performed in a rubber sealed glass vial. First the buffer of the apo-hydrogenase sample was exchanged to D_2O buffer with pD 8.0. Then, prior to addition of the precursor, this sample was incubated with D_2 gas for one hour. The first five minutes of the maturation the gas was purged continuously. Thereafter, the atmosphere was exchanged three times during one hour. The desalting column was equilibrated with D_2O buffer and the atmosphere in the anaerobic chamber contained 2.5% D_2.

Protein concentrations were determined with UV/vis spectroscopy. Titration with one equivalent thionine acetate or three equivalents dithionite resulted in the oxidized and reduced states of the proteins. When needed, the proteins were rebuffered three times in concentrators (see above).

FTIR spectroscopy and FTIR spectroelectrochemistry

FTIR spectra were obtained using Vertex 80v or IFS 66v/s FTIR spectrometer from Bruker Optics with N_2 cooled mercury cadmium telluride (MCT) detectors. Sample preparations and measurements were carried out under anaerobic conditions. Samples were immobilized between CaF_2 windows and placed in an air-tight sample holder. The sample chambers of the FTIR spectrometers are continuously purged with dry nitrogen. Spectra were recorded with 20 kHz velocity in double-sided forward backward mode with phase resolution of 16, zero filling factor of 2 and Blackman-Harris-3-term apodization. Data processing was performed using home-written scripts in the Matlab® programming environment. FTIR spectroelectrochemistry was carried out at pH 6.0 with 100 mM $K_xH_yPO_4$ as previously described but without use of redox mediators.[1] Spectra were recorded on a Bruker IFS 66v/s spectrometer with an aperture of 2.5–3 mm and thermostated sample (288 K). An equilibration time of 40-60 min was used between two applied potentials (Autolab PGSTAT101; NOVA software).

EPR spectroscopy

X-band CW EPR spectra were recorded on a Bruker Elexsys 500 EPR spectrometer equipped with a standard TE102 rectangular resonator and an Oxford ESR900 helium flow cryostat.

DFT Computational Details

Density functional theory (DFT) calculations were performed using Orca 4.0 (build: Oct. 2017).

2-electron integrals were calculated using the linint2 library http://libint.valeyev.net.

Theory Level: BP86 using the RI approximation and basis set def2-TZVP. (F. Weigend and R. Ahlrichs, *Phys. Chem. Chem. Phys.* 7, 3297 (2005)). Auxiliary basis: def2/J (F. Weigend, *Phys. Chem. Chem. Phys.* 8, 1057 (2006)).

Core potentials [def2-ECP] parameters for ruthenium were obtained from TURBOMOLE (7.0.2).

Ce-Yb(ecp-28)	M. Dolg, H. Stoll, H.Preuss, J. Chem. Phys., 1989, 90, 1730-1734
Y-Cd(ecp-28), Hf-Hg(ecp-46)	D. Andrae,U. Haeussermann, M. Dolg, H. Stoll, H. Preuss, Theor. Chim. Acta, 1990, 77, 123-141.
In-Sb(ecp-28), Tl-Bi(ecp-46)	B. Metz, H. Stoll, M. Dolg, J. Chem. Phys., 2000, 113, 2563-2569.
Te-Xe(ecp-28), Po-Rn(ecp-46)	K. A. Peterson, D. Figgen, E. Goll, H. Stoll, M. Dolg, J. Chem. Phys., 2003, 119, 11113-11123
Rb(ecp-28), Cs(ecp-46)	T. Leininger, A. Nicklass, W. Kuechle, H. Stoll, M. Dolg, A. Bergner, Chem. Phys. Lett., 1996, 255, 274-280.
Sr(ecp-28), Ba(ecp-46)	M. Kaupp, P. V. Schleyer, H. Stoll and H. Preuss, J. Chem. Phys., 1991, 94, 1360-1366.
La(ecp-46)	M. Dolg, H. Stoll, A. Savin, H. Preuss, Theor. Chim. Acta, 1989, 75, 173-194.
Lu(ecp-28)	X. Cao, M. Dolg, J. Chem. Phys., 2001, 115, 7348-7355

Supplementary Figures

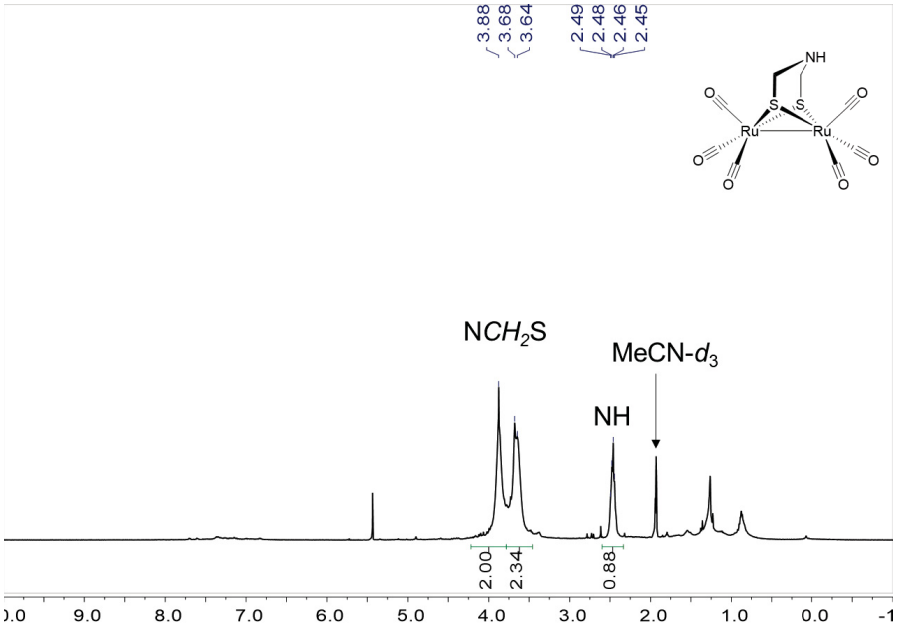

Figure S1. The ^{1}H NMR spectrum (500 MHz) of $Ru_2(ADT)(CO)_6$ in CD_3CN.

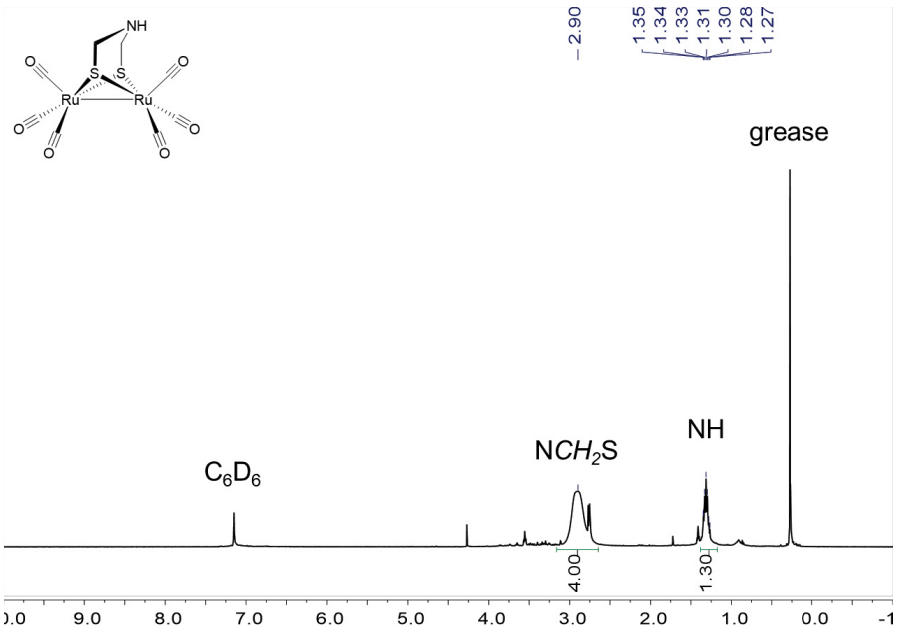

Figure S2. The ^{1}H NMR spectrum (500 MHz) of $Ru_2(ADT)(CO)_6$ in C_6D_6 solution.

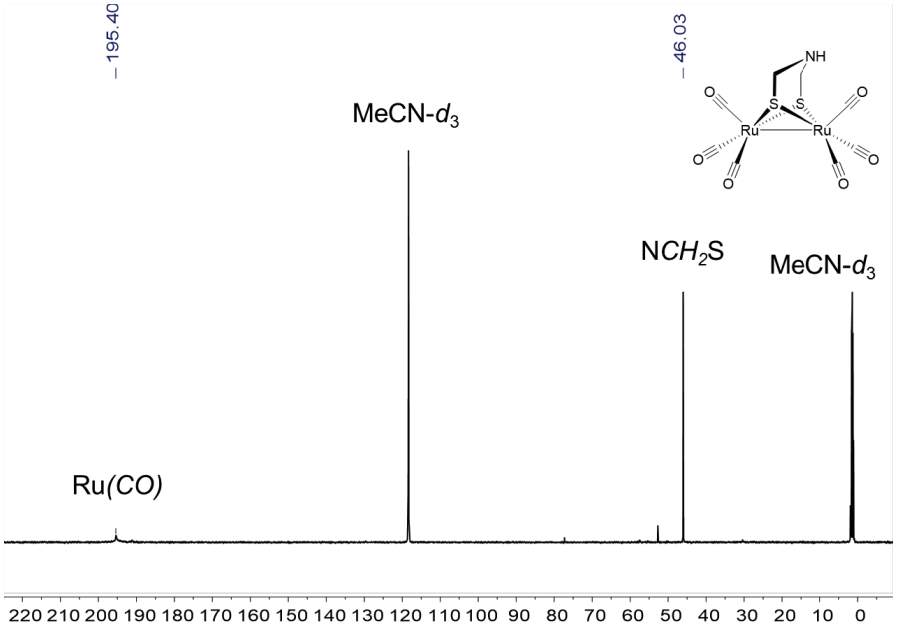

Figure S3. The $^{13}C\{^1H\}$ NMR (126 MHz) spectrum of $Ru_2(ADT)(CO)_6$ in CD_3CN solution.

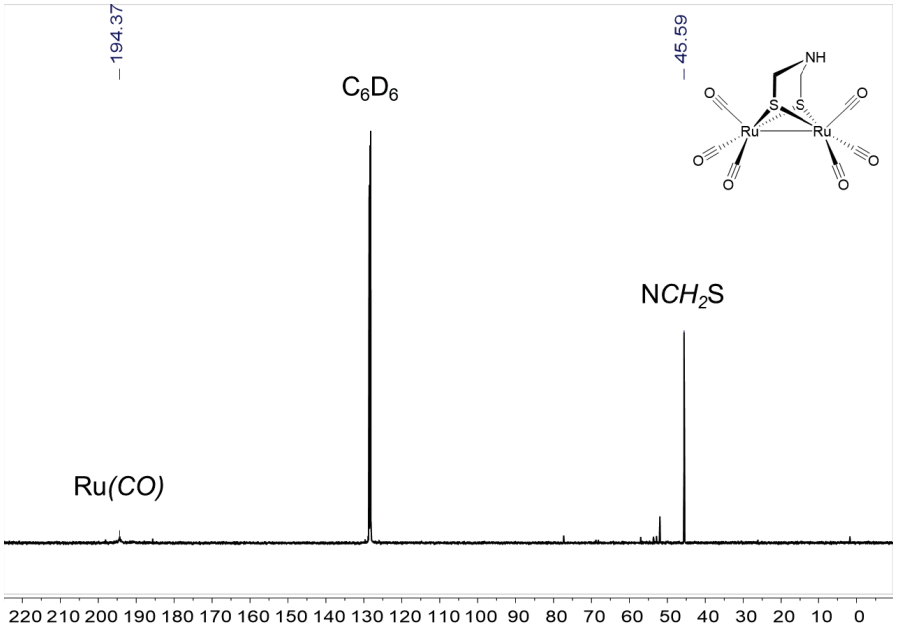

Figure S4. The $^{13}C\{^1H\}$ NMR spectrum (126 MHz) of $Ru_2(ADT)(CO)_6$ in C_6D_6 solution.

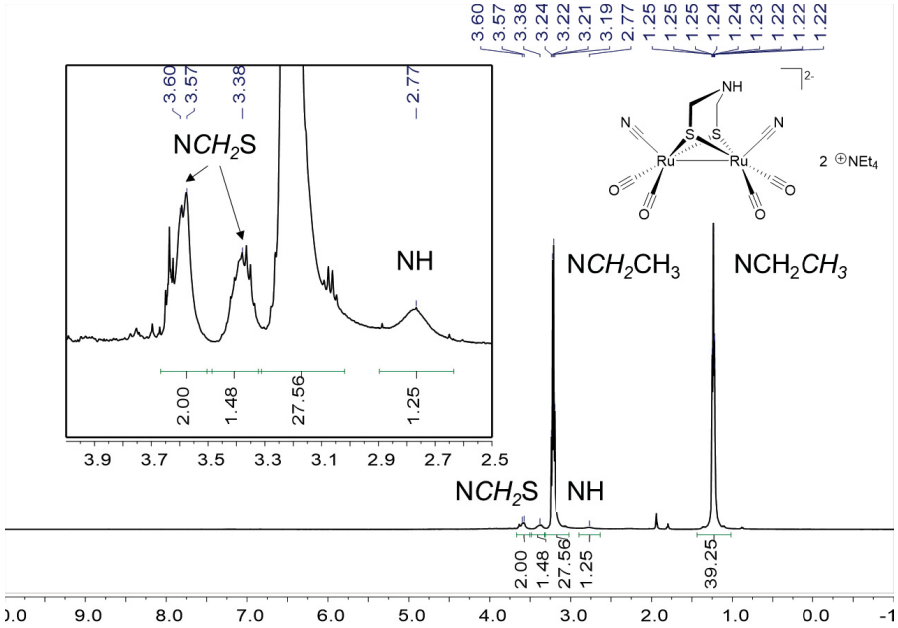

Figure S5. The ^{1}H NMR spectrum (500 MHz) of $[Ru_2(ADT)(CO)_4(CN)_2](NEt_4)_2$ in CD_3CN solution.

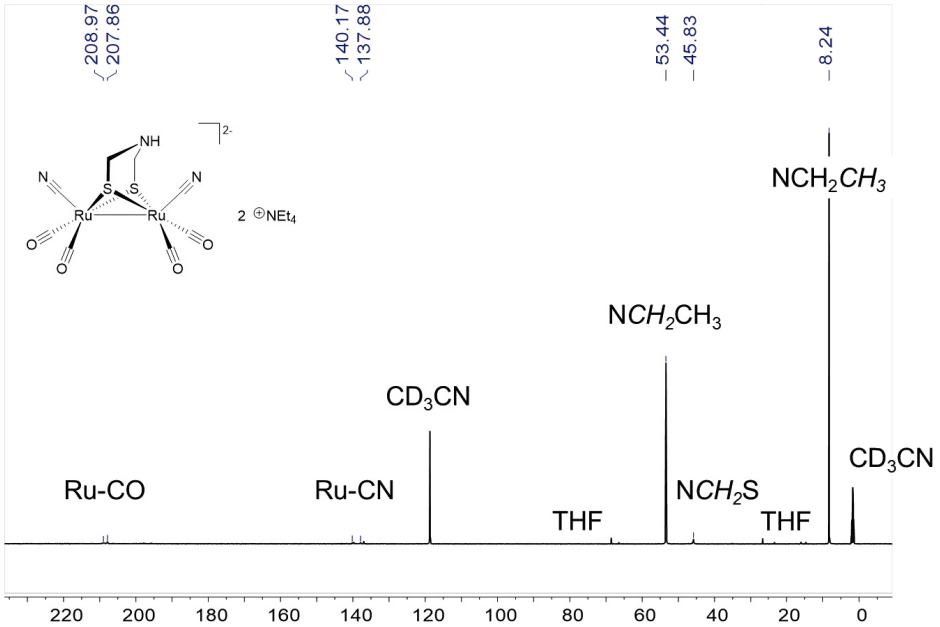

Figure S6. The $^{13}C\{^{1}H\}$ NMR spectrum (126 MHz) of $[Ru_2(ADT)(CO)_4(CN)_2](NEt_4)_2$ in CD_3CN solution.

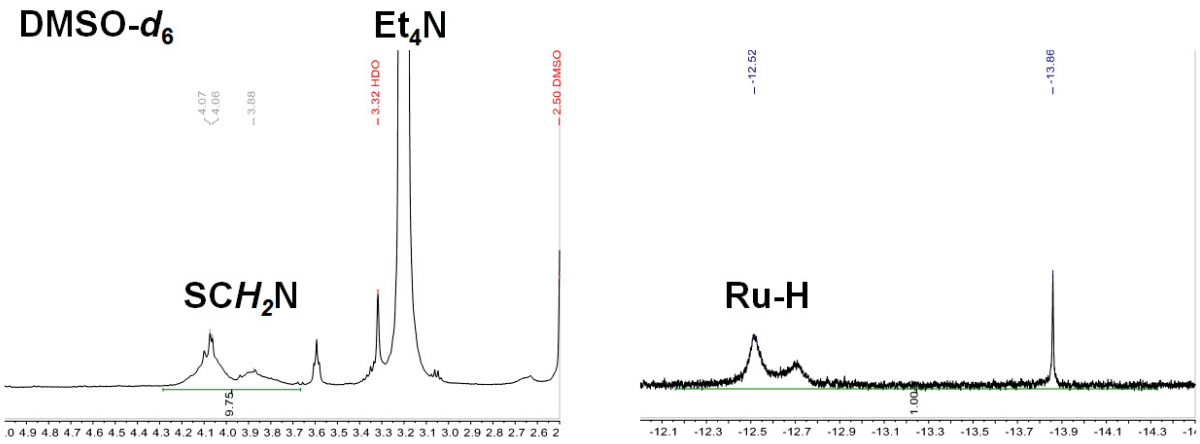

Figure S7. The ^{1}H NMR spectrum (126 MHz) of $[Ru_2(ADT)(CO)_4(CN)_2](NEt_4)_2$ + trichloroacetic acid in DMSO solution. The bridging hydride resonance occurs at -12.5 ppm.

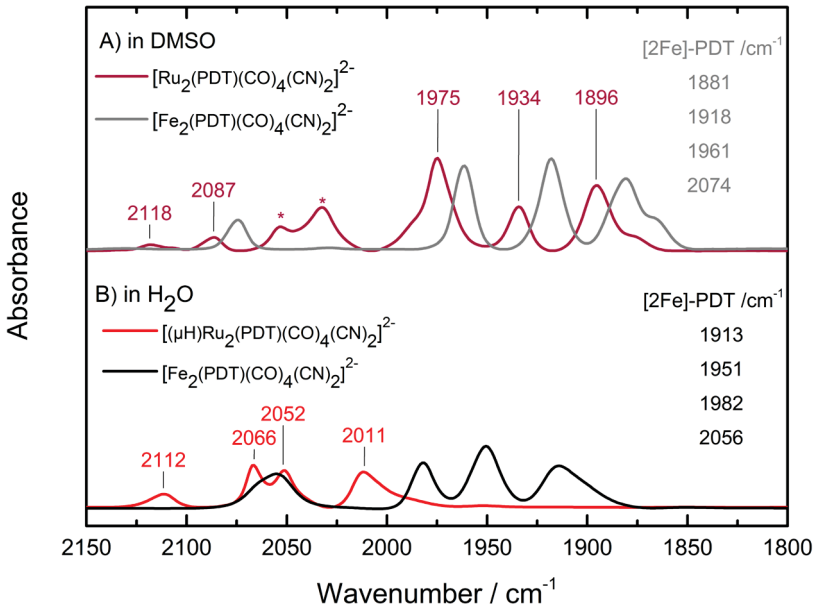

Figure S8 FTIR spectra of free [2Ru]-PDT complex dissolved in DMSO and H_2O. The features marked with asterisks originate from oxidative decomposition products. In H_2O [2Ru]-PDT shows the same bridging hydride as [2Ru]-ADT.

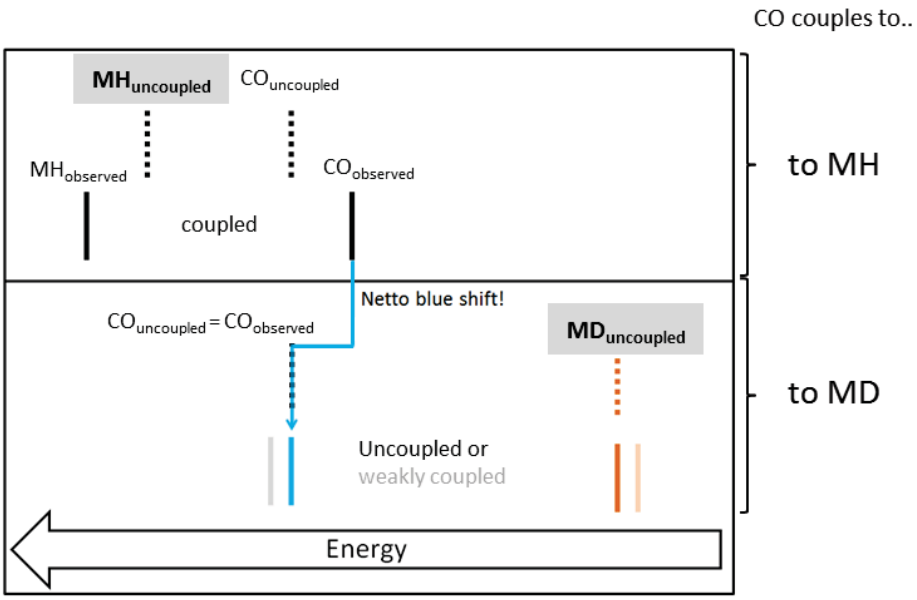

Figure S9. Coupling between metal-hydride (MH) or metal-deuteride vibration with the vibration of the CO in *trans* positon. The coupling of the CO stretch to the MH and MD vibrations depends on the relative energy of MH/MD. In case of MH being higher in energy than the μCO stretch, coupling between the MH and μCO stretch causes both bands to shift to higher and lower energies, respectively (upper part). This coupling is possible since both vibrations are in the same energy range. Through H/D exchange these vibrations become uncoupled, because the MD vibration is much lower in energy, and the μCO stretch shifts to its "uncoupled" position, i.e. to higher energy.

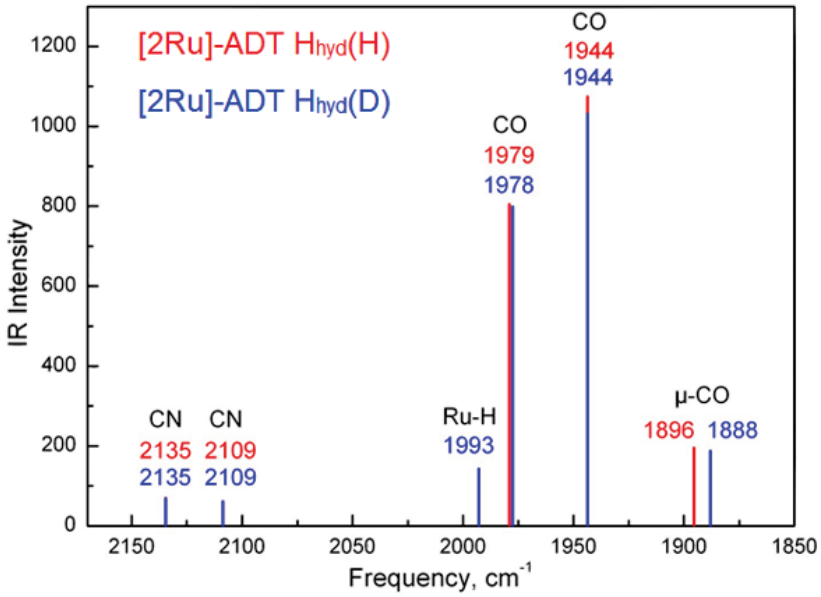

Figure S10. DFT calculated HydA1-[2Ru]$_H$-ADT H$_{hyd}$ FTIR spectrum as H$_{hyd}$(H) and H$_{hyd}$(D). Band 1888 cm^{-1} represents μCO and the band at 1993 cm^{-1} the Ru-H stretch. The corresponding Ru-D band is shifted to 1411 cm^{-1} (not shown here).

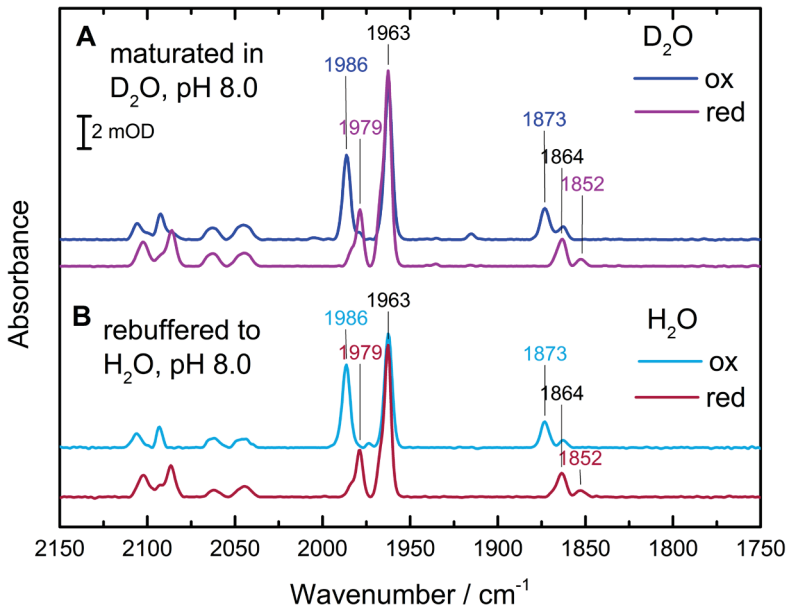

Figure S11. H/D exchange of HydA1-[2Ru]$_H$-PDT H$_{hyd}$(D) through rebuffering in H$_2$O. A Maturation in D_2O leads to blue shifted μCO at 1873 cm^{-1} (ox). **B** Rebuffering in H_2O does not increase the vibration at 1864 cm^{-1} which is the μCO vibration coupled to MH. Reduction of [4Fe-4S]$_H$ shifts most CO bands by approximately -10 cm^{-1}.

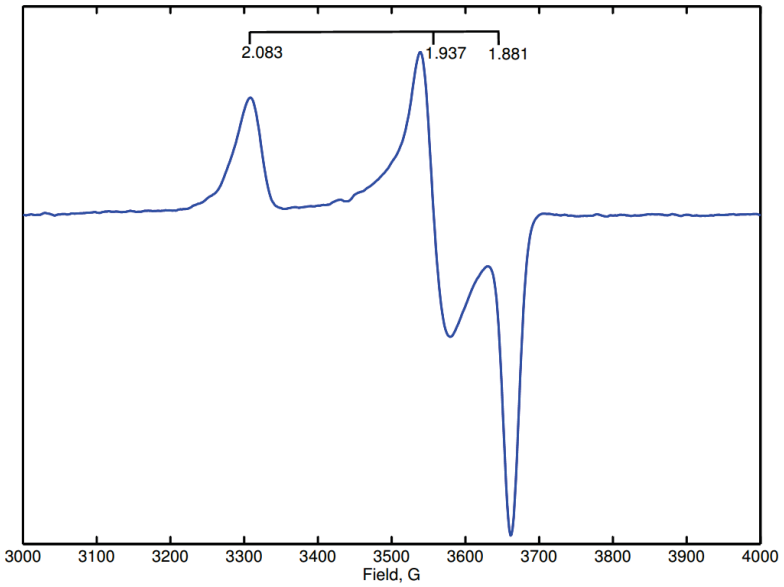

Figure S12. EPR of $[4Fe\text{-}4S]_H^+$ HydA1-$[2Ru]_H$-ADT H_{hyd}(H) at 10K. g-values are indicated. The unpaired electron is located on the $[4Fe\text{-}4S]_H$ subcluster and gives rise to an EPR spectrum consistent with a classical reduced cubane.

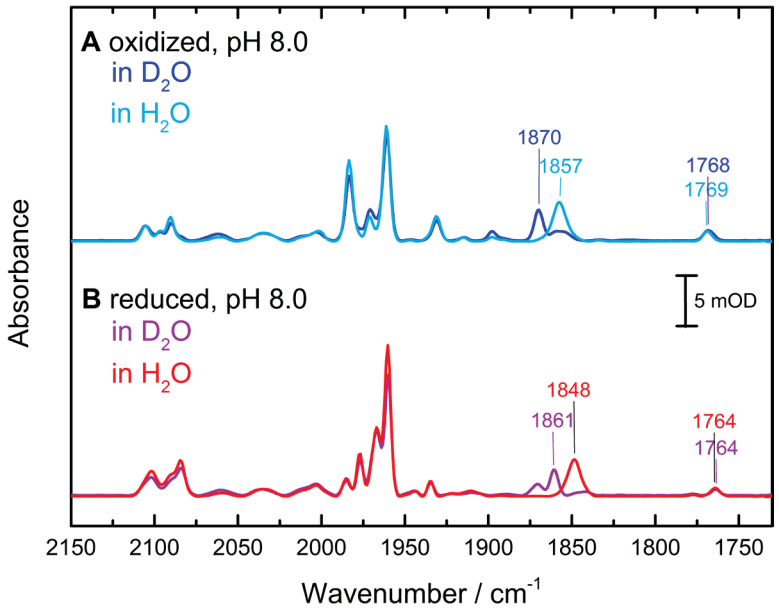

Figure S13: H/D exchange of HydA1-$[2Ru]_H$-ADT H_{hyd}(D) through rebuffering in H_2O. A Thionin-oxidized samples: Maturated in D_2O, rebuffered to H_2O **B** Dithionite-reduced samples: Maturated in D_2O, rebuffered to H_2O.

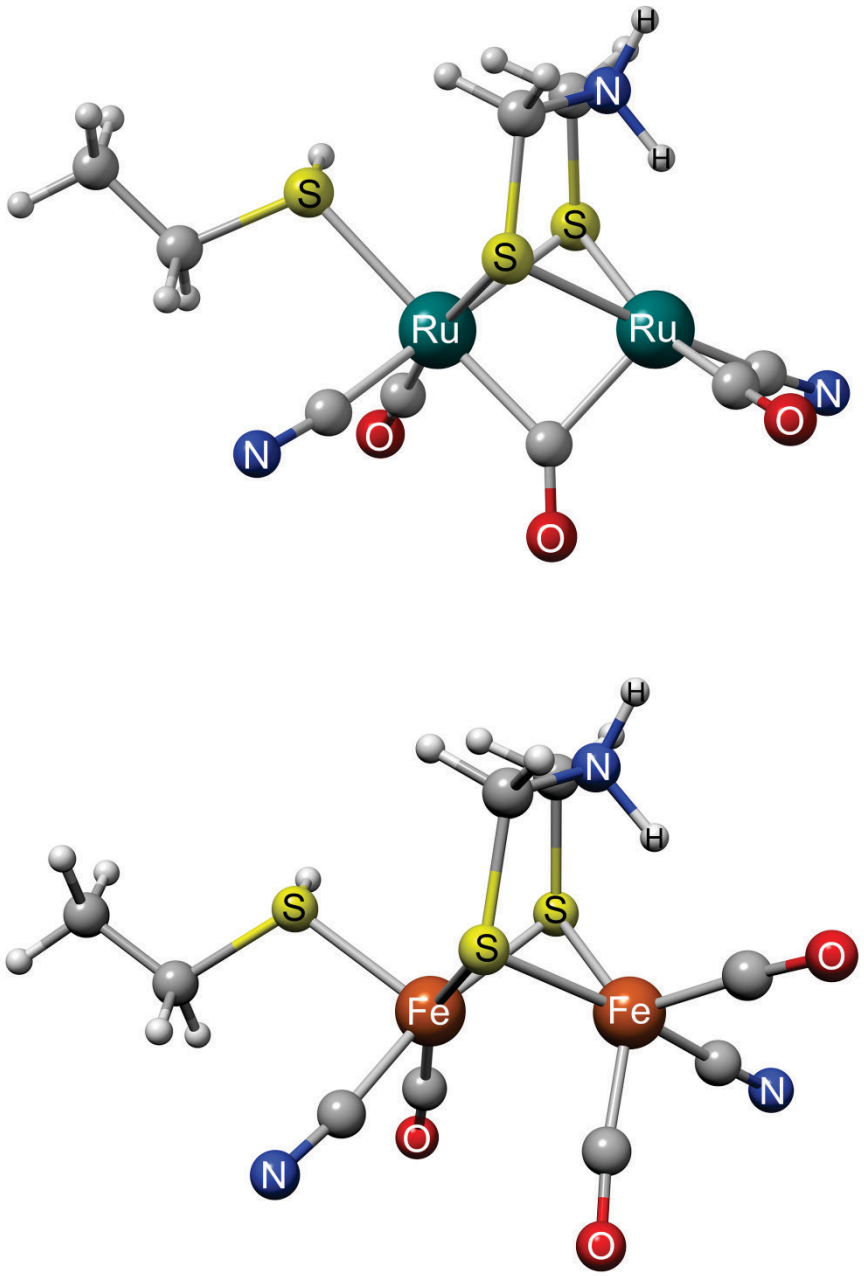

Figure S14. DFT geometry optimized structure of [2Ru]-ADT-NH_2^+ and [2Fe]-ADT-NH_2^+. The $[4Fe\text{-}4S]_H$ cluster is truncated and represented by $H_3C\text{-}CH_2\text{-}SH$. DFT calculations in Orca 4.0 as specified in DFT computational details.

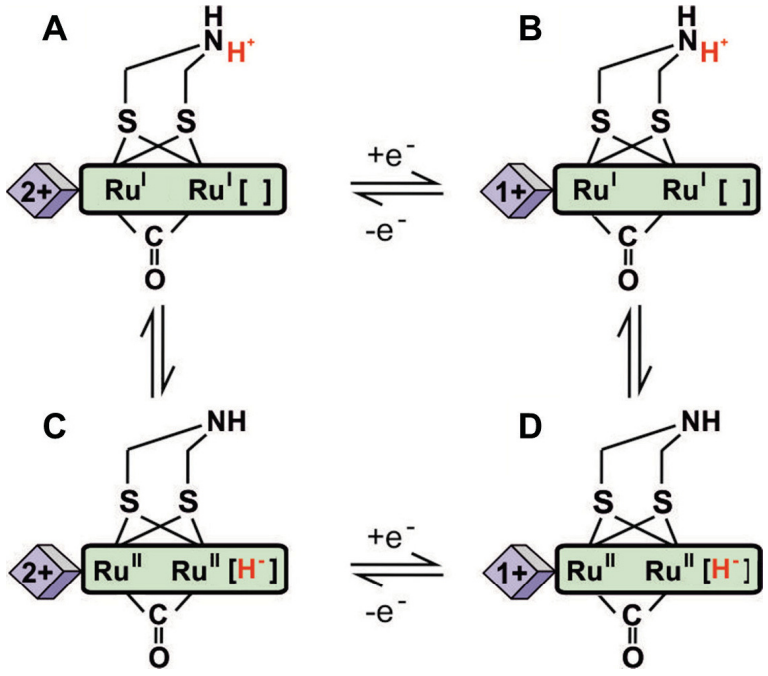

Figure S15: Observed redox states in HydA1-[2Ru]$_H$-ADT. Species **A** and **B** are the reduced states with a [Ru(I)Ru(I)] core being in a fast equilibrium with species **C** and **D**, the hydride states with a [Ru(II)Ru(II)] configuration. Redox events take place exclusively in the [4Fe-4S]$_H$ cluster.

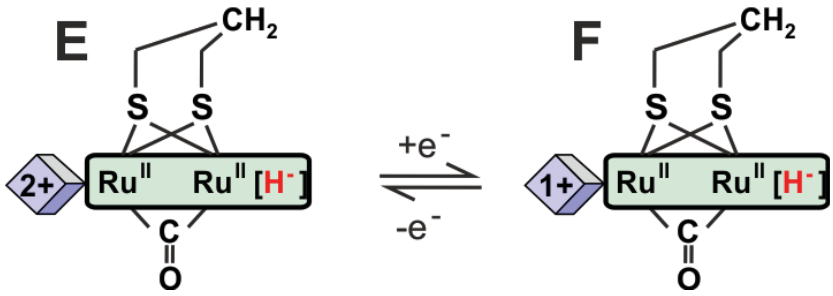

Figure S16: Observed redox states in HydA1-[2Ru]$_H$-PDT. Species **E** and **F** are identical to species **C** and **D** for **HydA1-[2Ru]$_H$-ADT** in figure S15. Redox events take place exclusively in the [4Fe-4S]$_H$ cluster.

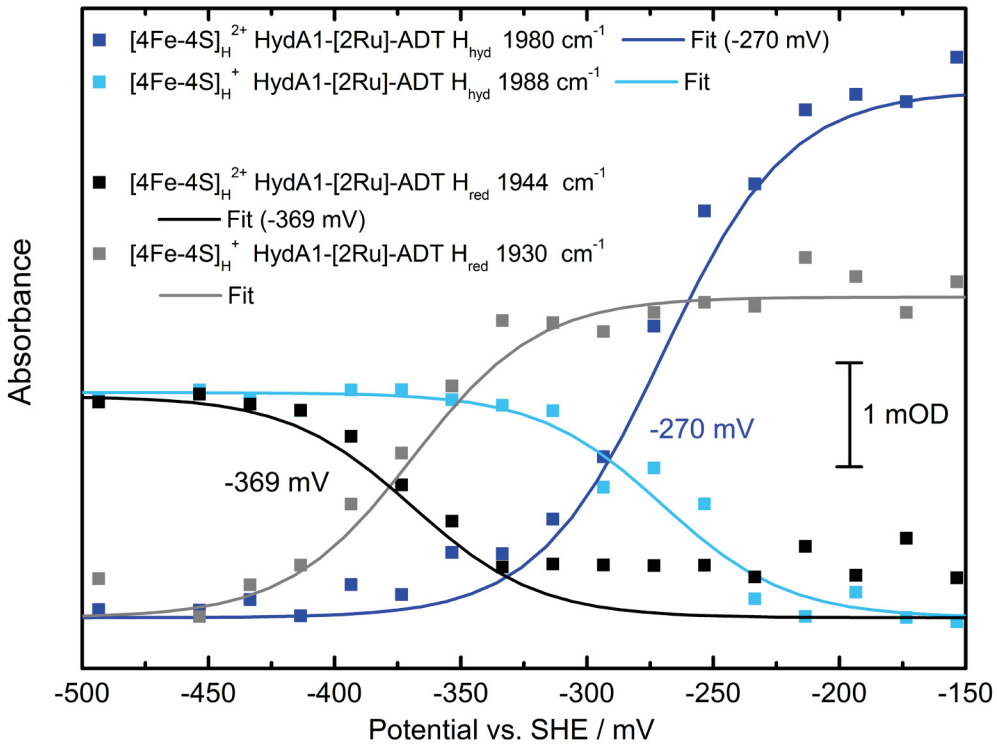

Figure S17. FTIR-spectroelectrochemistry on HydA1-[2Ru]$_H$-ADT at pH 6.0. The 1980 cm^{-1} band represents [4Fe-4S]$_H^{2+}$ HydA1-[2Ru]$_H$-ADT H_{hyd} while the 1988 cm^{-1} band represents the reduced [4Fe-4S]$_H^{+}$ HydA1-[2Ru]$_H$-ADT H_{hyd}. The 1944 cm^{-1} band represents [4Fe-4S]$_H^{2+}$ HydA1-[2Ru]$_H$-ADT H_{red} while the 1930 cm^{-1} band represents the reduced [4Fe-4S]$_H^{+}$ HydA1-[2Ru]$_H$-ADT H_{red}. Spectra are taken at 288 K with a resolution of 2 cm^{-1}.

REFERENCES

[1] C. Sommer, A. Adamska-Venkatesh, K. Pawlak, J. A. Birrell, O. Rüdiger, E. J. Reijerse, W. Lubitz, *Journal of the American Chemical Society* **2017**, *139*, 1440-1443.

[2] J. M. Kuchenreuther, C. S. Grady-Smith, A. S. Bingham, S. J. George, S. P. Cramer, J. R. Swartz, *PLoS One* **2010**, *5*, e15491-e15491.

5. CONCLUSIONS AND OUTLOOK

The yield of HydA1 from *Chlamydomonas reinhardtii* in the heterologous overexpression in *E. coli* could be improved to an average of 120 mg/l (about a factor of 2.5 compared to the previous lab protocol). With this improved yield more protein consuming methods, like nuclear resonance vibrational resonance spectroscopy (NRVS) and ^{1}H NMR can be established for [FeFe] hydrogenases. HydA1 could be successfully maturated with many different precursors leading to highly concentrated samples that were used in my thesis for EPR, ^{1}H NMR, FTIR, FTIR-spectroelectrochemistry, electrochemistry and biological assays.

HydA1-ADT was studied over a pH range from 5-10 with FTIR-spectroelectrochemistry uncovering the first essential protonation step in the catalytic cycle which is accompanied by a proton coupled electronic rearrangement with a pK_a of 7.2. It prepares the H-cluster for a second reduction at approximately the same potential as the first one. The calculated midpoint potentials are close to the potential of the $H_2/ 2H^+$ potential and range between -375 and -418 mV vs. SHE. With these midpoint potentials we presume that the energy landscape during the catalytic cycle is relatively flat, explaining the high turnover rates of 560 H_2/s with a pH optimum around 7.1. For hydrogenase inspired molecular catalyst this knowledge can be used in DFT calculations that predict possible molecular structures that fulfil this smooth energy landscape.

HydA1 maturated with [2Fe]-ADT was studied for the first time at room temperature in concentrated liquid solution with paramagnetic ^{1}H NMR spectroscopy. Despite the large size of HydA1 (48 kDa) ^{1}H NMR spectroscopy could be introduced as new and useful technique in [FeFe] hydrogenase research. It is possible to obtain information on the interaction between the $[4Fe\text{-}4S]_H$ cluster and the two iron site and follow the reactants directly under physiological conditions. The methylene protons of the ligand bridge could be distinguished from the β-CH_2 protons using a deuterated precursor complex. With the mutant HydA1-

C169A the terminal hydride which resonates at -9.6 ppm could be identified, which was previously only detected in frozen solutions (using NRVS) or in FTIR through the coupled vibration of the μCO ligand in *trans* position at ambient temperatures. ^{1}H NMR spectroscopy can also provide insight into the diamagnetic (EPR silent) states of the catalytic cycle. Furthermore sequence specific assignments can be obtained. For the diamagnetic states H_{red}, $H_{red}H^{+}$ and H_{sred}, optimized stabilization procedures, e.g. special mutants or altered precursors still need to be developed. Another idea is to engineer a new NMR measuring tube. Controlling the potential as well as a continuous buffer exchange over a dialysis membrane would help to stabilize redox states in the native hydrogenase.

^{1}H NMR spectroscopy for [FeFe] hydrogenases was for the first time applied to a S-to-Se substituted $[2Fe]_H$ site. It could be shown that the selenium substitution results in a reduced spin density on the bridging ligand. Selenium could also be incorporated via reconstitution in the cubane cluster. In the oxidized cubane cluster the effect of selenium is different. More spin density is transported to the irons leading to an increased chemical shift of the β-CH_2 protons. In the reduced state of the apo-enzyme a S= 7/2 high spin state could be detected with CW EPR. As soon as the $[4Fe\text{-}4Se]_H$ cluster is coupled to the $[2Fe]_H$ subsite spin cross over results in a S= 1/2 system.

With a new synthesis strategy to produce the aza-propane-diselenate bridging ligand within the precursor complex it was possible to achieve for the first time fully active [FeFe] hydrogenases with a modified active site. The selenium containing hydrogenase *Cp*I could be crystallized and the presence of the selenium atoms in the bridge were confirmed. The increase charge density of Se compared to S resulted in a redshifts of the H-cluster ligands. Unfortunately the selenium containing enzymes show stronger oxygen sensitivity than the native counterparts. With this study it was shown, that modifications can be applied without losing enzymatic activity.

After many modifications in the bridging ligand of the precursor complexes the question whether the irons could be exchanged by another metal remained. Of special interest is ruthenium that is used for inorganic molecular hydrogen catalysts. The maturation of HydA1 with [2Ru]-ADT and [2Ru]-PDT was successful and resulted in the first [RuRu] hydrogenases. For the procedure of artificial maturation this means that the metal is not an integral part of the recognition process. Both precursors lead to the formation of stable terminal hydrides, although the precursors in solution prefer a hydride in the bridging position. Here the structuring effect of the protein backbone becomes apparent. Unfortunately no activity could be measured for the [RuRu] hydrogenases. The Ru-H bond seems to be a thermodynamic sink. By altering the first ligand sphere around the rutheniums it might be possible to alter and activate the Ru-H bond and to obtain an active [RuRu] hydrogenase. As soon as activity can be measured studies on oxygen tolerance could be performed. This might give new information about the mechanism of the oxygen attack at the H-cluster.

The first successful metal exchange in the H-cluster of a [FeFe] hydrogenase causes to wonder if iron is Natures choice because of its abundant reserves. This question will be addressed in future studies by synthesizing precursor complexes containing different, rare metals and test the activity of the resulting hydrogenases.

6. REFERENCES

[1] C. Janiak, *Nichtmetallchemie, Vol. 3*, Aachen, **2007**.

[2] N. Armaroli, V. Balzani, *ChemSusChem* **2011**, *4*, 21-36.

[3] Arbeitsgruppe Energiebilanzen, **2017**, Bruttostromerzeugung in Deutschland 2016.

[4] CDU Deutschland, CSU Landesleitung, SPD, Koalitionsvertrag, **2013**, Deutschlands Zukunft Gestalten Koalitionsvertrag zwischen CDU, CSU und SPD.

[5] R. Cammack, M. Frey, R. Robson, *Hydrogen as a Fuel: Learning from Nature*, Taylor & Francis, London, **2001**.

[6] a) P. M. Vignais, B. Billoud, *Chem.Rev.* **2007**, *107*, 4206-4272; b) W. Lubitz, H. Ogata, O. Rüdiger, E. Reijerse, *Chem.Rev.* **2014**, *114*, 4081-4148.

[7] A. Melis, T. Happe, *Plant Physiology* **2001**, *127*, 740-748.

[8] C. Greening, A. Biswas, C. R. Carere, C. J. Jackson, M. C. Taylor, M. B. Stott, G. M. Cook, S. E. Morales, *The ISME Journal* **2016**, *10*, 761-777.

[9] N. Chongdar, J. A. Birrell, K. Pawlak, C. Sommer, E. J. Reijerse, O. Rüdiger, W. Lubitz, H. Ogata, *J. Am. Chem. Soc.* **2018**, *140*, 1057-1068.

[10] B. R. Glick, W. G. Martin, S. M. Martin, *Canadian Journal of Microbiology* **1980**, *26*, 1214-1223.

[11] A. I. Krasna, *Enzyme Microb.Technol.* **1979**, *1*, 165-172.

[12] A. J. Cornish, K. Gärtner, H. Yang, J. W. Peters, E. L. Hegg, *Journal of Biologial Chemistry* **2011**, *286*, 38341-38347.

[13] a) G. Goldet, C. Brandmayr, S. T. Stripp, T. Happe, C. Cavazza, J. C. Fontecilla-Camps, F. A. Armstrong, *J. Am. Chem. Soc.* **2009**, *131*, 14979-14989; b) J. Cohen, K. Kwiseon, P. King, M. Seibert, K. Schulten, *Structure* **2005**, *13*, 1321-1329.

[14] M. C. Posewitz, P. W. King, S. L. Smolinski, L. Zhang, M. Seibert, M. L. Ghirardi, *J Biol Chem.* **2004**, *279*, 25711-25720.

[15] E. Pilet, Y. Nicolet, C. Mathevon, T. Douki, J. C. Fontecilla-Camps, M. Fontecave, *FEBS Letters* **2009**, *583*, 506-511.

[16] Y. Nicolet, A. Pagnier, L. Zeppieri, L. Martin, P. Amara, J. C. Fontecilla-Camps, *ChemBioChem* **2015**, *16*, 397-402.

[17] Y. Nicolet, J. K. Rubach, M. C. Posewitz, P. Amara, C. Mathevon, M. Atta, M. Fontecave, J. C. Fontecilla-Camps, *J Biol Chem.* **2008**, *283*, 18861-18872.

[18] a) J. M. Kuchenreuther, W. K. Myers, T. A. Stich, S. J. George, Y. Nejatyjahromy, J. R. Swartz, R. D. Britt, *Science* **2013**, *342*, 472-475; b) J. M. Kuchenreuther, S. A. Shiigi, J. R. Swartz, *Methods Mol Biol.* **2014**, *1122*, 49-72.

[19] D. L. M. Suess, C. C. Pham, I. Bürstel, J. R. Swartz, S. P. Cramer, R. D. Britt, *J. Am. Chem. Soc.* **2016**, *138*, 1146-1149.

[20] J. M. Kuchenreuther, R. D. Britt, J. R. Swartz, *Plos one* **2012**, *7*, 45850.

[21] a) S. E. McGlynn, E. M. Shepard, M. A. Winslow, A. V. Naumov, K. S. Duschene, M. C. Posewitz, W. E. Broderick, J. W. Peters, *FEBS Letters* **2008**, *582*, 2183-2187; b) E. M. Shepard, S. E. McGlynn, A. L. Bueling, C. S. Grady-Smith, S. J. George, M. A. Winslow, S. P. Cramer, J. W. Peters, J. B. Broderick, *PNAS* **2010**, *107*, 10448-10453.

[22] V. Artero, G. Berggren, M. Atta, G. Caserta, S. Roy, L. Pecqueur, M. Fontecave, *Acc Chem Res* **2015**, *48*, 2380-2387.

[23] E. M. Shepard, A. S. Byer, P. Aggarwal, J. N. Betz, A. G. Scott, K. A. Shisler, R. J. Usselman, G. R. Eaton, S. S. Eaton, J. B. Broderick, *Biochemistry* **2016**, *56*, 3234-3247.

[24] G. Caserta, L. Pecqueur, A. Adamska-Venkatesh, C. Papini, S. Roy, V. Artero, M. Atta, E. Reijerse, W. Lubitz, *Nature Chemical Biology* **2017**, *13*, 779-784.

[25] G. Voordouw, J. E. Walker, S. Brenner, *Eur. J. Biochem.* **1985**, *148*, 509-514.

[26] G. Voordouw, W. R. Hagen, M. K. Krüse-Wolters, v. B.-A. A., C. Veeger, *Eur. J. Biochem.* **1987**, *162*, 31-36.

[27] D. W. Mulder, E. S. Boyd, R. Sarma, R. K. Lange, J. A. Endrizzi, J. B. Broderick, J. W. Peters, *Nature* **2010**, *465*, 248-252.

[28] C. J. Schwartz, J. L. Giel, T. Patschkowski, C. Luther, F. Ruzicka, H. Beinert, P. J. Kiley, *PNAS* **2001**, *98*, 14895-14900.
[29] M. K. Akhtar, P. R. Jones, *Appl Microbiol Biotechnol* **2008**, *78*, 853-862.
[30] D. W. Mulder, D. O. Ortillo, D. J. Gardenghi, A. V. Naumov, S. S. Ruebush, R. K. Szilagyi, B. Huynh, J. B. Broderick, J. W. Peters, *Biochemistry* **2009**, *48*, 6240-6248.
[31] J. M. Kuchenreuther, C. S. Grady-Smith, A. S. Bingham, S. J. George, S. P. Cramer, J. R. Swartz, *Plos one* **2010**, *5*, 1-7.
[32] a) G. Berggren, A. Adamska, C. Lambertz, T. R. Simmons, J. Esselborn, M. Atta, F. Mouesca J.M, E. Reijerse, W. Lubitz, T. Happe, V. Artero, M. Fontecave, *Nature* **2013**, *499*, 66-70; b) J. Esselborn, C. F. Lambertz, A. F. Adamska-Venkatesh, T. F. Simmons, G. F. Berggren, J. F. Noth, J. F. Siebel, A. F. Hemschemeier, V. F. Artero, E. J. Reijerse, M. Fontecave, W. Lubitz, T. Happe, *Nature Chemical Biology* **2013**, *9*, 607-610.
[33] J. A. Birrell, K. Wrede, K. Pawlak, P. Rodríguez-Maciá , O. Rüdiger, E. J. Reijerse, W. Lubitz, *Isr. J. Chem.* **2016**, *56*, 852-863.
[34] S. P. J. Albracht, W. Roseboom, E. C. Hatchikian, *J. Biol. Inorg. Chem.* **2006**, *11*, 88-101.
[35] A. Adamska-Venkatesh, D. Krawietz, J. F. Siebel, K. Weber, T. Happe, E. Reijerse, W. Lubitz, *J.Am.Chem.Soc.* **2014**, *136*, 11339-11346.
[36] A. Adamska, A. Silakov, C. Lambertz, O. Rüdiger, T. Happe, E. Reijerse, W. Lubitz, *Angew.Chem.Int.Ed.* **2012**, *51*, 11458-11462.
[37] Y. Nicolet, A. L. De Lacey, X. Vernède, V. M. Fernandez, C. E. Hatchikian, J. C. Fontecilla-Camps, *Journal of American Chemical Society* **2001**, *123*, 1596-1601.
[38] D. W. Mulder, Y. Guo, M. W. Ratzloff, P. W. King, *J.Am.Chem.Soc.* **2017**, *139*, 83-86.
[39] A. R. Finkelmann, H. M. Senn, M. Reiher, *Chem.Sci.* **2014**, *5*, 4474-4482.
[40] P. Knörzer, A. Silakov, C. E. Foster, F. A. Armstrong, W. Lubitz, T. Happe, *J Biol Chem.* **2012**, *287*, 1489-1499.
[41] L. Kertess, A. Adamska-Venkatesh, P. Rodríguez-Maciá, O. Rüdiger, W. Lubitz, T. Happe, *Chem.Sci.* **2017**, *8*, 8127-8137.
[42] O. Lampret, A. Adamska-Venkatesh, H. Konegger, F. Wittkamp, U. P. Apfel, E. J. Reijerse, W. Lubitz, O. Rüdiger, T. Happe, M. Winkler, *J. Am. Chem Soc.* **2017**, *139*, 18222-18230.
[43] E. J. Reijerse, C. C. Pham, V. Pelmenschikov, R. Gilbert-Wilson, A. Adamska-Venkatesh, J. F. Siebel, L. B. Gee, Y. Yoda, K. Tamasaka, W. Lubitz, T. B. Rauchfuss, S. P. Cramer, *Journal of American Chemical Society* **2017**, *139*, 4306-4309.
[44] M. Winkler, M. Senger, J. Duan, J. Esselborn, F. Wittkamp, E. Hofmann, U. P. Apfel, S. T. Stripp, T. Happe, *Nat.Commun.* **2017**, *8*, 16115.
[45] P. Chernev, C. Lambertz, A. Brünje, N. Leidel, K. G. Sigfridsson, R. Kositzki, C. H. Hsieh, S. Yao, R. Schiwon, M. Driess, C. Limberg, T. Happe, M. Haumann, *Inorg.Chem.* **2014**, *53*, 12164-12177.
[46] H. D. Kaesz, R. B. Saillant, *Chem.Rev.* **1972**, *72*, 231-281.
[47] P. Rodríguez-Maciá, K. Pawlak, O. Rüdiger, E. Reijerse, W. Lubitz, J. A. Birrell, *J. Am. Chem. Soc.* **2017**, *139*, 15122-15134.
[48] A. Silakov, B. Wenk, E. Reijerse, S. P. J. Albracht, W. Lubitz, *J Biol Inorg Chem* **2009**, *14*, 301-313.
[49] C. E. Foster, T. Krämer, A. F. Wait, A. Parkin, D. P. Jennings, T. Happe, J. E. McGrady, F. A. Armstrong, *J. Am. Chem. Soc.* **2012**, *134*, 7553-7557.
[50] W. Roseboom, A. L. De Lacey, V. M. Fernandez, C. E. Hatchikian, S. P. J. Albracht, *J. Biol. Inorg. Chem.* **2006**, *11*, 102-118.
[51] A. J. Pierik, M. Hulstein, W. R. Hagen, S. P. J. Albracht, *Eur.J.Biochem.* **1998**, *258*, 572-578.
[52] J. F. Siebel, A. Adamska-Venkatesh, E. Reijerse, W. Lubitz, *Biochemistry* **2015**, *54*, 1474-1483.
[53] A. Adamska-Venkatesh, T. R. Simmons, J. F. Siebel, V. Artero, M. Fontecave, E. Reijerse, W. Lubitz, *Phys.Chem.Chem.Phys* **2015**, *17*, 5421-5430.

[54] a) R. Malkin, J. C. Rabinowitz, *Biochemical and Biophysical Research Communications* **1966**, *23*, 822-827; b) J. Gaillard, J. M. Moulis, P. Auric, J. Meyer, *Biochemistry* **1986**, *25*, 464-468; c) J. Gaillard, J. M. Moulis, J. Meyer, *Inorg.Chem.* **1987**, *26*, 320-324; d) J. Noth, J. Esselborn, J. Güldenhaupt, A. Brünje, A. Sawyer, U. P. Apfel, K. Gerwert, E. Hofmann, M. Winkler, T. Happe, *Angew.Chem.Int.Ed.* **2016**, *55*, 8396-8400; e) J. Meyer, J. M. Moulis, *Biochemical and Biophysical Research Communications* **1981**, *103*, 667-673.

[55] R. Gilbert-Wilson, J. F. Siebel, A. Adamska-Venkatesh, C. C. Pham, E. Reijerse, H. Wang, S. P. Cramer, W. Lubitz, *J. Am. Chem. Soc.* **2015**, *137*, 8998-9005.

[56] C. C. Page, C. C. Moser, X. Chen, P. L. Dutton, *Nature* **1999**, *402*, 47-52.

[57] G. Hong, R. Patcher, *ACS Chem.Biol.* **2012**, *7*, 1268-1275.

[58] T. Lautier, P. Ezanno, C. Baffert, V. Fourmond, L. Cournac, J. C. Fontecilla-Camps, P. Soucaille, P. Bertrand, I. Meynial-Salles, C. L,ger, *Faraday Discuss* **2011**, *148*, 385-407.

[59] M. L. Ghirardi, R. K. Togasaki, M. Seibert, *Appl Biochem Biotechnol.* **1997**, *63*, 141.

[60] M. Seibert, T. Y. Flynn, M. L. Ghirardi, in *Biohydrogen II* (Eds.: J. Miyake, T. Matsunaga, A. S. Pietro), Pergamon, Oxford, **2001**, pp. 67-77.

[61] J. A. Birrell, O. Rüdiger, E. J. Reijerse, W. Lubitz, *Joule* **2017**, *1*, 61-76.

[62] J. F. Siebel, Heinrich-Heine Universität (Düsseldorf), **2015**.

[63] A. Silakov, C. Kamp, E. Reijerse, T. Happe, W. Lubitz, *Biochemistry* **2009**, *48*, 7780-7786.

[64] J. Noth, R. Kositzki, K. Klein, M. Winkler, M. Haumann, T. Happe, *Scientific Reports* **2015**, *5*, 13978.

[65] H. Beinert, R. H. Holm, E. Münck, *Science* **1997**, *277*, 653-659.

[66] J. C. Tsibris, M. J. Namtvedt, I. C. Gunsalus, *Biochem Biophys Res Commun.* **1968**, *30*, 323-327.

[67] B. Holton, X. Wu, A. I. Tsapin, D. M. Kramer, R. Malkin, T. Kallas, *Biochemistry* **1996**, *35*, 15485-15493.

[68] a) K. A. Johnson, P. S. Brereton, M. F. J. M. Verhagen, L. Calzolai, G. N. La Mar, M. W. W. Adams, I. J. Amster, *J. Am. Chem. Soc.* **2001**, *123*, 7935-7936; b) S. Rumpel, J. F. Siebel, M. Diallo, C. Farès, E. J. Reijerse, W. Lubitz, *ChemBioChem* **2015**, *16*, 1663-1669.

[69] K. Nakamoto, *Infrared Spectra of Inorganic and Coordination Compounds*, 2nd edition ed., Wiley-Interscience, New York, **1970**.

[70] P. R. Griffiths, J. A. de Haseth, *Fourier Transform Infrared Spectrometry, Vol. 2nd*, John Wiley & Sons. Inc., Hoboken, New Jersey, **2007**.

[71] A. Barth, *Biochimica et Biophysica Acta* **2007**, *1767*, 1073-1101.

[72] S. E. Glassford, B. Byrne, S. G. Kazarian, *Biochimica et Biophysica Acta* **2013**, *1834*, 2849-2858.

[73] K. Gerwert, *Biol.Chem.* **1999**, *380*, 931-935.

[74] S. Krimm, J. Bandekar, *Advances in Protein Chemistsry* **1986**, *39*, 181-364.

[75] S. Sonar, C. P. Lee, M. Coleman, N. Patel, X. Liu, T. Marti, H. Gobind Khorana, U. L. RajBhandary, K. J. Rothschild, *Nature Structural Biology* **1994**, *1*, 512-517.

[76] S. W. Englander, N. R. Kallenbach, *Quarterly Review of Biophysics* **1984**, *16*, 521-655.

[77] T. Liu, X. Wang, C. Hoffmann, D. L. DuBois, R. Morris Bullock, *Angew.Chem.Int.Ed.* **2014**, *53*, 5300-5304.

[78] P. J. Dyson, J. S. McIndoe, in *Transition Metal Carbonyl Cluster Chemistry*, Gordon and Breach Science Publishers, Amsterdam, **2000**, pp. 43-60.

[79] J. P. Allen, in *Biophysical Chemistry*, Wiley-Blackwell, Chichester, UK, **2008**, pp. 344-372.

[80] a) F. Bloch, *Phys. Rev.* **1946**, *70*, 460-474; b) M. H. Levitt, *Spin dynamics* second edition ed., John Wiley & Sons, Ltd, **2008**.

[81] H. Cheng, J. L. Markley, *Annu. Rev. Biophys. Biomol. Struct.* **1995**, *24*, 209-237.

[82] I. Bertini, C. Luchinat, M. Piccioli, in *Methods in Enzymology, Vol. 339* (Eds.: T. L. James, V. Dötsch, U. Schmitz), Academic Press, **2001**, pp. 314-340.

[83] a) K. Nagayama, Y. Ozaki, Y. Kyojoku, T. Hase, H. Matsubara, *J Biol Chem.* **1983**, *94*, 893-902; b) L. Banci, I. Bertini, L. D. Eltis, I. C. Felli, D. H. W. Kastrau, C. Luchinat, M. Piccioli, R. Pieratelli, M. C. Smith, *European Journal of Biochemistry* **1994**, *225*, 715-725.
[84] H. M. McConnell, R. E. Robertson, *The Journal of Chemical Physics* **1958**, *29*, 1361.
[85] R. J. Kurland, B. R. McGarvey, *Journal of Magnetic Resonance* **1970**, *2*, 286-301.
[86] I. Bertini, C. Luchinat, G. Parigi, R. Pieratelli, *ChemBioChem* **2005**, *6*, 1536-1549.
[87] I. Bertini, C. Luchinat, G. Parigi, E. Ravera, *NMR of Paramagnetic Molecules*, second edition ed., Elsevier, Amsterdam, **2017**.
[88] I. Bertini, F. Capozzi, C. Luchinat, M. Piccioli, A. J. Vila, *J. Am. Chem. Soc.* **1994**, *116*, 651-660.
[89] F. F. L. Ho, C. N. Reilley, *Anal. Chem.* **1969**, *41*, 1835-1841.
[90] M. Karplus, *J. Am. Chem. Soc.* **1963**, *85*, 2870-2281.
[91] L. Banci, I. Bertini, C. Luchinat, *Struct. Bond.* **1990**, *72*, 113-136.
[92] aM. I. Belinsky, *JBIC* **1996**, *1*, 186-188; bJ. Xia, Z. Hu, C. V. Popescu, P. A. Lindahl, E. Münck, *J. Am. Chem. Soc.* **1997**, *119*, 8301-8312.
[93] a) W. R. Dunham, G. Palmer, R. H. Sands, A. J. Bearden, *Biochim. Biophys. Acta.* **1971**, *253*, 373-384; b) C. V. Popescu, E. Münck, *J. Am. Chem. Soc.* **1999**, *121*, 7877-7884.
[94] a) A. Donaire, C. M. Gorst, Z. H. Zhou, M. A. A. Adams, G. N. La Mar, *J. Am. Chem. Soc.* **1994**, *116*; b) E. Lebrun, C. Simenel, F. Guerlesquin, M. Delepierre, *Magn. Reson. Chem.* **1996**, *34*, 873-880.
[95] I. Bertini, F. Briganti, C. Luchinat, A. Scozzafava, *Inorg. Chem.* **1990**, *29*, 1874.
[96] a) P. Middleton, D. P. E. Dickson, C. E. Johnson, J. D. Rush, *Eur. J. Biochem.* **1980**, *104*, 289-296; b) P. Kyritsis, R. Kümmerle, J. Gaspard Huber, J. Gaillard, B. Guigliarelli, C. Popescu, E. Münck, J. M. Moulis, *Biochemistry* **1999**, *38*, 6335-6345.
[97] a) J. A. Christner, E. Münck, P. A. Janick, L. M. Siegel, *J. Biol. Chem.* **1981**, *256*, 2098-2101; b) J. A. Christner, E. Münck, C. Janiak, L. M. Siegel, *J.Biol.Chem.* **1983**, *258*, 11147-11156.
[98] G. Palmer, *Biochem. Soc. Trans.* **1985**, *13*, 548-560.
[99] V. Chechik, E. Carter, D. Murphy, *Electron Paramagnetic Resonance*, Oxford University Press, New York, **2016**.
[100] W. R. Hagen, *Biomolecular EPR Spectroscopy*, CRC Press Taylor and Francis, Boca Raton, Florida, **2009**.
[101] K. A. Vincent, A. Parkin, F. A. Armstrong, *Chem.Rev.* **2007**, *107*, 4366-4413.
[102] C. Léger, P. Bertrand, *Chem. Rev.* **2008**, *108*, 2379-2438.
[103] A. K. Jones, S. E. Lamle, H. R. Pershad, K. A. Vincent, S. P. J. Albracht, F. A. Armstrong, *J. Am. Chem. Soc.* **2003**, *125*, 8505-8514.
[104] J. N. Butt, F. A. Armstrong, in *Bioinorganic Electrochemistry, Vol. 1* (Eds.: O. Hammerich, J. Ulstrup), Springer, **2008**, pp. 91-128.
[105] a) F. A. Armstrong, P. A. Cox, H. A. O. Hill, V. J. Lowe, B. N. Oliver, *J. Electroanal. Chem.* **1987**, *217*, 331-366; b) C. F. Blanford, F. A. Armstrong, *J. Solid State Electrochem.* **2006**, *10*, 826-832.
[106] O. Rüdiger, J. M. Abad, E. C. Hatchikian, V. M. Fernandez, A. L. De Lacey, *J. Am. Chem. Soc.* **2005**, *127*, 16008-16009.
[107] F. A. Armstrong, J. Hirst, *Proc. Natl. Acad. Sci.* **2011**, *180*, 14049-14054.
[108] K. A. Vincent, A. Parkin, O. Lenz, S. P. J. Albracht, J. C. Fontecilla-Camps, R. Cammack, B. Friedrich, F. A. Armstrong, *J. Am. Chem. Soc.* **2005**, *127*, 18179-18189.
[109] a) S. T. Stripp, G. Goldet, C. Brandmayr, O. Sanganas, K. A. Vincent, M. Haumann, F. A. Armstrong, T. Happe, *PNAS* **2009**, *106*, 17331-17336; b) C. Baffert, M. Demuez, L. Cournac, B. Burlat, B. Guigliarelli, P. Bertrand, L. Girbal, C. Léger, *Angew. Chem. Int. Ed.* **2008**, *47*, 2052-2054.

[110] a) M. W. Adams, *J. Biol. Chem.* **1987**, *262*, 15054-15061; b) C. Baffert, L. Bertini, T. Lautier, C. Greco, K. Sybirna, P. Ezanno, E. Etienne, P. Soucaille, P. Bertrand, H. Bottin, I. Meynial-Salles, L. De Gioia, C. Léger, *J. Am. Chem. Soc.* **2011**, *133*, 2096-2099.
[111] A. F. Wait, C. Brandmayr, S. T. Stripp, C. Cavazza, J. C. Fontecilla-Camps, T. Happe, F. A. Armstrong, *J. Am. Chem. Soc.* **2011**, *133*, 1282-1285.
[112] A. L. de Lacey, E. C. Hatchikian, A. Volbeda, M. Frey, J. C. Fontecilla-Camps, V. M. Fernandez, *J. Am. Chem. Soc.* **1997**, *119*, 7181-7189.
[113] Y. S. Jung, I. R. Vassiliev, J. H. Golbeck, *J. Biol. Inorg. Chem.* **1997**, *2*, 209-217.

7. SCIENTIFIC CV

CONSTANZE SOMMER

TILSITERSTR. 31 A, 45470 MÜLHEIM AN DER RUHR, GERMANY
Phone: +49 (0)208 306 3895
Constanze.Sommer@gmx.de

Education

PhD Max-Planck Institut für Chemische Energiekonversion, Mülheim an der Ruhr
Arbeitsgruppe: Biophysikalische Chemie
Heinrich-Heine Universität Düsseldorf**,** Biochemistry April 2014-May 2018
Thesis: Natural and Modified Active Sites in [FeFe] Hydrogenases
in the Crosshairs of Biophysical Methods
Advisor: Prof. Dr. W. Lubitz, Prof. Dr. H. Heise
Final Grade: Sehr gut

MSc Universität Bielefeld, Structure and function of macromolecules January 2014
Thesis: Selektive Isotopenmarkierung und
Infrarot- differenzspektroskopische Analyse eines Pflanzen-Cryptochroms
der Blaulichtrezeptor-Familie
Advisor: Dr. T. Kottke
Final grade of master degree: 1.5

BSc Universität Bielefeld, Biochemistry June 2012
Thesis: Biochemische und funktionelle Charakterisierung
der Arylsulfatasen I und K
Advisor: Prof. Dr. T. Dierks
Final grade of bachelor degree: 1.7

Scientific experience/ Applied techniques

PhD/ MSc

- Molecular biology work and recombinant overexpression in *E. coli* with affinity chromatography
- Isotope labeling of protein backbone as well as [4Fe-4S] cluster and hydrogenase active site
- Protein FT-IR spectroscopy: Light-induced difference spectroscopy, transmission and ATR mode
- FT-IR spectroscopy coupled with electrochemistry
- Basic Cyclovoltammetry and Chronoamperometry
- Mössbauer spectroscopy: Biological sample preparation and data analysis
- Analysis of gas chromatography as well as mass spectroscopy data

BSc

- Molecular biology and expression of arylsulfatases in human cell lines
- Biological activity assays based on fluorescence
- SDS-PAGE with Western blotting

Journal Publications

Sommer, C., Dietz, M.S., Patschkowski T., Mathes T., Kottke, T., Light-induced Conformational Changes in the Plant Cryptochrome Photolyase Homology Region Resolved by Selective Isotope Labeling and Infrared Spectroscopy, Photochemistry and Photobiology **2017**, 93, 881.

Mirmohades, M., Adamska-Venkatesh, A., Sommer, C., Reijerse, E., Lomoth, R., Lubitz, W., and Hammarström, L., (2016) Following [FeFe] Hydrogenase Active Site Intermediates by Time-Resolved Mid-IR Spectroscopy., *J. Phys. Chem. Lett*., **7**, 3290.

Sommer, C., Adamska-Venkatesh, A., Pawlak, K., Birrell, J.A., Rüdiger, O., Reijerse, E.J., and Lubitz, W. (2017) Proton Coupled Electronic Rearrangement within the H-Cluster as an Essential Step in the Catalytic Cycle of [FeFe] Hydrogenases. *J. Am. Chem. Soc.* **139**, 1440.

Rumpel, S., Ravera, E., Sommer, C., Reijerse, E., Farès, C., Luchinat, C., and Lubitz, W. (2017) ^{1}H NMR Spectroscopy of [FeFe] Hydrogenase: Insight into the Electronic Structure of the Active Site. *J. Am. Chem. Soc.* **140**, 131.

Kertess, L., Wittkamp, F., Sommer, C., Esselborn, J., Rüdiger, O., Reijerse, E.J., Hofmann, E., Lubitz, W., Winkler, M., Happe, T., and Apfel, U.P. (2017) Chalcogenide substitution in the [2Fe] cluster of [FeFe]-hydrogenases conserves high enzymatic activity. *Dalton Trans*. **46**, 16947.

Chongdar, N., Birrell, J.A., Pawlak, K., Sommer, C., Reijerse, E.J., Rüdiger, O., Lubitz, W., and Ogata, H. (2018) Unique Spectroscopic Properties of the H-Cluster in a Putative Sensory [FeFe] Hydrogenase. *J. Am. Chem. Soc.* **140**, 1057.

Pelmenschikov, V., Birrell, J.A., Pham, C.C., Mishra, N., Wang, H., Sommer, C., Reijerse, E., Richers, C.P., Tamasaku, K., Yoda, Y., Rauchfuss, T.B., Lubitz, W., and Cramer, S.P. (2017) Reaction Coordinate Leading to H_2 Production in [FeFe]-Hydrogenase Identified by Nuclear Resonance Vibrational Spectroscopy and Density Functional Theory. *J Am Chem Soc.* **139**, 16894.

Sommer, C., Rumpel, S., Farès, C. , Artero, V., Reijerse, E., Lubitz, W., (2018) Spectroscopic investigations of a semi-synthetic [FeFe] hydrogenase with propane di-selenol as bridging ligand in the binuclear subsite: comparison to the wild type and propane di-thiol variants. *J Biol Inorg Chem.* **23**, 481.

Rumpel, S., Sommer, C., Reijerse, E., Farès, C., and Lubitz, W., (2018) Direct Detection of the Terminal Hydride Intermediate in [FeFe] Hydrogenase by NMR Spectroscopy, *J Am Chem Soc.* **140**, 3863.

Caserta, G., Papini, C., Adamska-Venkatesh, A., Sommer, C., Pecqueur, L., Reijerse, E., Lubitz, W., Artero, A., Atta, M., del Barrio, M., Fourmond, V., Léger, C., Fontecave, M., (2018) Engineering an [FeFe]-Hydrogenase: Do Accessory Clusters Influence O_2 Resistance and Catalytic Bias?, *J Am Chem Soc.* **140**, 5516.

Sommer, C., Richers, C.P., Rumpel, S., Reijerse E., Lubitz, W., and Rauchfuss, T.B., (2018) [RuRu] Analogue of [FeFe]-Hydrogenase Traps the Key Hydride Intermediate in the Enzyme's Catalytic Cycle, *Angew. Chem. Int. Ed.*, **57**, 5429.

Poster & talks

Poster

Sommer. C., A., Roy, S., Reijerse, E., Artero, V., Lubitz, W., Spectroscopic insight in artificially maturated [FeFe]-hydrogenase from *C. reinhardtii*, **2015**, EFEPR summerschool, Berlin.

Sommer. C., Adamska-Venkatesh, A., Roy, S., Reijerse, E., Artero, V., Lubitz, W., Selenium Substitution in [FeFe]-Hydrogenase, **2016**, 11th Hydrogenase Conference, Marseille.

Sommer, C., Adamska-Venkatesh, A., Pawlak, K., Birrell, J.A., Rüdiger, O., Reijerse, E., Lubitz, W., Proton Coupled Electronic Rearrangement Within the H-Cluster of [FeFe] Hydrogenases, **2017**, Fachbeirat, Mülheim an der Ruhr.

Talks

Sommer, C., Magnetic Resonance and Infrared Spectroscopy of a [FeFe]-hydrogenase with modified active sites, **2016**, bio-N^3MR meeting, Düsseldorf.

Courses

Methods in Molecular Energy Research: Theory and Spectroscopy, Summerschool, **2014**, Wissenschaftspark Gelsenkirchen.

7th EFEPR summer school: Advanced Electron Paramagnetic Resonance (EPR) Spectroscopy, **2015**, Berlin.

Professional Membership

GBM – Gesellschaft für Biochemie und Molekularbiologie e.V.
Establishment of a Junior-GBM Bielefeld during my studies with presidentship for 2 years.

Technical Skills

- Origin 9.0G
- Gaussian03W
- MATLABR2010a
- MS Office

Languages

English: Fluent
German: Mother tongue
French: Basic knowledge

Personal Interests

- Scouting activities: Pfadfinderschaft St. Georg e.V.; includes trips with children abroad and supervision of groups during activities (e.g. archery, canoeing) in international camps.
- Attending weekly volleyball and badminton training

Mülheim an der Ruhr, 22.05.2018

_____

-Constanze Sommer-

8. ACKNOWLEDGEMENT

My thesis could not have been realized without many people who supported me. I want to express my gratitude to all who helped me with one or the other issue.

- First I want to thank Prof. Dr. W. Lubitz and the Max Planck Society for giving me the opportunity to apply many different biophysical techniques, building the frame to discover [FeFe] hydrogenases and their active site during my PhD.

- Prof. Dr. H. Heise for agreeing to be my second supervisor.

- Dr. E. Reijerse for his supervision, including endless “ping pong emails” and lots of patience

- All my cooperation partners who let me be a part of their projects or enriched my projects with their expertise.

- Dr. A. Adamska-Venkatesh, Dr. J. Siebel and Dr. K. Weber for the almost seamless handing over of the well-organized projects and excellent cooperation.

- Dr. S. Rumpel for exploring [FeFe] hydrogenases with NMR spectroscopy and sharing the office as well as many stories with me.

- Prof. Dr. E. Ravera and Prof. Dr. C. Luchinat (CERM Florence) for supporting our NMR studies.

- Dr. O Rüdiger for his help with electrochemistry experiments and the performance of ATR measurements. Dr. J.A. Birrell for the discussions and ideas about my projects and Dr. K. Pawlak for his work and enthusiasm during the writing of my first publication.

- L. Kertess and F. Wittkamp (from RUB Bochum) for the nice time working together on the partly stubborn *Cp*I with incorporated $[Fe_2(ADSe)(CO)_4(CN)_2]^{2-}$ cofactor.

- Dr. M. Winkler, E. Hoffman, Dr. J. Esselborn, Prof. Dr. T. Happe and Dr. U.-P. Apfel (from RUB Bochum) for the fruitful cooperation.

- Dr. S. Roy for inorganic sample preparation, Prof. Dr. V. Artero and Prof. Dr. M. Fontecave (from CEA) for their ideas and our discussion about the manuscript.

- Dr. C. Richers for inorganic sample preparation and Prof. Dr. T. Rauchfuss (both from University of Illinois) for hanging in the ruthenium project and answering my inorganic chemistry questions with great patience.

- The entire group of Biophysical Chemistry in Max Planck Institute for Chemical Energy Conversion, from the apprentices (especially Julia Zerbe and Erika Katzwinkel) to the group leaders, who provided a great environment for research.

- I would like to thank all the MPI-CEC administrative, technical and scientific staff for all the help and support.

- Especially for the work in the labs I want to thank N. Breuer, P. Malkowski, Yvonne Brandenburger, B. Nöring, G. Klihm, C. Laurich, M. Reus and also Dr. K. Wrede who had an answer to each question and supported me.

Apart from the scientific work I want to thank the group for all the baked cakes, our nice group days, the CFF and an absolutely unexpected secret Santa present 2017!

The biggest thank you deserves my family at home in Gieboldehausen and Einbeck. From every point of view you encouraged me to work in the field I'm passionate about – even though it was biochemistry. Last but not least I want to thank my partner for his patience and understanding in every situation.